

HIGHER ORDER DISCONTINUOUS FINITE ELEMENT METHODS FOR  
DISCRETE ORDINATES THERMAL RADIATIVE TRANSFER

A Dissertation  
by  
PETER GREGORY MAGINOT

Submitted to the Office of Graduate and Professional Studies of  
Texas A&M University  
in partial fulfillment of the requirements for the degree of  
DOCTOR OF PHILOSOPHY

Chair of Committee,      Jean C. Ragusa  
Co-Chair of Committee,   Jim E. Morel  
Committee Members,      Marvin L. Adams  
                                Jean-Luc Guermond  
Head of Department,      Yassin A. Hassan

August 2015

Major Subject: Nuclear Engineering

Copyright 2015 Peter Gregory Maginot

## ABSTRACT

The linear discontinuous finite element method (LDFEM) is the current work horse of the radiation transport community. The popularity of LDFEM is a result of LDFEM (and its  $Q^1$  multi-dimensional extensions) being both accurate and preserving the thick diffusion limit. In practice, the LDFEM equations must be “lumped” to mitigate negative radiation transport solutions. Negative solutions are non-physical, but are inherent to the mathematics of LDFEM and other spatial discretizations.

Ongoing changes in high performance computing (HPC) are dictating a preference for increased numbers of floating point operations (FLOPS) per unknown. Higher order discontinuous finite element methods (DFEM), those with polynomial trial spaces greater than linear, have been found to offer more accuracy per unknown than LDFEM. However, DFEM with higher degree trial spaces have received only limited attention due to their increased computational time per unknown, LDFEM’s preservation of the thick diffusion limit, and the relative accuracy of LDFEM compared to other historical spatial discretizations. As solution methods evolve to make the most efficient use of HPC, it is possible that the increased computational work of higher order DFEM may become a strength rather than a hindrance.

For higher order DFEM to be useful in practice, lumping techniques must be developed to inhibit negative radiation transport solutions. We will show that traditional mass matrix lumping does not guarantee positive solutions and limits the overall accuracy of the DFEM scheme. To solve this problem, we propose a new, quadrature based, self-lumping technique. Our self-lumping technique does not limit solution order of convergence, improves solution positivity, and can be easily adapted to account for the within cell variation of interaction cross section. To test

and demonstrate the characteristics of our self-lumping methodology, we apply our schemes to several test problems: a homogeneous, source-free pure absorber; a pure absorber with spatially varying cross section; a model fuel depletion problem; and finally, we solve the grey thermal radiative transfer equations.

## DEDICATION

To my wife, Kelli, for traveling with me along all the unforeseen curves of life.

To my mom and dad, for providing my foundation and inspiration.

## ACKNOWLEDGEMENTS

I am thankful for the years of teaching and guidance provided by my co-chairs Dr. Jean Ragusa and Dr. Jim Morel; you convinced me long ago that a career in research was worth the extra challenges, costs, and years of work. I would also like to thank Dr. Marvin Adams for initially guiding me to the Computational Methods Group at Texas A&M and for encouraging me to consider Lawrence Livermore National Laboratory for post-graduation employment. Additionally, I thank I would like to thank Dr. Jean-Luc Guermond for your time and feedback on this dissertation and the master's thesis that preceeded it. Finally, I wish to thank the Department of Energy Computational Science Graduate Fellowship (administered by the Krell institute under grant number DE-FG02-97ER25308) for financial support during this work.

## NOMENCLATURE

DFEM	Discontinuous finite element method
DSA	Diffusion synthetic acceleration
LDFEM	Linear discontinuous finite element method
S2SA	$S_2$ synthetic acceleration
SL	Self-lumping
$S_N$	Discrete ordinates method
TL	Traditional lumping
TRT	Thermal radiative transfer
$\vec{\Omega}$	Particle direction
$c$	Speed of light
$I$	Photon radiation intensity
$\psi$	Neutron transport angular flux
$T$	Temperature
$\sigma_t$	Total interaction opacity
$\sigma_s$	Scattering interaction opacity
$\sigma_a$	Absorption opacity
$B$	Planck function
$B_g$	Planck function integrated across photon energy group $g$
$\underline{i}$	Basis function $i$
$\Sigma_t$	Macroscopic neutron total interaction cross section
$\Sigma_s$	Macroscopic neutron scattering interaction cross section
$\Sigma_a$	Macroscopic neutron absorption interaction cross section
$\Sigma_f$	Macroscopic neuotrn fission interaction cross section

## TABLE OF CONTENTS

	Page
ABSTRACT . . . . .	ii
DEDICATION . . . . .	iv
ACKNOWLEDGEMENTS . . . . .	v
NOMENCLATURE . . . . .	vi
TABLE OF CONTENTS . . . . .	vii
LIST OF FIGURES . . . . .	x
LIST OF TABLES . . . . .	xxiv
1. INTRODUCTION . . . . .	1
1.1 Simplifications of the Thermal Radiative Transfer Equations . . . . .	2
1.2 Spatial and Temporal Discretization . . . . .	3
1.2.1 Time Integration . . . . .	4
1.2.2 Spatial Discretization with Discontinuous Finite Elements . . . . .	4
1.3 Progression Towards Higher Order DFEM Thermal Radiative Transfer	5
2. DISCONTINUOUS FINITE ELEMENTS FOR RADIATION TRANSPORT	6
2.1 History of DFEM for Neutron Transport . . . . .	6
2.2 Mass Matrix Lumping Techniques . . . . .	8
2.3 Lumping Techniques for the 1-D $S_N$ Neutron Transport Equation with Arbitrary Order DFEM . . . . .	10
2.3.1 Weak Form Derivation . . . . .	10
2.3.2 Traditional Lumping . . . . .	15
2.3.3 Quadrature-Based Lumping . . . . .	15
2.3.4 Source Moment Evaluation . . . . .	15
2.4 Quadrature Point Selection . . . . .	16
2.5 Numerical Results . . . . .	21
2.5.1 Incident Flux Single-Cell Outflow Comparison . . . . .	22
2.5.2 Fixed Source Single-Cell Inflow Comparison . . . . .	25
2.5.3 Single-Cell Taylor Series Analysis . . . . .	31

2.5.4	Convergence Rates for Spatially Discretized 1-D Domains . . . . .	35
2.6	Conclusions About Self-Lumping . . . . .	43
3.	DFEM METHODS FOR NEUTRON TRANSPORT FOR PROBLEMS WITH SPATIALLY VARYING CROSS SECTION . . . . .	45
3.1	Weak Form Derivation . . . . .	47
3.2	Numerical Schemes . . . . .	48
3.2.1	Exact Spatial Integration . . . . .	49
3.2.2	Self-Lumping Quadrature Integration . . . . .	51
3.3	Pure Absorber Numerical Results . . . . .	51
3.3.1	Single Cell Outflow Comparisons . . . . .	52
3.3.2	Multiple Cell Spatial Convergence Rates . . . . .	56
3.3.3	Consequences of Assuming a Cell-Wise Constant Cross Section	71
3.3.4	Flux-Weighting versus Volume-Averaged Cross Sections . . . . .	78
3.3.5	Effects of Mesh Spacing . . . . .	83
3.4	Conclusions to Be Carried Forward . . . . .	94
4.	ITERATIVE ACCELERATION FOR THE $S_N$ NEUTRON TRANSPORT EQUATIONS . . . . .	96
4.1	Iterative Solution of the Neutron Transport $S_N$ Equations . . . . .	96
4.2	Qualitative Comparison of Different Synthetic Acceleration Techniques	99
4.3	$S_2$ Synthetic Acceleration . . . . .	101
4.4	Modified Interior Penalty Diffusion Synthetic Acceleration . . . . .	107
4.5	Numerical Results Verifying Implementation and Performance of S2SA and MIP DSA . . . . .	114
4.5.1	Spatially Constant Cross Section Scattering Problem . . . . .	115
4.5.2	Spatially Varying Cross Section Scattering Problem . . . . .	127
4.6	Conclusions . . . . .	129
5.	FUEL DEPLETION PROBLEM . . . . .	132
5.1	Problem Physical Description . . . . .	132
5.1.1	Microscopic Cross Section and Yield Data . . . . .	136
5.1.2	Reactor Power Levels and Normalization . . . . .	139
5.2	Spatial Discretization . . . . .	140
5.2.1	Radiation Solution . . . . .	141
5.2.2	Nuclide Density . . . . .	143
5.3	Numerical Results . . . . .	146
6.	GREY THERMAL RADIATIVE TRANSFER- THEORY . . . . .	157
6.1	Linearization and Discretization of Grey TRT Equations . . . . .	158

6.1.1	SDIRK Time Integration . . . . .	158
6.1.2	Spatially Analytic Linearization . . . . .	160
6.1.3	Spatially Discretized Linearization . . . . .	171
6.1.4	Consistency of Pseudo Cross Sections . . . . .	177
6.2	Iterative Solution Process . . . . .	184
6.3	Methods for Tolerating Negative Solutions . . . . .	187
6.4	Adaptive Time Stepping Methods . . . . .	188
6.5	Software Implementation . . . . .	191
<b>7.</b>	<b>GREY THERMAL RADIATIVE TRANSFER- NUMERICAL RESULTS .</b>	<b>194</b>
7.1	Problems with Analytic Solutions . . . . .	196
7.1.1	Su-Olson Problem . . . . .	196
7.1.2	Method of Manufactured Solutions . . . . .	200
7.2	Thermal Radiative Transfer Simulations Without Analytic Solutions .	228
7.2.1	Unity Marshak Wave Problem . . . . .	228
7.2.2	Physical Marshak Wave Problem . . . . .	253
7.3	Effectiveness of MIP DSA for TRT Iterative Acceleration . . . . .	270
<b>8.</b>	<b>SUMMARY AND CONCLUSIONS . . . . .</b>	<b>274</b>
8.1	Summary . . . . .	274
8.2	Conclusions . . . . .	275
8.2.1	Future Work . . . . .	276
<b>REFERENCES . . . . .</b>		<b>278</b>

## LIST OF FIGURES

FIGURE	Page
2.1 Angular flux outflow as a function of $h$ , for different linear trial space DFEM schemes, from a homogeneous, single cell pure absorber. . . . .	23
2.2 Angular flux outflow as a function of $h$ , for different quadratic trial space DFEM schemes, from a homogeneous, single cell pure absorber. . . . .	23
2.3 Angular flux outflow as a function of $h$ , for different cubic trial space DFEM schemes, from a homogeneous, single cell pure absorber. . . . .	24
2.4 Angular flux outflow as a function of $h$ , for different quartic trial space DFEM schemes, from a homogeneous, single cell pure absorber. . . . .	24
2.5 Numerical inflow values as a function of $\frac{S_1}{S_0}$ for a single cell (vacuum case) with a $\delta$ -shaped source, using linear DFEM. . . . .	26
2.6 Numerical inflow values as a function of $\frac{S_1}{S_0}$ for a single cell (vacuum case) with a $\delta$ -shaped source, using quadratic DFEM. . . . .	27
2.7 Numerical inflow values as a function of $\frac{S_1}{S_0}$ for a single cell (vacuum case) with a $\delta$ -shaped source, using cubic DFEM. . . . .	28
2.8 Numerical inflow values as a function of $\frac{S_1}{S_0}$ for a single cell (vacuum case) with a $\delta$ -shaped source, using quartic DFEM. . . . .	28
2.9 Numerical inflow values as a function of $\frac{S_1}{S_0}$ , for a single cell (absorber case) with a $\delta$ -shaped source, using linear DFEM. . . . .	29
2.10 Numerical inflow values as a function of $\frac{S_1}{S_0}$ , for a single cell (absorber case) with a $\delta$ -shaped source, using quadratic DFEM. . . . .	29
2.11 Numerical inflow values as a function of $\frac{S_1}{S_0}$ , for a single cell (absorber case) with a $\delta$ -shaped source, using cubic DFEM. . . . .	30
2.12 Numerical inflow values as a function of $\frac{S_1}{S_0}$ , for a single cell (absorber case) with a $\delta$ -shaped source, using quartic DFEM. . . . .	30

2.13	Convergence rate of the $L_2$ norm of the error, $E_\psi$ , as a function of the mesh cell size for a pure absorber discretized with linear DFEM. . . . .	37
2.14	Convergence rate of the $L_2$ norm of the error, $E_\psi$ , as a function of the mesh cell size for a pure absorber discretized with quadratic DFEM. . . . .	38
2.15	Convergence rate of the $L_2$ norm of the error, $E_\psi$ , as a function of the mesh cell size for a pure absorber discretized with cubic DFEM. . . . .	38
2.16	Convergence rate of the $L_2$ norm of the error, $E_\psi$ , as a function of the mesh cell size for a pure absorber discretized with quartic DFEM. . . . .	39
2.17	Convergence rate for $E_{\psi,A}$ as a function of the mesh cell size for a homogeneous pure absorber and linear DFEM. . . . . . . . . . .	39
2.18	Convergence rate for $E_{\psi,A}$ as a function of the mesh cell size for a homogeneous pure absorber and quadratic DFEM. . . . . . . . . .	40
2.19	Convergence rate for $E_{\psi,A}$ as a function of the mesh cell size for a homogeneous pure absorber and cubic DFEM. . . . . . . . . .	40
2.20	Convergence rate for $E_{\psi,A}$ as a function of the mesh cell size for a homogeneous pure absorber and quartic DFEM. . . . . . . . . .	41
2.21	Convergence rate of $E_{\psi,out}$ as a function of the mesh cell size for a homogeneous pure absorber for linear DFEM. . . . . . . . . .	41
2.22	Convergence rate of $E_{\psi,out}$ as a function of the mesh cell size for a homogeneous pure absorber for quadratic DFEM. . . . . . . . .	42
2.23	Convergence rate of $E_{\psi,out}$ as a function of the mesh cell size for a homogeneous pure absorber for cubic DFEM. . . . . . . . .	42
2.24	Convergence rate of $E_{\psi,out}$ as a function of the mesh cell size for a pure absorber for quartic DFEM. . . . . . . . . .	43
3.1	Numerical outflow from single cell pure absorber with $\Sigma_t(x) = c_1 e^{c_2 x}$ , as a function of $c_2$ with constant optical thickness for linear DFEM. . . . .	54
3.2	Numerical outflow from single cell pure absorber with $\Sigma_t(x) = c_1 e^{c_2 x}$ , as a function of $c_2$ with constant optical thickness for quadratic DFEM. . . . .	54
3.3	Numerical outflow from single cell pure absorber with $\Sigma_t(x) = c_1 e^{c_2 x}$ , as a function of $c_2$ with constant optical thickness for cubic DFEM. . . . .	55

3.4	Numerical outflow from single cell pure absorber with $\Sigma_t(x) = c_1 e^{c_2 x}$ , as a function of $c_2$ with constant optical thickness for quartic DFEM.	55
3.5	Convergence of $E_\psi$ as a function of mesh size for a pure absorber with exponentially varying cross section discretized with linear DFEM. . .	59
3.6	Convergence of $E_\psi$ as a function of mesh size for a pure absorber with exponentially varying cross section discretized with quadratic DFEM.	59
3.7	Convergence of $E_\psi$ as a function of mesh size for a pure absorber with exponentially varying cross section discretized with cubic DFEM. . .	60
3.8	Convergence of $E_\psi$ as a function of mesh size for a pure absorber with exponentially varying cross section discretized with quartic DFEM. . .	60
3.9	Convergence of $E_{\psi_A}$ as a function of mesh size for a pure absorber with exponentially varying cross section discretized with linear DFEM.	61
3.10	Convergence of $E_{\psi_A}$ as a function of mesh size for a pure absorber with exponentially varying cross section discretized with quadratic DFEM.	61
3.11	Convergence of $E_{\psi_A}$ as a function of mesh size for a pure absorber with exponentially varying cross section discretized with cubic DFEM.	62
3.12	Convergence of $E_{\psi_A}$ as a function of mesh size for a pure absorber with exponentially varying cross section discretized with quartic DFEM. . .	62
3.13	Convergence of $E_{\psi_{out}}$ as a function of mesh size for a pure absorber with exponentially varying cross section discretized with linear DFEM.	63
3.14	Convergence of $E_{\psi_{out}}$ as a function of mesh size for a pure absorber with exponentially varying cross section discretized with quadratic DFEM. . . . .	63
3.15	Convergence of $E_{\psi_{out}}$ as a function of mesh size for a pure absorber with exponentially varying cross section discretized with cubic DFEM.	64
3.16	Convergence of $E_{\psi_{out}}$ as a function of mesh size for a pure absorber with exponentially varying cross section discretized with quartic DFEM.	64
3.17	Convergence of $E_{IR}$ as a function of mesh size for a pure absorber with exponentially varying cross section discretized with linear DFEM.	66
3.18	Convergence of $E_{IR}$ as a function of mesh size for a pure absorber with exponentially varying cross section discretized with quadratic DFEM.	67

3.19	Convergence of $E_{IR}$ as a function of mesh size for a pure absorber with exponentially varying cross section discretized with cubic DFEM.	67
3.20	Convergence of $E_{IR}$ as a function of mesh size for a pure absorber with exponentially varying cross section discretized with quartic DFEM.	68
3.21	Convergence of $E_{IR_A}$ as a function of mesh size for a pure absorber with exponentially varying cross section discretized with linear DFEM.	69
3.22	Convergence of $E_{IR_A}$ as a function of mesh size for a pure absorber with exponentially varying cross section discretized with quadratic DFEM.	69
3.23	Convergence of $E_{IR_A}$ as a function of mesh size for a pure absorber with exponentially varying cross section discretized with cubic DFEM.	70
3.24	Convergence of $E_{IR_A}$ as a function of mesh size for a pure absorber with exponentially varying cross section discretized with quartic DFEM.	70
3.25	Plots of the analytic $\psi(x)$ , CXS DFEM $\tilde{\psi}(x)$ , and cell-wise constant cross section analytic $\psi_C(x)$ , for the pure absorber with exponential cross section.	73
3.26	Plots of the analytic $IR(x)$ , CXS DFEM $\widetilde{IR}(x)$ , and cell-wise constant cross section analytic $IR_C(x)$ for the pure absorber with exponential cross section.	73
3.27	Plot of the linear trial space SLXS Lobatto and CXS DFEM approximations of $\tilde{\psi}(x)$ for the pure absorber problem with exponentially varying cross section.	74
3.28	Plot of the linear trial space SLXS Lobatto and CXS DFEM approximations of $\widetilde{IR}(x)$ for the pure absorber problem with exponentially varying cross section.	75
3.29	Plot of the CXS DFEM cell average angular flux at cell centers with linear interpolation for a pure absorber with exponentially varying spatial cross section.	77
3.30	Plot of the CXS DFEM cell average interaction rate at cell centers with linear interpolation for a pure absorber with exponentially varying spatial cross section.	77
3.31	$E_\psi$ for FW CXS vs. CXS DFEM for a pure absorber with exponentially varying cross section using a cubic DFEM trial space.	79

3.32	$E_{\psi_A}$ for FW CXS vs. CXS DFEM for a pure absorber with exponentially varying cross section using a cubic DFEM trial space. . . . .	79
3.33	$E_{IR}$ for FW CXS vs. CXS DFEM for a pure absorber with exponentially varying cross section using a cubic DFEM trial space. . . . .	80
3.34	$E_{IR_A}$ for FW CXS vs. CXS DFEM for a pure absorber with exponentially varying cross section using a cubic DFEM trial space. . . . .	80
3.35	Plot of the linear trial space FW CXS and CXS DFEM approximations to $\tilde{\psi}(x)$ for the pure absorber problem with exponentially varying spatial cross section. . . . .	81
3.36	Plot of the linear trial space FW CXS and CXS DFEM approximations to $\tilde{IR}(x)$ for the pure absorber problem with exponentially varying spatial cross section. . . . .	82
3.37	Asymptotic convergence of $E_\psi$ for the SLXS Lobatto scheme using a quadratic trial space with different mesh spacing methodologies. . . .	85
3.38	Asymptotic convergence of $E_{\psi_A}$ for the SLXS Lobatto scheme using a quadratic trial space with different mesh spacing methodologies. . . .	86
3.39	Asymptotic convergence of $E_{IR}$ for the SLXS Lobatto scheme using a quadratic trial space with different mesh spacing methodologies. . . .	86
3.40	Asymptotic convergence of $E_{IR_A}$ for the SLXS Lobatto scheme using a quadratic trial space with different mesh spacing methodologies. . . .	87
3.41	$E_\psi$ for SLXS Lobatto using a quadratic trial space scheme with different mesh spacing methodologies, at low resolutions. . . . .	88
3.42	$E_{\psi_A}$ for SLXS Lobatto using a quadratic trial space scheme with different mesh spacing methodologies, at low resolutions. . . . .	89
3.43	$E_{IR}$ for SLXS Lobatto using a quadratic trial space scheme with different mesh spacing methodologies, at low resolutions. . . . .	89
3.44	$E_{IR_A}$ for SLXS Lobatto using a quadratic trial space scheme with different mesh spacing methodologies, at low resolutions. . . . .	90
3.45	$E_\psi$ for SLXS Gauss using a quadratic trial space with different mesh spacing methodologies, at low resolutions. . . . .	90

3.46	$E_{\psi_A}$ for SLXS Gauss using a quadratic trial space with different mesh spacing methodologies, at low resolutions. . . . .	91
3.47	$E_{IR}$ for SLXS Gauss using a quadratic trial space with different mesh spacing methodologies, at low resolutions. . . . .	91
3.48	$E_{IR_A}$ fore SLXS Gauss using a quadratic trial space with different mesh spacing methodologies, at low resolutions. . . . .	92
3.49	$E_{\psi}$ for CXS DFEM using a quadratic trial space with different mesh spacing methodologies, at low resolutions. . . . .	92
3.50	$E_{\psi_A}$ for CXS DFEM using a quadratic trial space with different mesh spacing methodologies, at low resolutions. . . . .	93
3.51	$E_{IR}$ for CXS DFEM using a quadratic trial space with different mesh spacing methodologies, at low resolutions. . . . .	93
3.52	$E_{IR_A}$ for CXS DFEM using a quadratic trial space with different mesh spacing methodologies, at low resolutions. . . . .	94
4.1	Estimates of $\rho$ for different iterative techniques for $S_8$ , $c = 0.999$ , linear SL Gauss. . . . .	116
4.2	Estimates of $\rho$ for different iterative techniques for $S_8$ , $c = 0.999$ , linear SL Lobatto. . . . .	117
4.3	Estimate of $\rho$ for S2SA as a function of $S_N$ order for $c = 0.999$ for linear SL Gauss. . . . .	118
4.4	Estimate of $\rho$ for S2SA as a function of $S_N$ order for $c = 0.999$ for linear SL Lobatto. . . . .	118
4.5	Estimates of $\rho$ for S2SA as a function of $c$ for $S_8$ linear SL Gauss. . . . .	119
4.6	Estimates of $\rho$ for S2SA as a function of $c$ for $S_8$ linear SL Lobatto. . . . .	119
4.7	Estimates of $\rho$ for S2SA with $S_8$ , $c = 0.999$ , SL Gauss as a function of trial space degree. . . . .	120
4.8	Estimates of $\rho$ for S2SA with $S_8$ , $c = 0.999$ , SL Lobatto as a function of trial space degree. . . . .	120
4.9	Estimate of $\rho$ for MIP DSA as a function of $S_N$ order for $c = 0.999$ linear SL Gauss. . . . .	121

4.10 Estimate of $\rho$ for MIP DSA as a function of $S_N$ order for $c = 0.999$ linear SL Lobatto. . . . .	122
4.11 Estimate of $\rho$ for MIP DSA as a function of $c$ for $S_8$ linear SL Gauss. . . . .	123
4.12 Estimate of $\rho$ for MIP DSA as a function of $c$ for $S_8$ linear SL Lobatto. . . . .	123
4.13 $\rho$ for MIP DSA as a function of $c$ for $S_8$ linear SL Gauss, with $Z_{MIP} = 4$ . . . . .	124
4.14 $\rho$ for MIP DSA as a function of $c$ for $S_8$ linear SL Lobatto, with $Z_{MIP} = 4$ . . . . .	125
4.15 Estimate of $\rho$ for MIP DSA as a function of $P$ for $S_8$ , $c = 0.999$ , SL Gauss with $Z_{MIP} = 2$ . . . . .	125
4.16 Estimate of $\rho$ for MIP DSA as a function of $P$ for $S_8$ , $c = 0.999$ , SL Lobatto with $Z_{MIP} = 2$ . . . . .	126
4.17 $\rho$ for MIP DSA as a function of $P$ for $S_8$ , $c = 0.999$ , SL Gauss with $Z_{MIP} = 4$ . . . . .	126
4.18 Estimates of $\rho$ for MIP DSA as a function of $P$ for $S_8$ , $c = 0.999$ , SL Lobatto with $Z_{MIP} = 4$ . . . . .	127
4.19 Estimate of $\rho$ for S2SA as a function of $\overline{\Sigma_t \Delta x}$ and $P$ , with SLXS Gauss. . . . .	128
4.20 Estimate of $\rho$ for S2SA as a function of $\overline{\Sigma_t \Delta x}$ and $P$ , with SLXS Lobatto. . . . .	129
4.21 Estimate of $\rho$ for MIP DSA with SLXS Gauss as a function of $\overline{\Sigma_t \Delta x}$ and $P$ . . . . .	130
4.22 Estimate of $\rho$ for MIP DSA with SLXS Lobatto as a function of $\overline{\Sigma_t \Delta x}$ and $P$ . . . . .	130
5.1 Depletion problem fuel/moderator lattice. . . . .	132
5.2 Depletion problem possible transmutation paths and mechanisms. . . . .	134
5.3 Example normalized scalar flux profiles at beginning of fuel burn-up cycle. . . . .	139
5.4 Example normalized scalar flux profiles at end of fuel burn-up cycle. . . . .	140
5.5 Normalized total scalar flux error for the depletion problem at end of cycle, for linear DFEM. . . . .	147

5.6	Normalized total scalar flux error for the depletion problem at end of cycle, for quadratic DFEM. . . . .	148
5.7	Normalized total scalar flux error for the depletion problem at end of cycle, for cubic DFEM. . . . .	148
5.8	Normalized total scalar flux error for the depletion problem at end of cycle, for quartic DFEM. . . . .	149
5.9	Normalized fissile nuclide density error for the depletion problem at end of cycle, for linear DFEM . . . . .	150
5.10	Normalized fissile nuclide density error for the depletion problem at end of cycle, for quadratic DFEM. . . . .	150
5.11	Normalized fissile nuclide density error for the depletion problem at end of cycle, for cubic DFEM. . . . .	151
5.12	Normalized fissile nuclide density error for the depletion problem at end of cycle, for quartic DFEM. . . . .	151
5.13	Normalized fertile nuclide density error for the depletion problem at end of cycle, for linear DFEM. . . . .	152
5.14	Normalized fertile nuclide density error for the depletion problem at end of cycle, for quadratic DFEM.. . . . .	152
5.15	Normalized fertile nuclide density error for the depletion problem at end of cycle, for cubic DFEM. . . . .	153
5.16	Normalized fertile nuclide density error for the depletion problem at end of cycle, for quartic DFEM. . . . .	153
5.17	Normalized parasitic absorber fission product error for the depletion problem at end of cycle, for linear DFEM. . . . .	154
5.18	Normalized parasitic absorber fission product error for the depletion problem at end of cycle, for quadratic DFEM. . . . .	154
5.19	Normalized parasitic absorber fission product error for the depletion problem at end of cycle, for cubic DFEM. . . . .	155
5.20	Normalized parasitic absorber fission product error for the depletion problem at end of cycle, for quartic DFEM. . . . .	155

7.1	$S_2$ radiation energy density profile for Su-Olson problem. . . . .	198
7.2	$S_2$ material energy density profile for Su-Olson problem. . . . .	198
7.3	$S_8$ radiation energy density profile for Su-Olson problem. . . . .	199
7.4	$S_8$ material energy density profile for Su-Olson problem. . . . .	199
7.5	Convergence of $E_\phi$ for the TL scheme in problem MMS1. . . . .	203
7.6	Convergence of $E_\phi$ for the SL Lobatto scheme in problem MMS1. . .	203
7.7	Convergence of $E_\phi$ for the SL Gauss scheme in problem MMS1. . . .	204
7.8	Convergence of $E_T$ for the TL scheme in problem MMS1. . . . .	204
7.9	Convergence of $E_T$ for the SL Lobatto scheme in problem MMS1. . .	205
7.10	Convergence of $E_T$ for the SL Gauss scheme in problem MMS1. . .	205
7.11	Convergence of $E_{\phi_A}$ for the SL Lobatto scheme in problem MMS1. . .	207
7.12	Convergence of $E_{\phi_A}$ for the SL Gauss scheme in problem MMS1. . . .	207
7.13	Convergence of $E_{T_A}$ for the SL Lobatto scheme in problem MMS1. . .	208
7.14	Convergence of $E_{T_A}$ for the SL Gauss scheme in problem MMS1. . . .	208
7.15	Convergence of $E_\phi$ for the SL Lobatto scheme in problem MMS2. . .	210
7.16	Convergence of $E_\phi$ for the SL Gauss scheme in problem MMS2. . . .	211
7.17	Convergence of $E_T$ for the SL Lobatto scheme in problem MMS2. . .	211
7.18	Convergence of $E_T$ for the SL Gauss scheme in problem MMS2. . . .	212
7.19	Convergence of $E_{T_A}$ for the SL Lobatto scheme in problem MMS2. . .	213
7.20	Convergence of $E_{T_A}$ for the SL Gauss scheme in problem MMS2. . . .	213
7.21	Convergence of $E_\phi$ for the SLXS Lobatto scheme in problem MMS2. .	214
7.22	Convergence of $E_\phi$ for the SLXS Gauss scheme in problem MMS2. . .	214
7.23	Convergence of $E_T$ for the SLXS Lobatto scheme in problem MMS2. .	215
7.24	Convergence of $E_T$ for the SLXS Gauss scheme in problem MMS2. . .	215

7.25 Convergence of $E_{\phi_A}$ for the SLXS Lobatto scheme in problem MMS2.	216
7.26 Convergence of $E_{\phi_A}$ for the SLXS Gauss scheme in problem MMS2. .	216
7.27 Convergence of $E_{T_A}$ for the SLXS Lobatto scheme in problem MMS2.	217
7.28 Convergence of $E_{T_A}$ for the SLXS Gauss scheme in problem MMS2. .	217
7.29 Convergence of $E_T$ for the SLXS Gauss scheme in problem MMS2 using $\epsilon_T = 10^{-8}$ and $\epsilon_\phi = 10^{-10}$ . . . . .	219
7.30 Convergence of $E_\phi$ for the SLXS Lobatto scheme in problem MMS2 using $\epsilon_T = 10^{-8}$ and $\epsilon_\phi = 10^{-10}$ . . . . .	220
7.31 Convergence of $E_\phi$ for SLXS Lobatto scheme for steady state test problem. . . . .	221
7.32 Convergence of $E_\phi$ for SLXS Gauss scheme, for steady state test problem.	222
7.33 Convergence of $E_T$ for SLXS Lobatto scheme, for steady state test problem. . . . .	222
7.34 Convergence of $E_T$ for SLXS Gauss scheme, for steady state test prob- lem. . . . .	223
7.35 Convergence of $E_{\phi_A}$ for SLXS Lobatto scheme, for steady state test problem. . . . .	224
7.36 Convergence of $E_{\phi_A}$ for SLXS Gauss scheme, for steady state test problem. . . . .	224
7.37 Convergence of $E_{T_A}$ for SLXS Lobatto scheme, for steady state test problem. . . . .	225
7.38 Convergence of $E_{T_A}$ for SLXS Gauss scheme, for steady state test problem. . . . .	225
7.39 Convergence of $E_\phi$ for different time integrators as a function of $\Delta t$ . .	227
7.40 Convergence of $E_T$ for different time integrators as a function of $\Delta t$ . .	227
7.41 Linear SL Lobatto radiation solution for the unity Marshak wave prob- lem assuming cell-wise constant volumetric averaged opacities. . . . .	230
7.42 Linear SL Lobatto temperature solution for the unity Marshak wave problem assuming cell-wise constant volumetric averaged opacities. . . . .	230

7.43 Linear SL Lobatto temperature solution for the unity Marshak wave problem near the wavefront. . . . .	231
7.44 Linear SLXS Lobatto angle integrated intensity solution with 80 cells. . . . .	232
7.45 Linear SLXS Lobatto temperature solution with 80 cells. . . . .	232
7.46 Linear SLXS Lobatto radiation solution near wavefront with increasing spatial mesh refinement. . . . .	233
7.47 Linear SLXS Lobatto temperature solution near wavefront with increasing spatial mesh refinement. . . . .	233
7.48 Quartic SLXS Gauss radiation solution near wavefront with increasing spatial mesh refinement. . . . .	234
7.49 Quartic SLXS Gauss temperature solution near wavefront with increasing spatial mesh refinement. . . . .	235
7.50 SLXS Lobatto radiation energy density solution with 320 cells for different $P$ near Marshak wavefront. . . . .	236
7.51 SLXS Lobatto material temperature solution with 320 cells for different $P$ near Marshak wavefront. . . . .	236
7.52 Quartic SLXS Lobatto radiation energy density solution with 1280 cells for different time refinements near the Marshak wavefront. . . . .	237
7.53 Quartic SLXS Lobatto temperature solution with 1280 cells for different time refinements near the Marshak wavefront. . . . .	238
7.54 Plot of the radiation energy density on a logarithmic scale for different high resolution simulations near the Marshak wavefront. . . . .	239
7.55 Plot of the angular intensity on a logarithmic scale near the transport boundary layer at the Marshak wave front. . . . .	240
7.56 $S_8$ and $S_2$ material temperature profiles. . . . .	241
7.57 $S_8$ and $S_2$ radiation energy density profiles. . . . .	242
7.58 Logarithmic plot of $S_8$ intensities for the unity Marshak wave problem.	243
7.59 Logarithmic plot of intensity near glancing $\mu = +0.1834$ boundary layer. . . . .	244

7.60	Logarithmic plot of intensity boundary layers near thermal wavefront.	245
7.61	Comparison of $S_8$ and $S_{32}$ material temperature profiles for the unity Marshak wave problem. . . . .	246
7.62	Comparison of $S_8$ and $S_{32}$ angle integrated intensity solutions for the unity Marshak wave problem. . . . .	246
7.63	$S_{32}$ intensity solutions for all $\mu_d > 0$ , for the unity Marshak wave problem. . . . .	247
7.64	$S_{32}$ radiation energy density at different times for the unity Marshak wave problem. . . . .	248
7.65	$S_{32}$ material temperature solution at different times for the unity Marshak wave problem. . . . .	248
7.66	$S_{32}$ radiation energy density at $t = 0.1$ for the unity Marshak wave problem. . . . .	249
7.67	$S_{32}$ radiation energy density at $t = 2$ for the unity Marshak wave problem. . . . .	250
7.68	$S_{32}$ angular intensity for $\mu_d > 0$ at $t = 0.1$ for the unity Marshak wave problem. . . . .	250
7.69	$S_{32}$ angular intensity for $\mu_d > 0$ at $t = 2$ for the unity Marshak wave problem. . . . .	251
7.70	$S_8$ radiation energy density solutions for the modified unity Marshak wave problem with $\sigma_a = \frac{1000}{T^3}$ at different times using linear SLXS Lobatto, and 1000 spatial cells for $x \in [0, 1]$ . . . . .	252
7.71	$S_8$ material temperature solutions for modified unity Marshak wave problem with $\sigma_a = \frac{1000}{T^3}$ at different times using linear SLXS Lobatto, and 1000 spatial cells for $x \in [0, 1]$ . . . . .	253
7.72	$S_8$ angle integrated intensity solutions at various times for physical Marshak wave problem generated using 100 spatial cells and cubic SLXS Lobatto. . . . .	254
7.73	Temperature solutions at various times for physical Marshak wave problem generated using 100 spatial cells and cubic SLXS Lobatto. . . . .	255

7.74 Time step sizes selected for different adaptive criterion applied to a linear SLXS Lobatto discretization of the physical Marshak wave problem with $S_2$ angular quadrature and 50 spatial cells. . . . .	256
7.75 Time step sizes selected for adaptive criteria for volumetric radiation source driven problem. . . . .	260
7.76 Time step sizes for modified point-wise adaptive criteria for cubic SLXS Lobatto discretization of the physical Marshak wave problem with different $T_{offset}$ . . . . .	261
7.77 Time step sizes for modified point-wise adaptive criteria for cubic SLXS Lobatto discretization of the physical Marshak wave problem with different $T_{offset}$ . . . . .	261
7.78 Zoom in of $\Delta t$ trace for the modified point-wise adaptive criteria using linear SLXS Lobatto discretizations of the physical Marshak wave problem with 50 and 100 cells. . . . .	262
7.79 Time step traces for the modified point-wise adaptive scheme with $T_{offset} = 1$ [eV] for linear and cubic SLXS Lobatto with 100 spatial cells. . . . .	263
7.80 Time step sizes for volumetric and modified point-wise adaptive criteria for cubic SLXS Lobatto discretization of the physical Marshak wave problem. . . . .	264
7.81 Time step sizes for volumetric adaptive criteria with $N_{cg} = 1$ and $N_{cg} = 100$ for cubic SLXS Lobatto in 100 cell physical Marshak wave problem. . . . .	265
7.82 Time step sizes for volumetric adaptive criteria with $N_{cg} = 1$ and $N_{cg} = 100$ for cubic SLXS Lobatto in 100 cell physical Marshak wave problem. . . . .	266
7.83 Comparison of angle integrated intensity for different adaptive criteria at $t = 0.1$ [sh]. . . . .	267
7.84 Comparison of temperature for different adaptive criteria at $t = 0.1$ [sh].	268
7.85 Comparison of angle integrated intensity for different adaptive criteria at $t = 0.1$ [sh] with cubic SLXS Lobatto using 100 cells vs. linear SLXS Lobatto using 100 cells and the point-wise adaptive criteria. . .	269



## LIST OF TABLES

TABLE	Page
2.1 Nomenclature of numerical schemes. . . . .	9
2.2 Accuracy of self-lumping closed Newton-Cotes quadratures for DFEM trial spaces of polynomial degree $P$ . . . . .	17
2.3 Accuracy of self-lumping Gauss quadratures for DFEM trial spaces of polynomial degree $P$ . . . . .	18
2.4 Accuracy of self-lumping Lobatto quadratures for DFEM trial spaces of polynomial degree $P$ . . . . .	18
2.5 Equivalence of traditional lumping and closed Newton-Cotes quadrature approximation of the mass matrix. . . . .	20
2.6 Local truncation error analysis in $\tilde{\psi}_{in,d}$ for a single cell problem with constant cross section, for Exact DFEM and TL. . . . .	32
2.7 Local truncation error analysis in $\tilde{\psi}_{in,d}$ for a single cell problem with constant cross section, for SL Newton-Cotes, SL Gauss, and SL Lobatto. . . . .	33
2.8 Local truncation error analysis in $\tilde{\psi}_{A,d}$ for a single cell problem with constant cross section, for Exact DFEM and TL. . . . .	33
2.9 Local truncation error analysis in $\tilde{\psi}_{A,d}$ for a single cell problem with constant cross section, for SL Newton-Cotes, SL Gauss, and SL Lobatto	33
2.10 Local truncation error analysis in $\tilde{\psi}_{out,d}$ for a single cell with constant cross section, for Exact DFEM and TL. . . . .	34
2.11 Local truncation error analysis in $\tilde{\psi}_{out,d}$ for a single cell with constant cross section, for SL Newton-Cotes, SL Gauss, and SL Lobatto. . . . .	34
3.1 Nomenclature of numerical schemes considered for the pure absorber problem with a spatially exponential cross section. . . . .	49
3.2 Shorthand notation of different cell spacing schemes. . . . .	83

5.1	Fuel atom density data. . . . .	133
5.2	Water atom density data. . . . .	133
5.3	Water microscopic cross section, in barns [ $10^{-24} \text{ cm}^2$ ]. Moderator is composed only of $H_2O$ . . . . .	137
5.4	Fuel microscopic cross sections, in barns [ $10^{-24} \text{ cm}^2$ ]. . . . .	137
5.5	Average neutron yield per fission, and fission microscopic cross section [ $10^{-24} \text{ cm}^2$ ]. . . . .	137
5.6	Radiative capture fraction, and fission probability for fissile and fertile nuclides. . . . .	138
5.7	Parasitic absorber fission product, scattering fission product, and inert nuclide microscopic cross section data in barns [ $10^{-24} \text{ cm}^2$ ]. . . . .	138
5.8	Fission product branch ratios and parasitic absorber fission product regeneration fraction. . . . .	138
7.1	Time steps taken for different adaptive time stepping criterion for physical Marshak wave problem using $S_2$ angular quadrature, spatially discretized with linear SLXS Lobatto, 50 cells, and $\Delta T_{goal} = 0.01$ . . .	258
7.2	Time steps taken for different adaptive time stepping criterion for physical Marshak wave problem discretized with cubic SLXS Lobatto and 100 cells. . . . .	259
7.3	Iteration count for different TRT model problems. . . . .	271
7.4	Iteration count for a very optically thick TRT problem. . . . .	272
7.5	Average number of inner iterations per thermal iteration using different convergence criteria. . . . .	273

## 1. INTRODUCTION

This dissertation is dedicated to the solution of the thermal radiative transfer (TRT) equations. The TRT equations:

$$\frac{1}{c} \frac{\partial I}{dt} + \vec{\Omega} \cdot \vec{\nabla} I + \sigma_t I = \int_0^\infty \int_{4\pi} \sigma_s(\vec{\Omega}' \rightarrow \vec{\Omega}, E' \rightarrow E) I d\vec{\Omega}' dE' + \sigma_a B \quad (1.1a)$$

$$C_v \frac{dT}{dt} = \int_0^\infty \sigma_a (\phi - 4\pi B) dE, \quad (1.1b)$$

are a nonlinear system of equations that describe the exchange of energy between a photon radiation field and a non-moving material. Radiation intensity,  $I$ , is a seven dimensional field dependent upon spatial location,  $\vec{x}$ ; photon energy,  $E$ ; photon direction of travel,  $\vec{\Omega}$ ; and time  $t$ .  $c$  is the speed of light. Material opacities for all interactions,  $\sigma_t$ ; absorption,  $\sigma_a$ ; and scattering,  $\sigma_s$  are functions of photon energy and material temperature,  $T$ . Material heat capacity,  $C_v$ , is also a function of material temperature. The angle integrated radiation intensity,  $\phi$ , is an integral over all photon directions of the the photon intensity and is a function of space and photon energy. Finally, the Planck function,  $B$ , is a function of photon energy and material temperature. While materials at all temperatures emit photon radiation, the radiation emission is proportional to  $T^4$ . Thus, solution of the radiative transfer equations is most important in situations where materials are very hot. Solving the thermal radiative transfer equations is an important component of the simulation of different scientific and engineering problems including astrophysics supernova explosions and high energy density physics laboratory experiments such as the ones conducted at the National Ignition Facility.

## 1.1 Simplifications of the Thermal Radiative Transfer Equations

In this dissertation, we make a number of simplifying assumptions to make solution of Eqs. (1.1) more tractable. First, we limit our focus to 1-D Cartesian (slab) geometry. The assumption of slab geometry is not required, but slab geometry radiation transport simulations require significantly less computational time. Further, any methods that have a possibility of being viable for radiation transport in multiple spatial dimensions must also work well in slab geometry.

Second, we approximate the continuous angle dependence of the intensity using the discrete ordinates ( $S_N$ ) method. The  $S_N$  method approximates the true definition of the angle integrated intensity,

$$\phi(\vec{x}, E, t) = \int_{4\pi} I(\vec{x}, \vec{\Omega}, E, t) d\vec{\Omega},$$

using quadrature integration,

$$\phi(\vec{x}, E, t) \approx \sum_{d=1}^{N_{dir}} w_d I(\vec{x}, \vec{\Omega}_d, E, t). \quad (1.2)$$

In Eq. (1.2),  $\{w_d, \vec{\Omega}_d\}_{d=1,\dots,N_{dir}}$  is the set of  $N_{dir}$  quadrature weights  $w_d$  and discrete directions,  $\vec{\Omega}_d$  and corresponding intensities  $I_d$ .

Finally, we treat the photon energy dependence assuming a grey, or photon energy integrated model. The grey assumption assumes suitable opacities,  $\sigma_{grey}$  exist such

that

$$\int_0^\infty \sigma(E)I(E)dE = \sigma_{grey}I_{grey} \quad (1.3a)$$

$$\int_0^\infty \sigma(E)\phi(E)dE = \sigma_{grey}\phi_{grey} \quad (1.3b)$$

$$\int_0^\infty \sigma(E)B(E, T)dE = \sigma_{grey}B_{grey}(T), \quad (1.3c)$$

where  $I_{grey}$ ,  $\phi_{grey}$ , and  $B_{grey}$  are photon energy integrated quantities,

$$I_{grey} = \int_0^\infty I(E)dE \quad (1.4)$$

$$\phi_{grey} = \int_0^\infty \phi(E)dE \quad (1.5)$$

$$B_{grey} = \int_0^\infty B(E, T)dE. \quad (1.6)$$

For the remainder of this work, we will forgo explicitly denoting quantities as grey, and unless otherwise noted, all quantities should be assumed to be photon energy integrated (grey). Though the assumption of Eqs. (1.3) does not hold unless all opacities are constant in energy, methods developed for the grey case are readily extensible to the multi-frequency treatment of photon energy dependence, and the multi-frequency approximation is by far the most common treatment of thermal radiative transfer photon energy dependence[1].

## 1.2 Spatial and Temporal Discretization

To complete a description of the approach we will take to solve Eqs. (1.1), we now describe how we will discretize the spatial and temporal variables.

### *1.2.1 Time Integration*

The appearance of the speed of light in Eq. (1.1) results in the TRT equations being very stiff. To solve the such a stiff system of equations would require either an impractically small time step, or the use of implicit methods. We elect to use Diagonally Implicit Runge-Kutta (DIRK) methods to advance our TRT solution in time. The simplest of DIRK scheme is the first order implicit Euler scheme, but S-stable DIRK schemes with higher order convergence exist [2].

### *1.2.2 Spatial Discretization with Discontinuous Finite Elements*

The linear discontinuous finite element method (LDFEM) has long been used to solve the discrete ordinates neutron transport equation [3]. Through manipulation, the thermal radiative transfer equations can be transformed into a form that is equivalent to the neutron transport equation with pseudo- scattering, fission, and fixed sources. This makes it possible to use the same methods and techniques developed for neutron transport to assist in solving the thermal radiative transfer equations. LDFEM has achieved wide spread acceptance in the neutron transport community because it is accurate [4] and highly damped. Because it possesses the thick diffusion limit [5], LDFEM has also been applied to the  $S_N$  TRT equations. Morel, Wareing, and Smith first considered the application of LDFEM to the  $S_N$  TRT equations in [6]. Mass matrix lumped LDFEM was shown to preserve the thick equilibrium diffusion limit [6]. This suggests that discontinuous finite element (DFEM) schemes can be used to accurately solve the TRT equations in both diffusive and transport effects dominated regions.

### 1.3 Progression Towards Higher Order DFEM Thermal Radiative Transfer

For higher order (quadratic and higher polynomial degree trial spaces) DFEM to be accurate and practical for solving Eqs. (1.1) we must demonstrate that higher order DFEM:

1. are “robust”,
2. account for within cell spatial variation of opacity accurately, and
3. can be accelerated using appropriate iterative acceleration techniques.

By “robust”, we mean that that calculated radiation outflow from a spatial cell is strictly positive for all cell widths and optical thicknesses.

In Section 2 we use a steady-state, mono-energetic, source-free pure absorber neutron transport problem with a cross section that is constant in space to examine the robustness of different radiation transport DFEM matrix lumping techniques. Next, we extend the techniques developed by Adams [7, 8], for a spatial discretization scheme related to LDFEM to address the within cell spatial variation of opacity, for higher order DFEM in Section 3 . Then, we examine iterative acceleration techniques compatible with higher order DFEM spatial discretizations in Section 4. In preparation for solving the coupled, non-linear TRT equations, in Section 5 we combine all of the strategies we have developed in Sections 2-4 and apply them to a coupled system of linear equations to solve a two-group fuel depletion problem that uses explicit Euler time differencing. In Section 6 we develop the necessary theory and simulation procedures to solve the grey thermal radiative transfer equations using higher order DFEM, fully deriving the necessary equations, and acceleration techniques. Finally we give numerical results in Section 7 that verify our newly developed DFEM methods and demonstrate their capabilities on a series of test problems.

## 2. DISCONTINUOUS FINITE ELEMENTS FOR RADIATION TRANSPORT

In Section 1, we briefly mentioned that through manipulation, the thermal radiative transfer equations can be put into a form equivalent to the neutron transport equation with pseudo-scattering, fission, and fixed sources. We will fully demonstrate the linearization process in Section 6, but for now we take for granted that solving for the neutron transport equation’s angular flux,  $\psi$ , is related to solving Eq. (1.1) for  $I$ . Additionally, we will assume that a steady-state, source-free, pure absorber neutron transport problem taxes DFEM schemes in a manner similar to the way DFEM schemes are tested in time-dependent thermal radiative transfer simulations, in particular Marshak wave type problems [9]. This section draws primarily from our previously published work in [10] and [11].

### 2.1 History of DFEM for Neutron Transport

The linear discontinuous finite element method (LDFEM) for discrete ordinates neutron transport is widely used and has been extensively studied [12, 13, 14, 15]. However, the DFEM technique is not limited to linear trial spaces. Reed et al. [3] used arbitrary order DFEM  $S_N$  neutron transport in TRIPLET but, due to data storage limitations at the time, only LDFEM was computationally practical. As a result of these historical computing limitations, the accuracy of LDFEM [4], and LDFEM possessing the thick diffusion limit [5], the majority of reported DFEM radiation transport literature has focused on the LDFEM approximation. Higher order DFEM methods have received periodic attention; some older examples include the work of Walters [16] and Hennart and del Valle [17, 18]. More recent investigations of higher order DFEM trial spaces include those of Warsa and Prinja [19] and Wang and Ragusa [20, 21]. The primary focus of the work in [17, 18, 19, 20, 21] was the

convergence rate of arbitrary order DFEM schemes.

Negative angular flux solutions of the neutron transport equation obtained with LDFEM have been well documented in [13, 14, 15]. While these negativities do not affect the order of convergence and can be tolerated for certain applications [22], some nonlinear problems, particularly radiative transfer calculations, can diverge if the angular intensities are negative. As a result, several methods to eliminate or inhibit negative solutions have been developed and can be categorized into one of three categories: ad-hoc fix-ups [13], strictly non-negative solution representations [14], and matrix lumping [15]. The first two methods result in nonlinear systems of equations, while matrix lumping yields linear systems of equations. By definition, ad-hoc fix-ups and strictly non-negative solution representations yield non-negative outflows in 1-D, 2-D, and 3-D geometries, regardless of material properties. Mass matrix lumping (applied to LDFEM) yields strictly positive outflows only in 1-D geometries, though it does otherwise inhibit negativities [15].

Solution positivity of even degree unlumped DFEM methods for 1-D problems has been noted previously [16, 17, 18]. In comparing DFEM methods to nodal transport methods, Walters derived the quadratic DFEM scheme from the nodal transport equations using the Padé(2,3) approximation to the exponential term and noted that this approximation would result in a strictly positive outflow, regardless of cell optical thickness [16]. Hennart and del Valle then showed for slab geometry that all even  $P$  degree polynomial DFEM schemes approximate the cell outflow angular flux as a Padé( $P, P + 1$ ) function, which is a strictly positive approximation of the exponential [17, 18]. The positivity of even degree unlumped DFEM for 1-D problems was also shown in [19].

## 2.2 Mass Matrix Lumping Techniques

In this Section, we examine the idea of mass matrix lumping and its ability to ensure positive angular flux solutions of the neutron transport equation for arbitrary degree DFEM trial spaces in non-scattering 1-D slab geometries. We consider traditional lumping (TL), that constructs a diagonal mass matrix by collapsing all off-diagonal entries onto the main diagonal [15], and quadrature-based self-lumping (SL) methods [23], that yield a diagonal mass matrix by numerically integrating the DFEM equations using the DFEM interpolatory points as quadrature points. Restricting ourselves to equally-spaced interpolation points, self-lumping numerical integration with the greatest degree of accuracy is achieved through the use of closed Newton-Cotes formulae [24]. However, Newton-Cotes formulas with a large number of integration points are known to be oscillatory and are of relatively low-order accuracy, integrating polynomials at most of degree equal to the number of integration points. By considering solution representations that employ quadrature points as the interpolatory points, for example Gauss-Legendre (hereafter Gauss) or Lobatto-Gauss-Legendre (hereafter Lobatto) quadrature points [24], we wish to find methods that are self-lumping with a significantly higher accuracy. We analyze the combinations of Lagrange interpolatory points and numerical integration strategies given in Table 2.1 for positivity of the angular flux solution, local truncation error order, and spatial convergence order as a function of trial space polynomial degree.

We limit the consideration of exact numerical integration schemes to those with equally-spaced interpolatory points, due to the fact that exact integration with any particular set of interpolatory points will always yield the same DFEM solution.

It has long been noted that traditional lumping (TL) with equally-spaced interpolatory points for 1-D LDFEM is equivalent to using the trapezoidal quadrature

Table 2.1: Nomenclature of numerical schemes.

Interpolation Point Type	Integration Strategy	Method Short Hand Name
Equally-Spaced	Exact spatial integration, with collapsing of mass matrix entries to the main diagonal	TL
Equally-Spaced	Numerical integration via Newton-Cotes quadrature restricted to interpolation points	SL Newton-Cotes
Gauss Quadrature	Numerical integration via Gauss quadrature restricted to interpolation points	SL Gauss
Lobatto Quadrature	Numerical integration via Lobatto quadrature restricted to interpolation points	SL Lobatto
Equally-Spaced	Exact spatial integration	Exact DFEM

rule to approximately integrate the mass matrix [25] while exactly integrating the gradient operator. Since the trapezoidal rule is identical to the closed Newton-Cotes formula with two points, we hypothesize that, for finite elements of arbitrary order using equally-spaced interpolatory points, traditional lumping is equivalent to using a closed Newton-Cotes formula to compute the mass matrix while exactly integrating the gradient operator. We demonstrate the equivalence between traditional lumping and closed Newton-Cotes formulae in the computation of the mass matrix.

Self-lumping (SL) based on Newton-Cotes formulae differs from traditional lumping in that SL Newton-Cotes generally does not exactly integrate the gradient operator. Coincidentally, the gradient operator is exactly integrated for linear/quadratic trial spaces using a 2-point/3-point Newton-Cotes formula, respectively. However, for higher degree polynomial trial spaces, the corresponding Newton-Cotes formula does not exactly integrate the gradient operator.

Self-lumping based on either Gauss or Lobatto quadratures exactly integrates the gradient operator in 1-D slab geometry for all degree of polynomial trial spaces; thus, there is no need to distinguish between exact integration and quadrature integration of the gradient operator for the SL Gauss and SL Lobatto schemes.

### 2.3 Lumping Techniques for the 1-D $S_N$ Neutron Transport Equation with Arbitrary Order DFEM

We now derive the weak form of the 1-D  $S_N$  neutron transport equations discretized with DFEM and define the different mass matrix lumping techniques.

#### 2.3.1 Weak Form Derivation

Consider the 1-D slab geometry  $S_N$  neutron transport equation:

$$\mu_d \frac{d\psi_d}{dx} + \Sigma_t \psi_d = Q_d, \quad (2.1)$$

where  $\psi_d$  is the angular flux  $[1/[cm^2 - sec - ster]]$  in the  $\mu_d$  direction,  $\mu_d$  is the  $d$ 'th directional cosine relative to the  $x$ -axis,  $\Sigma_t$  is the total interaction cross section  $[cm^{-1}]$ , and  $Q_d$  is a total source (fixed+scattering+fission) angular source in the direction of  $\mu_d$   $[1/[cm^3 - sec - ster]]$ . In all that follows, we consider only non-scattering, non-fissioning media (pure absorbers), thus  $Q_d$  will only be non-trivial if a fixed source is present in the problem. The scalar flux,  $\phi$   $[n/cm^2 - sec]$ , is defined as

$$\phi(x) = 2\pi \int_{-1}^1 \psi(x, \mu_d) d\mu_d. \quad (2.2)$$

For simplicity, we derive the DFEM equations for a single-cell domain, with  $x \in [x_L, x_R]$ . A known angular flux,  $\psi_{in,d}$ , is defined on the incoming face of the domain for all  $\mu_d$ . For  $\mu_d > 0$ ,  $\psi_{in,d}$  is defined only at  $x_L$  and for  $\mu_d < 0$ ,  $\psi_{in,d}$  is defined

at  $x_R$ . We begin our derivation by first transforming the physical geometry to a reference element,  $s \in [-1, 1]$ . This affine transformation is such that:

$$x = \bar{x} + \frac{\Delta x}{2}s, \quad (2.3a)$$

$$dx = \frac{\Delta x}{2}ds, \quad (2.3b)$$

with  $\bar{x} = \frac{x_L+x_R}{2}$ , and  $\Delta x = x_R - x_L$ . We seek a numerical approximation to the true angular flux  $\psi_d$  using Lagrange polynomials of degree  $P$ :

$$\psi_d(s) \approx \tilde{\psi}_d(s) = \sum_{j=1}^{N_P} \psi_{j,d} b_j(s), \quad (2.4)$$

where the  $\tilde{\psi}_d(s)$  denotes the numerical approximation. The basis functions  $b_j$  are the canonical Lagrange polynomials with interpolatory points  $s_j$ ,

$$b_j(s) = \prod_{\substack{k=1 \\ k \neq j}}^{N_P} \frac{s - s_k}{s_j - s_k}, \quad (2.5)$$

and  $N_P = P + 1$ . To determine the  $N_P$  unknown coefficients of Eq. (2.4), we follow a standard discontinuous Galerkin procedure, successively multiplying Eq. (2.1) by weight function  $b_i$  and integrating by parts, hence generating  $N_P$  moment equations ( $1 \leq i \leq N_P$ ). We assume that the cross sections are constant per cell. Inserting our solution representation  $\tilde{\psi}_d$ , the  $i$ -th moment equation is given by:

$$\begin{aligned} \mu_d \left[ b_i(1)\tilde{\psi}_d(1) - b_i(-1)\tilde{\psi}_d(-1) - \int_{-1}^1 \tilde{\psi}_d(s) \frac{db_i}{ds} ds \right] &+ \frac{\Delta x \Sigma_t}{2} \int_{-1}^1 b_i(s) \tilde{\psi}_d(s) ds \\ &= \frac{\Delta x}{2} \int_{-1}^1 b_i(s) Q_d(s) ds. \end{aligned} \quad (2.6)$$

We now introduce the upwind approximation to define the angular flux at the cell edges. For  $\mu_d > 0$  the angular flux at the cell interfaces is

$$\tilde{\psi}_d(-1) = \psi_{in,d} \text{ and} \quad (2.7a)$$

$$\tilde{\psi}_d(1) = \sum_{j=1}^{N_P} \psi_{j,d} b_j(1). \quad (2.7b)$$

Similarly for  $\mu_d < 0$ :

$$\tilde{\psi}_d(-1) = \sum_{j=1}^{N_P} \psi_{j,d} b_j(-1) \text{ and} \quad (2.8a)$$

$$\tilde{\psi}_d(1) = \psi_{in,d}. \quad (2.8b)$$

In Eq. (2.7a) and Eq. (2.8b),  $\psi_{in,d}$  is either the known angular flux outflow from the upwind cell or a boundary condition. Inserting the definition of  $\tilde{\psi}_d(s)$ , Eq. (2.6) becomes, for  $\mu_d > 0$ ,

$$\begin{aligned} \mu_d \left[ b_i(1) \left( \sum_{j=1}^{N_P} \psi_{j,d} b_j(1) \right) - b_i(-1) \psi_{in,d} - \int_{-1}^1 \left( \sum_{j=1}^{N_P} \psi_{j,d} b_j(s) \right) \frac{db_i}{ds} ds \right] + \\ \frac{\Delta x \Sigma_t}{2} \int_{-1}^1 b_i(s) \left( \sum_{j=1}^{N_P} \psi_{j,d} b_j(s) \right) ds = \frac{\Delta x}{2} \int_{-1}^1 b_i(s) Q_d(s) ds, \end{aligned} \quad (2.9)$$

and, for  $\mu_d < 0$ ,

$$\begin{aligned} \mu_d \left[ b_i(1) \psi_{in,d} - b_i(-1) \left( \sum_{j=1}^{N_P} \psi_{j,d} b_j(-1) \right) - \int_{-1}^1 \left( \sum_{j=1}^{N_P} \psi_{j,d} b_j(s) \right) \frac{db_i}{ds} ds \right] \\ + \frac{\Delta x \Sigma_t}{2} \int_{-1}^1 b_i(s) \left( \sum_{j=1}^{N_P} \psi_{j,d} b_j(s) \right) ds = \frac{\Delta x}{2} \int_{-1}^1 b_i(s) Q_d(s) ds. \end{aligned} \quad (2.10)$$

Considering all of the  $N_P$  moment equations at once we can write both Eq. (2.9) and Eq. (2.10) in a single matrix form:

$$(\mu_d \mathbf{G} + \Sigma_t \mathbf{M}) \vec{\psi}_d = \vec{Q}_d + \mu_d \psi_{in,d} \vec{f}. \quad (2.11)$$

In Eq. (2.11) we have made use of the following definitions: the vector of unknowns is given by

$$\vec{\psi}_d = [\psi_{1,d} \ \dots \ \psi_{N_P,d}]^T, \quad (2.12)$$

the mass matrix  $\mathbf{M}$  is:

$$\mathbf{M}_{ij} = \frac{\Delta x}{2} \int_{-1}^1 b_i(s) b_j(s) \ ds, \quad (2.13)$$

the fixed source moment vector,  $\vec{Q}_d$ , is a column vector of length  $N_P$ :

$$\vec{Q}_{d,i} = \frac{\Delta x}{2} \int_{-1}^1 b_i(s) Q_d(s) \ ds, \quad (2.14)$$

and  $\vec{f}$  is a column vector of length  $N_P$ :

$$\vec{f}_i = \begin{cases} b_i(-1) & \text{for } \mu_d > 0 \\ -b_i(1) & \text{for } \mu_d < 0 \end{cases}. \quad (2.15)$$

$\mathbf{G}$  is a  $N_P \times N_P$  matrix which we refer to as the gradient operator. When  $\mu_d > 0$ ,  $\mathbf{G}$  is given by:

$$\mathbf{G}_{ij} = b_i(1)b_j(1) - \int_{-1}^1 \frac{db_i}{ds} b_j(s) \ ds. \quad (2.16a)$$

For  $\mu_d < 0$ ,  $\mathbf{G}$  is:

$$\mathbf{G}_{ij} = -b_i(-1)b_j(-1) - \int_{-1}^1 \frac{db_i}{ds} b_j(s) \ ds. \quad (2.16b)$$

When interpolatory points are not located at the cell interfaces (i.e., at  $s = \pm 1$ ), it can be noted that

1.  $\vec{f}$  has  $N_P$  non-zero entries and
2.  $b_i(\pm 1)b_j(\pm 1) \neq 0$  for all  $i, j = 1, \dots, N_P$ .

When a Lagrange interpolatory point exists on the cell edges, then  $\vec{f}$  has only one non-zero entry and the product  $b_i(\pm 1)b_j(\pm 1) \neq 0$  only when  $i = j = N_P$  for  $\mu_d > 0$  or when  $i = j = 1$  for  $\mu_d < 0$ , as is the case when equally-spaced points or a Lobatto quadrature are used as interpolation points.

We evaluate the integrals of Eq. (2.13) and Eq. (2.16) using a numerical quadrature. A method exactly integrates a quantity when the quadrature rule used to evaluate the integral is accurate for polynomials of degree equal to or greater than the polynomial degree of the integrand. In general, the matrices are dense and their entries are computed as:

$$\mathbf{M}_{ij} \approx \frac{\Delta x}{2} \sum_{q=1}^{N_q} w_q b_i(s_q) b_j(s_q), \quad (2.17)$$

$$\mathbf{G}_{ij} \approx sg(\mu_d) b_i(sg(\mu_d)) b_j(sg(\mu_d)) - \sum_{q=1}^{N_q} w_q \left. \frac{db_i}{ds} \right|_{s=s_q} b_j(s_q), \quad (2.18)$$

where  $N_q$  is the number of quadrature points to be used,  $w_q$  are the weights associated with quadrature points  $s_q$ , and  $sg(a)$  is the sign function defined as

$$sg(a) = \begin{cases} +1 & \text{if } a > 0 \\ -1 & \text{if } a < 0 \end{cases}. \quad (2.19)$$

### 2.3.2 Traditional Lumping

The traditional lumping (TL) scheme replaces  $\mathbf{M}$  with  $\widehat{\mathbf{M}}$ , the latter being formed by collapsing row entries onto the main diagonal via the following formula [15]:

$$\widehat{\mathbf{M}}_{ij} = \begin{cases} \sum_{j=1}^{N_P} \mathbf{M}_{ij} & \text{for } i = j \\ 0 & \text{otherwise} \end{cases}. \quad (2.20)$$

### 2.3.3 Quadrature-Based Lumping

An alternative method of mass matrix lumping restricts the quadrature points to the interpolatory points where:

$$b_i(s_j) = \begin{cases} 1 & \text{if } s_i = s_j \\ 0 & \text{otherwise} \end{cases}, \quad i = 1, \dots, N_P, \quad (2.21)$$

and the quadrature integration of Eq. (2.17) reduces to:

$$\mathbf{M}_{ij} = \begin{cases} \frac{\Delta x}{2} w_i & i = j \\ 0 & \text{otherwise} \end{cases}. \quad (2.22)$$

As mentioned previously, we refer to the implicit lumping of Eq. (2.22) as self-lumping (SL). Self-lumping is a method to automatically generate a diagonal mass matrix. We note that self-lumping does not imply that the quadrature formula inexactly integrates the mass matrix.

### 2.3.4 Source Moment Evaluation

Historically, when discussing lumping techniques, the focus has been on matrix lumping [15] and little attention was paid to lumping source terms. For instance,

consider a  $\delta$ -shaped volumetric sources (i.e., equal to 0 everywhere except at one given point). In such a case, the evaluation of  $\vec{Q}_d$  using quadrature-based self-lumping schemes is an open question. Obviously, quadrature-based schemes cannot evaluate Eq. (2.14) for  $\delta$ -sources. To address this, we expand the source on a Legendre polynomial basis:

$$\widehat{S}_d(s) = \sum_{n=0}^P S_n P_n(s) \quad (2.23a)$$

$$\text{with } S_n = \frac{2n+1}{2} \int_{-1}^1 Q_d(s) P_n(s) ds, \quad (2.23b)$$

and evaluate  $\vec{Q}_d$  as follows

$$\vec{Q}_{d,i} = \frac{\Delta x}{2} \int_{-1}^1 b_i(s) \widehat{S}_d(s) ds. \quad (2.24)$$

Note that if the right-hand-side of Eq. (2.24) is exactly integrated, this is equivalent to exactly integrating Eq. (2.14).

## 2.4 Quadrature Point Selection

We now discuss the properties of different numerical quadratures as applied to the 1-D DFEM  $S_N$  neutron transport equations. We consider three different types of interpolatory points: equally-spaced, Gauss quadrature, and Lobatto quadrature. On the  $[-1, 1]$  interval, the  $N_P = P + 1$  equally spaced interpolation points for a degree  $P$  polynomial trial space are:

$$s_j = -1 + (j-1) \frac{2}{P}, \quad j = 1, \dots, N_P. \quad (2.25)$$

Self-lumping using equally-spaced interpolation points requires numerical integration with closed Newton-Cotes quadrature formulae. The  $N_P$  weights,  $w_j$ , used for

Newton-Cotes numerical integration at the interpolation points do not follow a concise pattern, so we refer the reader to [24]. The Gauss quadrature points are the  $N_P$  roots of the Legendre polynomial,  $P_{N_P}(s)$  [24]. The corresponding weights are:

$$w_j = \frac{2}{(1 - s_j^2)} [P'_{N_P}(s_j)]^2. \quad (2.26)$$

Lobatto quadrature points have fixed endpoints,  $s_1 = -1$ ,  $s_{N_P} = 1$ . The remaining  $N_P - 2$  points are the roots of  $P'_{N_P-1}(s)$  [24], with corresponding weights:

$$w_j = \begin{cases} \frac{2}{N_P(N_P-1)} & j = 1, j = N_P \\ \frac{2}{N_P(N_P-1)[P_{N_P-1}(s_j)]^2} & \text{otherwise} \end{cases}. \quad (2.27)$$

The highest polynomial degree a particular self-lumping quadrature formula exactly integrates is given in Table 2.2 for Newton-Cotes, in Table 2.3 for Gauss, and Table 2.4 for Lobatto quadratures. Also listed in Table 2.2 - Table 2.4 is the maximum polynomial degree of the integrands present in the gradient and mass matrices.

Table 2.2: Accuracy of self-lumping closed Newton-Cotes quadratures for DFEM trial spaces of polynomial degree  $P$ .

Polynomial Degree of $\tilde{\psi}$	$N_P = P + 1$	Degree of <b>M</b> integrand	Degree of <b>G</b> integrand	Quadrature Accuracy
1	2	2	1	1
2	3	4	3	3
3	4	6	5	3
4	5	8	7	5
5	6	10	9	5
$P$	$P + 1$	$2P$	$2P - 1$	Odd $\tilde{\psi}$ : $P$ Even $\tilde{\psi}$ : $P + 1$

Table 2.3: Accuracy of self-lumping Gauss quadratures for DFEM trial spaces of polynomial degree  $P$ .

Polynomial Degree of $\tilde{\psi}$	$N_P = P + 1$	Degree of <b>M</b> integrand	Degree of <b>G</b> integrand	Quadrature Accuracy
1	2	2	1	3
2	3	4	3	5
3	4	6	5	7
4	5	8	7	9
5	6	10	9	11
$P$	$P + 1$	$2P$	$2P - 1$	$2P + 1$

Table 2.4: Accuracy of self-lumping Lobatto quadratures for DFEM trial spaces of polynomial degree  $P$ .

Polynomial Degree of $\tilde{\psi}$	$N_P = P + 1$	Degree of <b>M</b> integrand	Degree of <b>G</b> integrand	Quadrature Accuracy
1	2	2	1	1
2	3	4	3	3
3	4	6	5	5
4	5	8	7	7
5	6	10	9	9
$P$	$P + 1$	$2P$	$2P - 1$	$2P - 1$

Since the accuracy of an  $N_P = P + 1$  point Gauss quadrature integration exceeds the polynomial degree of the **M** and **G** integrands for a trial space of degree  $P$ , using the SL Gauss scheme will strictly yield the same numerical solution as any DFEM scheme that exactly integrates **M** and **G**. Thus, the SL Gauss scheme yields the same numerical solution as the Exact DFEM scheme.

For linear and quadratic trial spaces, self-lumping methods using either Lobatto or equally-spaced interpolation points will yield identical solutions. This is a direct result of the two- and three-point Lobatto quadrature formulae being identical to the two- and three-point closed Newton-Cotes quadratures. This equivalence does

not hold for higher degree polynomial trial spaces because the Lobatto quadrature points will no longer correspond to the equally-spaced quadrature points.

By definition, TL uses equally-spaced interpolation points and exactly integrates the gradient operator. For cell-wise constant cross sections, TL is equivalent to a numerical integration scheme that:

1. uses equally-spaced interpolation points,
2. integrates the gradient operator exactly, and
3. uses a Newton-Cotes quadrature restricted to the DFEM interpolation points to compute the mass matrix.

To prove the third point, consider the following. With traditional lumping,  $\mathbf{M}_{ij}$  is exactly computed and then a row-sum operation is performed on the rows of  $\mathbf{M}$ ; thus the entries of the diagonal mass matrix computed for TL are

$$\begin{aligned}\widehat{\mathbf{M}}_{ii} &= \sum_{j=1}^{N_P} \frac{\Delta x}{2} \int_{-1}^1 b_i(s) b_j(s) \, ds = \frac{\Delta x}{2} \int_{-1}^1 b_i(s) \left[ \sum_{j=1}^{N_P} b_j(s) \right] \, ds \\ &= \frac{\Delta x}{2} \int_{-1}^1 ds \, b_i(s) \quad \forall i = 1, \dots, N_P ,\end{aligned}\quad (2.28)$$

because  $\sum_j^{N_P} b_j(s) = 1 \forall s \in [-1, +1]$  by definition. The integral  $\frac{\Delta x}{2} \int_{-1}^1 b_i(s) \, ds$  is exactly integrated using a closed Newton-Cotes formula with  $N_P = P+1$  points since  $b_i(s)$  is a polynomial of degree  $P$ . Finally, when the  $b_i$  functions are defined using equally-spaced points, the use of a closed Newton-Cotes formula with  $N_P$  points yields

$$\widehat{\mathbf{M}}_{ii} = \frac{\Delta x}{2} \int_{-1}^1 b_i(s) \, ds = \frac{\Delta x}{2} \sum_{q=1}^{N_P} w_q b_i(s_q) = \frac{\Delta x}{2} w_i ,\quad (2.29)$$

because  $b_i(s_q) = \delta_{iq}$ . Thus, the diagonal mass matrix computed using TL contains the closed Newton-Cotes weights as diagonal entries and is equivalent to approximating

$\mathbf{M}$  using closed Newton-Cotes quadrature in Eq. (2.22). We also numerically verify this in Table 2.5 for polynomial degrees up to 4, assuming  $\Delta x = 2$ . For linear and

Table 2.5: Equivalence of traditional lumping and closed Newton-Cotes quadrature approximation of the mass matrix.

$P$	Exact Integration of $\mathbf{M}$	Row Sums of $\mathbf{M}$	Newton-Cotes $w$ with $P + 1$ points
1	$\begin{bmatrix} \frac{2}{3} & \frac{1}{3} \\ \frac{1}{3} & \frac{2}{3} \end{bmatrix}$	$\begin{bmatrix} 1 \\ 1 \end{bmatrix}$	$\begin{bmatrix} 1 \\ 1 \end{bmatrix}$
2	$\begin{bmatrix} \frac{4}{15} & \frac{2}{15} & -\frac{1}{15} \\ \frac{2}{15} & \frac{16}{15} & \frac{1}{15} \\ -\frac{1}{15} & \frac{2}{15} & \frac{4}{15} \end{bmatrix}$	$\begin{bmatrix} \frac{1}{3} \\ \frac{4}{3} \\ \frac{1}{3} \end{bmatrix}$	$\begin{bmatrix} \frac{1}{3} \\ \frac{4}{3} \\ \frac{1}{3} \end{bmatrix}$
3	$\begin{bmatrix} \frac{16}{105} & \frac{38}{280} & -\frac{3}{70} & \frac{19}{840} \\ \frac{33}{280} & \frac{27}{35} & -\frac{27}{280} & -\frac{3}{70} \\ -\frac{3}{70} & -\frac{27}{280} & \frac{27}{35} & \frac{33}{280} \\ \frac{19}{840} & -\frac{3}{70} & \frac{38}{280} & \frac{16}{105} \end{bmatrix}$	$\begin{bmatrix} \frac{1}{4} \\ \frac{3}{4} \\ \frac{3}{4} \\ \frac{1}{4} \end{bmatrix}$	$\begin{bmatrix} \frac{1}{4} \\ \frac{3}{4} \\ \frac{3}{4} \\ \frac{1}{4} \end{bmatrix}$
4	$\begin{bmatrix} \frac{292}{2835} & \frac{296}{2835} & -\frac{58}{945} & \frac{8}{405} & -\frac{29}{2835} \\ \frac{296}{2835} & \frac{256}{405} & -\frac{128}{945} & \frac{256}{2835} & \frac{8}{405} \\ -\frac{58}{945} & -\frac{128}{945} & \frac{208}{315} & -\frac{128}{945} & -\frac{58}{945} \\ \frac{8}{405} & \frac{256}{2835} & -\frac{128}{945} & \frac{256}{405} & \frac{296}{2835} \\ -\frac{29}{2835} & \frac{8}{405} & -\frac{58}{945} & \frac{296}{2835} & \frac{292}{2835} \end{bmatrix}$	$\begin{bmatrix} \frac{7}{45} \\ \frac{32}{45} \\ \frac{4}{15} \\ \frac{32}{45} \\ \frac{7}{45} \end{bmatrix}$	$\begin{bmatrix} \frac{7}{45} \\ \frac{32}{45} \\ \frac{4}{15} \\ \frac{32}{45} \\ \frac{7}{45} \end{bmatrix}$

quadratic trial spaces, the 2-point and 3-point Newton-Cotes quadrature formulae exactly integrate the gradient operator, as shown in Table 2.2. Thus, for linear and quadratic trial spaces, schemes that use

1. equally-spaced interpolation points and traditional lumping,
2. equally-spaced interpolation points and self-lumping numerical integration, or
3. Lobatto quadrature interpolation points and self-lumping numerical integration,

will yield identical solutions.

## 2.5 Numerical Results

In this Section, we present numerical results for two 1-D slab problems. For the first problem, we consider a source-free pure absorber with vacuum boundary conditions on the right, a known angular flux  $\psi_{in,d}$  incident on the left face, and a spatially constant total cross section  $\Sigma_t$ . The second problem consists of a slab with vacuum boundary conditions on both sides, no scattering, constant  $\Sigma_t$ , and a fixed  $\delta$ -source.

For  $\mu_d > 0$ , the numerical approximations to the angular flux near the cell inflow and outflow are as follows:

$$\tilde{\psi}_{in,d} = \sum_{j=1}^{N_P} \psi_{j,d} b_j(-1) \text{ and} \quad (2.30)$$

$$\tilde{\psi}_{out,d} = \sum_{j=1}^{N_P} \psi_{j,d} b_j(1). \quad (2.31)$$

Regardless of the sign of  $\mu_d$ , the numerical approximation to the cell average angular flux is defined as:

$$\tilde{\psi}_{A,d} = \frac{1}{2} \sum_{j=1}^{N_P} w_j \psi_{j,d}. \quad (2.32)$$

We used the following quadrature weight normalization:  $\sum_{j=1}^{N_P} w_j = 2$ . In Eq. (2.30), Eq. (2.31), and Eq. (2.32),  $\psi_{j,d}$  are the components of  $\vec{\psi}_d$ , the numerical solution obtained by solving Eq. (2.11). Hence, the numerical angular flux solution of any of the previously discussed DFEM schemes can be obtained as a function of  $h$ , the number of mean free paths divided by  $\mu_d$ ,

$$h = \frac{\Sigma_t \Delta x}{\mu_d}. \quad (2.33)$$

### 2.5.1 Incident Flux Single-Cell Outflow Comparison

For the incident-flux problem, the analytical solution of Eq. (2.1) is:

$$\psi(x, \mu_d) = \begin{cases} \psi_{in,d} \exp\left[-\frac{\Sigma_t(x-x_L)}{\mu_d}\right] & \text{for } \mu_d > 0 \\ 0 & \text{for } \mu_d < 0 \end{cases}. \quad (2.34)$$

The analytic angular flux outflow,  $\psi_{out,d} = \psi(x_R, \mu_d)$ , is:

$$\psi_{out,d} = \psi_{in,d} \exp[-h]. \quad (2.35)$$

Similarly, the analytic average angular flux within the cell,  $\psi_{A,d}$ , is:

$$\psi_{A,d} = \frac{1}{\Delta x} \int_{x_L}^{x_R} \psi(x, \mu_d) dx = \frac{\psi_{in,d}}{h} (1 - \exp[-h]). \quad (2.36)$$

The solution components are given by

$$\vec{\psi}_d = \psi_{in,d} (\mathbf{G} + \mathbf{M})^{-1} \vec{f}, \quad (2.37)$$

and since  $\mathbf{M} \propto h$ , we can compare the various choices of interpolatory points and numerical integration strategies solely as a function of  $h$ .

Figures 2.1-2.4 show the numerically calculated cell outflow,  $\tilde{\psi}_{out,d}$ , as a function of  $h$  for all methods considered. All methods converge to the analytical solution as  $h \rightarrow 0$ , thus we have zoomed in the range where the methods visually differ (i.e.,  $h \geq 1$ ). We observe that:

- SL Gauss yields strictly positive outflows for even degree polynomial trial spaces,

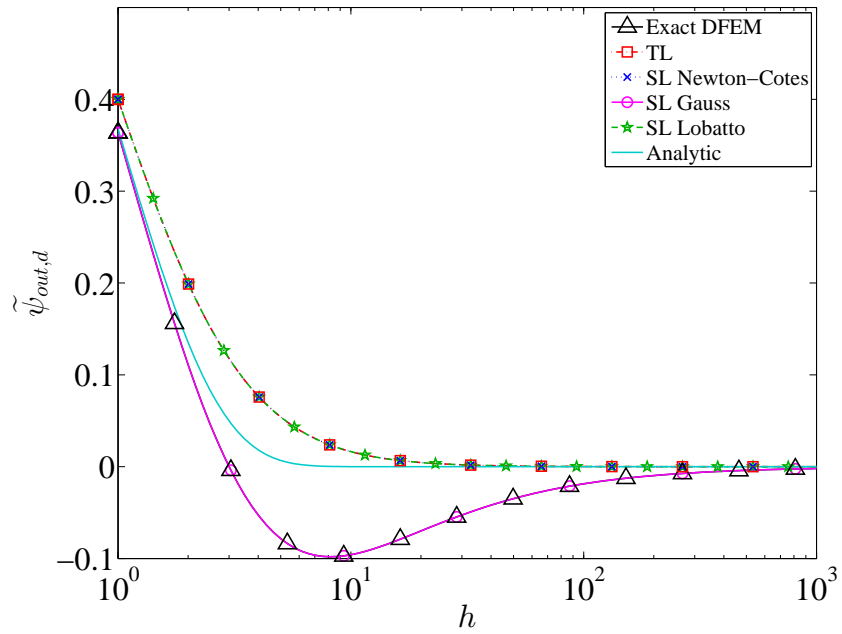


Figure 2.1: Angular flux outflow as a function of  $h$ , for different linear trial space DFEM schemes, from a homogeneous, single cell pure absorber.

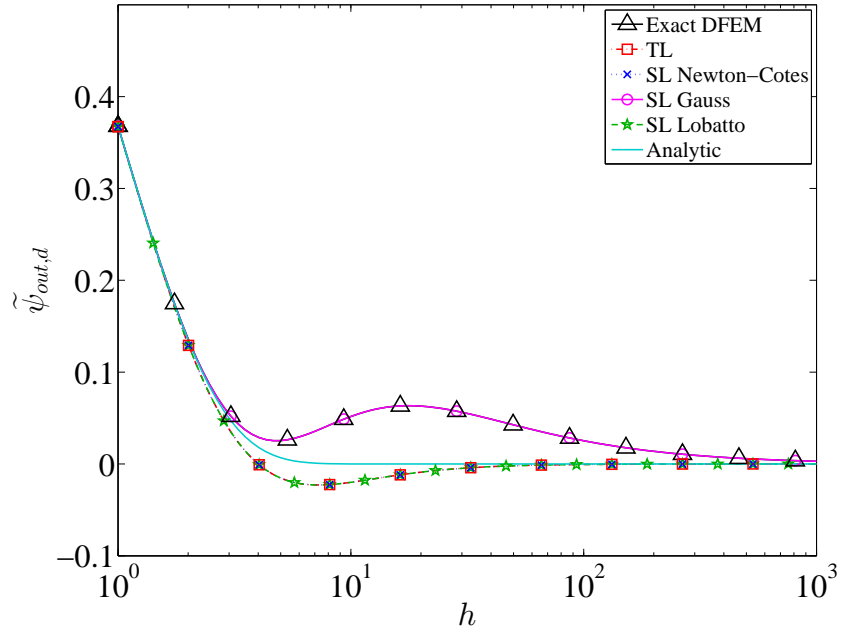


Figure 2.2: Angular flux outflow as a function of  $h$ , for different quadratic trial space DFEM schemes, from a homogeneous, single cell pure absorber.

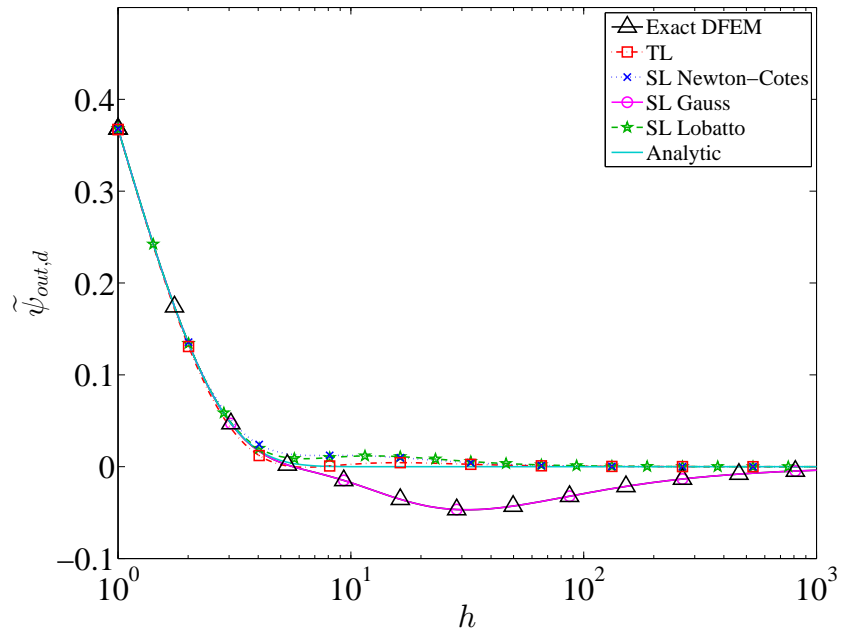


Figure 2.3: Angular flux outflow as a function of  $h$ , for different cubic trial space DFEM schemes, from a homogeneous, single cell pure absorber.

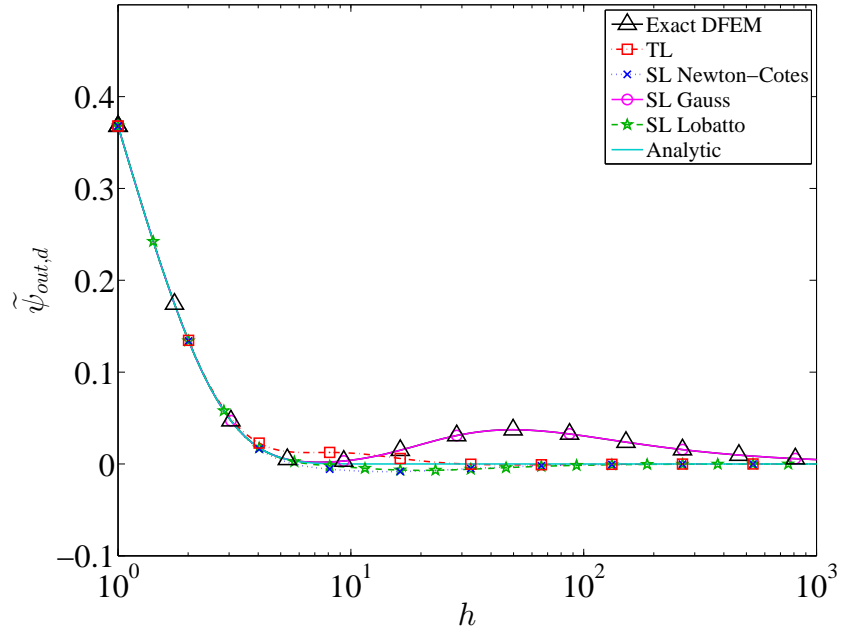


Figure 2.4: Angular flux outflow as a function of  $h$ , for different quartic trial space DFEM schemes, from a homogeneous, single cell pure absorber.

- SL Lobatto and SL Newton-Cotes yield strictly positive outflows for odd degree polynomial trial spaces, and
- TL yields strictly positive outflows only for a linear trial space.

We also numerically verify the remarks made of Section 2.4, that is:

- SL Gauss is equivalent to Exact DFEM,
- SL Lobatto, SL Newton-Cotes, and TL are equivalent for linear and quadratic trial spaces, and
- for even degree trial spaces, the outflow value computed by SL Gauss is not monotonically decreasing as a function of  $h$  for cells of intermediate optical thickness (the same was noted in [19] for Exact DFEM).

### 2.5.2 Fixed Source Single-Cell Inflow Comparison

As noted in [14], it is possible for LDFEM to yield negative solutions near cell inflows for source driven problems. In this second problem, we use a  $\delta$ -source:

$$Q_d(x) = \begin{cases} \delta(x - x_o) & \text{for } \mu_d > 0 \\ 0 & \text{for } \mu_d < 0 \end{cases}, \quad (2.38)$$

$x \in [-1, 1]$ , and  $-1 \leq x_o \leq 1$ . The analytic solution to this problem for  $\mu_d > 0$  is:

$$\psi(x, \mu_d) = \begin{cases} \exp\left[-\frac{\Sigma_t(x-x_o)}{\mu_d}\right] & x \geq x_o \\ 0 & x < x_o \end{cases}. \quad (2.39)$$

(For  $\mu_d < 0$ ,  $\psi(x, \mu_d) = 0$ .) We now examine the numerical approximation to the angular flux near the cell inflow,  $\tilde{\psi}_{in,d}$ , for various integration schemes, trial space degrees, and as a function of the ratio of the first Legendre moment of the source,  $S_1$ ,

to the zero-th Legendre moment of the source,  $S_0$ . Note that the physical range of that ratio,  $\frac{S_1}{S_0}$ , is  $[-3, 3]$ , corresponding to a  $\delta$ -source at the left cell edge ( $\frac{S_1}{S_0} = -3$ ) or at the right edge ( $\frac{S_1}{S_0} = 3$ ).

We first consider the case of a vacuum ( $\Sigma_t = 0$ ), thus only testing the effect of quadrature accuracy in evaluating  $\vec{Q}_d$  and  $\mathbf{G}$ . In Figs. 2.5-2.8, we plot  $\tilde{\psi}_{in,d}$  for three schemes:

1. Lobatto quadrature, which is exact for  $\mathbf{G}$  and approximate for the source moments, Eq. (2.24) ,
2. Gauss quadrature: which is exact for both  $\mathbf{G}$  and the source moments, and
3. Newton-Cotes quadrature: which is approximate for both  $\mathbf{G}$  and the source moments.

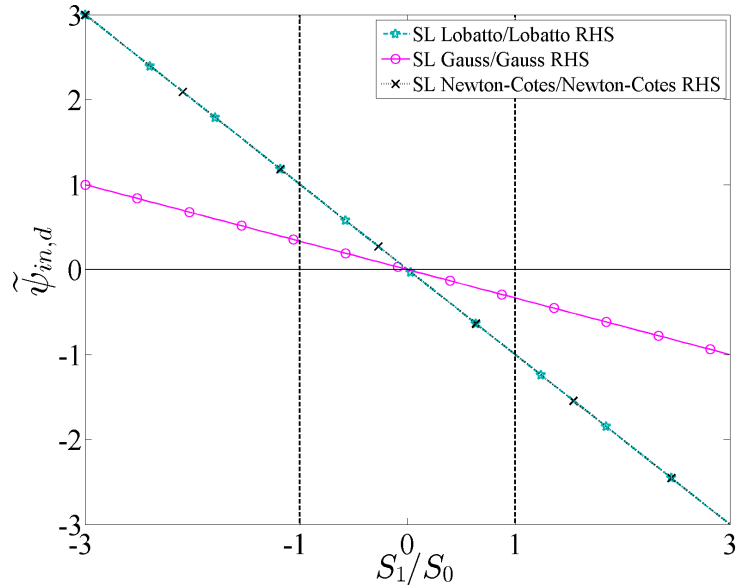


Figure 2.5: Numerical inflow values as a function of  $\frac{S_1}{S_0}$  for a single cell (vacuum case) with a  $\delta$ -shaped source, using linear DFEM.

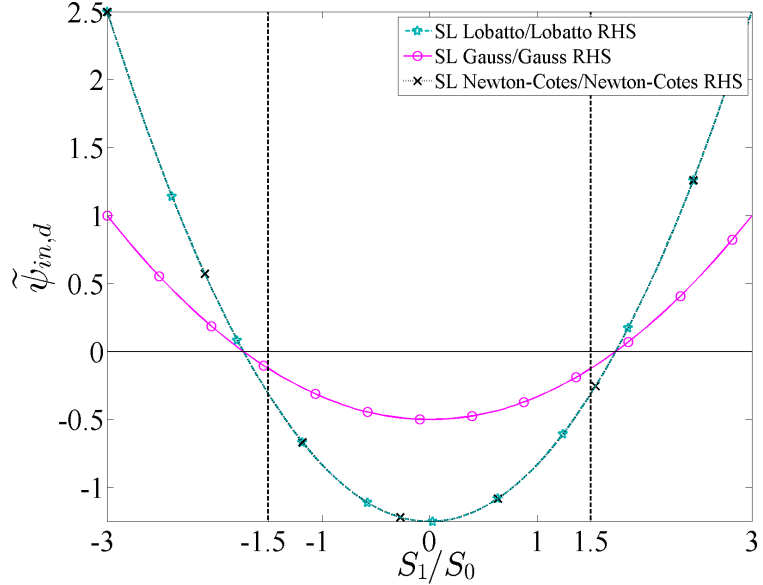


Figure 2.6: Numerical inflow values as a function of  $\frac{S_1}{S_0}$  for a single cell (vacuum case) with a  $\delta$ -shaped source, using quadratic DFEM.

The dotted vertical lines in Figs. 2.5-2.8 correspond to the extrema values of  $\frac{S_1}{S_0}$  that yield a strictly positive polynomial source representation of degree  $P$  (indeed, the degree- $P$  Legendre expansion of the  $\delta$ -source is not everywhere positive for a wide range of possible  $\frac{S_1}{S_0}$  that are physically realizable). For all trial space degrees, the Gauss scheme exhibits less negativity than either of the other two schemes. The dramatic difference between the Gauss scheme and the Lobatto scheme is solely due to the quadrature formula used to evaluate  $\vec{Q}_d$  since both schemes exactly integrate **G**. The Newton-Cotes scheme exhibits less severe negativities than the Lobatto scheme but is less robust than the Gauss scheme. Given the results shown in Figs. 2.5-2.8, we conclude that the most robust schemes exactly integrate the source moments, Eq. (2.24).

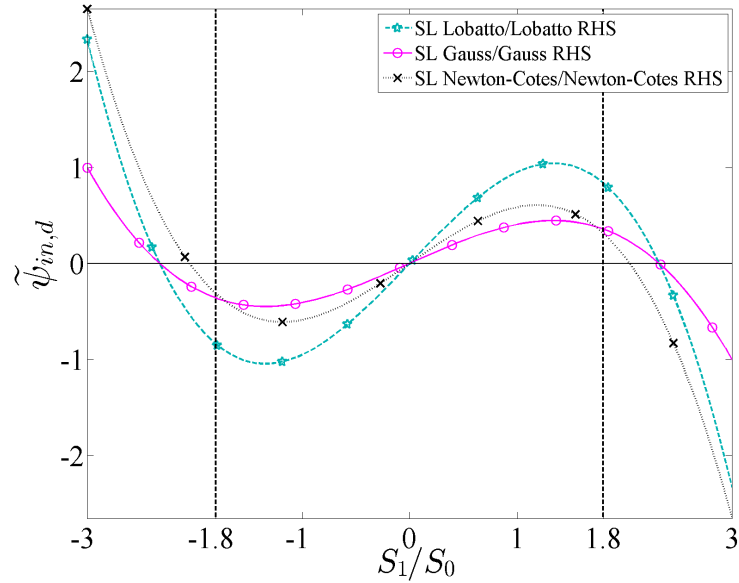


Figure 2.7: Numerical inflow values as a function of  $\frac{S_1}{S_0}$  for a single cell (vacuum case) with a  $\delta$ -shaped source, using cubic DFEM.

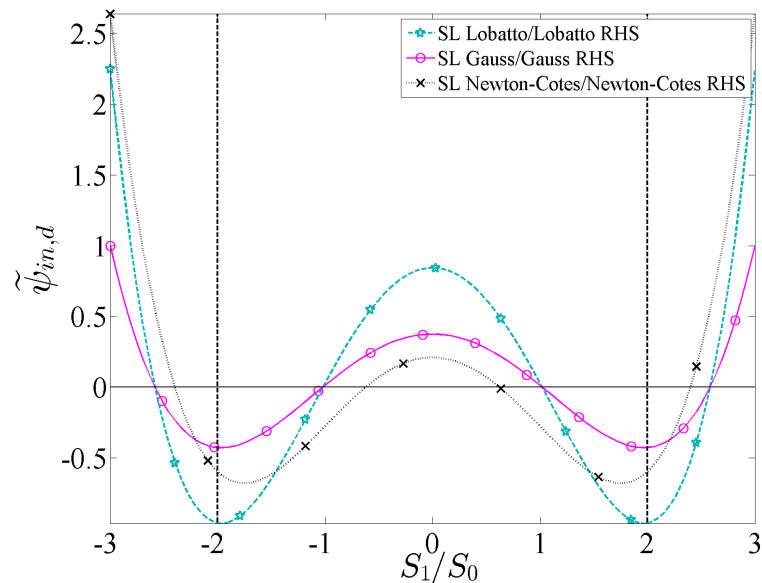


Figure 2.8: Numerical inflow values as a function of  $\frac{S_1}{S_0}$  for a single cell (vacuum case) with a  $\delta$ -shaped source, using quartic DFEM.

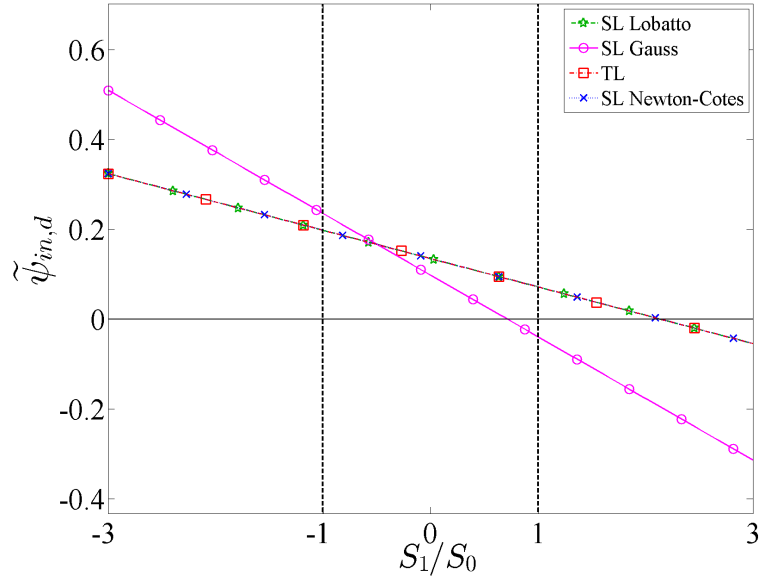


Figure 2.9: Numerical inflow values as a function of  $\frac{S_1}{S_0}$ , for a single cell (absorber case) with a  $\delta$ -shaped source, using linear DFEM.

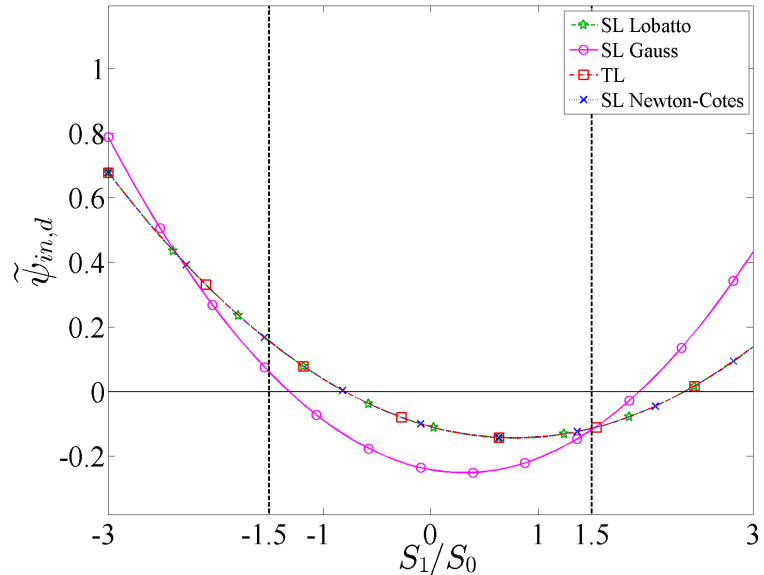


Figure 2.10: Numerical inflow values as a function of  $\frac{S_1}{S_0}$ , for a single cell (absorber case) with a  $\delta$ -shaped source, using quadratic DFEM.

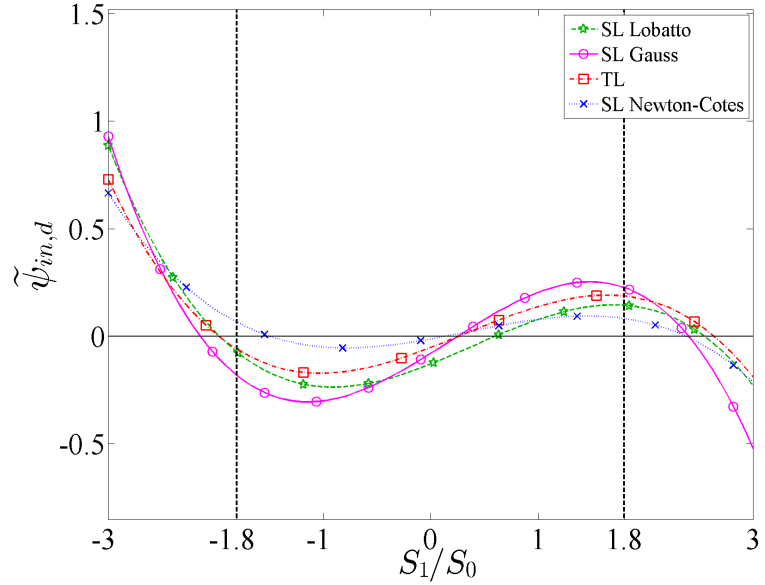


Figure 2.11: Numerical inflow values as a function of  $\frac{S_1}{S_0}$ , for a single cell (absorber case) with a  $\delta$ -shaped source, using cubic DFEM.

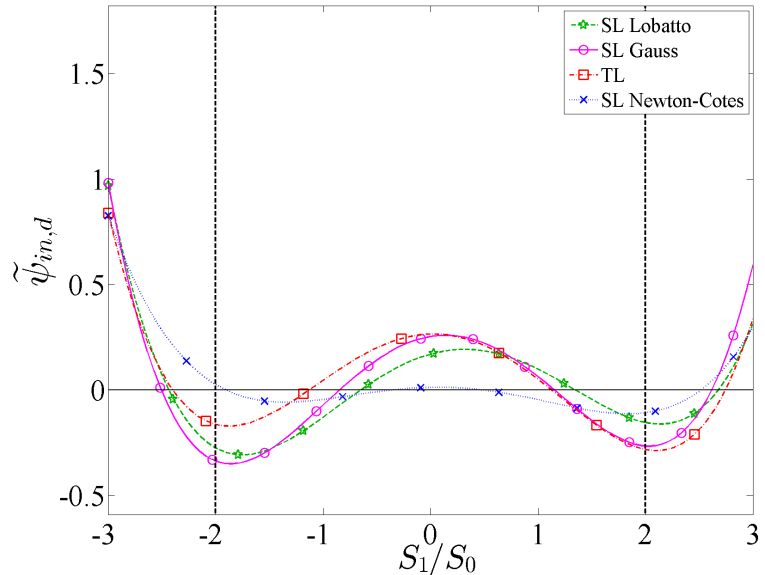


Figure 2.12: Numerical inflow values as a function of  $\frac{S_1}{S_0}$ , for a single cell (absorber case) with a  $\delta$ -shaped source, using quartic DFEM.

In Figs. 2.9-2.12, we again examine the positivity of  $\tilde{\psi}_{in,d}$ , but for a non-vacuum case. Total cell optical thickness was chosen to be 5 mean free paths in Figs. 2.9-2.12 because this value led to the clearest plots. The relative behaviors observed do not change with cell optical thickness, but using a thicker domain reduces the magnitude for the values of  $\tilde{\psi}_{in,d}$ . All methods in Figs. 2.9-2.12 exactly integrate Eq. (2.24). Regardless of trial space chosen, all schemes exhibit some negativities, but the SL Gauss scheme exhibits the greatest negativities and oscillations. The SL Newton-Cotes scheme presents the least severe negativities.

### 2.5.3 Single-Cell Taylor Series Analysis

Next, we perform a local truncation error analysis by comparing the Taylor series expansions for the exact and numerical angular fluxes as a function of powers of  $h$  for the source-free, incident flux pure absorber problem. Matlab [26] has been employed to perform the symbolic Taylor series expansions about  $h = 0$ . We denote the Taylor-expanded quantities using the subscript  $T$ . The expansions for the analytical inflow, cell average, and outflow are given below:

$$\psi_{in,d,T} = \psi_{in,d} \quad (2.40a)$$

$$\psi_{A,d,T} = \psi_{in,d} \left( 1 - \frac{h}{2} + \frac{h^2}{6} - \frac{h^3}{24} + \frac{h^4}{120} - \frac{h^5}{720} \dots \right) \quad (2.40b)$$

$$\psi_{out,d,T} = \psi_{in,d} \left( 1 - h + \frac{h^2}{2} - \frac{h^3}{6} + \frac{h^4}{24} - \frac{h^5}{120} \dots \right). \quad (2.40c)$$

The Taylor expansions of the numerical analogues to the quantities in Eqs. (2.40) depend on the trial space polynomial degree, the choice of interpolatory points, and the numerical integration strategy. For brevity, we omit giving these numerical analogues. Table 2.6 gives the lowest order term for the difference between  $\psi_{in,d,T}$  and the numerical analogs for the Exact DFEM and TL schemes. The same information

for the SL Newton-Cotes, SL Gauss, and SL Lobatto schemes is given in Table 2.7. The differences between  $\psi_{A,d,T}$  and the respective numerical analogs are given in Table 2.8 for Exact DFEM and TL, and Table 2.9 for the SL Newton-Cotes, SL Gauss, and SL Lobatto schemes. Differences between  $\psi_{out,d,T}$  and the corresponding numerical analogs are given in Table 2.10 for Exact DFEM and TL and Table 2.11 gives the lowest order difference between the SL Newton-Cotes, SL Gauss, and SL Lobatto approximations of  $\psi_{out,d,T}$ . In Tables 2.6-2.11 all entries are listed as  $q(C)$ , to be read as “the difference between the analytic taylor expansion and the numeric analog is  $Ch^q$  with  $h = \Sigma_t \Delta x / \mu$ ”. Entries of “Machine Precision” in Tables 2.6-2.11 are meant to indicate that the difference between the analytic Taylor expansion and Taylor expansion of the numerical approximation was inconclusive due to all coefficients being within machine precision.

Table 2.6: Local truncation error analysis in  $\tilde{\psi}_{in,d}$  for a single cell problem with constant cross section, for Exact DFEM and TL.

Polynomial Degree of $\tilde{\psi}$	Exact DFEM	TL
1	2 ( $2 \times 10^{-1}$ )	2 ( $5 \times 10^{-1}$ )
2	3 ( $2 \times 10^{-2}$ )	3 ( $4 \times 10^{-2}$ )
3	4 ( $1 \times 10^{-3}$ )	2 ( $7 \times 10^{-2}$ )
4	5 ( $7 \times 10^{-5}$ )	3 ( $1 \times 10^{-2}$ )
5	6 ( $3 \times 10^{-6}$ )	2 ( $5 \times 10^{-2}$ )
6	7 ( $1 \times 10^{-7}$ )	3 ( $1 \times 10^{-2}$ )
7	8 ( $4 \times 10^{-9}$ )	2 ( $5 \times 10^{-2}$ )

Table 2.7: Local truncation error analysis in  $\tilde{\psi}_{in,d}$  for a single cell problem with constant cross section, for SL Newton-Cotes, SL Gauss, and SL Lobatto.

Polynomial Degree of $\tilde{\psi}$	SL Newton-Cotes	SL Gauss	SL Lobatto
1	2 ( $5 \times 10^{-1}$ )	2 ( $2 \times 10^{-1}$ )	2 ( $5 \times 10^{-1}$ )
2	3 ( $4 \times 10^{-2}$ )	3 ( $2 \times 10^{-2}$ )	3 ( $4 \times 10^{-2}$ )
3	2 ( $1 \times 10^{-1}$ )	4 ( $1 \times 10^{-3}$ )	4 ( $3 \times 10^{-3}$ )
4	3 ( $1 \times 10^{-2}$ )	5 ( $7 \times 10^{-5}$ )	5 ( $1 \times 10^{-4}$ )
5	2 ( $6 \times 10^{-2}$ )	6 ( $3 \times 10^{-6}$ )	6 ( $7 \times 10^{-6}$ )
6	3 ( $9 \times 10^{-3}$ )	7 ( $1 \times 10^{-7}$ )	7 ( $3 \times 10^{-7}$ )
7	2 ( $4 \times 10^{-2}$ )	8 ( $4 \times 10^{-9}$ )	8 ( $8 \times 10^{-9}$ )

Table 2.8: Local truncation error analysis in  $\tilde{\psi}_{A,d}$  for a single cell problem with constant cross section, for Exact DFEM and TL.

Polynomial Degree of $\tilde{\psi}$	Exact DFEM	TL
1	3 ( $1 \times 10^{-2}$ )	2 ( $2 \times 10^{-1}$ )
2	5 ( $1 \times 10^{-4}$ )	4 ( $2 \times 10^{-3}$ )
3	7 ( $7 \times 10^{-7}$ )	3 ( $3 \times 10^{-3}$ )
4	9 ( $2 \times 10^{-9}$ )	5 ( $8 \times 10^{-5}$ )
5	11 ( $5 \times 10^{-12}$ )	3 ( $1 \times 10^{-3}$ )
6	13 ( $7 \times 10^{-15}$ )	5 ( $7 \times 10^{-5}$ )
7	Machine Precision	3 ( $1 \times 10^{-3}$ )

Table 2.9: Local truncation error analysis in  $\tilde{\psi}_{A,d}$  for a single cell problem with constant cross section, for SL Newton-Cotes, SL Gauss, and SL Lobatto

Polynomial Degree of $\tilde{\psi}$	SL Newton-Cotes	SL Gauss	SL Lobatto
1	2 ( $2 \times 10^{-1}$ )	3 ( $1 \times 10^{-2}$ )	2 ( $2 \times 10^{-1}$ )
2	4 ( $2 \times 10^{-3}$ )	5 ( $1 \times 10^{-4}$ )	4 ( $2 \times 10^{-3}$ )
3	4 ( $6 \times 10^{-4}$ )	7 ( $7 \times 10^{-7}$ )	6 ( $1 \times 10^{-5}$ )
4	6 ( $8 \times 10^{-6}$ )	9 ( $2 \times 10^{-9}$ )	8 ( $5 \times 10^{-8}$ )
5	6 ( $2 \times 10^{-6}$ )	11 ( $5 \times 10^{-12}$ )	10 ( $1 \times 10^{-10}$ )
6	8 ( $2 \times 10^{-8}$ )	13 ( $7 \times 10^{-15}$ )	12 ( $2 \times 10^{-13}$ )
7	8 ( $3 \times 10^{-9}$ )	Machine Precision	Machine Precision

Table 2.10: Local truncation error analysis in  $\tilde{\psi}_{out,d}$  for a single cell with constant cross section, for Exact DFEM and TL.

Polynomial Degree of $\tilde{\psi}$	Exact DFEM	TL
1	4 ( $1 \times 10^{-2}$ )	3 ( $2 \times 10^{-1}$ )
2	6 ( $1 \times 10^{-4}$ )	5 ( $2 \times 10^{-3}$ )
3	8 ( $7 \times 10^{-7}$ )	4 ( $3 \times 10^{-3}$ )
4	10 ( $2 \times 10^{-9}$ )	6 ( $1 \times 10^{-2}$ )
5	12 ( $5 \times 10^{-12}$ )	4 ( $1 \times 10^{-3}$ )
6	14 ( $7 \times 10^{-15}$ )	6 ( $7 \times 10^{-5}$ )
7	Machine Precision	4 ( $1 \times 10^{-3}$ )

Table 2.11: Local truncation error analysis in  $\tilde{\psi}_{out,d}$  for a single cell with constant cross section, for SL Newton-Cotes, SL Gauss, and SL Lobatto.

Polynomial Degree of $\tilde{\psi}$	SL Newton-Cotes	SL Gauss	SL Lobatto
1	3 ( $2 \times 10^{-1}$ )	4 ( $1 \times 10^{-2}$ )	3 ( $2 \times 10^{-1}$ )
2	5 ( $2 \times 10^{-3}$ )	6 ( $1 \times 10^{-4}$ )	5 ( $2 \times 10^{-3}$ )
3	5 ( $6 \times 10^{-4}$ )	8 ( $7 \times 10^{-7}$ )	7 ( $1 \times 10^{-5}$ )
4	7 ( $8 \times 10^{-6}$ )	10 ( $2 \times 10^{-9}$ )	9 ( $5 \times 10^{-8}$ )
5	7 ( $2 \times 10^{-6}$ )	12 ( $5 \times 10^{-12}$ )	11 ( $1 \times 10^{-10}$ )
6	9 ( $2 \times 10^{-8}$ )	14 ( $7 \times 10^{-15}$ )	13 ( $2 \times 10^{-13}$ )
7	9 ( $3 \times 10^{-9}$ )	Machine Precision	Machine Precision

This local truncation error analysis illustrates the following.

1. Exact DFEM and SL Gauss, which are equivalent, exactly integrate the mass matrix, and are the most accurate,
2. TL does not guarantee increasing order of accuracy by using higher degree polynomial trial spaces,

3. TL converges at most third or fifth order for  $\tilde{\psi}_{A,d}$  and fourth or sixth order for  $\tilde{\psi}_{out,d}$  for odd or even polynomial trial spaces, respectively,
4. SL Newton-Cotes increases in accuracy with higher degree polynomial trial spaces, but only for  $\tilde{\psi}_{out,d}$  and  $\tilde{\psi}_{A,d}$ ,
5. TL and SL Newton-Cotes are at most second order or third order accurate for  $\tilde{\psi}_{in,d}$  for odd or even polynomial trial spaces, respectively,
6. SL Gauss is order  $2P+1$  accurate in calculating  $\tilde{\psi}_{A,d}$  and order  $2P+2$  accurate in calculating  $\tilde{\psi}_{out,d}$ ,
7. SL Lobatto is order  $2P$  accurate in calculating  $\tilde{\psi}_{A,d}$  and order  $2P+1$  in calculating  $\tilde{\psi}_{out,d}$ ,
8. SL Gauss, SL Lobatto, and Exact DFEM are accurate to order  $P+1$  in calculating  $\tilde{\psi}_{in,d}$ , and
9. SL Gauss is more accurate than SL Lobatto (smaller error constant) in computing  $\tilde{\psi}_{in,d}$ , but not an order of  $h$ .

#### 2.5.4 Convergence Rates for Spatially Discretized 1-D Domains

Here, we consider a homogeneous pure absorber material placed in a 1-D slab configuration and uniformly mesh the domain using  $N_{cells}$  cells. We use:  $x \in [0, 10 \text{ cm}]$ ,  $\Sigma_t = 1 [\text{cm}^{-1}]$ , no external sources, vacuum conditions on the right face of the slab, and a normally incident unit beam on the left face. The analytical solution to this problem is trivial to obtain:

$$\psi(x, \mu_d) = \begin{cases} \exp[-\Sigma_t x] & \mu_d = 1 \\ 0 & \text{otherwise} \end{cases}. \quad (2.41)$$

The  $L_2$  norm of the error is:

$$E_\psi = \sqrt{\sum_{i=1}^{N_{cells}} \int_{x_{i-1/2}}^{x_{i+1/2}} \left( \psi(x, \mu_d) - \tilde{\psi}_{d,i}(x) \right)^2 dx}, \quad (2.42)$$

where we recall that  $\tilde{\psi}_{d,i}(x)$  is the DFEM approximation of the angular flux in cell  $i$ .

To evaluate the above integral, we use a high-order Gauss quadrature set  $(x_{f,q}, w_{f,q})$  that employs a large number of quadrature points:

$$E_\psi \approx \sqrt{\sum_{i=1}^{N_{cells}} \frac{\Delta x_i}{2} \sum_{q=1}^{N_{qf}} w_{f,q} \left( \psi(x_{f,q}, \mu_d) - \tilde{\psi}_d(x_{f,q}) \right)^2}. \quad (2.43)$$

Values of  $E_\psi$  shown here are calculated using  $N_{qf} = 10$ . In addition to the  $L_2$  error, we also present the cell average angular flux error,  $E_{\psi_A}$ , defined as

$$E_{\psi_A} = \sqrt{\sum_{i=1}^{N_{cells}} \Delta x_i \left( \psi_{A,d,i} - \tilde{\psi}_{A,d,i} \right)^2}, \quad (2.44)$$

and the cell outflow error,  $E_{\psi_{out}}$ , given by:

$$E_{\psi_{out}} = \sqrt{\sum_{i=1}^{N_{cells}} \Delta x_i \left( \psi(x_{i+1/2}, \mu_d) - \tilde{\psi}_{out,d,i} \right)^2}. \quad (2.45)$$

In Eq. (2.43), Eq. (2.44), and Eq. (2.45),  $\Delta x_i$  is the cell width of cell  $i$  and  $\psi_{A,d,i}$  is the exact cell-averaged angular flux in cell  $i$ , which, for  $\mu_d = 1$ , is simply:

$$\psi_{A,d,i} = \exp[-\Sigma_t x_{i-1/2}] \frac{1}{\Delta x_i} (1 - \exp[-\Sigma_t \Delta x_i]). \quad (2.46)$$

In the plots that follow, we omit plotting the errors of Exact DFEM since the Exact DFEM solution is identical to that of SL Gauss. For linear and quadratic polynomi-

als, we plot only SL Lobatto and omit plotting TL and SL Newton-Cotes since these methods yield identical solutions for linear and quadratic trial spaces. Figures

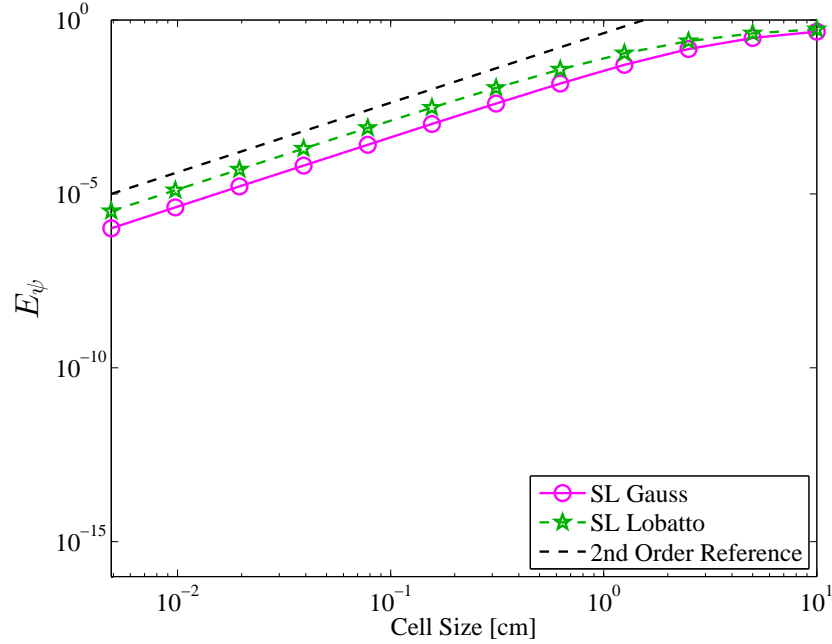


Figure 2.13: Convergence rate of the  $L_2$  norm of the error,  $E_\psi$ , as a function of the mesh cell size for a pure absorber discretized with linear DFEM.

2.13-2.16 mirror the results of Table 2.6 and Table 2.7, which is expected since the convergence rate of  $E_\psi$  will be limited by the slowest converging local approximation which is  $\tilde{\psi}_{in,d}$ . Similarly, Figs. 2.17-2.20 are the multiple-cell analogue of the local truncation error analysis of  $\tilde{\psi}_{A,d}$  given in Table 2.8 and Table 2.9.  $E_{\psi_{out}}$ , as shown in Figs. 2.21-2.24, does not converge at the local truncation error rates of Table 2.10 and Table 2.11.

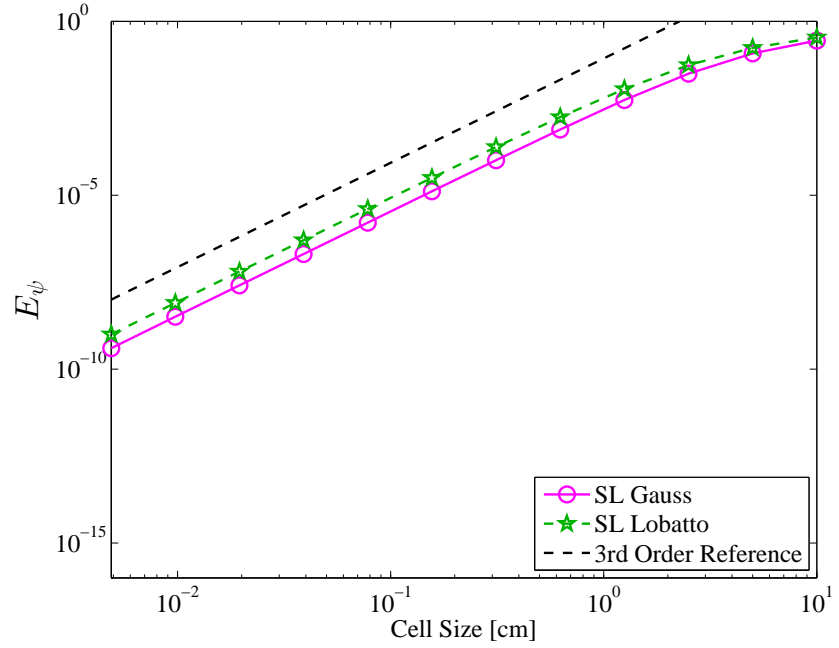


Figure 2.14: Convergence rate of the  $L_2$  norm of the error,  $E_\psi$ , as a function of the mesh cell size for a pure absorber discretized with quadratic DFEM.

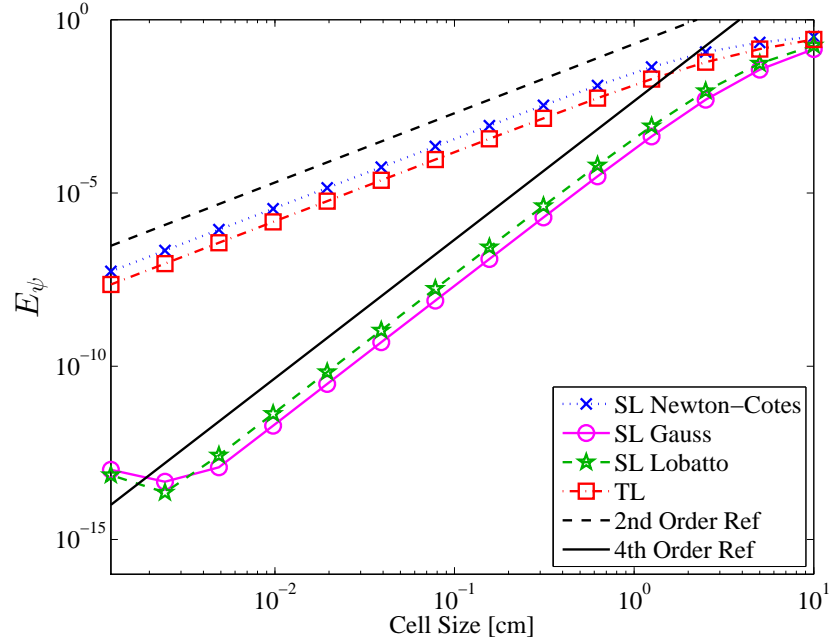


Figure 2.15: Convergence rate of the  $L_2$  norm of the error,  $E_\psi$ , as a function of the mesh cell size for a pure absorber discretized with cubic DFEM.

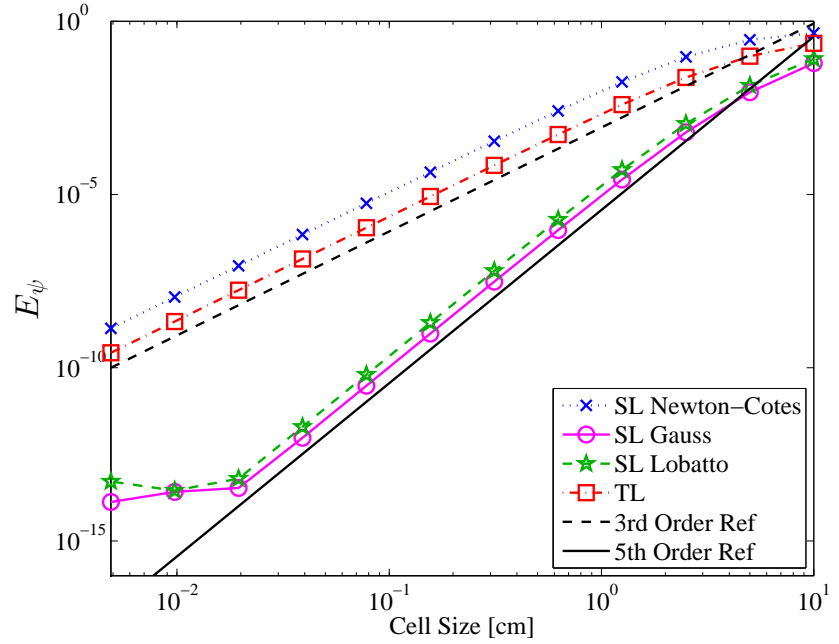


Figure 2.16: Convergence rate of the  $L_2$  norm of the error,  $E_\psi$ , as a function of the mesh cell size for a pure absorber discretized with quartic DFEM.

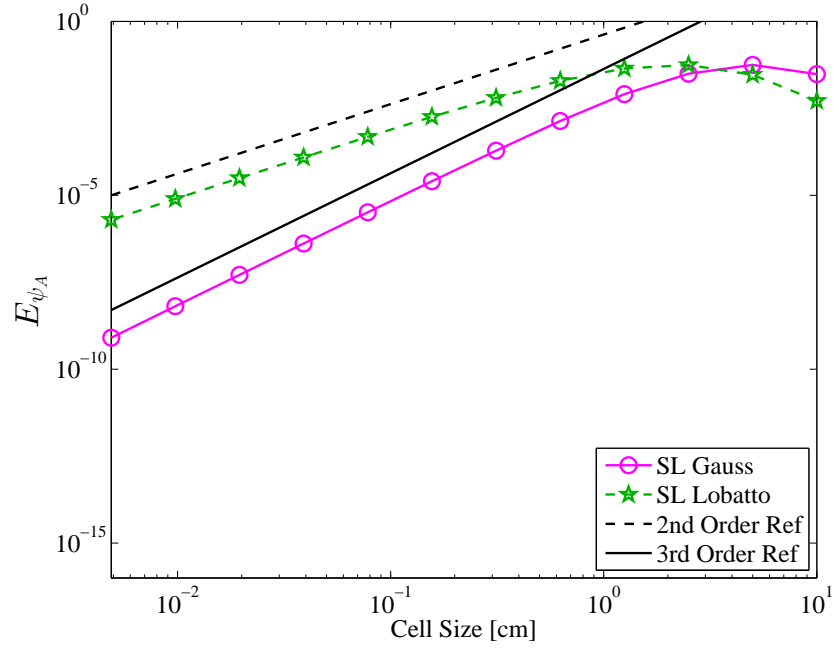


Figure 2.17: Convergence rate for  $E_{\psi,A}$  as a function of the mesh cell size for a homogeneous pure absorber and linear DFEM.

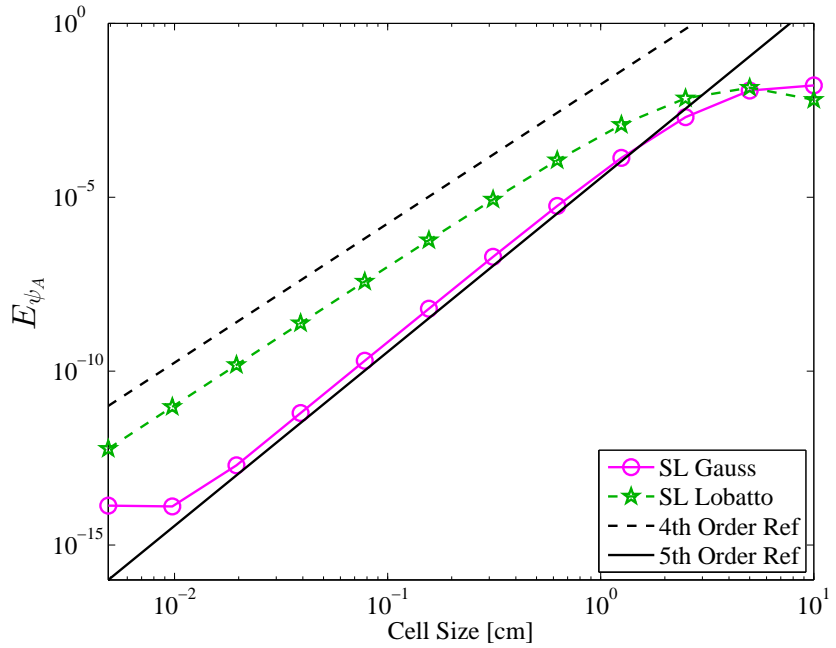


Figure 2.18: Convergence rate for  $E_{\psi,A}$  as a function of the mesh cell size for a homogeneous pure absorber and quadratic DFEM.

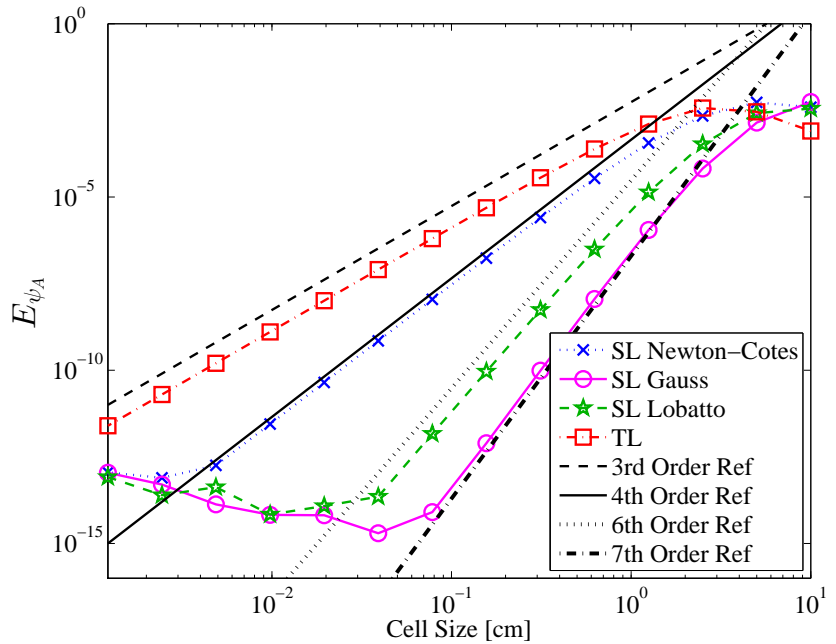


Figure 2.19: Convergence rate for  $E_{\psi,A}$  as a function of the mesh cell size for a homogeneous pure absorber and cubic DFEM.

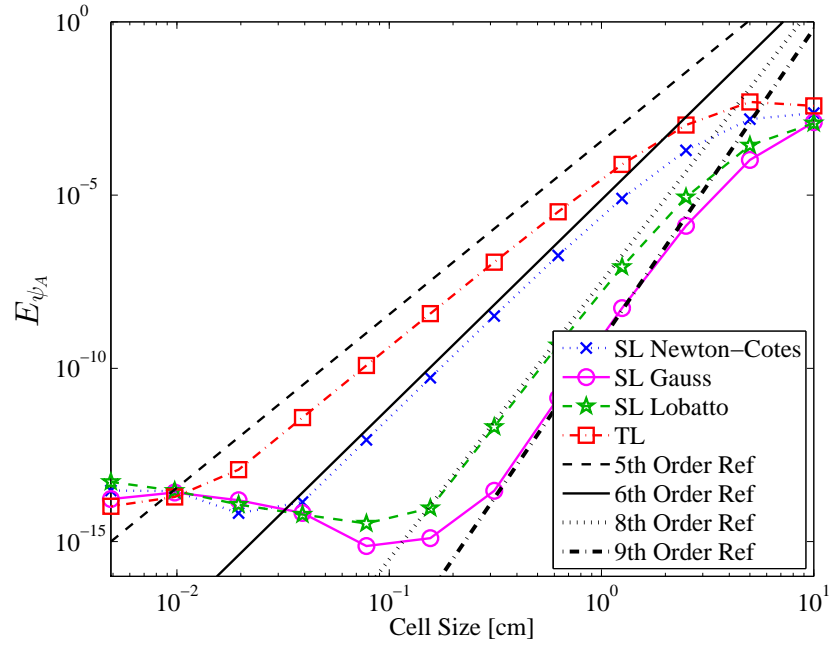


Figure 2.20: Convergence rate for  $E_{\psi,A}$  as a function of the mesh cell size for a homogeneous pure absorber and quartic DFEM.

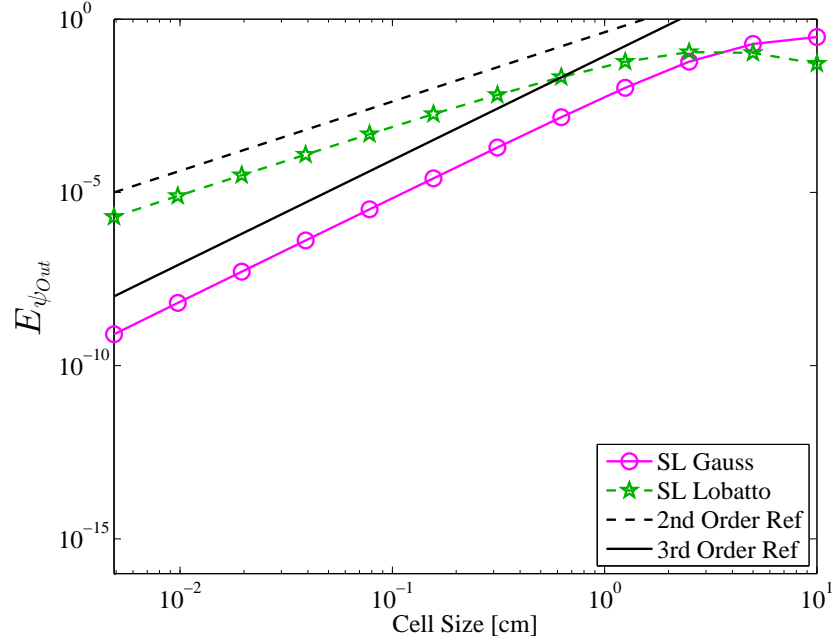


Figure 2.21: Convergence rate of  $E_{\psi,out}$  as a function of the mesh cell size for a homogeneous pure absorber for linear DFEM.

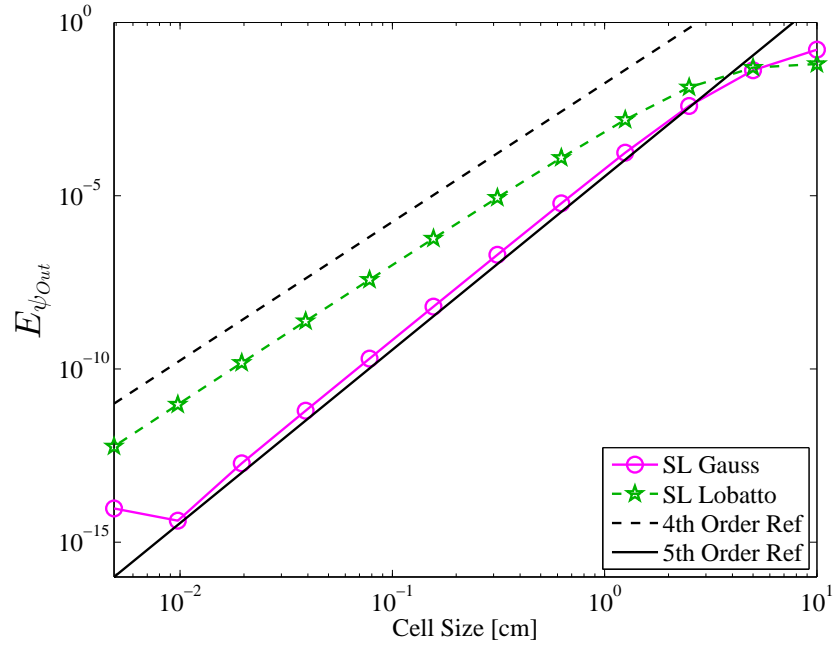


Figure 2.22: Convergence rate of  $E_{\psi,out}$  as a function of the mesh cell size for a homogeneous pure absorber for quadratic DFEM.

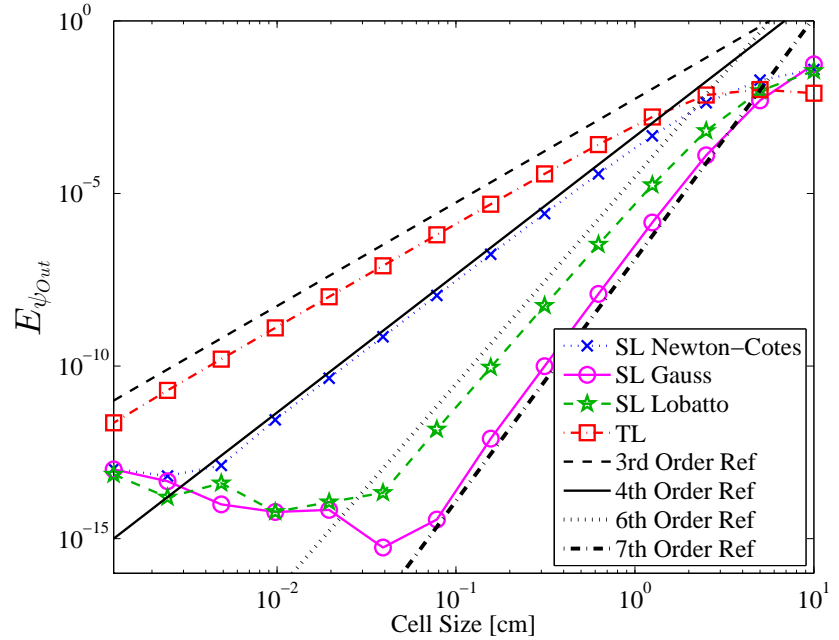


Figure 2.23: Convergence rate of  $E_{\psi,out}$  as a function of the mesh cell size for a homogeneous pure absorber for cubic DFEM.

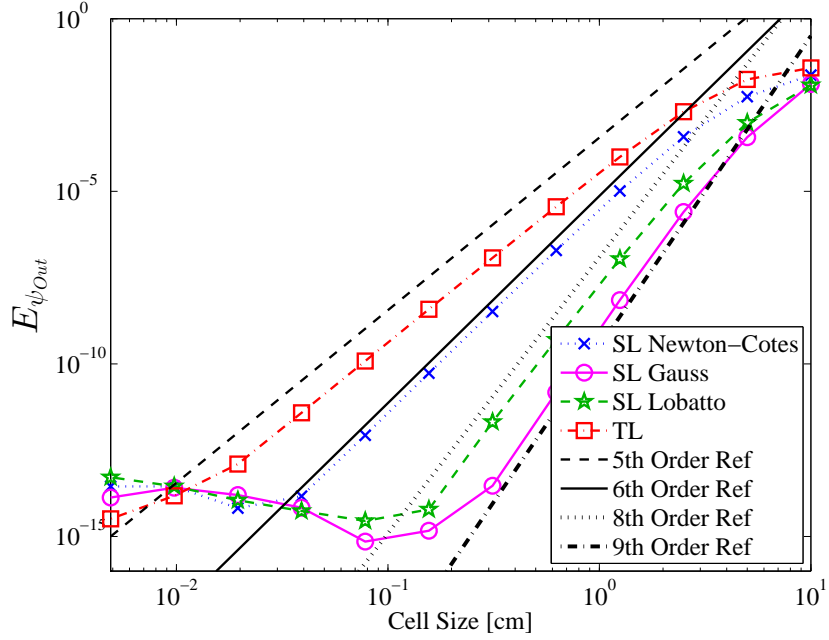


Figure 2.24: Convergence rate of  $E_{\psi,out}$  as a function of the mesh cell size for a pure absorber for quartic DFEM.

The accumulation of errors in multiple-cell problems causes  $E_{\psi,out}$  to globally converge one order of accuracy lower than the local truncation orders given in Table 2.10 and Table 2.11. It should be noted that the plateauing of errors  $E_\psi$ ,  $E_{\psi_A}$ , and  $E_{\psi,out}$  to values  $\approx 10^{-14}$  in Figs. 2.13-2.16, Figs. 2.17-2.20, and Figs. 2.21-2.24, respectively, is simply a result of our numerical solutions being limited by machine precision (double precision).

## 2.6 Conclusions About Self-Lumping

We have shown that, for arbitrary degree polynomial trial space DFEM, a diagonal mass matrix does not necessarily ensure strictly positive angular flux outflow in a purely absorbing slab with spatially constant cross section. Indeed, the TL scheme was neither robust or accurate for polynomial trial space degree greater than linear. Also, we have shown that by using quadrature-based lumping schemes and choosing

DFEM interpolation points that are not equally spaced, robust, accurate polynomial DFEM schemes can be obtained. Based on the observed robustness, accuracy, and spatial convergence order results, we conclude that, for applications requiring robust solution techniques, the SL Lobatto scheme with odd degree polynomial trial space DFEM should be used to discretize the angular flux . If  $p$ -adaptivity is desired, software should be developed such that the ability to use either Lobatto (for odd trial space degrees) or Gauss (for even trial space degree) quadrature as the DFEM interpolation points is possible. However, given the non-monotonic behavior of the outflow angular flux as a function of the cell optical thickness when employing the SL Gauss scheme with even degree trial spaces for under-resolved problems, using SL Lobatto with an odd degree trial space would seem to be more accurate than using SL Gauss, despite SL Gauss being more accurate in the asymptotic (fine mesh) limit. Finally, though not as accurate SL Lobatto or SL Gauss, we will continue to consider SL Newton-Cotes due to its observed robustness.

### 3. DFEM METHODS FOR NEUTRON TRANSPORT FOR PROBLEMS WITH SPATIALLY VARYING CROSS SECTION

For many problems of interest to the nuclear science and engineering community, macroscopic cross sections in neutronics and opacities in radiative transfer calculations cannot accurately be described as piecewise constants in space. Cross sections and opacities are functions of continuously varying quantities such as temperature, density, burn-up history, etc. [27]. An example simulation that is not adequately described with cell-wise constant cross sections includes nuclear reactor isotopic depletion calculations. In thermal radiative transfer, interaction opacities can be rapidly varying functions of temperature. For example, consider Marshak wave problems and the canonical  $T^{-3}$  dependence [9] of absorption opacity. Across cells near the heated/cold material interface, opacity variations of several orders of magnitude are easily possible.

Historically, the neutron transport and thermal radiative transfer communities assumed interaction cross section and opacities, respectively, that were cell-wise constant [1, 6, 15]. Adams first described [7] and then presented computational results [8] for a “simple” corner balance (SCB) spatial discretization method that explicitly accounted for the spatial variation of opacity within individual spatial cells. The SCB scheme (which can be shown to be related to a LDFEM for certain geometries) accounts for opacity spatial variation within each cell via vertex-based quadrature evaluation. Similar strategies have been adapted to LDFEM radiative diffusion [9] and LDFEM TRT [28] calculations. For accurate TRT solutions, use of higher order DFEM will require the development of corresponding higher order strategies for treating the within cell spatial variation of opacities. However, the majority of

neutron transport literature has only considered the case of cell-wise constant cross sections, see [1, 15, 21, 29]. The work of Kavenoky and Lautard [30] and more recently Santandrea and Bellier [31] are notable exceptions in neutron transport. In [30], continuous cubic finite element diffusion calculations that assume a linearly varying spatial cross section within each mesh cell were compared to results obtained using the same spatial discretization but with the assumption that cross sections are constant in each cell. Similarly, [31] compared the results of a linear characteristic scheme that assumes a linearly varying cross section in each spatial cell to those of a linear characteristic scheme that assumes a constant cross section in each cell.

In this section, we analyze the effects of cross-section spatial dependence on solution accuracy, as we did in our previously published work in [32]. Our work differs from [7, 8, 30, 31] by considering a discontinuous finite element (DFEM) spatial discretization of the slab geometry  $S_N$  transport equation using arbitrary degree polynomial finite element trial spaces. In addition, like [7] and [8] we do not make any approximation to the particular spatial shape of the cross-section spatial variation in each cell. We build on the quadrature integration ideas presented in Section 2 and employ a numerical quadrature to evaluate the mass matrix integrals that involve cross sections as a function of space. In general, the quadrature integration of the DFEM interaction term with arbitrary spatial cross section form will not be exact. However, we showed in Section 2 that exact computation of integrals appearing in the DFEM weak form, when cross sections are spatially constant, is not required to achieve high-order accuracy with high-order DFEM approximations. Building on this idea, we investigate the effects of using numerical quadratures to compute DFEM mass matrices, accounting for the spatial variation of cross section in space. As in Section 2 we use self-lumping numerical quadratures [23, 25], restricting quadrature integration points to the DFEM polynomial interpolation points. Results are com-

pared as a function of DFEM polynomial trial space degree and interpolation point type.

We demonstrate that assuming a piecewise constant cross section in each cell, when the cross section is not cell-wise constant in space, has several undesirable effects. Considering a source-free, purely absorbing medium, we show that DFEM schemes that assume a cell-wise constant cross section are at most second-order accurate for the angular flux solution and limited to at most first-order accuracy for the interaction rate solution, regardless of the DFEM polynomial trial space degree. We also show that assuming a piecewise constant cross section results in a highly discontinuous, non-monotonic spatial interaction rate. This phenomena has likely been present in published numerical results for problems with non-piecewise constant cross section but was not observed previously due to the choice of data presentation.

We then consider schemes that explicitly account for cross-section spatial variation within individual mesh cells. First, the positivity and robustness of different schemes are discussed using a source-free pure absorber problem. Next, we demonstrate that self-lumping schemes that evaluate the DFEM weak form integrals involving cross section with quadrature result in fully accurate schemes for arbitrary degree polynomial DFEM. By fully accurate we mean schemes that achieve the same order of convergence for problems with spatially varying and cell-wise constant cross section, for a given DFEM approximation order

### 3.1 Weak Form Derivation

We begin by repeating the DFEM neutron transport equation derived in Section 2:

$$(\mu_d \mathbf{G} + \Sigma_t \mathbf{M}) \vec{\psi}_d = \vec{Q}_d + \mu_d \psi_{in,d} \vec{f}. \quad (3.1)$$

To account for the within cell variation of cross section, we need only make one change to Eq. (3.1). We introduce the concept of a reaction matrix,  $\mathbf{R}_\Sigma$  where  $\Sigma$  is any interaction cross section or other material property:

$$(\mu_d \mathbf{G} + \mathbf{R}_{\Sigma_t}) \vec{\psi}_d = \vec{Q}_d + \mu_d \psi_{in,d} \vec{f}. \quad (3.2)$$

The  $N_P \times N_P$  reaction matrix,  $\mathbf{R}_{\Sigma_t}$  is defined as:

$$\mathbf{R}_{\Sigma_t,ij} = \frac{\Delta x}{2} \int_{-1}^1 \Sigma_t(s) b_i(s) b_j(s) ds. \quad (3.3)$$

Note that if  $\Sigma_t$  is indeed spatially constant within the mesh cell, there is no approximation in removing  $\Sigma_t(s)$  from the integral of Eq. (3.3), giving

$$\mathbf{R}_{\Sigma_t,ij} = \frac{\Delta \Sigma_t}{2} \int_{-1}^1 b_i(s) b_j(s) ds, \quad (3.4)$$

which is equivalent to

$$\mathbf{R}_{\Sigma_t} = \Sigma_t \mathbf{M}. \quad (3.5)$$

### 3.2 Numerical Schemes

We consider two classes of numerical methods in this paper. The first class uses exact spatial integration to evaluate the integrals that define  $\mathbf{R}_{\Sigma_t}$ . A second class of methods uses numerical quadrature to evaluate  $\mathbf{R}_{\Sigma_t}$ ,  $\mathbf{M}$ , and  $\mathbf{G}$ . Specifically, we limit our discussion of quadrature-based integration to so called self-lumping methods [11]. Self-lumping methods, first discussed in [23, 25] for parabolic problems, use numerical quadrature restricted to the finite element interpolation points, and thus naturally yield diagonal mass matrices. A shorthand notation is given in Table 3.1 for all of the numerical methods considered in this section and described in detail in the

remainder of this section.

Table 3.1: Nomenclature of numerical schemes considered for the pure absorber problem with a spatially exponential cross section.

Interpolation Point Type	$\mathbf{R}_{\Sigma_t}$ Matrix Integration Strategy	Method Short Hand Name
Equally-Spaced	Exact Integration using true $\Sigma_t(x)$	EXS DFEM
Equally-Spaced	$\Sigma_t(x) \approx \hat{\Sigma}_t$ , $\mathbf{R}_{\Sigma_t} \approx \hat{\Sigma}_t \mathbf{M}$ Exact Integration of $\mathbf{M}$	CXS DFEM
Equally-Spaced	Self-Lumping via Newton-Cotes Quadrature	SLXS Newton-Cotes
Lobatto Quadrature	Self-Lumping via Lobatto Quadrature	SLXS Lobatto
Gauss Quadrature	Self-Lumping via Gauss Quadrature	SLXS Gauss

### 3.2.1 Exact Spatial Integration

By exact spatial integration, we mean schemes that compute the entries of  $\mathbf{M}$  and  $\mathbf{G}$  exactly. Here, we achieve this by using equally-spaced interpolation points and employing a Gauss-Legendre quadrature rule [24] that exactly integrates the respective integrands of  $\mathbf{M}$  and  $\mathbf{G}$ . Two schemes use exact spatial integration. One approximates the spatially varying cross section as a cell-wise constant cross section. The other uses the exact cross section when integrating the weak form DFEM quantities involving cross section. The scheme that assumes a cell-wise constant cross section represents the state of the practice in the neutron transport community,

while the second scheme represents the ideal scenario for DFEM transport schemes in problems with spatially varying cross sections.

### *3.2.1.1 Exact Cross Section*

The exact cross section, exact spatial integration scheme (EXS DFEM) attempts to analytically integrate the full definition of  $\mathbf{R}_{\Sigma_t}$ . Note that since  $\Sigma_t(x)$  can be an arbitrary function, analytic integration of  $\mathbf{R}_{\Sigma_t}$  is in general impossible. Likewise, quadrature integration is unlikely to be exact. In our testing of the EXS DFEM scheme, we use a 20-point Gauss-Legendre quadrature to approximately integrate Eq. (3.3). Alternatively, adaptive quadrature, with a controllable tolerance, may be used such that the quadrature error in evaluating Eq. (3.3) could be reduced below some small tolerance.

### *3.2.1.2 Constant Cross Section*

Historically, neutronics and some radiative transfer calculations have approximated spatially varying cross sections by assuming cell-wise constant cross sections [1, 6, 15, 29]. That is, some evaluation of the true  $\Sigma_t(s)$  within a given cell is used to determine a constant value,  $\hat{\Sigma}_t$ , within each cell. Under this simplification,  $\mathbf{R}_{\Sigma_t}$  is approximated as:

$$\mathbf{R}_{\Sigma_t} = \hat{\Sigma}_t \mathbf{M}. \quad (3.6a)$$

In our test problems, the constant cross section scheme (CXS DFEM) uses the volumetric average of  $\Sigma_t(s)$  to generate  $\hat{\Sigma}_t$ :

$$\hat{\Sigma}_t = \frac{1}{2} \int_{-1}^1 \Sigma_t(s) \, ds. \quad (3.7)$$

### 3.2.2 Self-Lumping Quadrature Integration

Schemes that are self-lumping evaluate the integrals of Eq. (3.3) using numerical quadrature. In Section 2 we showed that by definition, self-lumping schemes create diagonal mass matrices. Self-lumping schemes also create diagonal reaction matrices:

$$\mathbf{R}_{\Sigma_t,ij} = \begin{cases} w_i \frac{\Delta x}{2} \Sigma_t(s_i) & i = j \\ 0 & \text{otherwise} \end{cases} \quad (3.8)$$

Though the choice of interpolation points does not affect exact integration schemes, as shown in Section 2, the choice of interpolation points was shown to influence both the robustness and accuracy of self-lumping schemes. We consider equally-spaced closed Newton-Cotes, Lobatto-Gauss-Legendre, and Gauss-Legendre quadratures as interpolation points for self-lumping schemes. We do not expect any self-lumping scheme to exactly integrate  $\mathbf{R}_{\Sigma_t}$ , as the integrand defining  $\mathbf{R}_{\Sigma_t}$  will generally not be a polynomial.

## 3.3 Pure Absorber Numerical Results

A beam of radiation,  $\psi_{in}(\mu_d)$ , is incident on the left face of the slab, the right face is a vacuum boundary,  $x \in [0, x_R]$ , and there are no fixed volumetric sources in the medium. We consider  $\Sigma_t(x)$  to be of the form,

$$\Sigma_t(x) = c_1 e^{c_2 x}, \quad (3.9)$$

with  $c_1$  and  $c_2$  are constants [ $cm^{-1}$ ], with  $c_1 > 0$  and  $c_2 \neq 0$ . The analytic angular flux solution for a source-free pure absorber with an exponentially varying cross section

is:

$$\psi(x, \mu) = \begin{cases} \psi_{in}(\mu) \exp\left[\frac{c_1}{\mu c_2}(1 - e^{c_2 x})\right] & \mu = \mu_d \\ 0 & \text{otherwise} \end{cases}. \quad (3.10)$$

By definition, the outflow angular flux from cell  $i$ ,  $\psi_{out,i}$  is  $\psi(x_{i+1/2}, \mu_d)$  and the average angular flux within cell  $i$ ,  $\psi_{A,i}$  as

$$\psi_{A,i} = \frac{1}{\Delta x_i} \int_{x_{i-1/2}}^{x_{i+1/2}} \psi(x, \mu_d) dx, \quad (3.11)$$

with  $\Sigma_t(x)$  defined as in Eq. (3.9). The analytical average flux value is:

$$\psi_{A,i} = \frac{\psi_{in}(\mu_d)}{\Delta x_i} \exp\left[\frac{c_1}{\mu_d c_2}\right] \left[ E_1\left(\frac{c_1 e^{c_2 x_{i+1/2}}}{\mu_d c_2}\right) - E_1\left(\frac{c_1 e^{c_2 x_{i-1/2}}}{\mu_d c_2}\right) \right], \quad (3.12)$$

with  $E_1$  the exponential integral [24].

### 3.3.1 Single Cell Outflow Comparisons

The only variable cross-section schemes that yields strictly positive angular outflows in a source-free pure absorber are the SLXS Lobatto and SLXS Newton-Cotes schemes using a linear trial space. For  $\mu_d > 0$ , consider a source-free, purely absorbing cell with known inflow,  $\psi_{in}(\mu_d)$ , of width  $\Delta x$ , and the total cross section at each interpolation point is  $\Sigma_{t,j}$ . Regardless of the actual functional form of the cross section within the cell, the linear DFEM SLXS Lobatto and SLXS Newton-Cotes schemes' numerical angular flux outflow,  $\tilde{\psi}_d(1)$ , is:

$$\tilde{\psi}_d(1) = \frac{2\mu_d^2 \psi_{in}(\mu_d)}{2\mu_d^2 + \Delta x^2 \Sigma_{t,1} \Sigma_{t,2} + \Delta x \mu_d \Sigma_{t,1} + \Delta x \mu_d \Sigma_{t,2}}. \quad (3.13)$$

Equation 3.13 is strictly positive when  $\Sigma_t(x) \geq 0$ , suggesting that the strictly positive outflow results observed in [11] might hold for an arbitrarily varying spatial cross sec-

tion. However, the results of [11] do not hold for higher-order DFEM approximations for spatially dependent cross sections.

To demonstrate that negative cell outflows are possible, we carry out the following test. In Figs. 3.1-3.4, we plot the angular flux outflow of each method as a function of trial space degree, and the parameter  $c_2$ . We hold the total cell optical thickness to 20 mean-free-path (MFP), vary  $c_2 \in [1, 10]$ , fix  $x_R = 1$ , and  $\mu_d = 1$ . With an exponential cross section, the cell optical thickness in MFP of a cell with  $x \in [0, x_R]$  is:

$$MFP = \int_0^{x_R} \Sigma_t(x) dx = \frac{c_1}{c_2} (e^{c_2 x_R} - 1). \quad (3.14)$$

To maintain a constant optical thickness in Figs. 3.1-3.4,  $c_1$  is required to be:

$$c_1 = \frac{c_2 MFP}{e^{c_2 x_R} - 1}. \quad (3.15)$$

Figures 3.1-3.4 confirms that SLXS Lobatto (and the equivalent SLXS Newton-Cotes scheme) with a linear trial space is the only scheme that explicitly accounts for the spatial variation of cross and maintains a strictly positive angular flux outflow regardless of the shape of  $\Sigma_t(x)$ . From Figs. 3.1-3.4 we also observe that  $\tilde{\psi}_{out}$  varies for every method as a function of the shape of  $\Sigma_t(x)$ , with the obvious exception of CXS DFEM. Considering that the analytic angular flux outflow is only a function of total cell MFP:

$$\psi_{out,i} = \psi_{in}(\mu_d) \exp \left[ - \int_0^{x_{i+1/2}} \Sigma_t(x) dx / \mu_d \right] = \psi_{in}(\mu_d) \exp [-MFP / \mu_d], \quad (3.16)$$

it is unphysical and undesirable that  $\tilde{\psi}_{out}$ , for the SLXS Gauss, SLXS Lobatto, SLXS Newton-Cotes, and EXS DFEM schemes, depends on the spatial shape of  $\Sigma_t(x)$ .

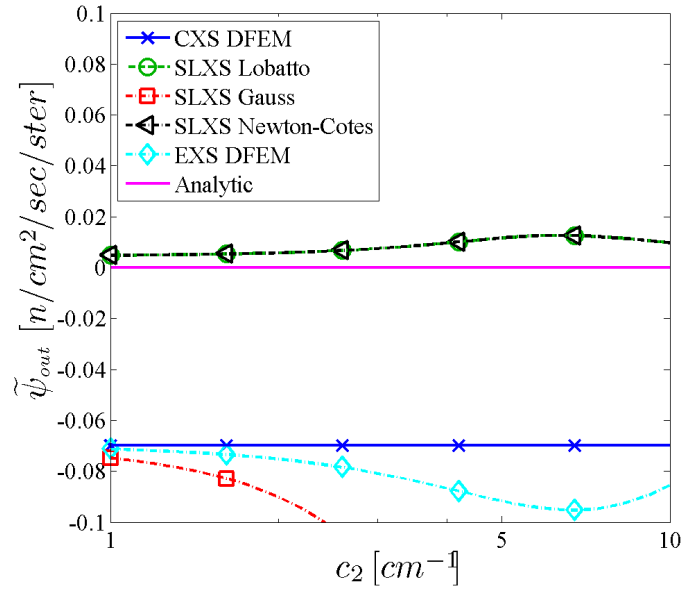


Figure 3.1: Numerical outflow from single cell pure absorber with  $\Sigma_t(x) = c_1 e^{c_2 x}$ , as a function of  $c_2$  with constant optical thickness for linear DFEM.

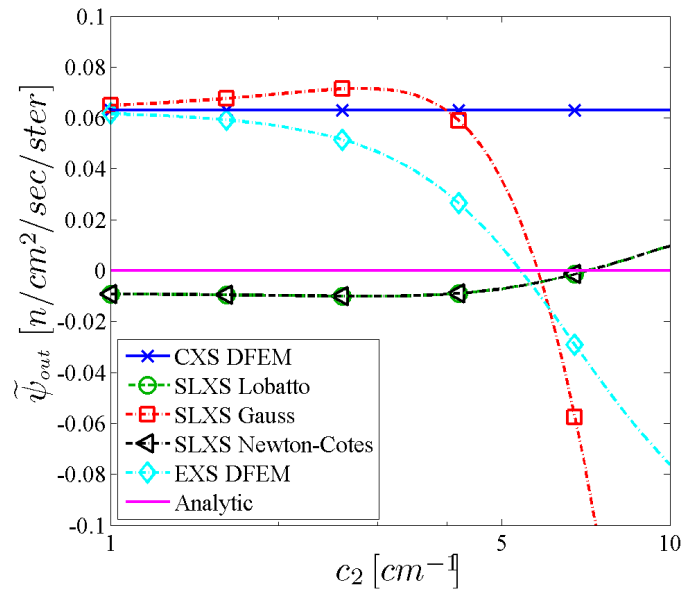


Figure 3.2: Numerical outflow from single cell pure absorber with  $\Sigma_t(x) = c_1 e^{c_2 x}$ , as a function of  $c_2$  with constant optical thickness for quadratic DFEM.

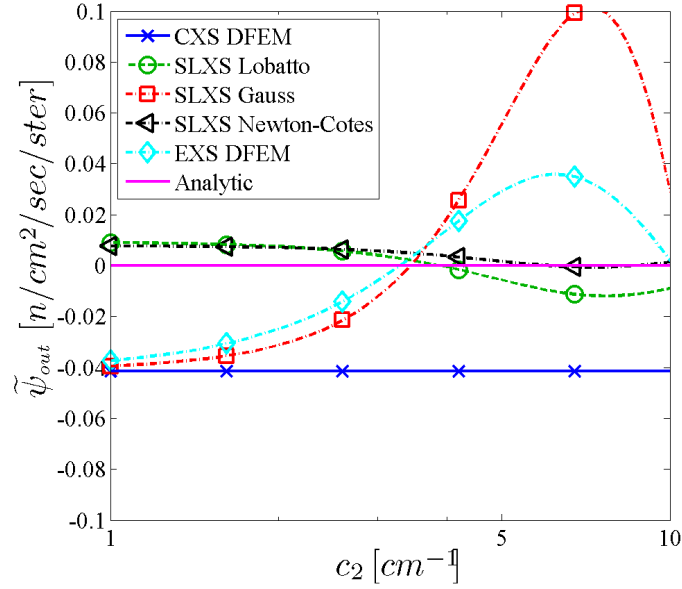


Figure 3.3: Numerical outflow from single cell pure absorber with  $\Sigma_t(x) = c_1 e^{c_2 x}$ , as a function of  $c_2$  with constant optical thickness for cubic DFEM.

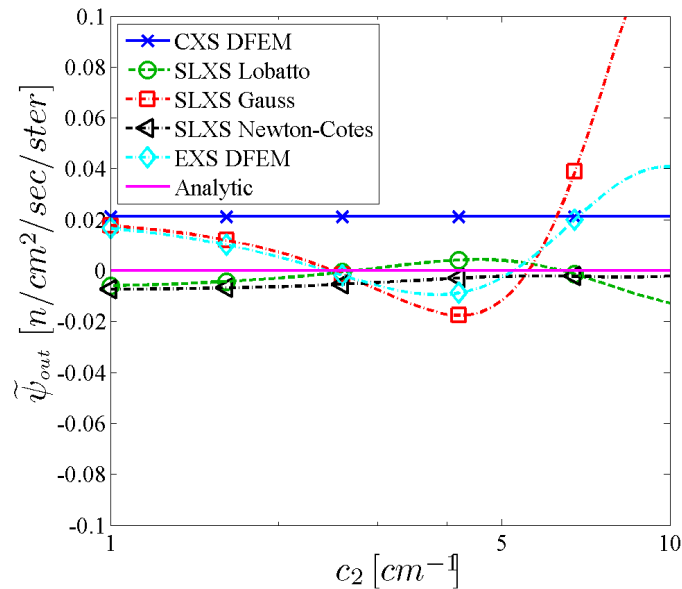


Figure 3.4: Numerical outflow from single cell pure absorber with  $\Sigma_t(x) = c_1 e^{c_2 x}$ , as a function of  $c_2$  with constant optical thickness for quartic DFEM.

### 3.3.2 Multiple Cell Spatial Convergence Rates

We now consider the order of spatial convergence for the following schemes: CXS DFEM, SLXS Gauss, SLXS Lobatto, and SLXS Newton-Cotes. Since exact integration of  $\mathbf{R}_{\Sigma_t}$  is generally not feasible, we no longer consider the EXS DFEM scheme. Convergence results of the following angular flux errors as a function of the polynomial approximation order are presented:

$$E_{\psi} = \sqrt{\sum_{i=1}^{N_{cells}} \int_{x_{i-1/2}}^{x_{i+1/2}} \left( \tilde{\psi}_d(x) - \psi(x, \mu_d) \right)^2 dx} \quad (3.17a)$$

$$E_{\psi_A} = \sqrt{\sum_{i=1}^{N_{cells}} \Delta x_i \left( \tilde{\psi}_{A,i} - \psi_{A,i} \right)^2} \quad (3.17b)$$

$$E_{\psi_{out}} = \sqrt{\sum_{i=1}^{N_{cells}} \Delta x_i \left( \tilde{\psi}_{out,i} - \psi(x_{i+1/2}, \mu_d) \right)^2}. \quad (3.17c)$$

In Eqs. (3.17),  $\Delta x_i$  is the width of cell  $i$ , cell  $i$  spans  $[x_{i-1/2}, x_{i+1/2}]$ ,  $\tilde{\psi}_d(x)$  is the DFEM numerical approximation,  $\psi(x, \mu_d)$  is the analytic solution (see Eq. (3.10)). The problem is spatially discretized using  $N_{cells}$  spatial cells of equal width. We approximate the integrals defining the  $L^2$  norm of the angular flux error,  $E_{\psi}$ , using a high-order Gauss quadrature set,  $(w_{f,q}, s_{f,q})$ , with  $N_{qf}$  points, such that:

$$\int_{x_{i-1/2}}^{x_{i+1/2}} \left( \tilde{\psi}(x) - \psi(x, \mu_d) \right)^2 dx \approx \frac{\Delta x_i}{2} \sum_{q=1}^{N_{qf}} w_{f,q} \left( \tilde{\psi}(s_{f,q}) - \psi(s_{f,q}, \mu_d) \right)^2. \quad (3.18)$$

For the results that follow,  $N_{qf} = 10$ . We recall the definitions for the numerical approximations of the cell average angular flux,  $\tilde{\psi}_{A,i}$ , and the outflow angular flux,

$\tilde{\psi}_{out,i}$ :

$$\tilde{\psi}_{A,i} = \frac{1}{2} \sum_{j=1}^{N_P} w_j \psi_{i,j} \quad (3.19a)$$

$$\tilde{\psi}_{out,i} = \sum_{j=1}^{N_P} \psi_{i,j} b_j(1). \quad (3.19b)$$

We also consider the convergence of the numerical interaction rate,  $\widetilde{IR}(x)$  to the true interaction rate  $IR(x)$ . First, we define the analytic reaction rate for our beam problem:

$$IR(x) = \Sigma_t(x) \psi(x, \mu_d). \quad (3.20)$$

Similarly, we define a cell average interaction rate as:

$$IR_{A,i} = \frac{1}{\Delta x_i} \int_{x_{i-1/2}}^{x_{i+1/2}} \Sigma_t(x) \psi(x, \mu_d) dx. \quad (3.21)$$

Defining a point-wise numerical approximation,  $\widetilde{IR}(x)$ , to the analytic interaction rate for the self-lumping schemes presents a unique problem, since only a numerical quadrature is used to approximate the integrand of  $\mathbf{R}$ . Quadrature integration only requires point evaluations of  $\Sigma_t(x)$ , not knowledge of  $\Sigma_t(x)$  in between quadrature points. However, for the purpose of plotting the SLXS schemes, we define:

$$\widetilde{IR}(s) = \sum_{j=1}^{N_P} b_j(s) \psi_{j,d} \Sigma_t(s_j). \quad (3.22)$$

We approximate the cell average interaction rate in cell  $i$  as:

$$\widetilde{IR}_{A,i} = \frac{1}{2} \sum_{j=1}^{N_P} w_j \Sigma_t(s_j) \psi_{j,d}. \quad (3.23)$$

In Eq. (3.23),  $\Sigma_t(s_j) = \hat{\Sigma}_t$  for the CXS DFEM scheme, and  $\Sigma_t(s_j)$  is the point evaluation of the true cross section for all other schemes.

We consider two measures to assess the error of the DFEM schemes' approximation of the true interaction rate,  $IR(x)$ . The first,  $E_{IR}$  is an approximation of the  $L^2$  norm of interaction rate error:

$$E_{IR} = \sqrt{\sum_{i=1}^{N_{cells}} \frac{\Delta x_i}{2} \sum_{q=1}^{N_P} w_q \left( IR(s_q) - \Sigma_t(s_q) \tilde{\psi}(s_q, \mu_d) \right)^2}. \quad (3.24)$$

We reiterate that, for the self-lumping schemes,  $\widetilde{IR}(s)$  is only truly defined at the DFEM interpolation points.  $E_{IR_A}$  measures the convergence of the average interaction rate:

$$E_{IR_A} = \sqrt{\sum_{i=1}^{N_{cells}} \Delta x_i (IR_{A,i} - \widetilde{IR}_{A,i})^2}. \quad (3.25)$$

For our convergence study, we consider a source-free purely absorbing slab with a cross section that varies exponentially in space as in Eq. (3.9) with  $c_1 = 0.1$  and  $c_2 = 2 \ln(10)$ . A beam of radiation is incident on the left face in the direction of  $\mu_d = 1$ , vacuum boundary conditions exist on the right face of the slab, and  $x \in [0, 1]$ . The convergence of the  $E_\psi$ ,  $E_{\psi_A}$ , and  $E_{\psi_{out}}$  as a function of the choice of numerical scheme for linear through quartic trial space polynomial degree are given in Figs. 3.5-3.8, Figs. 3.9-3.12, and Figs. 3.13-3.16, respectively.

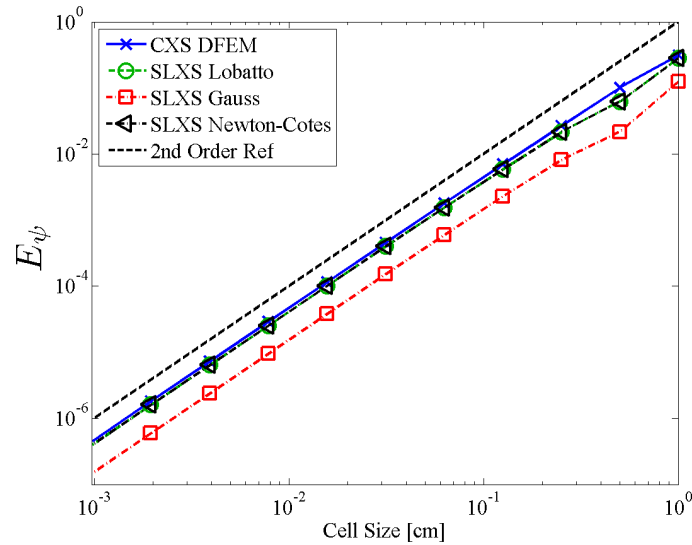


Figure 3.5: Convergence of  $E_\psi$  as a function of mesh size for a pure absorber with exponentially varying cross section discretized with linear DFEM.

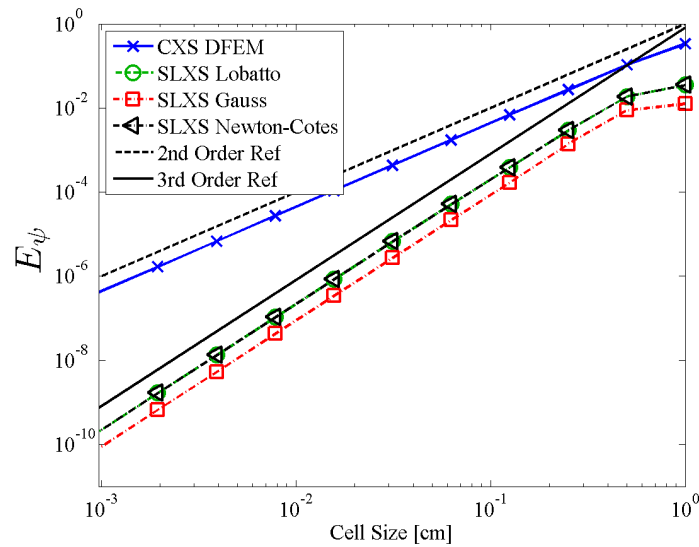


Figure 3.6: Convergence of  $E_\psi$  as a function of mesh size for a pure absorber with exponentially varying cross section discretized with quadratic DFEM.

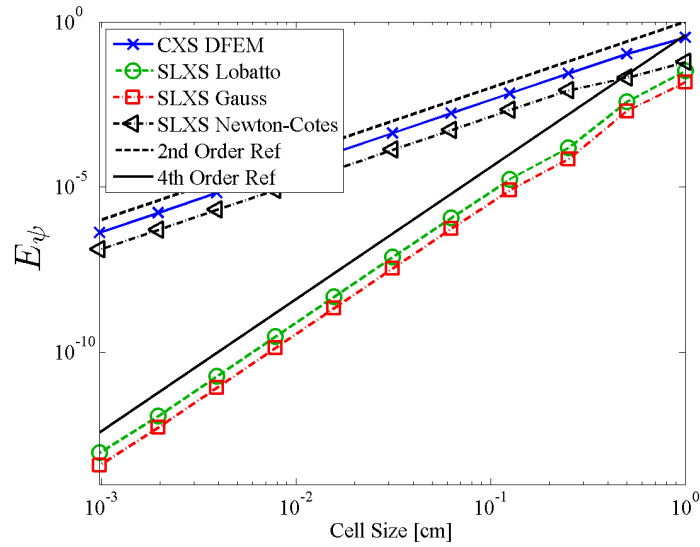


Figure 3.7: Convergence of  $E_\psi$  as a function of mesh size for a pure absorber with exponentially varying cross section discretized with cubic DFEM.

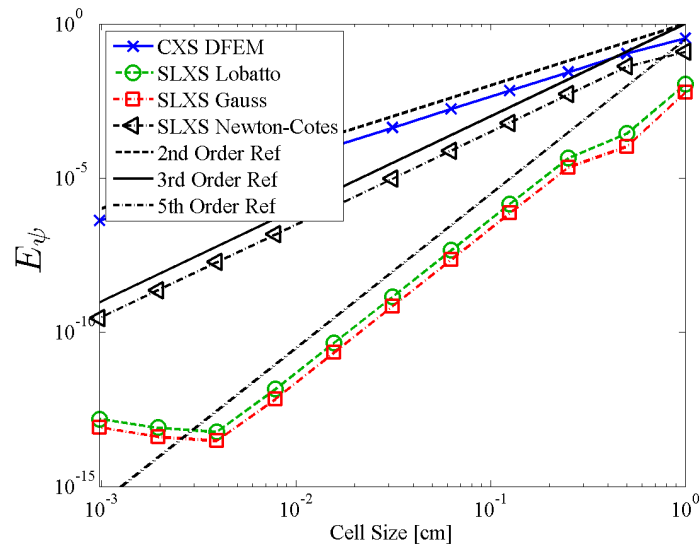


Figure 3.8: Convergence of  $E_\psi$  as a function of mesh size for a pure absorber with exponentially varying cross section discretized with quartic DFEM.

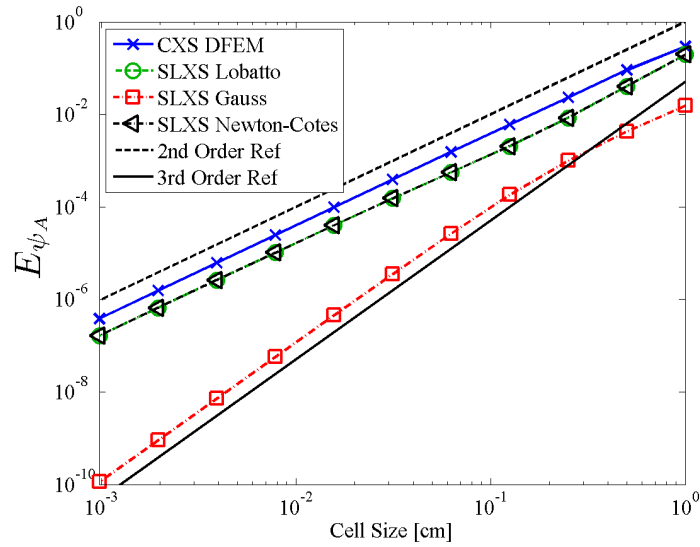


Figure 3.9: Convergence of  $E_{\psi_A}$  as a function of mesh size for a pure absorber with exponentially varying cross section discretized with linear DFEM.

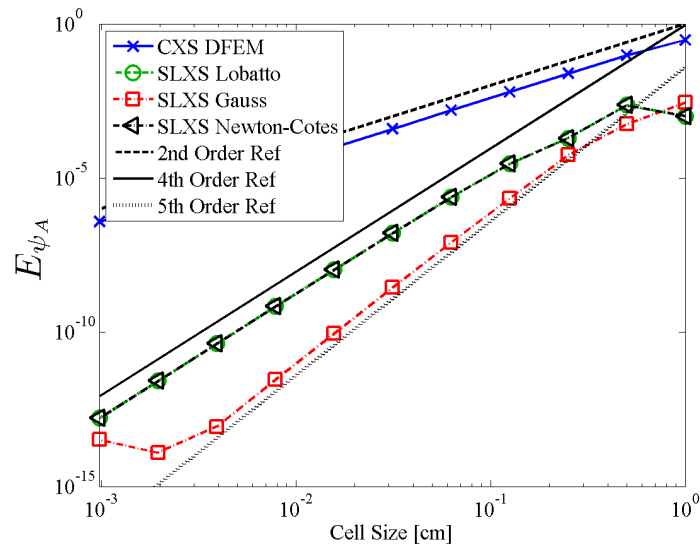


Figure 3.10: Convergence of  $E_{\psi_A}$  as a function of mesh size for a pure absorber with exponentially varying cross section discretized with quadratic DFEM.

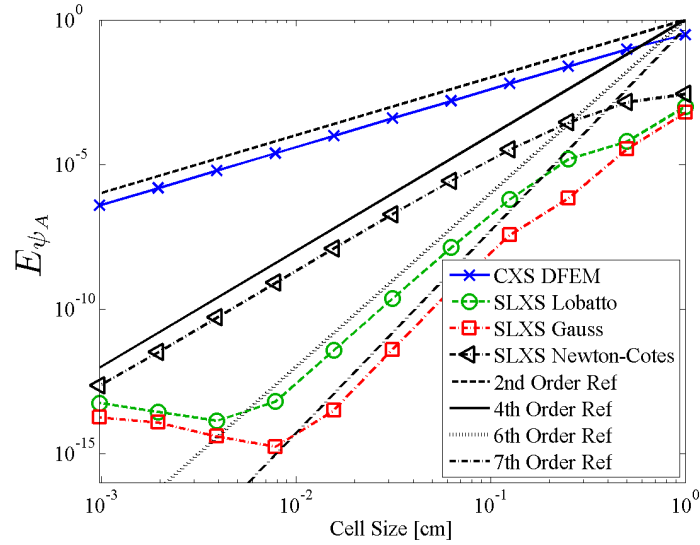


Figure 3.11: Convergence of  $E_{\psi_A}$  as a function of mesh size for a pure absorber with exponentially varying cross section discretized with cubic DFEM.

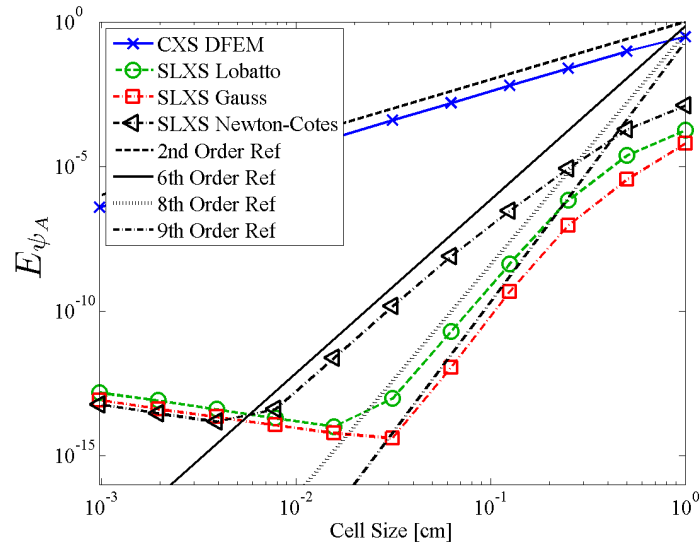


Figure 3.12: Convergence of  $E_{\psi_A}$  as a function of mesh size for a pure absorber with exponentially varying cross section discretized with quartic DFEM.

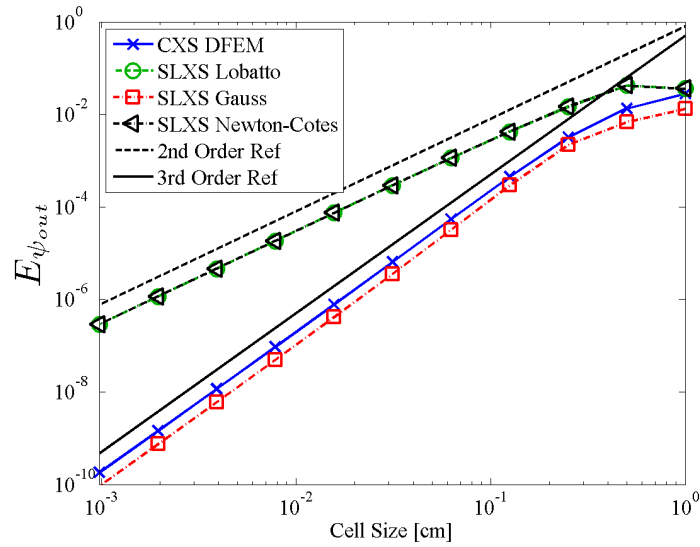


Figure 3.13: Convergence of  $E_{\psi_{out}}$  as a function of mesh size for a pure absorber with exponentially varying cross section discretized with linear DFEM.

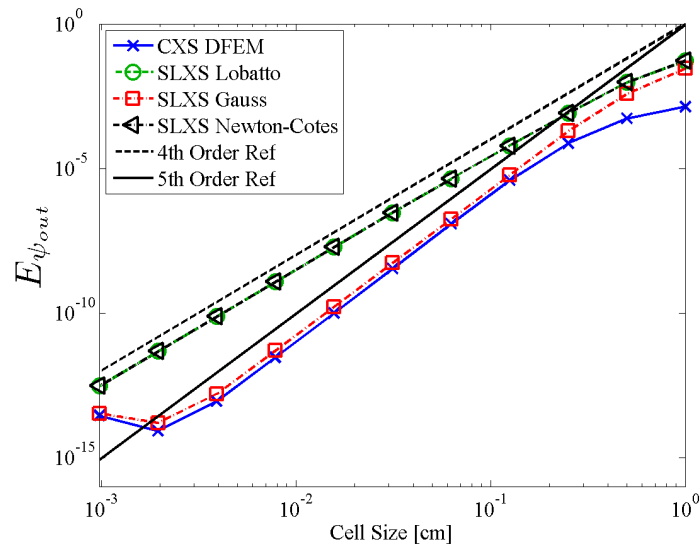


Figure 3.14: Convergence of  $E_{\psi_{out}}$  as a function of mesh size for a pure absorber with exponentially varying cross section discretized with quadratic DFEM.

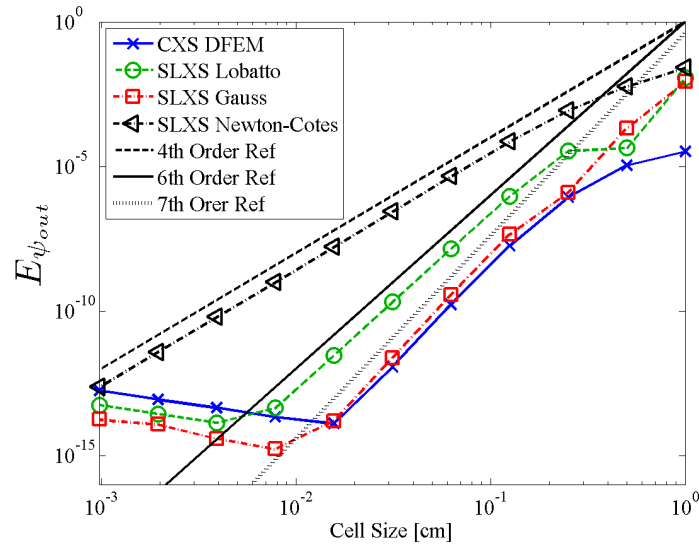


Figure 3.15: Convergence of  $E_{\psi_{out}}$  as a function of mesh size for a pure absorber with exponentially varying cross section discretized with cubic DFEM.

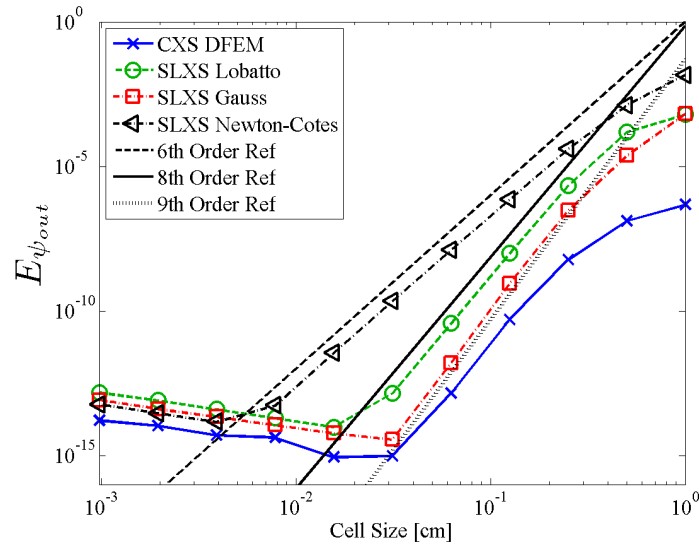


Figure 3.16: Convergence of  $E_{\psi_{out}}$  as a function of mesh size for a pure absorber with exponentially varying cross section discretized with quartic DFEM.

The plateauing of numerical errors for various high-order methods using very small cell sizes in Figs. 3.5-3.16 is a consequence of having reached machine precision. The lines in Figs. 3.5-3.16 that extend to values smaller than machine precision are reference lines.

Figures 3.5-3.16 show that, for a linear angular flux trial space, CXS DFEM achieves the same orders of spatial convergence as observed with Exact DFEM in [11]. However, as the degree of the DFEM trial space is increased, the CXS DFEM scheme does not show an increase in the order of the spatial convergence rate of  $E_\psi$  and  $E_{\psi_A}$ ; the convergence rate of CXS DFEM is limited to at most second order for both  $E_\psi$  and  $E_{\psi_A}$ , regardless of the trial space polynomial degree. The increase in order of convergence of CXS DFEM for  $E_{\psi_{out}}$  as trial space is increased is a result of angular flux outflow in the CXS DFEM discretization being only a function of the cell optical thickness, which is preserved exactly by our definition of  $\hat{\Sigma}_t$ ; see Eq. (3.7).

Of the self-lumping schemes, SLXS Newton-Cotes is the least accurate. SLXS Newton-Cotes convergence of  $E_\psi$  is limited to at most second order for odd degree polynomial trial spaces and third order for even degree trial spaces. Convergence of  $E_{\psi_A}$  and  $E_{\psi_{out}}$  for the SLXS Newton-Cotes scheme generally increases with an increase in the DFEM polynomial trial space degree, but is only proportional to  $P$ . Both SLXS Lobatto and SLXS Gauss converge  $E_\psi$ ,  $E_{\psi_A}$ , and  $E_{\psi_{out}}$  similarly to the study carried out in [11] with a spatially constant cross section.

The spatial convergence of  $E_\psi$  for SLXS Lobatto and SLXS Gauss is order  $P + 1$ . Though SLXS Lobatto and SLXS Gauss converge with the same order of spatial convergence for  $E_\psi$ , SLXS Gauss is more accurate than SLXS Lobatto by a constant. SLXS Gauss converges  $E_{\psi_A}$  and  $E_{\psi_{out}} \propto 2P + 1$ , whereas SLXS Lobatto converges both  $\propto 2P$ . SLXS Gauss and SLXS Lobatto converge angular flux error quantities

for the case of a spatially varying cross section with the same rates of convergence as their constant cross-section analogs did in [11]. This suggests that exactly integrating the interaction term in the DFEM moment equations is not essential for developing arbitrarily high-order accuracy DFEM schemes for radiation transport.

Convergence of  $E_{IR}$  as function of numerical scheme for linear - quartic trial spaces is given in Figs. 3.17-3.20. We observe the detrimental effect of approxi-

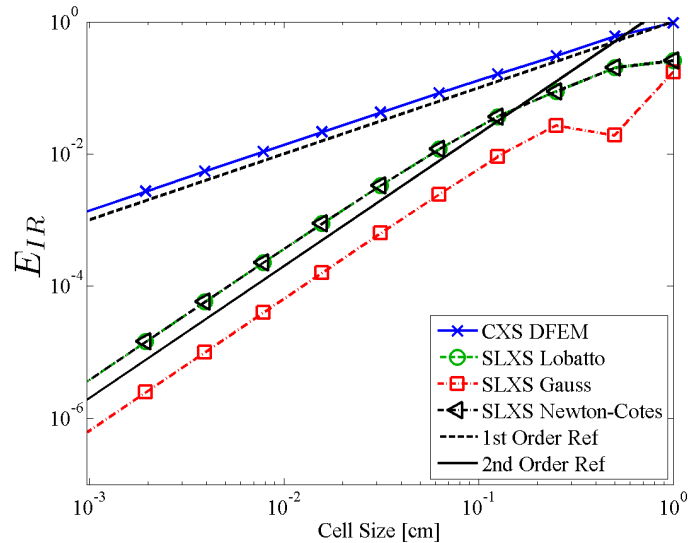


Figure 3.17: Convergence of  $E_{IR}$  as a function of mesh size for a pure absorber with exponentially varying cross section discretized with linear DFEM.

mating a spatially varying cross section with a constant in each spatial cell when we examine the  $L_2$  convergence results for the interaction rate,  $E_{IR}$ , for the CXS DFEM scheme. Regardless of angular flux trial space polynomial degree, CXS DFEM converges  $E_{IR}$  to only first order in space. However, the self-lumping schemes exhibit the same trends in converging  $E_{IR}$  (in the  $L^2$ -norm sense) as exhibited in converging  $E_\psi$ :

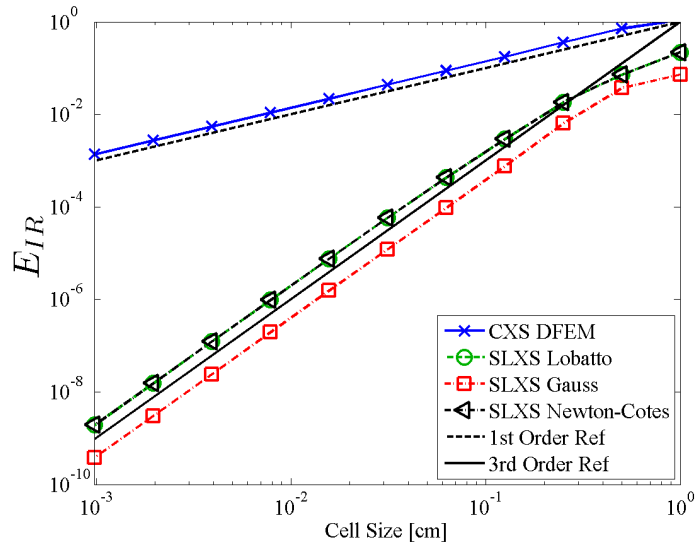


Figure 3.18: Convergence of  $E_{IR}$  as a function of mesh size for a pure absorber with exponentially varying cross section discretized with quadratic DFEM.

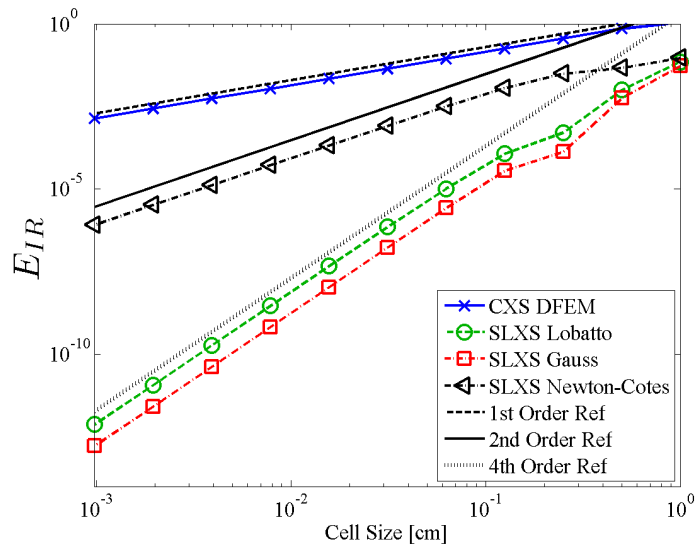


Figure 3.19: Convergence of  $E_{IR}$  as a function of mesh size for a pure absorber with exponentially varying cross section discretized with cubic DFEM.

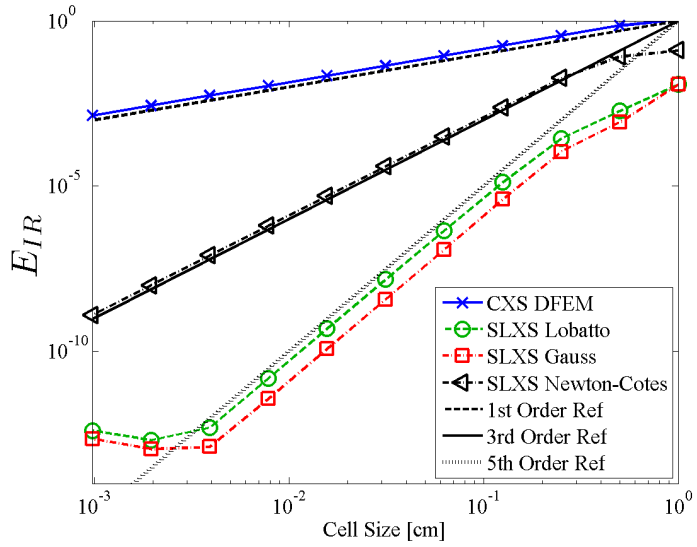


Figure 3.20: Convergence of  $E_{IR}$  as a function of mesh size for a pure absorber with exponentially varying cross section discretized with quartic DFEM.

- SLXS Lobatto and SLXS Gauss converge  $E_{IR}$  with order  $P + 1$ ,
- SLXS Gauss is more accurate than SLXS Lobatto by a constant, and
- SLXS Newton-Cotes converges  $E_{IR}$  second order in space for odd degree trial spaces and third order in space for even degree trial spaces.

Convergence data for  $E_{IR_A}$  as function of cell size for linear - quartic trial spaces is given in Figs. 3.21-3.24. The convergence results for the error in cell average interaction rate,  $E_{IR_A}$ , shown in Figs. 3.21-3.24, do not behave as intuitively as the convergence rates for  $E_{IR}$  observed in Figs. 3.17-3.20. Given the poor performance of CXS DFEM in converging  $E_{IR}$ , one would expect that CXS DFEM would converge  $E_{IR_A}$  poorly as well. However, this is not the case and CXS DFEM converges  $E_{IR_A}$  with the same order of convergence as the best performing self-lumping scheme considered.

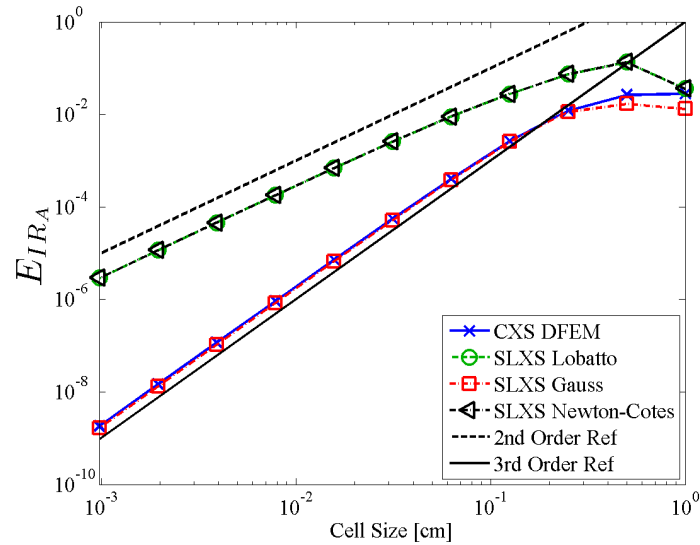


Figure 3.21: Convergence of  $E_{IR_A}$  as a function of mesh size for a pure absorber with exponentially varying cross section discretized with linear DFEM.

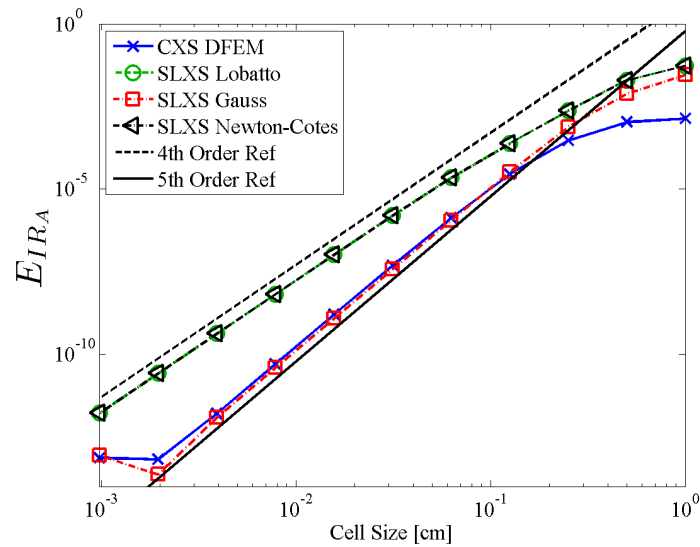


Figure 3.22: Convergence of  $E_{IR_A}$  as a function of mesh size for a pure absorber with exponentially varying cross section discretized with quadratic DFEM.

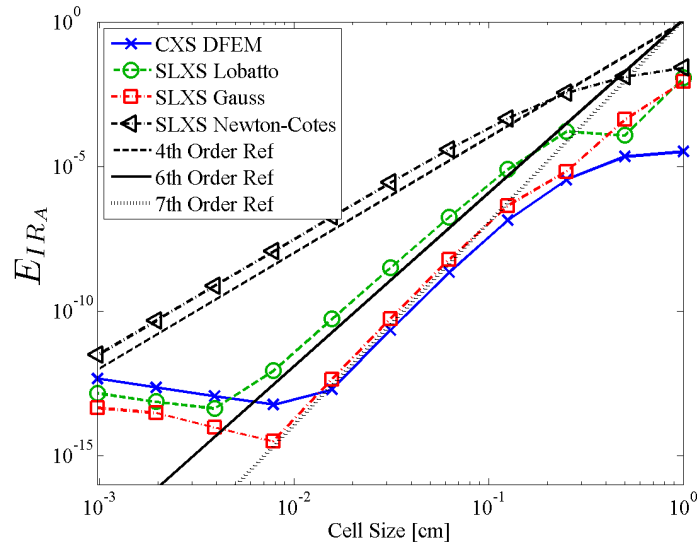


Figure 3.23: Convergence of  $E_{IR_A}$  as a function of mesh size for a pure absorber with exponentially varying cross section discretized with cubic DFEM.

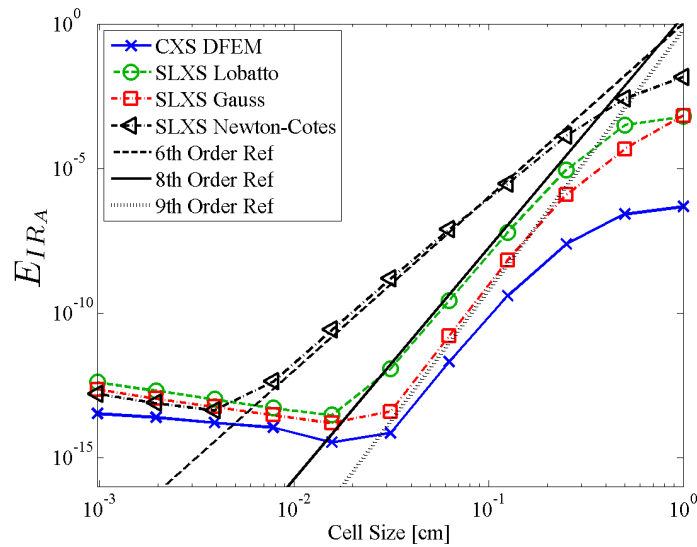


Figure 3.24: Convergence of  $E_{IR_A}$  as a function of mesh size for a pure absorber with exponentially varying cross section discretized with quartic DFEM.

CXS DFEM converges  $E_{IR_A}$  with a high-order of accuracy because of the locally conservative properties of DFEM approximations, that is:

$$\text{Particles Into Cell} - \text{Particles Out of Cell} = \text{Total Interactions in Cell}. \quad (3.26)$$

As shown in Figs. 3.13-3.16, CXS DFEM converges the quantities on the left hand side of Eq. (3.26) with the same order of accuracy as any self-lumping scheme considered; CXS DFEM is at least as accurate in calculating the particles into a cell (outflow from the previous cell) and out of the cell (outflow from the current cell) as any other scheme considered. Since Eq. (3.26) holds regardless of the numerical scheme considered, it follows that CXS DFEM converges  $E_{IR_A}$ , the term in the right hand side of Eq. (3.26) summed over all cells, with the maximum order of convergence displayed by any of the DFEM schemes we consider here. Figures 3.21-3.24 validate this conclusion. CXS DFEM and SLXS Gauss exhibit the highest order of spatial convergence, converging  $E_{IR_A}$  with order  $\propto 2P + 1$ . SLXS Newton-Cotes and SLXS Lobatto converge  $E_{IR_A}$  with the same orders of convergence each method exhibits in converging  $E_{\psi_A}$ . For this problem SLXS Lobatto converges  $E_{IR_A} \propto 2P$  and SLXS Newton-Cotes converged  $E_{IR_A} \propto P$ .

### 3.3.3 Consequences of Assuming a Cell-Wise Constant Cross Section

To more fully understand the poor convergence of point-wise error in angular flux and interaction rate,  $E_\psi$  and  $E_{IR}$ , associated with CXS DFEM we now examine more closely the CXS DFEM spatial approximations to  $\psi(x, \mu_d)$  and  $IR(x)$ . We again consider a pure absorber with total absorption cross section that varies exponentially in space with  $c_1 = 0.1$ , and  $c_2 = 2 \ln(10)$ . A beam of radiation is incident on the left face in the direction of  $\mu_d = 1$ , vacuum boundary conditions are applied on the right face of the slab, and  $x \in [0, 1]$ .

In Fig. 3.25, we plot the exact  $\psi(x)$  and in Fig. 3.26, we plot  $IR(x)$ . Additionally we plot the respective CXS DFEM numerical approximations,  $\tilde{\psi}(x)$  and  $\widetilde{IR}(x)$ , using  $N_{cells} = 5$ , and  $\hat{\Sigma}_{t,i}$  as defined in Eq. (3.7). Also plotted in Fig. 3.25 and Fig. 3.26, we plot the analytic angular flux and reaction rate, respectively, one would obtain if the cell average cross section,  $\hat{\Sigma}_{t,i}$ , had been used instead of the true  $\Sigma_t(x)$ . We refer to these analytic solutions as  $\psi_C(x)$  and  $IR_C(x)$ .

Since CXS DFEM is a discontinuous scheme, some discontinuity is expected in the plot of  $\tilde{\psi}$  in Fig. 3.25 and of  $\widetilde{IR}$  in Fig. 3.26. However, the discontinuities present in Fig. 3.26 are highly disconcerting. The analytic  $IR(x)$  is smooth and does not vary rapidly within individual mesh cells, yet there are significant, non-monotonic discontinuities in the CXS DFEM interaction rate solution to the pure absorber problem with exponentially varying cross section. The noticeably poor behavior of  $\widetilde{IR}(x)$  in Fig. 3.26 is inherent to the assumption of a cell-wise constant cross section. This inherent error of approximating a continuously varying cross section with cell-wise constants is clearly visible when comparing the plots of  $IR_C(x)$  to  $IR(x)$  in Fig. 3.26. The only difference and source of error in  $IR_C(x)$  is the assumption of a cell-wise constant cross section. Figure 3.25 and Fig. 3.26 does not suggest that linear DFEM is unsuitable for use in problems with spatially varying cross sections. Rather, comparing the CXS DFEM  $\tilde{\psi}(x)$  to  $\psi_C(x)$  in Fig. 3.25 and  $\widetilde{IR}(x)$  to  $IR_C(x)$  in Fig. 3.26, we see that CXS DFEM is very accurate when compared to the analytic solution of the problem CXS DFEM is solving, a pure absorber with cell-wise constant cross section.

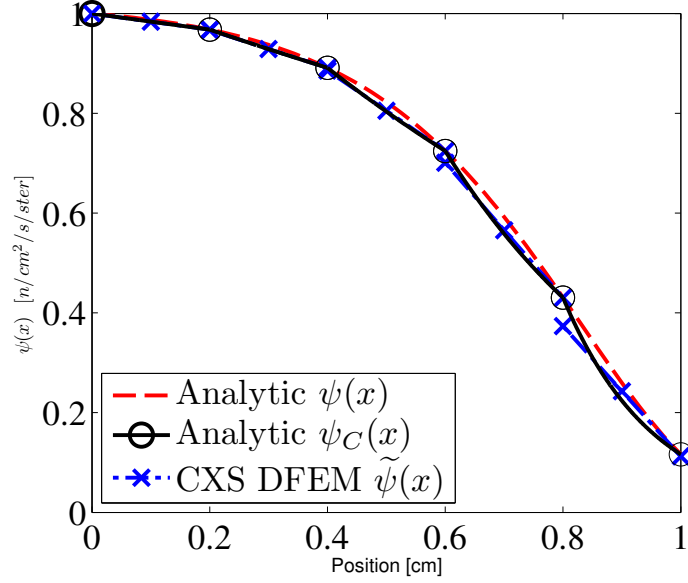


Figure 3.25: Plots of the analytic  $\psi(x)$ , CXS DFEM  $\tilde{\psi}(x)$ , and cell-wise constant cross section analytic  $\psi_C(x)$ , for the pure absorber with exponential cross section.

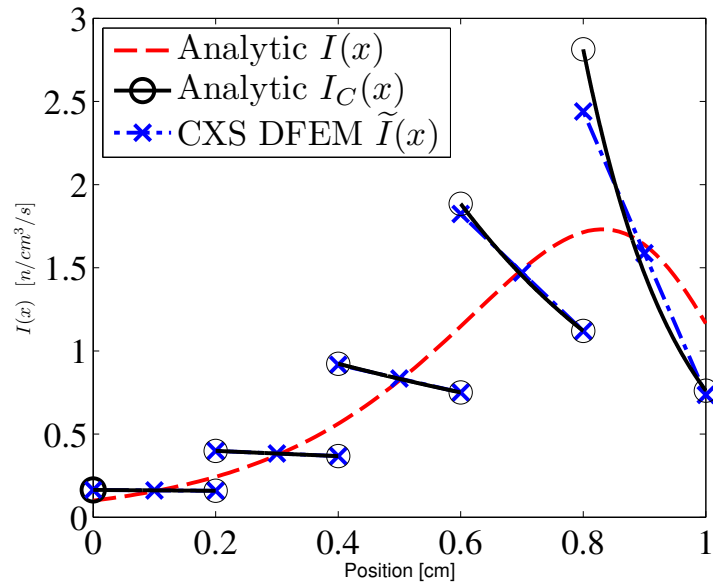


Figure 3.26: Plots of the analytic  $IR(x)$ , CXS DFEM  $\widetilde{IR}(x)$ , and cell-wise constant cross section analytic  $IR_C(x)$  for the pure absorber with exponential cross section.

Given the poor accuracy of CXS DFEM in approximating the true  $\psi(x)$  and  $IR(x)$ , we wish to see how a scheme that does not assume a cell-wise constant cross section behaves. Consider  $\tilde{\psi}(x)$  and  $\widetilde{IR}(x)$  obtained with SLXS Lobatto using a linear DFEM trial space and five spatial cells, shown in Fig. 3.27 and Fig. 3.28, for the same problem. In Fig. 3.27, the differences between the angular flux solutions obtained using (1) a cell-wise constant cross section (CXS DFEM) and (2) evaluating cross section values at quadrature points (SLXS Lobatto) are small.

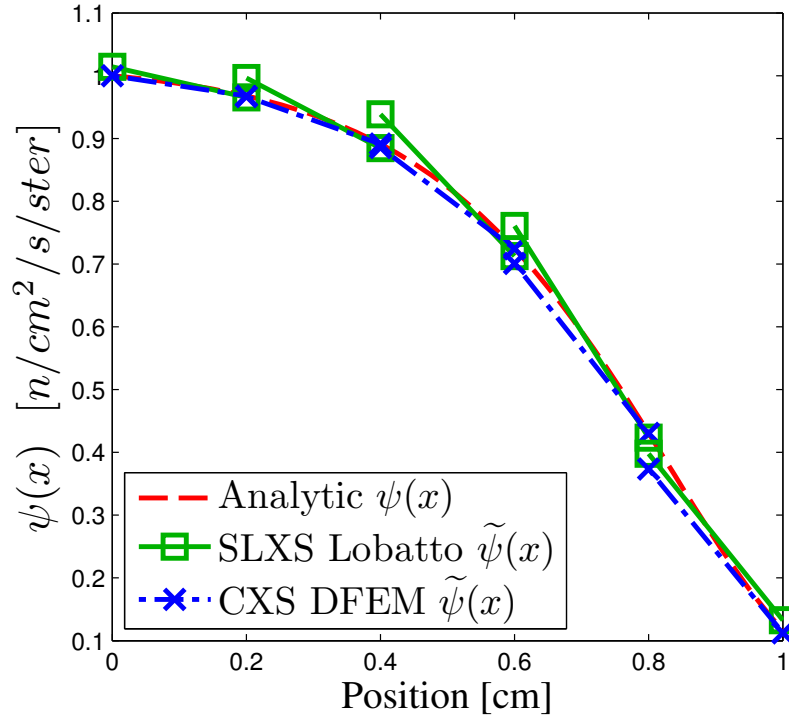


Figure 3.27: Plot of the linear trial space SLXS Lobatto and CXS DFEM approximations of  $\tilde{\psi}(x)$  for the pure absorber problem with exponentially varying cross section.

This is not the case when comparing the different approximations to the interaction rate,  $\widetilde{IR}(x)$ , in Fig. 3.28. Though there are discontinuities in the SLXS Lobatto  $\widetilde{IR}(x)$ , the discontinuities are smaller and the SLXS Lobatto  $\widetilde{IR}(x)$  is monotonic unlike the CXS DFEM  $\widetilde{IR}(x)$ . The SLXS Lobatto  $\widetilde{IR}(x)$  is clearly more accurate than the CXS DFEM  $\widetilde{IR}(x)$ .

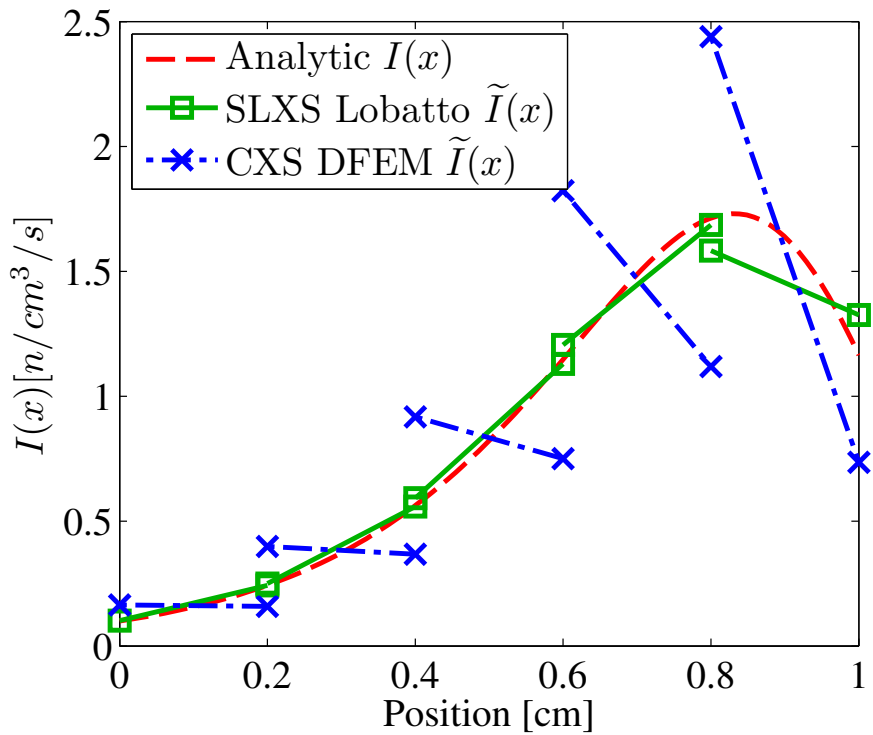


Figure 3.28: Plot of the linear trial space SLXS Lobatto and CXS DFEM approximations of  $\widetilde{IR}(x)$  for the pure absorber problem with exponentially varying cross section.

In this problem, there are two possible sources of error that could cause a DFEM to be inaccurate: inexact matrix evaluation and not incorporating cross-section spatial variation into the scheme. By definition, CXS DFEM exactly integrates the mass matrix, and we showed in Section 2 that schemes that exactly integrate the mass

matrix are more accurate than schemes that only approximately integrate the mass matrix, like SLXS Lobatto. Thus, the poor accuracy of CXS DFEM relative to SLXS Lobatto is entirely caused by the approximation of a spatially varying cross section with a cell-wise constant value.

The “blading” in  $\widetilde{IR}(x)$  has not previously been reported in neutron transport or thermal radiative transport community literature. We are likely not the first to have generated these large, non-monotonic discontinuities. In fact, we believe that blading has frequently been present in DFEM both neutron transport and thermal radiative transfer simulations but has likely gone unnoticed due to the prevalence of linear DFEM and simplified data visualization using cell midpoint values.

To demonstrate that a minor choice in data presentation can obscure the existence of blading, consider Fig. 3.29 and Fig. 3.30 that linearly interpolate between  $\widetilde{\psi}_{A,i}$  and  $\widetilde{IR}_{A,i}$  plotted at cell centers. Though Fig. 3.29 is visually indistinguishable from Fig. 3.25, the blading of  $\widetilde{IR}(x)$  present in Fig. 3.26 is not at all visually present in Fig. 3.30. Interaction rate terms are present in other radiation transport physics. In particular, we think of the radiative transfer analog to the neutronics interaction rate, absorption rate density. We hypothesize here, and will show in Section 6 that assuming cell-wise constants opacities for problems with temperature dependent opacities introduces blading in thermal radiative transfer temperature solutions, via the material energy equation’s absorption rate density term.

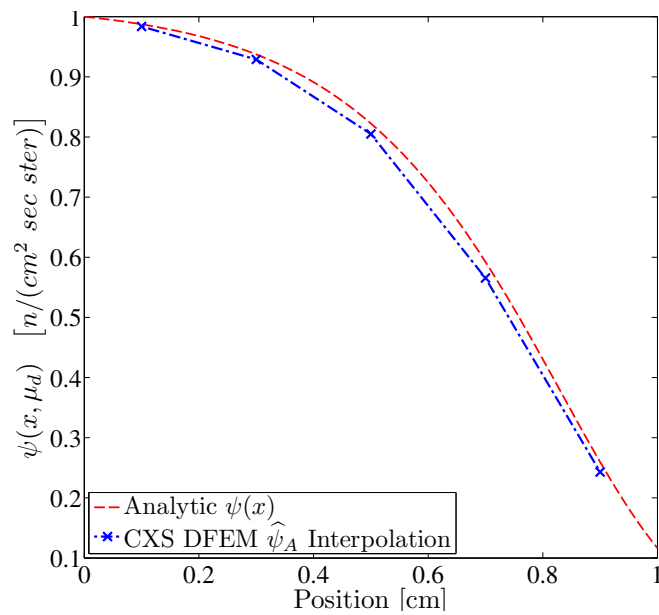


Figure 3.29: Plot of the CXS DFEM cell average angular flux at cell centers with linear interpolation for a pure absorber with exponentially varying spatial cross section.

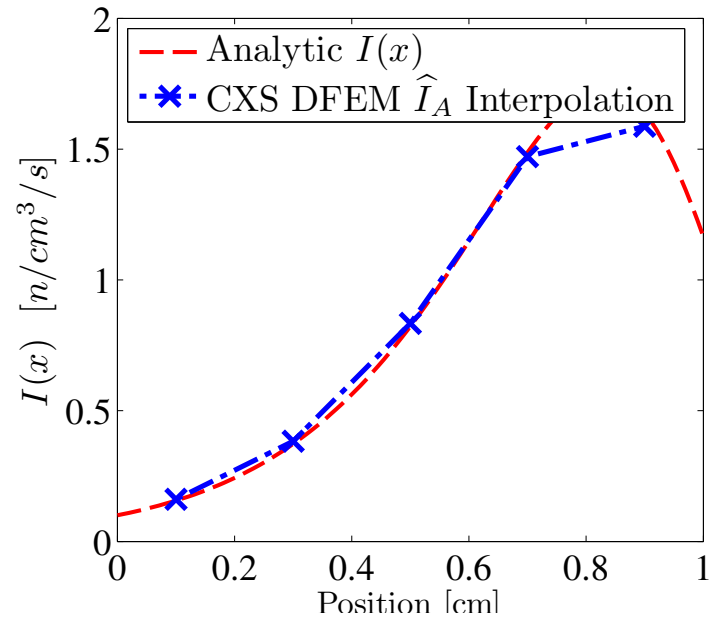


Figure 3.30: Plot of the CXS DFEM cell average interaction rate at cell centers with linear interpolation for a pure absorber with exponentially varying spatial cross section.

### 3.3.4 Flux-Weighting versus Volume-Averaged Cross Sections

In our results thus far, we have only considered volume-averaged cell-wise cross sections(the CXS DFEM scheme). However, in reactor physics problems, a flux-weighted cross section is often used to generate spatially averaged cross sections [33]. We now introduce the flux-weighted cell-wise constant cross section scheme (FW CXS), which differs from the CXS DFEM scheme only by how  $\hat{\Sigma}$  is defined in each cell. For the FW CXS scheme, we define  $\hat{\Sigma}_i$  as

$$\hat{\Sigma}_i = \frac{\int_{x_{i-1/2}}^{x_{i+1/2}} \Sigma(x) \psi(x, \mu_d) dx}{\int_{x_{i-1/2}}^{x_{i+1/2}} \psi(x, \mu_d) dx}. \quad (3.27)$$

In practice, flux-weighting is often done using the scalar flux in order not to have angle-dependent total cross section. However for the beam problem we consider here,  $\psi(x, \mu_d)$  is proportional to the scalar flux.

We first compare the accuracy of FW CXS versus volume-averaged CXS DFEM for a cubic DFEM trial space, as shown in Figs. 3.31-3.34. In Figs. 3.31-3.34, we omit a plot of  $E_{\psi_{out}}$  as we have already demonstrated that the accuracy of any method in calculating  $E_{\psi_{out}}$  determines the method's accuracy in calculating  $E_{IR_A}$ . That is, if  $E_{IR_A}$  converges at a given rate,  $E_{\psi_{out}}$  converges at the same rate.

Figures 3.31-3.33 show that FW CXS scheme is more accurate than CXS DFEM when comparing  $E_\psi$ ,  $E_{\psi_A}$  and, at low resolutions,  $E_{IR}$ . However, though designed to preserve cell average interaction rates, FW CXS scheme is not only less accurate than CXS DFEM in calculating cell average interaction rates, it converges  $E_{IR_A}$  at most second order in space, whereas a volume-averaged cross section converges  $E_{IR_A} \propto 2P + 1$  for the pure absorber problem.

Finally, we consider the FW CXS scheme's  $\tilde{\psi}(x)$  in Fig. 3.35 and  $\widetilde{IR}(x)$  in

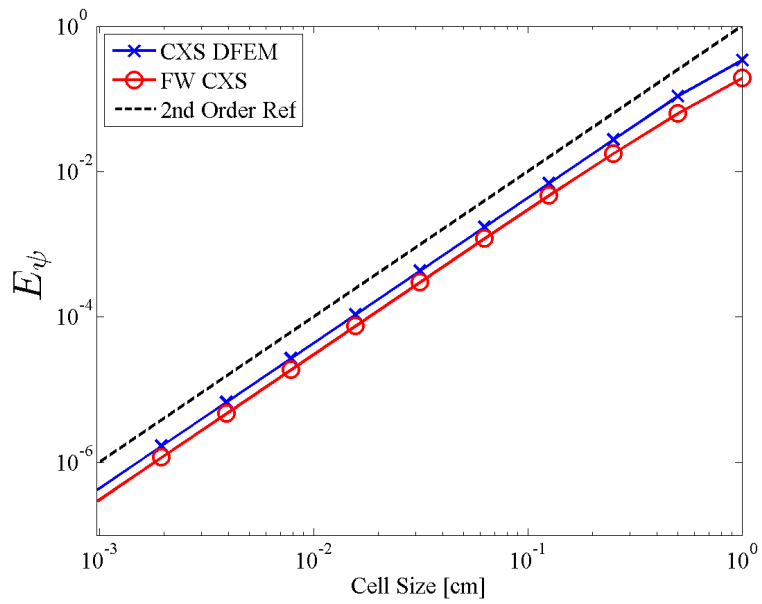


Figure 3.31:  $E_\psi$  for FW CXS vs. CXS DFEM for a pure absorber with exponentially varying cross section using a cubic DFEM trial space.

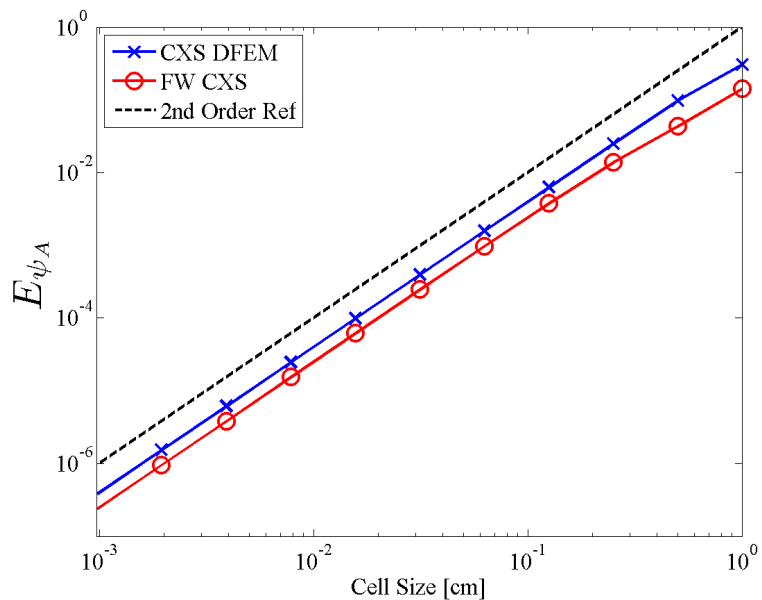


Figure 3.32:  $E_{\psi_A}$  for FW CXS vs. CXS DFEM for a pure absorber with exponentially varying cross section using a cubic DFEM trial space.

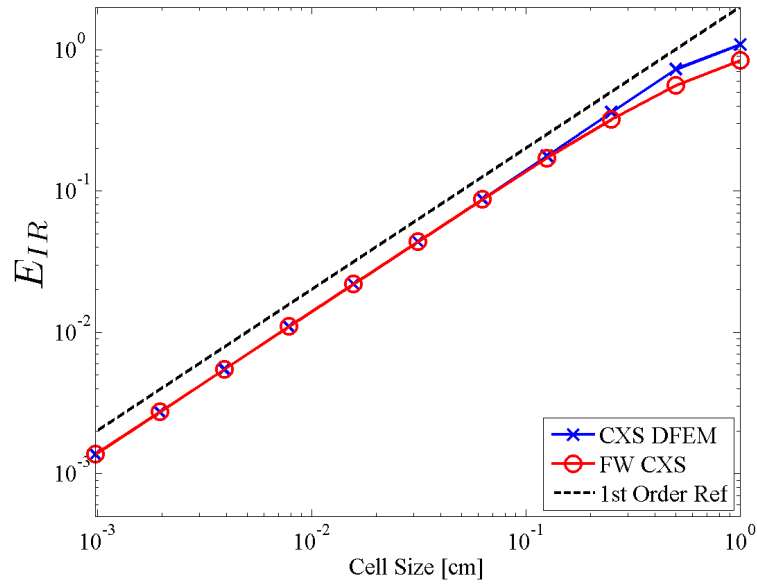


Figure 3.33:  $E_{IR}$  for FW CXS vs. CXS DFEM for a pure absorber with exponentially varying cross section using a cubic DFEM trial space.

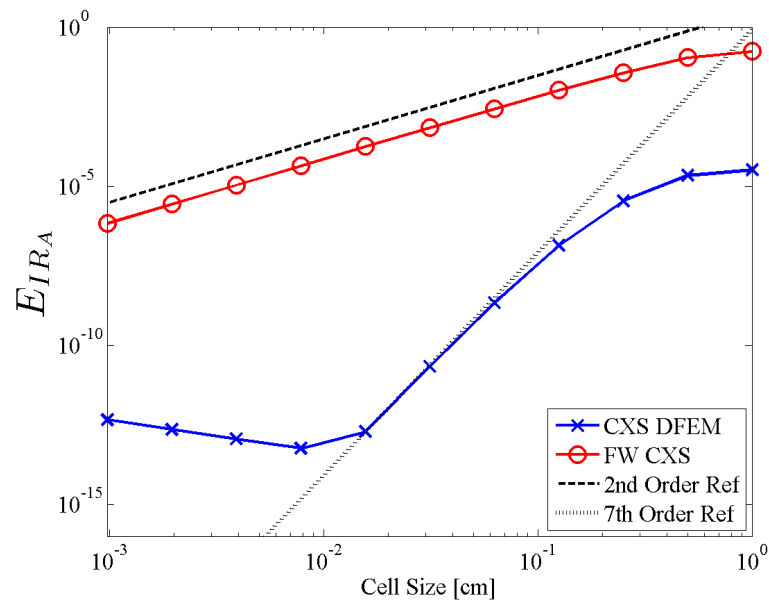


Figure 3.34:  $E_{IR_A}$  for FW CXS vs. CXS DFEM for a pure absorber with exponentially varying cross section using a cubic DFEM trial space.

Fig. 3.36. In Fig. 3.35 and Fig. 3.36 the FW CXS and CXS DFEM schemes calculate slightly different solution representations. However, the FW CXS scheme exhibits the same interaction rate blading phenomena as the CXS DFEM scheme, reiterating that blading is a result of approximating a spatially varying cross section as a cell-wise constant. The choice of cell-wise cross section does not eliminate blading.

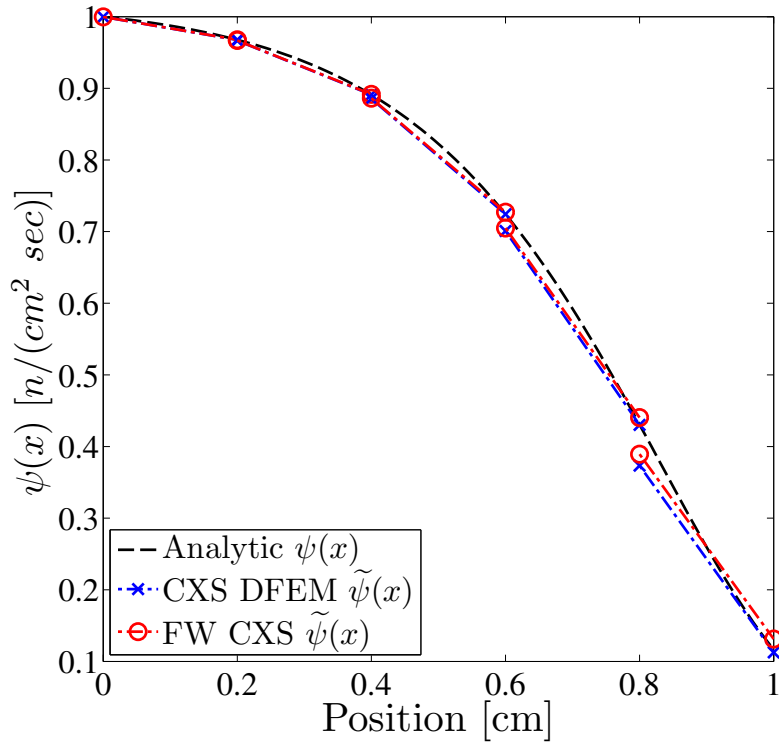


Figure 3.35: Plot of the linear trial space FW CXS and CXS DFEM approximations to  $\tilde{\psi}(x)$  for the pure absorber problem with exponentially varying spatial cross section.

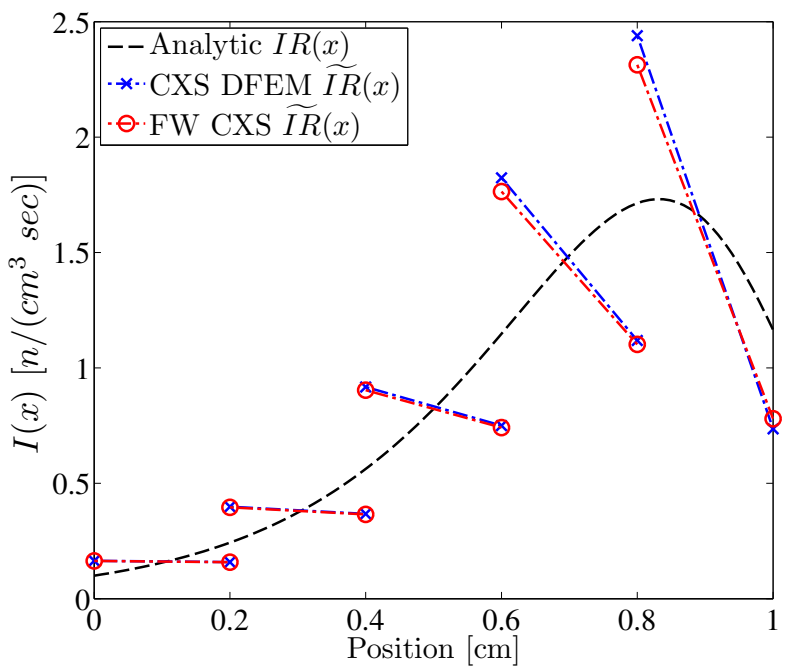


Figure 3.36: Plot of the linear trial space FW CXS and CXS DFEM approximations to  $\widetilde{IR}(x)$  for the pure absorber problem with exponentially varying spatial cross section.

### 3.3.5 Effects of Mesh Spacing

In practice, computational domains are not necessarily discretized with uniform grids; rather cells are concentrated in regions where the solution is known or assumed to vary rapidly. For the pure absorber problem, we compare two alternative methods of mesh spacing (logarithmic grids and equal optical thickness grids, see Table 3.2), to the results obtained with equally-spaced mesh cells. We derive how to generate these meshes in Section 3.3.5.1 and give results in Section 3.3.5.2.

Table 3.2: Shorthand notation of different cell spacing schemes.

Spacing Label	Spacing Type
EQUAL	Equally-spaced cells
MFP	Constant optical thickness cells
LOG	Logarithmically spaced cells

#### 3.3.5.1 Generating Improved Spatial Meshes

Two alternative meshing strategies are compared to equally-spaced meshed. In the following, we will use a shorthand notation, given in Table 3.2. With the MFP meshing strategy, we find each cell width by determining the width of each cell from  $i = 1$  (leftmost cell) to  $i = N_{cell}$  as outlined by Eq. (3.28): First, we determine the average cell optical thickness:

$$\bar{h} = \frac{\int_{x_{1/2}}^{x_{N_{cell}+1/2}} \Sigma_t(x) dx}{N_{cell}}. \quad (3.28a)$$

Then, we solve the following equation for  $x_{i+1/2}$ :

$$\int_{x_{i-1/2}}^{x_{i+1/2}} \Sigma_t(x) dx - \bar{h} = 0, \quad (3.28b)$$

yielding

$$x_{i+1/2} = \frac{1}{c_2} \log \left[ \frac{c_2(\bar{h} + \Sigma_t(x_{i-1/2}))}{c_1} \right]. \quad (3.28c)$$

There are several ways to specify LOG spacing, but we elected to set a ratio, 0.6, between adjacent cell sizes with the caveat that we would set a minimum cell size,  $\Delta x_{min}$ . In our convergence testing, at the first refinement when  $\Delta x_{N_{cell}} < \Delta x_{min}$ , the grid is “fixed” and all further refinements uniformly refine the ”fixed” grid.  $\Delta x_{N_{cell}}$  is the cell width for the right most cell where, for  $R < 1$ ,

$$\Delta x_i = \Delta x_1 R^{i-1}, \quad i \in [1, N_{cell}]. \quad (3.29)$$

$\Delta x_1$  is determined by requiring that the geometric series of cell widths completely fill the space:

$$\Delta x_1 = (x_{N_{cell}+1/2} - x_{1/2}) \frac{1 - R}{1 - R^{N_{cell}}} \quad (3.30)$$

The grid is “fixed” by resetting the width of every cell whose width, if set to the value required for a purely logarithmically spaced grid with  $R$  would be below  $\Delta x_{min}$ , to  $\Delta x_{min}$ . After imposing this, cell widths are determined by requiring the cells that were not reset to fill the problem space logarithmically using  $R$ . If there is no minimum cell width, at high mesh refinements, most cells will be infinitesimally small and the large cells will never be refined, causing error to stagnate. Logarithmic spacing represents the “smart” meshing strategy most likely to be employed in engineering practice as it requires the least amount of solution information prior to problem

execution. For all of our calculations, we set  $R = 0.6$  and  $\Delta x_{min} = 10^{-3}$  [cm].

### 3.3.5.2 Mesh Spacing Results

We begin our discussion of alternate mesh spacing by first noting that the choice of mesh spacing method does not alter asymptotic convergence rates, as shown in Figs. 3.37-3.40. The convergence of the SLXS Lobatto scheme using a quadratic trial space for  $E_\psi$  is shown in Fig. 3.37, for  $E_{\psi_A}$  in Fig. 3.38, for  $E_{IR}$  in Fig. 3.39, and for  $E_{IR_A}$  in Fig. 3.40. Regardless of the choice of mesh spacing, all error quantities of interest converge at the same asymptotic rate. Plots showing other trial space degrees and DFEM schemes are omitted for brevity. We also omit showing the convergence of  $E_{\psi_{out}}$  as we have already demonstrated that the convergence rate of  $E_{\psi_{out}}$  and  $E_{IR_A}$  are related and identical.

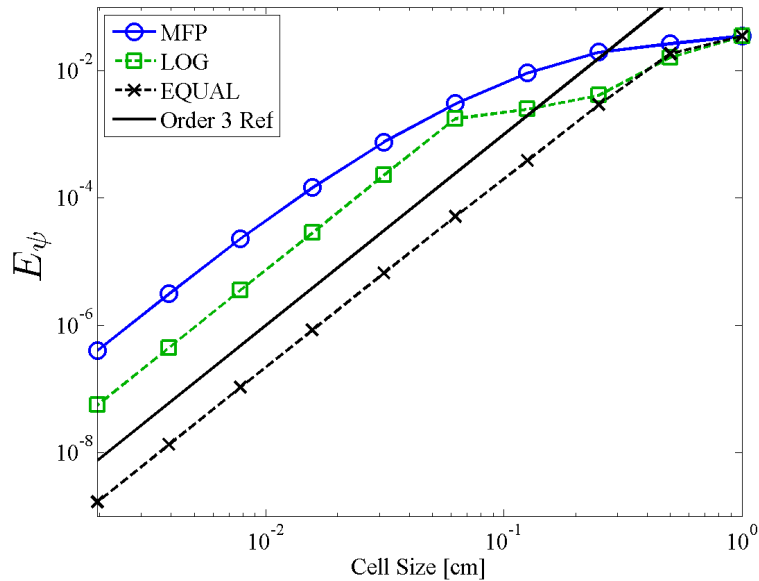


Figure 3.37: Asymptotic convergence of  $E_\psi$  for the SLXS Lobatto scheme using a quadratic trial space with different mesh spacing methodologies.

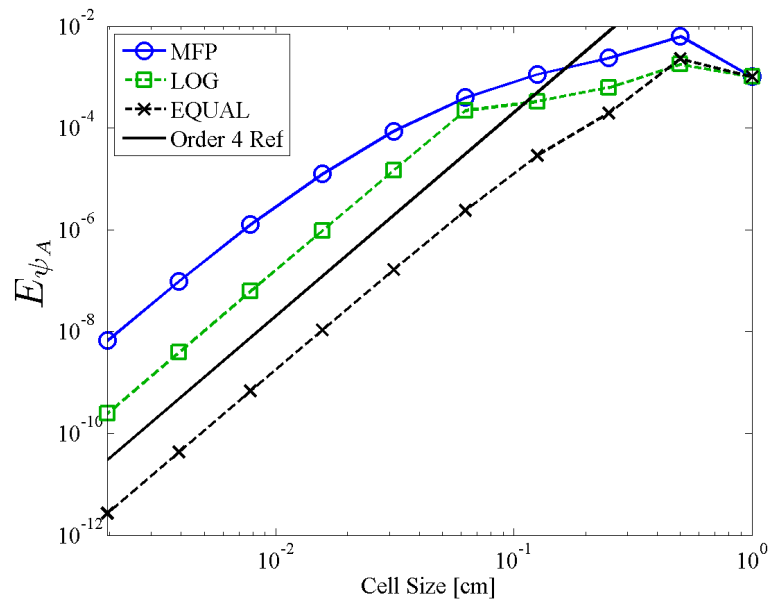


Figure 3.38: Asymptotic convergence of  $E_{\psi_A}$  for the SLXS Lobatto scheme using a quadratic trial space with different mesh spacing methodologies.

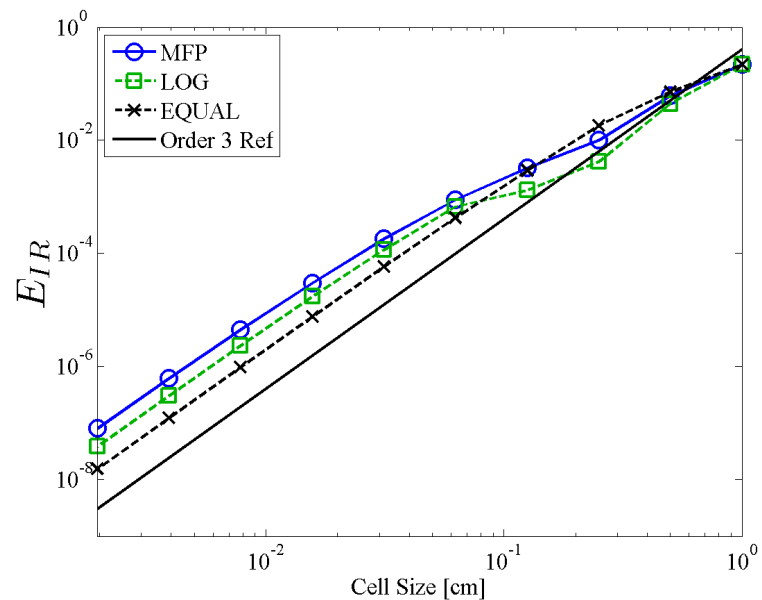


Figure 3.39: Asymptotic convergence of  $E_{IR}$  for the SLXS Lobatto scheme using a quadratic trial space with different mesh spacing methodologies.

At mesh refinements that are not in the asymptotic convergence regime, the intelligent meshing can result in a significant reduction in error. Consider the difference smart meshing has in reducing  $E_\psi$ ,  $E_{\psi_A}$ ,  $E_{IR}$ , and  $E_{IR_A}$  for the SLXS Lobatto scheme in Figs. 3.41-3.44, for the SLXS Gauss scheme in Figs. 3.45-3.48, and for CXS DFEM in Figs. 3.49-3.52 when using a quadratic DFEM trial space at low cell resolutions.

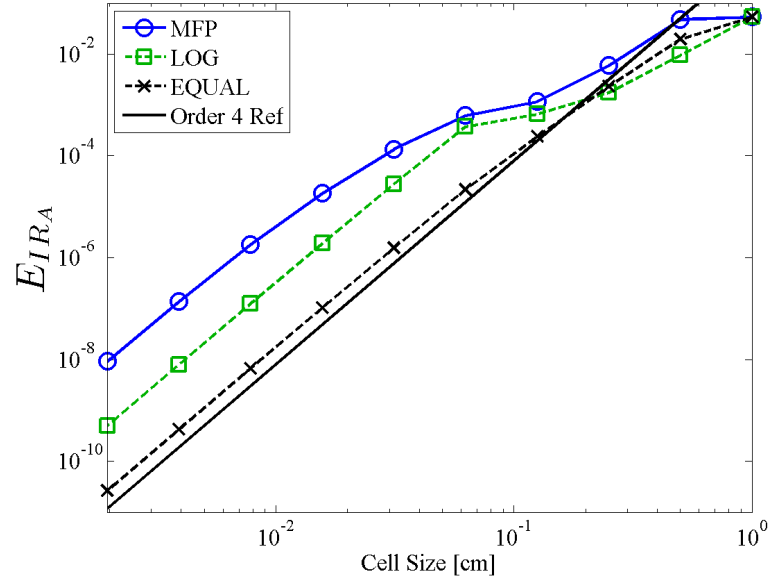


Figure 3.40: Asymptotic convergence of  $E_{IR_A}$  for the SLXS Lobatto scheme using a quadratic trial space with different mesh spacing methodologies.

First, we note that any particular mesh spacing methodology results in solutions that are more accurate for certain quantities, but not for all quantities. For example, with the self-lumping schemes,  $E_\psi$  is generally smaller when using an equally spaced mesh, but using the LOG mesh results in orders of magnitude improvement in  $E_{IR}$  and  $E_{IR_A}$  on coarse meshes. Figures 3.49-3.52, CXS DFEM again illustrates that LOG spacing is more accurate in calculating interaction rate quantities than an equally-spaced mesh and equally-spaced meshes are generally more accurate than other meshing strategies for calculating angular flux quantities. However, CXS DFEM shows a two order of magnitude reduction in calculating  $E_{IR_A}$  when using a mesh that has a uniform optical thickness in each cell. This is a direct result of CXS DFEM converging as  $\hat{\sigma}\Delta x \rightarrow 0$ .

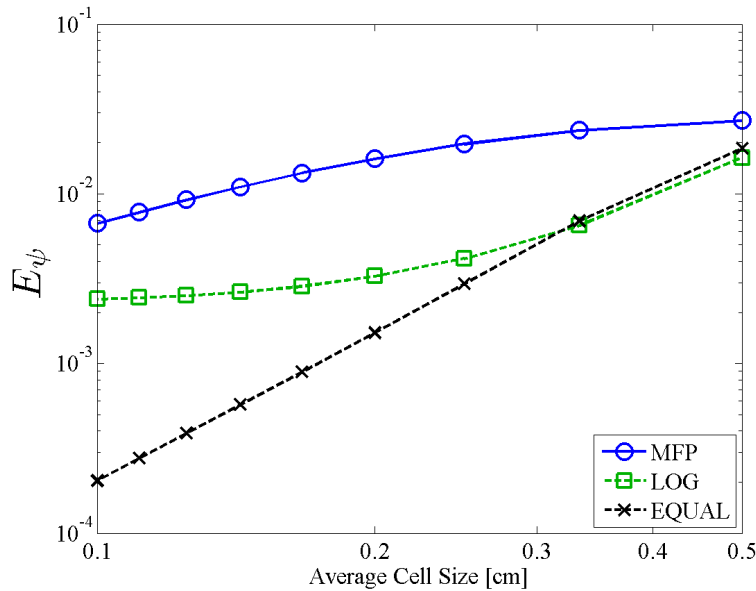


Figure 3.41:  $E_\psi$  for SLXS Lobatto using a quadratic trial space scheme with different mesh spacing methodologies, at low resolutions.

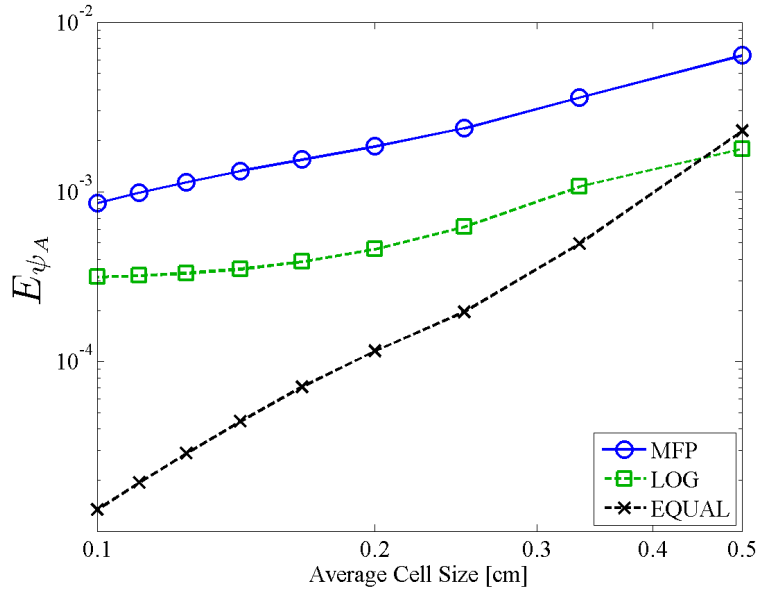


Figure 3.42:  $E_{\psi_A}$  for SLXS Lobatto using a quadratic trial space scheme with different mesh spacing methodologies, at low resolutions.

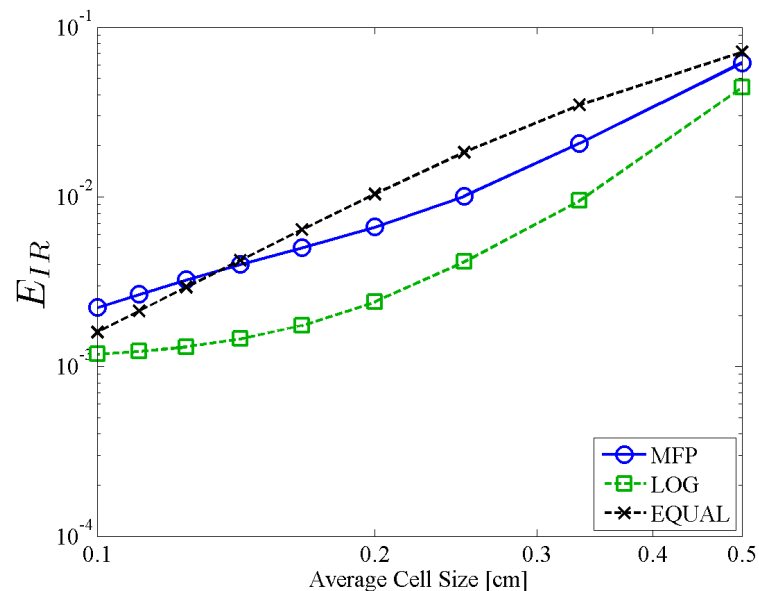


Figure 3.43:  $E_{IR}$  for SLXS Lobatto using a quadratic trial space scheme with different mesh spacing methodologies, at low resolutions.

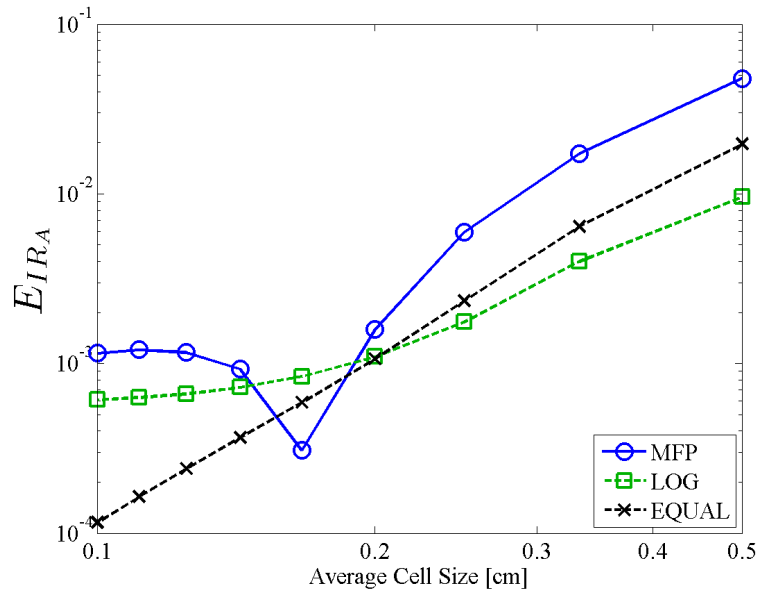


Figure 3.44:  $E_{IR_A}$  for SLXS Lobatto using a quadratic trial space scheme with different mesh spacing methodologies, at low resolutions.

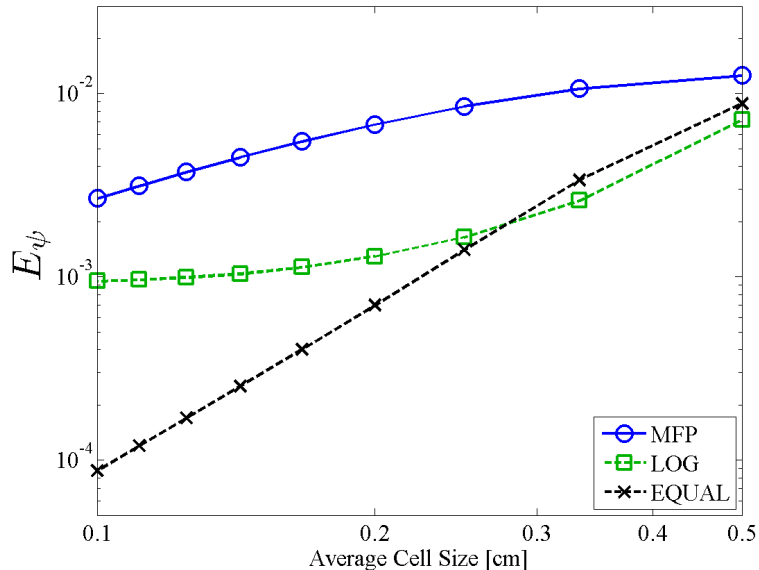


Figure 3.45:  $E_\psi$  for SLXS Gauss using a quadratic trial space with different mesh spacing methodologies, at low resolutions.

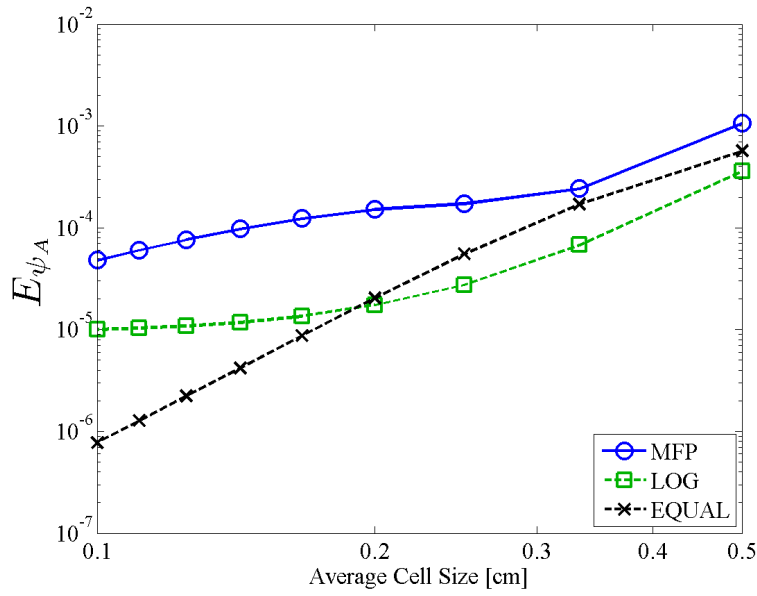


Figure 3.46:  $E_{\psi_A}$  for SLXS Gauss using a quadratic trial space with different mesh spacing methodologies, at low resolutions.

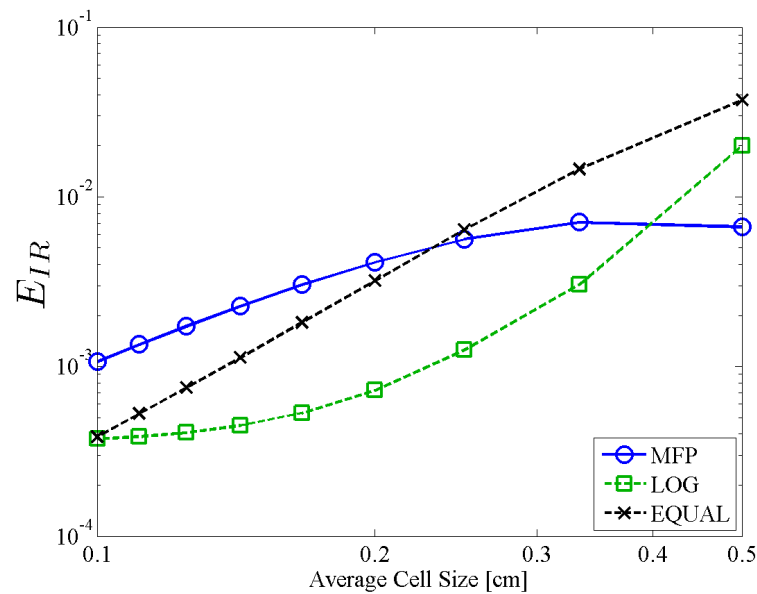


Figure 3.47:  $E_{IR}$  for SLXS Gauss using a quadratic trial space with different mesh spacing methodologies, at low resolutions.

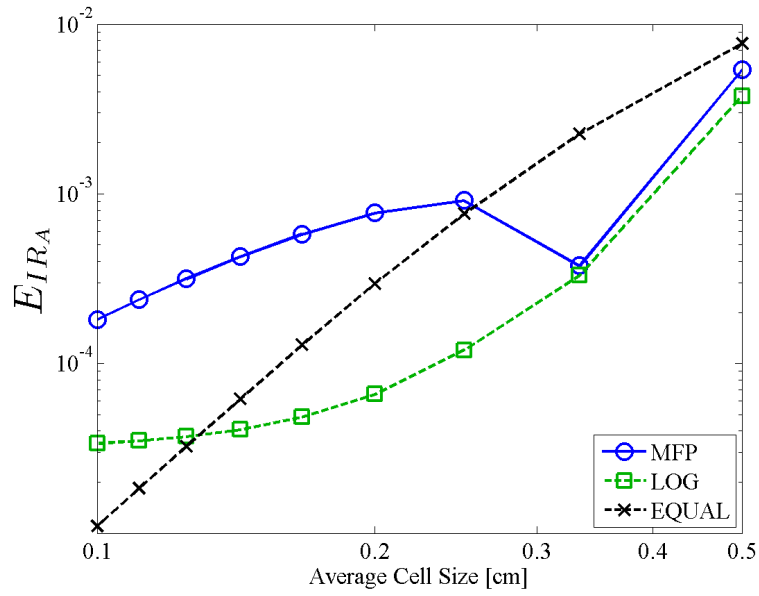


Figure 3.48:  $E_{IR_A}$  fore SLXS Gauss using a quadratic trial space with different mesh spacing methodologies, at low resolutions.

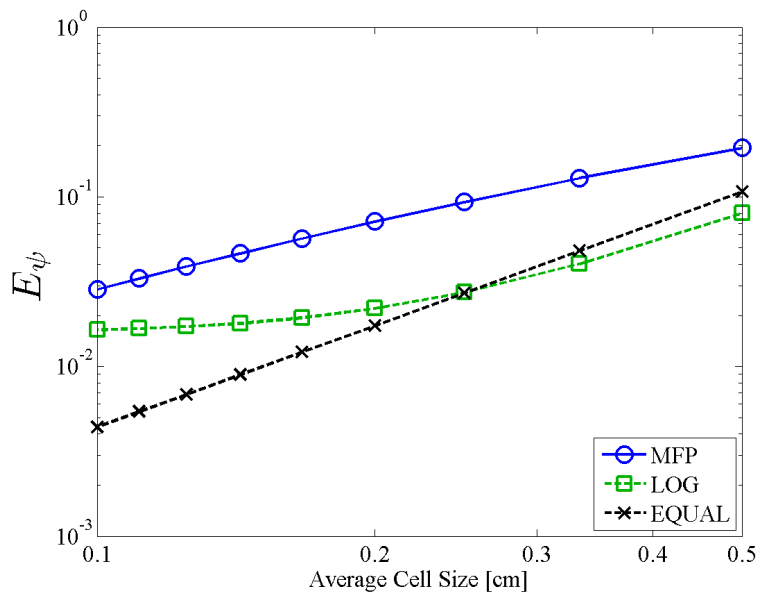


Figure 3.49:  $E_\psi$  for CXS DFEM using a quadratic trial space with different mesh spacing methodologies, at low resolutions.

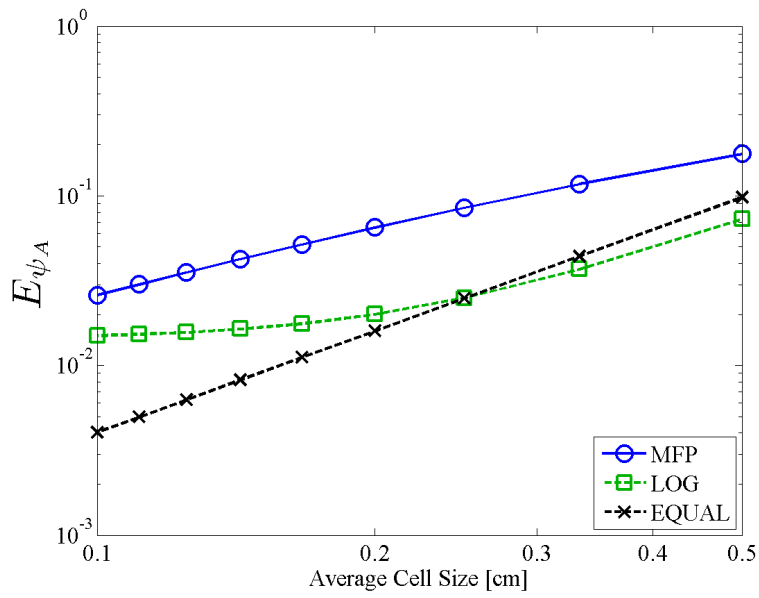


Figure 3.50:  $E_{\psi_A}$  for CXS DFEM using a quadratic trial space with different mesh spacing methodologies, at low resolutions.

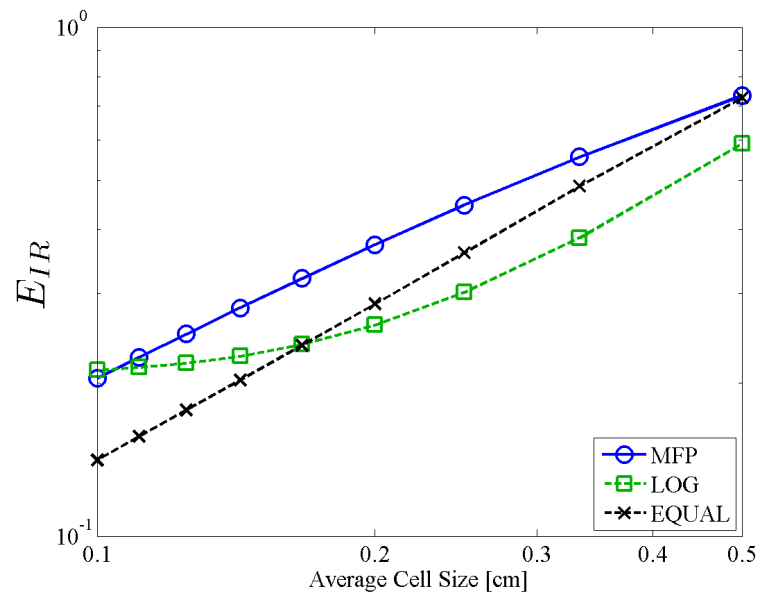


Figure 3.51:  $E_{IR}$  for CXS DFEM using a quadratic trial space with different mesh spacing methodologies, at low resolutions.

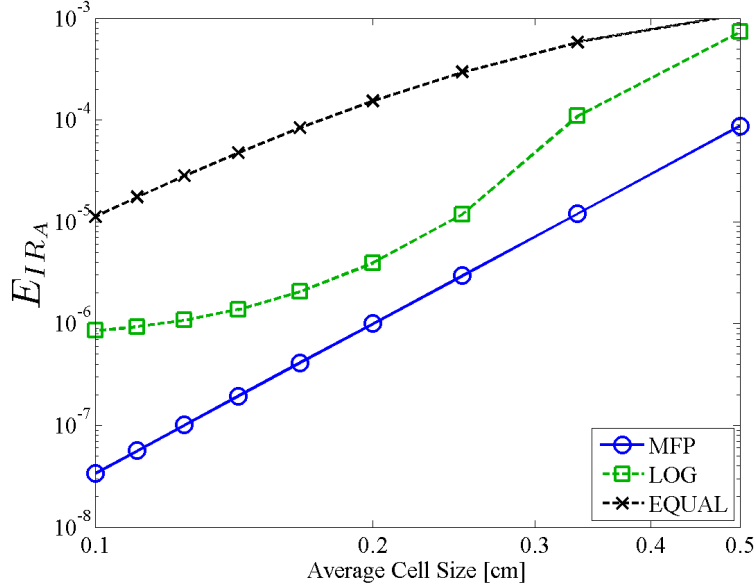


Figure 3.52:  $E_{IR_A}$  for CXS DFEM using a quadratic trial space with different mesh spacing methodologies, at low resolutions.

### 3.4 Conclusions to Be Carried Forward

The SLXS Lobatto and SLXS Gauss schemes are accurate for problems  $S_N$  neutron transport problems that have within cell spatial interaction cross-section variation. Though no less accurate for the case of spatially varying cross sections than for cell-wise constant cross section, the SLXS Newton-Cotes scheme will no longer be considered. SLXS Newton-Cotes is not as asymptotically accurate as SLXS Gauss or SLXS Lobatto schemes, though the SLXS Lobatto scheme is equivalent to SLXS Newton-Cotes for linear and quadratic trial spaces. We continued to consider a self-lumping scheme using closed Newton-Cotes quadrature due to the robustness SL Newton-Cotes exhibited for the cell-wise constant cross section case. However, since no scheme other than linear SLXS Lobatto will yield strictly positive angular flux outflow for arbitrary within cell cross section variation, we conclude that SLXS

Lobatto has all of the strengths exhibited by SLXS Newton-Cotes, with the added benefit of increased accuracy.

We have also documented that the assumption of a cell-wise constant cross section will in general be less accurate than using a self-lumping scheme that explicitly accounts for within cell variation of cross section when constructing  $\mathbf{R}$ . Though the CXS DFEM was more accurate than self-lumping schemes in calculating  $E_{IR_A}$ , and  $E_{\psi_{out}}$ , when using the exact volume average cross section, this is more a function of our test problem being a pure absorber than an inherent benefit of CXS DFEM that will be true for all problems of interest.

## 4. ITERATIVE ACCELERATION FOR THE $S_N$ NEUTRON TRANSPORT EQUATIONS

Thus far, we have omitted a discussion of how the global system of angular flux unknowns is solved, focusing instead on the solution of a single system of equations that describes the unknowns of a single spatial cell, for a single discrete direction. In Section 4.1, we explain the fundamental iterative techniques used to solve the neutron transport equation for all of the angular flux unknowns. In Section 4.2 we discuss two different synthetic acceleration techniques compatible with our chosen spatial discretizations of the transport equation. In Section 4.3 we derive the  $S_2$  synthetic acceleration (S2SA) technique [34] and in Section 4.4 we derive a modified interior penalty (MIP) diffusion synthetic acceleration [35] (DSA) operator. Finally, in Section 4.5, we verify the implementation of each for a set of test problems with spatially constant and spatially varying interaction cross sections.

### 4.1 Iterative Solution of the Neutron Transport $S_N$ Equations

To describe the iterative process by which the discrete ordinates neutron transport equations are solved, we re-visit the spatially analytic, steady-state, mono-energetic discrete ordinates neutron transport equation, but do not have a monolithic right hand side source. Rather, we treat the right hand side as having both an isotropic scattering component, and a fixed source component, as given in Eq. (4.1).

$$\mu \frac{d\psi_d}{dx} + \Sigma_t \psi_d = \frac{\Sigma_s}{4\pi} \phi + S_d . \quad (4.1)$$

The traditional practice is to solve Eq. (4.1) iteratively with Richardson iteration. Each Richardson iteration is referred to as a transport sweep, where for a fixed

right hand side,  $\psi_d$  is updated direction by direction, cell by cell, sweeping from each direction's incident boundary through the entire mesh with upwinding at cell interfaces. Introducing iteration index  $\ell$ , this process can be written as:

$$\mu \frac{d\psi_d^{(\ell+1)}}{dx} + \Sigma_t \psi_d^{(\ell+1)} = \frac{\Sigma_s}{4\pi} \phi^{(\ell)} + S_d. \quad (4.2)$$

After we find,  $\psi_d^{(\ell+1)}$ , we update  $\phi^{(\ell+1)}$  using the discrete ordinates definition:

$$\phi^{(\ell+1)} = 2\pi \sum_{d=1}^{N_{dir}} w_d \psi_d^{(\ell+1)}. \quad (4.3)$$

Though convergent, the source iteration process can converge arbitrarily slow, as shown by Larsen[36], when  $\frac{\Sigma_s}{\Sigma_t} \rightarrow 1$ . To accelerate the convergence of source iteration, the diffusion synthetic acceleration (DSA) technique was developed [37]. DSA is best explained through example.

To start, we consider to a single source iteration:

$$\mu \frac{d\psi_d^{(\ell+1/2)}}{dx} + \Sigma_t \psi_d^{(\ell+1/2)} = \frac{\Sigma_s}{4\pi} \phi^{(\ell)} + S_d. \quad (4.4)$$

Subtracting Eq. (4.1) from Eq. (4.4) yields:

$$\mu \frac{d\delta\psi_d^{(\ell+1/2)}}{dx} + \Sigma_t \delta\psi_d^{(\ell+1/2)} = \frac{\Sigma_s}{4\pi} \delta\phi^{(\ell)}, \quad (4.5)$$

where we have defined the iterative error of the angular flux,  $\delta\psi_d^{(\ell+1)}$ ,

$$\psi_d = \psi_d^{(\ell+1)} + \delta\psi_d^{(\ell+1)}, \quad (4.6)$$

and scalar flux iterative error,  $\delta\phi^{(\ell)}$

$$\phi = \phi^{(\ell)} + \delta\phi_d^{(\ell)}. \quad (4.7)$$

Subtracting  $\frac{\Sigma_s}{4\pi}\delta\phi^{(\ell)}$  from both sides of Eq. (4.5), we see arrive at:

$$\mu \frac{d\delta\psi_d^{(\ell+1/2)}}{dx} + \Sigma_t \delta\psi_d^{(\ell+1/2)} - \frac{\Sigma_s}{4\pi} \delta\phi^{(\ell+1/2)} = \frac{\Sigma_s}{4\pi} \delta\phi^{(\ell)} - \frac{\Sigma_s}{4\pi} \delta\phi^{(\ell+1/2)}. \quad (4.8)$$

Recognizing:

$$\phi = \phi^{(\ell+1/2)} + \delta\phi^{(\ell+1/2)}, \quad (4.9a)$$

$$\phi = \phi^{(\ell)} + \delta\phi^{(\ell)}, \quad (4.9b)$$

$$\phi^{(\ell+1/2)} - \phi^{(\ell)} = (\phi - \delta\phi^{(\ell+1/2)}) - (\phi - \delta\phi^{(\ell)}), \text{ and} \quad (4.9c)$$

$$\delta\phi^{(\ell)} - \delta\phi^{(\ell+1)} = \phi^{(\ell+1/2)} - \phi^{(\ell)}, \quad (4.9d)$$

Eq. (4.8) becomes:

$$\mu \frac{d\delta\psi_d^{(\ell+1/2)}}{dx} + \Sigma_t \delta\psi_d^{(\ell+1/2)} = \frac{\Sigma_s}{4\pi} \delta\phi^{(\ell+1/2)} + \frac{\Sigma_s}{4\pi} (\phi^{(\ell+1/2)} - \phi^{(\ell)}). \quad (4.10)$$

Equation 4.10 indicates that if we could solve a transport problem with a driving source equal to the difference between two scattering iterates,

$$\frac{\Sigma_s}{4\pi} (\phi^{(\ell+1/2)} - \phi^{(\ell)}), \quad (4.11)$$

then we could get the iterative error of iteration  $\delta\phi^{(\ell+1/2)}$ , add to the  $\phi^{(\ell+1/2)}$  we already have, and then have the exact solution,  $\phi$ . However, solving Eq. (4.10) is as difficult as solving the original problem in Eq. (4.1). Alternatively, if we could solve

an approximation to Eq. (4.10), perhaps the result would satisfy:

$$\phi \approx \Delta\phi^{(\ell+1/2)} + \phi^{(\ell+1/2)}, \quad (4.12)$$

where  $\Delta\phi^{(\ell+1/2)}$  comes from the lower order approximation to Eq. (4.10). The idea of using a lower order operator to approximately solve Eq. (4.10) is central to synthetic acceleration.

## 4.2 Qualitative Comparison of Different Synthetic Acceleration Techniques

We consider two synthetic acceleration techniques that have received significant attention in the neutron transport and thermal radiative transfer literature,  $S_2$  synthetic acceleration (S2SA)[34] and diffusion synthetic acceleration (DSA)[37]. Both methods of synthetic acceleration has both advantages and disadvantages relating to the computational efficiency and iterative effectiveness of each method.

The S2SA method was shown to be iteratively effective in both slab and 1-D spherical geometries. Additionally, it is easily compatible with any DFEM spatial discretization of the  $S_N$  neutron transport equations. S2SA solves for  $\psi_+$  and  $\psi_-$  using a single global matrix solve, rather than a direction by direction solve for the full transport  $\psi_d$  unknowns. The full transport scalar flux iterative update is then defined as,

$$\Delta\phi^{(\ell+1/2)} \approx 2\pi [w_+\psi_+ + w_-\psi_-], \quad (4.13)$$

where  $w_+$ ,  $w_-$  correspond to the weights of a direction quadrature (typically Gauss) set with corresponding discrete direction  $\mu_+$  and  $\mu_-$ , and  $\psi_+$ ,  $\psi_-$  are the fundamental unknowns of the  $S_2$  discretization. Thus, S2SA uses the same local matrices of Eq. (3.2) as the full transport operator. However, the S2SA global matrix that must be inverted to solve for  $\psi_+$  and  $\psi_-$  is extremely difficult to invert for multiple spatial

dimensions. This makes S2SA iteratively effective, but computationally expensive, limiting the extensibility of any techniques that require S2SA. But since our initial focus is on solving slab geometry neutron transport problems, we will continue to consider S2SA as it is readily adaptable to our new spatial discretization schemes.

[34]

Gelbard and Hageman first showed in [37] that diffusion synthetic acceleration (DSA) could be used to accelerate the convergence of source iteration in neutron transport since the diffusion operator effectively attenuates the slowly varying error modes that hinder the convergence of source iteration. To be unconditionally effective, Larsen showed that DSA needed to be derived in a method consistent with the spatial and angular discretization of the transport equation [36]. Adams and Martin first showed that partially consistent diffusion discretizations could be used to effectively accelerate DFEM spatial discretizations of the neutron transport equation [38]. Though shown to be unconditionally stable for certain geometries the M4S DSA proposed in [38] has been shown to be unstable for unstructured multi-dimensional geometries [39]. To allow more general applicability, we wish to consider a more advanced DSA discretization. Alternative DSA discretizations that have been applied successfully to unstructured multi-dimensional geometries include: the partially consistent WLA DSA proposed in [40], the fully consistent DSA (FCDSA) proposed in [39], and the partially consistent MIP DSA proposed in [35]. WLA DSA produces a symmetric positive definite (SPD) diffusion matrix and is unconditionally stable, but the spectral radius of the WLA DSA scheme increases on distorted mesh cells and for optically thick cells with scattering ratios very close to unity [39, 40]. While the FCDSA scheme remains effective in optically thick cells, it creates a diffusion operator that is very difficult and costly to invert[39]. The MIP DSA discretization [35] of Wang and Ragusa generates a SPD diffusion operator, remains effective for all

cell optical thicknesses, has been successfully applied to high order DFEM  $S_N$  transport, and can be used with adaptive mesh refinement. Further, it was shown in [41] that the MIP DSA diffusion operator can be inverted very quickly using advanced preconditioners such as algebraic multi-grid. Thus, if we can show that a MIP DSA discretization is iteratively effective for neutron transport problems discretized with our higher order DFEM methods that account for the spatial variation of cross section within each cell, we will have found a scheme that is most likely to prove useful in meaningful (multiple spatial dimensions) thermal radiative transfer simulations.

We will derive an S2SA operator in Section 4.3 and MIP DSA operator in Section 4.4. The S2SA operator re-uses a lot of the transport sweep capability we have already developed with our high order DFEM of Section 3, but is computationally challenging to invert (in multiple spatial dimensions), and the MIP DSA operator we define in Section 4.4 requires significant derivation independent of the DFEM neutron transport methodology we have already derived, but is computationally efficient to invert.

### 4.3 $S_2$ Synthetic Acceleration

We begin our derivation by repeating the  $S_2$ , spatially analytic angular flux update equations from Morel (Eqs. (12a) and (12b) in [34]), noting that we have elected to use  $\psi^+$  and  $\psi^-$  instead of  $c^+$  and  $c^-$ ,  $\Sigma$  represents macroscopic interaction cross sections rather than  $\sigma$ , and we define  $\phi = 2\pi \sum_d w_d \psi_d$ :

$$\mu_+ \frac{d\psi^+}{dx} + \Sigma_t \psi^+ = \frac{\Sigma_s}{4\pi} \Delta\phi + \frac{\Sigma_s}{4\pi} (\phi^{(\ell+1/2)} - \phi^{(\ell)}) \quad (4.14a)$$

$$\mu_- \frac{d\psi^-}{dx} + \Sigma_t \psi^- = \frac{\Sigma_s}{4\pi} \Delta\phi + \frac{\Sigma_s}{4\pi} (\phi^{(\ell+1/2)} - \phi^{(\ell)}) . \quad (4.14b)$$

In Eqs. (4.14) we are assuming scattering is isotropic only. Spatially discretizing with a  $P$  degree DFEM as in Chapter 3, for an interior cell,  $c$ , we have:

$$(\mu_+ \mathbf{G}_+ + \mathbf{R}_{\Sigma_t}) \vec{\psi}_c^+ = \frac{1}{4\pi} \mathbf{R}_{\Sigma_s} \vec{\Delta\phi}_c + \frac{1}{4\pi} \mathbf{R}_{\Sigma_s} \left( \vec{\phi}_c^{(\ell+1/2)} - \vec{\phi}_c^{(\ell)} \right) + \mu_+ \psi_{in,+} \vec{f}_+ \quad (4.15a)$$

$$(\mu_- \mathbf{G}_- + \mathbf{R}_{\Sigma_t}) \vec{\psi}_c^- = \frac{1}{4\pi} \mathbf{R}_{\Sigma_s} \vec{\Delta\phi}_c + \frac{1}{4\pi} \mathbf{R}_{\Sigma_s} \left( \vec{\phi}_c^{(\ell+1/2)} - \vec{\phi}_c^{(\ell)} \right) + \mu_- \psi_{in,-} \vec{f}_-. \quad (4.15b)$$

All reaction matrices are evaluated in cell  $c$ , unless otherwise noted with a subscript. In Eqs. (4.15), we note that  $\mu_+ > 0$  and  $\mu_- < 0$ , and as such use the  $\pm$  subscripts to define the appropriate  $\mathbf{G}$  and  $\vec{f}$ , defined in Eqs. (4.16) and Eqs. (4.17), respectively:

$$\mathbf{G}_{+,i,j} = b_i(1)b_j(1) - \int_{-1}^1 \frac{db_i}{ds} b_j(s) \, ds \quad (4.16a)$$

$$\mathbf{G}_{-,i,j} = -b_i(-1)b_j(-1) - \int_{-1}^1 \frac{db_i}{ds} b_j(s) \, ds, \quad (4.16b)$$

$$\vec{f}_{+,i} = b_i(-1) \quad (4.17a)$$

$$\vec{f}_{-,i} = -b_i(1). \quad (4.17b)$$

Noting that the inflow to cells on the interior is the outflow from the appropriate cell, for and using the definitions of Eqs. (2.7b) and Eqs. (2.8b), we define  $\psi_{in,+} \vec{f}_+$  and  $\psi_{in,-} \vec{f}_-$  entirely in terms of  $\vec{\psi}_{c-1}^+$  and  $\vec{\psi}_{c+1}^-$ ,

$$\psi_{in,+} \vec{f}_+ = \mathbf{U}_+ \vec{\psi}_{c-1}^+ \quad (4.18a)$$

$$\psi_{in,-} \vec{f}_- = \mathbf{U}_- \vec{\psi}_{c+1}^-, \quad (4.18b)$$

where

$$\mathbf{U}_+ = \begin{bmatrix} b_1(-1) \\ \vdots \\ b_{N_P}(-1) \end{bmatrix} [b_1(1) \dots b_{N_P}(1)] \quad (4.19a)$$

$$\mathbf{U}_- = \begin{bmatrix} b_1(1) \\ \vdots \\ b_{N_P}(1) \end{bmatrix} [b_1(-1) \dots b_{N_P}(-1)] . \quad (4.19b)$$

Finally, assuming a symmetric angular quadrature,

$$\frac{1}{4\pi} \mathbf{R}_{\Sigma_s} \vec{\Delta\phi}_c = \frac{1}{2} \mathbf{R}_{\Sigma_s} (\vec{\psi}_c^+ + \vec{\psi}_c^-) , \quad (4.20)$$

we may write Eqs. (4.15) as:

$$(\mu_+ \mathbf{G}_+ + \mathbf{R}_{\Sigma_t}) \vec{\psi}_c^+ - \frac{1}{2} \mathbf{R}_{\Sigma_s} (\vec{\psi}_c^+ + \vec{\psi}_c^-) - \mu_+ \mathbf{U}_+ \vec{\psi}_{c-1}^+ = \frac{1}{4\pi} \mathbf{R}_{\Sigma_s} (\vec{\phi}_c^{(\ell+1/2)} - \vec{\phi}_c^{(\ell)}) \quad (4.21a)$$

$$(\mu_- \mathbf{G}_- + \mathbf{R}_{\Sigma_t}) \vec{\psi}_c^- - \frac{1}{2} \mathbf{R}_{\Sigma_s} (\vec{\psi}_c^+ + \vec{\psi}_c^-) - \mu_- \mathbf{U}_- \vec{\psi}_{c+1}^- = \frac{1}{4\pi} \mathbf{R}_{\Sigma_s} (\vec{\phi}_c^{(\ell+1/2)} - \vec{\phi}_c^{(\ell)}) . \quad (4.21b)$$

Thus, the S2SA scheme uses all of the same matrices, in particular we think of  $\mathbf{R}_{\Sigma_t}$  and  $\mathbf{R}_{\Sigma_s}$ , that we have already defined in our higher fidelity transport model. To find  $\psi^+$  and  $\psi^-$ , we must then solve a system of  $2 \times N_P \times N_{cell}$  linear equations with  $2 \times N_P \times N_{cell}$  unknowns. It is important to note that S2SA can accelerate not only the scalar flux, but also the first angular moment,  $J$ , of the  $S_N$  neutron transport equations

To complete our derivation of the S2SA scheme, we must now define appropriate boundary conditions. We will focus only on the leftmost boundary, though similar

equations for the right boundary can be defined analogously. It is sufficient for our purposes to consider problems only with specified incident flux boundary conditions and reflective boundaries. With incident flux conditions, we wish for the accelerated iterate to maintain the same inflow current as the specified boundary condition. Allowing for non-isotropic incident fluxes, the incident current,  $J^+$  specified by our problem is:

$$\sum_{d=N_{dir}/2+1}^{N_{dir}} w_d \mu_d \psi_{in,d}. \quad (4.22)$$

Given the S2SA equations were derived via the assumption of a  $P_1$  angular flux, the additive angular flux correction for direction  $d$  is:

$$\Delta\phi = 2\pi (\psi^+ + \psi^-) \quad (4.23a)$$

$$\Delta J = 2\pi (\mu_+ \psi^+ + \mu_- \psi^-) \quad (4.23b)$$

$$\Delta\psi_d = \frac{\Delta\phi}{4\pi} + \mu_d \frac{3\Delta J}{4\pi}. \quad (4.23c)$$

Wishing to maintain  $J^+$ , we have:

$$J^+ = 2\pi \sum_{d=N_{dir}/2+1}^{N_{dir}} w_d \mu_d \left[ \psi_{in,d} + \frac{\Delta\phi}{4\pi} + \mu_d \frac{3\Delta J}{4\pi} \right], \quad (4.24)$$

which implies

$$0 = \sum_{d=N_{dir}/2+1}^{N_{dir}} w_d \mu_d \left[ \frac{\Delta\phi}{4\pi} + \mu_d \frac{3\Delta J}{4\pi} \mu_d \right]. \quad (4.25)$$

Inserting the definitions of Eqs. (4.23), and allowing for DFEM interpolation points that do not exist at the left boundary:

$$0 = \sum_{d=N_{dir}/2+1}^{N_{dir}} w_d \mu_d \left[ \frac{1}{2} \left( \psi_{in}^+ + \vec{L} \vec{\psi}_1^- \right) + \frac{3\mu_d}{2} \left( \mu_+ \psi_{in}^+ + \mu_- \vec{L} \vec{\psi}_1^- \right) \right], \quad (4.26)$$

where

$$\vec{L} = [b_1(-1) \dots b_{N_P}(-1)] . \quad (4.27)$$

Defining constants dependent on the  $S_N$  quadrature used,

$$\langle \mu^+ \rangle = \sum_{\mu_d > 0} w_d \mu_d \quad (4.28a)$$

$$\langle \mu^+ \rangle_2 = \sum_{\mu_d > 0} w_d \mu_d^2 , \quad (4.28b)$$

Eq. (4.26) becomes

$$0 = \frac{\langle \mu^+ \rangle}{2} \psi_{in}^+ + \frac{\langle \mu^+ \rangle}{2} \vec{L} \vec{\psi}_1^- + \frac{3}{2} \langle \mu^+ \rangle_2 \left( \mu_+ \psi_{in}^+ + \mu_- \vec{L} \vec{\psi}_1^- \right) . \quad (4.29)$$

Solving Eq. (4.29) for  $\psi_{in}^+$ ,

$$\psi_{in}^+ = - \left( \frac{\langle \mu^+ \rangle}{2} + \frac{3}{2} \langle \mu^+ \rangle_2 \mu_+ \right)^{-1} \left( \frac{\langle \mu^+ \rangle}{2} + \frac{3}{2} \langle \mu^+ \rangle_2 \mu_- \right) \vec{L} \vec{\psi}_1^- . \quad (4.30)$$

Defining a constant,  $C_{inc}$ ,

$$C_{inc} = - \left( \frac{\langle \mu^+ \rangle}{2} + \frac{3}{2} \langle \mu^+ \rangle_2 \mu_+ \right)^{-1} \left( \frac{\langle \mu^+ \rangle}{2} + \frac{3}{2} \langle \mu^+ \rangle_2 \mu_- \right) , \quad (4.31)$$

and substituting into Eqs. (4.15), we have

$$(\mu_+ \mathbf{G}_+ + \mathbf{R}_{\Sigma_t}) \vec{\psi}_1^+ = \frac{1}{4\pi} \mathbf{R}_{\Sigma_s} \vec{\Delta\phi}_1 + \frac{1}{4\pi} \mathbf{R}_{\Sigma_s} \left( \vec{\phi}_1^{(\ell+1/2)} - \vec{\phi}_1^{(\ell)} \right) + \mu_+ C_{inc} \left( \vec{L} \vec{\psi}_1^- \right) \vec{f}_+ \quad (4.32a)$$

$$(\mu_- \mathbf{G}_- + \mathbf{R}_{\Sigma_t}) \vec{\psi}_1^- = \frac{1}{4\pi} \mathbf{R}_{\Sigma_s} \vec{\Delta\phi}_1 + \frac{1}{4\pi} \mathbf{R}_{\Sigma_s} \left( \vec{\phi}_1^{(\ell+1/2)} - \vec{\phi}_1^{(\ell)} \right) + \mu_- \psi_{in,-} \vec{f}_- . \quad (4.32b)$$

Noting that  $\vec{f}_+ \vec{L}$  creates an  $N_P \times N_P$  matrix, and inserting all of our other definitions,

we have the equations for cell 1 for incident angular flux boundary conditions

$$(\mu_+ \mathbf{G}_+ + \mathbf{R}_{\Sigma_t}) \vec{\psi}_1^+ - \frac{1}{2} \mathbf{R}_{\Sigma_s} (\vec{\psi}_1^+ + \vec{\psi}_1^-) - \mu_+ C_{inc} \vec{f}_+ \vec{L} \vec{\psi}_1^- = \frac{1}{4\pi} \mathbf{R}_{\Sigma_s} (\vec{\phi}_1^{(\ell+1/2)} - \vec{\phi}_1^{(\ell)}) \quad (4.33a)$$

$$(\mu_- \mathbf{G}_- + \mathbf{R}_{\Sigma_t}) \vec{\psi}_1^- - \frac{1}{2} \mathbf{R}_{\Sigma_s} (\vec{\psi}_1^+ + \vec{\psi}_1^-) - \mu_- \mathbf{U}_- \vec{\psi}_2^- = \frac{1}{4\pi} \mathbf{R}_{\Sigma_s} (\vec{\phi}_1^{(\ell+1/2)} - \vec{\phi}_1^{(\ell)}) . \quad (4.33b)$$

For reflective conditions, we have a zero current on the left edge:

$$0 = 2\pi \sum_d w_d \mu_d \psi_d^{(\ell+1/2)} \quad (4.34)$$

$$0 = 2\pi \sum_d w_d \mu_d \left[ \psi_d^{(\ell+1/2)} + \frac{\Delta\phi}{4\pi} + \mu_d \frac{3\Delta J}{2} \right] . \quad (4.35)$$

Equation 4.34 implies

$$0 = \sum_d w_d \mu_d \left[ \frac{1}{2} (\psi_{in,+} + \vec{L} \vec{\psi}_1^-) + \frac{3\mu_d}{2} (\mu_+ \psi_{in,+} + \mu_- \vec{L} \vec{\psi}_1^-) \right] . \quad (4.36)$$

Expanding our earlier quadrature definitions,

$$\langle \mu \rangle = \sum_d w_d \mu_d \quad (4.37a)$$

$$\langle \mu^2 \rangle = \sum_d w_d \mu_d^2 \quad (4.37b)$$

we now solve for  $\psi_{in,+}$  as a function of  $\vec{\psi}_1^-$ :

$$\psi_{in,+} = - \left( \frac{\langle \mu \rangle}{2} + \frac{3\mu_+}{2} \langle \mu^2 \rangle \right)^{-1} \left( \frac{\langle \mu \rangle}{2} + \frac{3\mu_-}{2} \langle \mu^2 \rangle \right) \vec{L} \vec{\psi}_1^- . \quad (4.38)$$

Defining another constant,  $C_{ref}$ ,

$$C_{ref} = - \left( \frac{\langle \mu \rangle}{2} + \frac{3\mu_+}{2} \langle \mu^2 \rangle \right)^{-1} \left( \frac{\langle \mu \rangle}{2} + \frac{3\mu_-}{2} \langle \mu^2 \rangle \right) \quad (4.39)$$

, the leftmost cell equations with a reflective boundary condition are:

$$(\mu_+ \mathbf{G}_+ + \mathbf{R}_{\Sigma_t}) \vec{\psi}_1^+ - \frac{1}{2} \mathbf{R}_{\Sigma_s} (\vec{\psi}_1^+ + \vec{\psi}_1^-) - \mu_+ C_{ref} \vec{f}_+ \vec{L} \vec{\psi}_1^- = \frac{1}{4\pi} \mathbf{R}_{\Sigma_s} (\vec{\phi}_1^{(\ell+1/2)} - \vec{\phi}_1^{(\ell)}) \quad (4.40a)$$

$$(\mu_- \mathbf{G}_- + \mathbf{R}_{\Sigma_t}) \vec{\psi}_1^- - \frac{1}{2} \mathbf{R}_{\Sigma_s} (\vec{\psi}_1^+ + \vec{\psi}_1^-) - \mu_- \mathbf{U}_- \vec{\psi}_2^- = \frac{1}{4\pi} \mathbf{R}_{\Sigma_s} (\vec{\phi}_1^{(\ell+1/2)} - \vec{\phi}_1^{(\ell)}) . \quad (4.40b)$$

#### 4.4 Modified Interior Penalty Diffusion Synthetic Acceleration

We now derive the modified interior penalty diffusion synthetic acceleration (MIP DSA) operator introduced by Ragusa and Wang [35], and also considered by Turcksin and Ragusa [41]. To accelerate the convergence of  $N_P \times N_{cell}$  spatial unknowns of the scalar flux, we will need to solve a system of  $N_P \times N_{cell}$  linear equations with  $N_P \times N_{cell}$  unknowns. Adapted from [35], the MIP DSA update will attempt to solve the diffusion approximation of Eq. (4.10),

$$-\nabla \cdot D \nabla \Delta \phi + \Sigma_a \Delta \phi = \Sigma_s (\phi^{(\ell+1/2)} - \phi^{(\ell)}) , \quad (4.41)$$

where we use the standard definitions [33],

$$D = \frac{1}{3\Sigma_t} \quad (4.42)$$

$$\Sigma_a = \Sigma_t - \Sigma_s . \quad (4.43)$$

MIP DSA is presented in the standard finite element bilinear form

$$b_{MIP}(\Delta\phi, b_*) = l_{MIP}(b_*) , \quad (4.44)$$

with

$$\begin{aligned} b_{MIP}(\Delta\phi, b_*) &= (\Sigma_a \Delta\phi, b_*)_{\mathcal{D}} + \left( D \vec{\nabla} \Delta\phi, \vec{\nabla} b_* \right)_{\mathcal{D}} \\ &\quad + (\kappa_e [\![\Delta\phi]\!], [\![b_*]\!])_{E_h^i} \\ &\quad + ([\![\Delta\phi]\!], \{D\partial_n b_*\})_{E_h^i} \\ &\quad + (\{D\partial_n \Delta\phi\}, [\![b_*]\!])_{E_h^i} \\ &\quad + (\kappa_e \Delta\phi, b_*)_{\partial\mathcal{D}^d} - \frac{1}{2} (\Delta\phi, D\partial_n b_*)_{\partial\mathcal{D}^d} \\ &\quad - \frac{1}{2} (D\partial_n \Delta\phi, b_*)_{\partial\mathcal{D}^d} , \end{aligned} \quad (4.45)$$

and

$$l_{MIP}(b_*) = (\Sigma_s (\phi^{(\ell+1/2)} - \phi^{(\ell)}), b_*) + (J_{inc}, b_*)_{\partial\mathcal{D}^r} . \quad (4.46)$$

In Eqs. (4.44)-(4.46),  $b_*$  is any/every basis function (also referred to as test functions), the  $(f, g)_{E_h^i}$  operator acting on quantities  $f$  and  $g$  is a sum over all cell interior edges:

$$(f, g)_{E_h^i} = \sum_{c=1}^{N_{cell-1}} (f, g)_{c+1/2} , \quad (4.47)$$

the jump operator,  $[\![f]\!]_{c+1/2}$ , is defined as

$$[\![f]\!]_{c+1/2} = f(x_{c+1/2}^+) - f(x_{c+1/2}^-) , \quad (4.48)$$

where  $x_{c+1/2}$  is the position of cell edge  $c + 1/2$ , the average operator,  $\{\{f\}\}_{c+1/2}$ , is

$$\{\{f\}\}_{c+1/2} = \frac{1}{2} \left[ f(x_{c+1/2}^+) + f(x_{c+1/2}^-) \right], \quad (4.49)$$

and  $\partial_n$  is the edge directed normal dotted into the gradient operator. On the interior, the direction of  $\partial_n$  does not matter as long as it is consistent. We we assume the edge normal always pointing from left to right, thus  $\partial_n = \frac{d}{dx}$ . However, on the domain boundary, the edge directed normal must point outwards. Also in Eqs (4.45)-(4.46), the  $(f, g)_\mathcal{D}$  operator is an integration of quantities  $f$  and  $g$  over the entire domain  $\mathcal{D}$ :

$$(f, g)_\mathcal{D} = \sum_{c=1}^{N_{cell}} (f, g)_c \quad (4.50)$$

$$(f, g)_c = \int_{x_{c-1/2}}^{x_{c+1/2}} f g \, dx. \quad (4.51)$$

Finally,  $\kappa_e$  is defined on edge  $c - 1/2$  as

$$\kappa_e = \kappa_{c-1/2} = \max \left( \frac{1}{4}, \kappa_{c-1/2}^{IP} \right), \quad (4.52)$$

and  $\kappa_{c-1/2}^{IP}$  is defined as:

$$\kappa_{c-1/2}^{IP} = \frac{Z_{MIP}}{2} p_c(p_c + 1) \frac{D_c}{\Delta x_c} \Big|_{x_{c-1/2}^+} + \frac{Z_{MIP}}{2} p_{c-1}(p_{c-1} + 1) \frac{D_{c-1}}{\Delta x_{c-1}} \Big|_{x_{c-1/2}^-}, \quad (4.53)$$

where  $Z_{MIP}$  is a stability constant. Unless otherwise stated, we use  $Z_{MIP} = 2$ , as recommended by Wang and Ragusa[35]. Larger values of  $Z_{MIP}$  will increase scheme stability (by adding numerical diffusion), but if chosen too large, will affect the accuracy of the spatial discretization. Terms denoted by  $\partial\mathcal{D}^d$  indicate Dirichlet boundary

terms (specified incident angular boundary condition), and terms applicable only for reflective (Neumann) boundary conditions are denoted with a  $\partial\mathcal{D}^r$ .

Focusing now on an interior mesh cell,  $c$ , and the  $N_P b_i$  that are non-zero in that cell, we now go about defining all of the terms of Eq. (4.45). First, we consider the volumetric integration terms, defining

$$(\Sigma_a \Delta\phi, b_*) = \mathbf{R}_{\Sigma_a} \vec{\Delta\phi}_c, \quad (4.54)$$

and

$$(D\vec{\nabla}\Delta\phi, \vec{\nabla}b_*) = \mathbf{S}. \quad (4.55)$$

In Eq. (4.55), we have defined:

$$\mathbf{S}_{ij} = \frac{2}{\Delta x_c} \int_{-1}^1 \frac{1}{3\Sigma_t(s)} \frac{db_i}{ds} \frac{db_j}{ds} ds. \quad (4.56)$$

Now we treat the edge terms. We begin by defining  $\llbracket\Delta\phi\rrbracket$  on each edge,

$$\llbracket\Delta\phi\rrbracket_{c-1/2} = \vec{L}\vec{\Delta\phi}_c - \vec{R}\vec{\Delta\phi}_{c-1}, \quad (4.57a)$$

$$\llbracket\Delta\phi\rrbracket_{c+1/2} = \vec{L}\vec{\Delta\phi}_{c+1} - \vec{R}\vec{\Delta\phi}_c, \quad (4.57b)$$

where we've defined

$$\vec{L} = [b_1(-1) \dots b_{N_P}(-1)] \quad (4.58a)$$

$$\vec{R} = [b_1(1) \dots b_{N_P}(1)]. \quad (4.58b)$$

Treating all test functions for cell  $c$  at once, we now define  $\llbracket b_* \rrbracket$ :

$$\llbracket b_* \rrbracket_{c-1/2} = \vec{L}^T - \vec{0} \quad (4.59a)$$

$$\llbracket b_* \rrbracket_{c+1/2} = \vec{0} - \vec{R}^T, \quad (4.59b)$$

where  $\vec{0}$  is a length  $N_P$  column vector whose entries are all identically zero. Now we define the average operator on the edges  $\{\{D\partial_n \Delta\phi\}\}$  and  $\{\{D\partial_n b_*\}\}$ . On edges  $c - 1/2$  and  $c + 1/2$ ,

$$\{\{D\partial_n \Delta\phi\}\}_{c-1/2} = \frac{D(x_{c-1/2}^+)}{\Delta x_c} \vec{L}_s \vec{\Delta\phi}_c + \frac{D(x_{c-1/2}^-)}{\Delta x_{c-1}} \vec{R}_s \vec{\Delta\phi}_{c-1} \quad (4.60a)$$

$$\{\{D\partial_n \Delta\phi\}\}_{c+1/2} = \frac{D(x_{c+1/2}^+)}{\Delta x_{c+1}} \vec{L}_s \vec{\Delta\phi}_{c+1} + \frac{D(x_{c+1/2}^-)}{\Delta x_c} \vec{R}_s \vec{\Delta\phi}_c, \quad (4.60b)$$

where

$$\vec{L}_s = \left[ \frac{db_1}{ds} \Big|_{s=-1} \dots \frac{db_{N_P}}{ds} \Big|_{s=-1} \right] \quad (4.61a)$$

$$\vec{R}_s = \left[ \frac{db_1}{ds} \Big|_{s=1} \dots \frac{db_{N_P}}{ds} \Big|_{s=1} \right]. \quad (4.61b)$$

On edges  $c - 1/2$  and  $c + 1/2$ ,

$$\{\{D\partial_n b_*\}\}_{c-1/2} = \frac{D(x_{c-1/2}^+)}{\Delta x_c} \vec{L}_s^T \quad (4.62a)$$

$$\{\{D\partial_n b_*\}\}_{c+1/2} = \frac{D(x_{c+1/2}^+)}{\Delta x_c} \vec{R}_s^T. \quad (4.62b)$$

Combining Eq. (4.54), Eq. (4.55), Eqs. (4.57), Eqs. (4.59), Eqs. (4.60), and Eqs.

(4.62), we have the left hand side of the cell  $c$  MIP DSA equations:

$$\begin{aligned}
& \mathbf{R}_{\Sigma_a} \vec{\Delta\phi}_c + \mathbf{S} \vec{\Delta\phi}_c \\
& + \left\{ \left[ \kappa_{c-1/2} \vec{L}^T \left( \vec{L} \vec{\Delta\phi}_c - \vec{R} \vec{\Delta\phi}_{c-1} \right) \right] - \left[ \kappa_{c+1/2} \vec{R}^T \left( \vec{L} \vec{\Delta\phi}_{c+1} - \vec{R} \vec{\Delta\phi}_c \right) \right] \right\} \\
& + \left\{ \frac{D(x_{c-1/2}^+)}{\Delta x_c} \vec{L}_s^T \left( \vec{L} \vec{\Delta\phi}_c - \vec{R} \vec{\Delta\phi}_{c-1} \right) + \frac{D(x_{c+1/2}^-)}{\Delta x_c} \vec{R}_s^T \left( \vec{L} \vec{\Delta\phi}_{c+1} - \vec{R} \vec{\Delta\phi}_c \right) \right\} \\
& + \left\{ \vec{L}^T \left( \frac{D(x_{c-1/2}^+)}{\Delta x_c} \vec{L}_s \vec{\Delta\phi}_c + \frac{D(x_{c-1/2}^-)}{\Delta x_{c-1}} \vec{R}_s \vec{\Delta\phi}_{c-1} \right) \dots \right. \\
& \quad \left. - \vec{R}^T \left( \frac{D(x_{c+1/2}^+)}{\Delta x_{c+1}} \vec{L}_s \vec{\Delta\phi}_{c+1} + \frac{D(x_{c+1/2}^-)}{\Delta x_c} \vec{R}_s \vec{\Delta\phi}_c \right) \right\}, \quad (4.63)
\end{aligned}$$

and the right hand side on the interior is obviously

$$\mathbf{R}_{\Sigma_s} \left( \vec{\phi}_c^{(\ell+1/2)} - \vec{\phi}_c^{(\ell)} \right). \quad (4.64)$$

In Eq. (4.63) and Eq. (4.64),  $\mathbf{R}_{\Sigma_a}$ ,  $\mathbf{R}_{\Sigma_s}$ , and  $\mathbf{S}$  are evaluated in cell  $c$ . Arranging Eq. (4.63) to isolate  $\vec{\Delta\phi}_{c-1}$ ,  $\vec{\Delta\phi}_c$ , and  $\vec{\Delta\phi}_{c+1}$ , we have

$$\begin{aligned}
& \left\{ -\kappa_{c-1/2} \vec{L}^T \vec{R} - \frac{D(x_{c-1/2}^+)}{\Delta x_c} \vec{L}_s^T \vec{R} + \frac{D(x_{c-1/2}^-)}{\Delta x_{c-1}} \vec{L}^T \vec{R}_s \right\} \vec{\Delta\phi}_{c-1} \\
& \left\{ \mathbf{R}_{\Sigma_a} + \mathbf{S} + \kappa_{c-1/2} \vec{L}^T \vec{L} + \kappa_{c+1/2} \vec{R}^T \vec{R} + \frac{D(x_{c-1/2}^+)}{\Delta x_c} \vec{L}_s^T \vec{L} - \frac{D(x_{c+1/2}^-)}{\Delta x_c} \vec{R}_s^T \vec{R} \right. \\
& \quad \left. + \frac{D(x_{c-1/2}^+)}{\Delta x_c} \vec{L}^T \vec{L}_s - \frac{D(x_{c+1/2}^-)}{\Delta x_c} \vec{R}^T \vec{R}_s \right\} \vec{\Delta\phi}_c \\
& \left\{ -\kappa_{c+1/2} \vec{R}^T \vec{L} + \frac{D(x_{c+1/2}^-)}{\Delta x_c} \vec{R}_s^T \vec{L} - \frac{D(x_{c+1/2}^+)}{\Delta x_{c+1}} \vec{R}^T \vec{L}_s \right\} \vec{\Delta\phi}_{c+1} \quad (4.65)
\end{aligned}$$

We now consider the leftmost cell, so that we derive appropriate boundary conditions. We will derive equations for reflective and incident current boundary condi-

tions. Equations for the right boundary can be derived analogously. Starting with incident flux boundary conditions, we must define the  $(\kappa_{1/2}\Delta\phi, b_*)$ ,  $(\Delta\phi, D\partial_n b_*)$ , and  $(D\partial_n\Delta\phi, b_*)$  operators. They are:

$$(\kappa_{1/2}\Delta\phi, b_*) = \kappa_{1/2}\vec{L}^T\vec{L}\vec{\Delta\phi}_1 \quad (4.66a)$$

$$(\Delta\phi, D\partial_n b_*) = -\frac{2D(x_{1/2}^+)}{\Delta x_1}\vec{L}_s^T\vec{L}\vec{\Delta\phi}_1 \quad (4.66b)$$

$$(D\partial_n\Delta\phi, b_*) = -\frac{2D(x_{1/2}^+)}{\Delta x_1}\vec{L}^T\vec{L}_s\vec{\Delta\phi}_1, \quad (4.66c)$$

where we remind the reader that on the left edge,  $\partial_n = -\frac{\partial}{\partial x}$ . Combing with the cell integral quantities, and the interior edge terms, for problems with an incident flux boundary condition, the leftmost cell equations are

$$\begin{aligned} \mathbf{R}_{\Sigma_a}\vec{\Delta\phi}_1 + \mathbf{S}\vec{\Delta\phi}_1 + \kappa_{1/2}\vec{L}^T\vec{L}\vec{\Delta\phi}_1 + \frac{D(x_{1/2}^+)}{\Delta x_1}\vec{L}_s^T\vec{L}\vec{\Delta\phi}_1 + \frac{D(x_{1/2}^+)}{\Delta x_1}\vec{L}^T\vec{L}_s\vec{\Delta\phi}_1 \\ - \kappa_{3/2}\vec{R}^T\left(\vec{L}\vec{\Delta\phi}_2 - \vec{R}\vec{\Delta\phi}_1\right) + \frac{D(x_{3/2}^-)}{\Delta x_1}\vec{R}_s^T\left(\vec{L}\vec{\Delta\phi}_2 - \vec{R}\vec{\Delta\phi}_1\right) \\ - \vec{R}^T\left(\frac{D(x_{3/2}^-)}{\Delta x_1}\vec{R}_s\vec{\Delta\phi}_1 + \frac{D(x_{3/2}^+)}{\Delta x_2}\vec{L}_s\vec{\Delta\phi}_2\right) = \mathbf{R}_{\Sigma_s}\left(\vec{\phi}_1^{(\ell+1/2)} - \vec{\phi}_1^{(\ell)}\right). \end{aligned} \quad (4.67)$$

If the left edge satisfies a reflective condition, the leftmost cell equations are:

$$\begin{aligned} \mathbf{R}_{\Sigma_a}\vec{\Delta\phi}_1 + \mathbf{S}\vec{\Delta\phi}_1 - \kappa_{3/2}\vec{R}^T\left(\vec{L}\vec{\Delta\phi}_2 - \vec{R}\vec{\Delta\phi}_1\right) + \\ \frac{D(x_{3/2}^-)}{\Delta x_1}\vec{R}_s^T\left(\vec{L}\vec{\Delta\phi}_2 - \vec{R}\vec{\Delta\phi}_1\right) \\ - \vec{R}^T\left(\frac{D(x_{3/2}^-)}{\Delta x_1}\vec{R}_s\vec{\Delta\phi}_1 + \frac{D(x_{3/2}^+)}{\Delta x_2}\vec{L}_s\vec{\Delta\phi}_2\right) \\ = \mathbf{R}_{\Sigma_s}\left(\vec{\phi}_1^{(\ell+1/2)} - \vec{\phi}_1^{(\ell)}\right) + C_{MIP}\vec{L}^T, \end{aligned} \quad (4.68)$$

where  $C_{MIP}$  is the incident partial current,

$$C_{MIP} = 2\pi \sum_{\mu_d > 0} w_d \mu_d \psi_d^{(\ell+1/2)}. \quad (4.69)$$

#### 4.5 Numerical Results Verifying Implementation and Performance of S2SA and MIP DSA

We will consider two test problems to compare the effectiveness of S2SA and MIP DSA compared against source iteration, abbreviated as SI in the following results. To measure effectiveness, we will numerically compare the spectral radius,  $\rho$  of each scheme. The spectral radius of an iterative technique is the largest magnitude eigenvalue of the iterative operator. For an iteration scheme to be convergent, it must be true  $d < 1$ . After sufficiently many iterations, the following is true:

$$\|\delta\phi^{(\ell+1)}\| \leq \rho \|\delta\phi^{(\ell)}\|, \quad (4.70)$$

where  $\|\cdot\|$  is a valid norm and  $\delta\phi^{(\ell)}$  is the error as defined in Eq. (4.7). We will numerically test our methods by considering a trivial solution problem. That is to say we will solve a problem with vacuum boundary conditions on all edges and no volumetric solutions. However, rather than initialize with a zero solution, we set the values of  $\phi^{(0)}$  to be random numbers  $\in [0, 1]$ . We then use 150 iterations to estimate  $\rho$ , taking the last value to be the converged estimate of  $\rho$ . In Section 4.5.1 we present results for a scattering medium with a spatially constant cross section and in Section 4.5.2, we consider a scattering medium with spatially varying interaction cross section.

In the plots of Section 4.5.1 and Section 4.5.2 we will examine  $\rho$  as a function of scattering ratio,  $c$ ,  $S_N$  order, DFEM trial space degree, iterative technique, DFEM

interpolation point type, and cell optical thickness,  $\Sigma_t \Delta x$ .

#### 4.5.1 Spatially Constant Cross Section Scattering Problem

Our first test problem with is a 20 [cm] slab with spatially homogeneous cross section. We use at least 10 cells in all simulations in Figs. 4.1-4.8. For  $\Sigma_t \Delta x >= 2$ , we increase  $\Sigma_t$  to the necessary value to obtain the desired  $\Sigma_t \Delta x$ , while holding  $\Delta x = 2[\text{cm}]$  constant. For  $\Sigma_t \Delta x < 2$ , we hold  $\Sigma_t = 1[\text{cm}^{-1}]$  constant, while increasing the number of cells to achieve the desired  $\Sigma_t \Delta x$ .

The purpose of the following section is to

1. verify that results from our S2SA implementation for linear SL Gauss are qualitatively similar to those presented in [34],
2. determine whether S2SA is an effective iterative acceleration technique, for SL Gauss and SL Lobatto DFEM with  $P \in [1, 4]$ ,
3. verify that results from our MIP DSA implementation used in conjunction with SL Gauss, gives results similar to those presented in [35] for  $P \in [1, 4]$ , and
4. determine whether MIP DSA is an effective iterative acceleration technique for SL Lobatto DFEM.

In Fig. 4.1, we compare SI, S2SA, and MIP DSA for linear SL Gauss, with  $S_8$  angular quadrature, and  $c = 0.999$ . We see that as expected,  $\rho$  for source iteration  $\approx c$  [36]. Additionally, we see that MIP DSA achieves a  $\rho$  similar to that given in Figs. 6 and 7 of [35]. Likewise, our S2SA implementation estimates  $\rho \leq \approx 0.2$ , which agrees well with the Fourier analysis of [34] a true spectral radius of  $0.2127c$ . Since the analysis of [34] is for an infinite medium, we expect our estimate of  $\rho$  to be less.

In Fig. 4.2, we compare the  $\rho$  estimates of SI, S2SA, and MIP DSA for linear SL

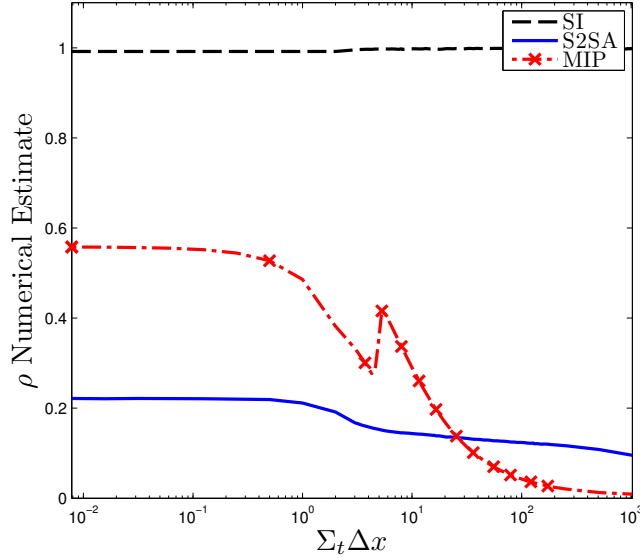


Figure 4.1: Estimates of  $\rho$  for different iterative techniques for  $S_8$ ,  $c = 0.999$ , linear SL Gauss.

Lobatto differencing. Results indicate that both S2SA and MIP DSA are compatible with SL Lobatto neutron transport. MIP DSA for linear SL Gauss exhibits the same peaking as observed with linear SL Gauss, though the peak is slightly smoother. We now examine the sensitivity of S2SA and MIP DSA to different values of  $c$ ,  $S_N$ , and DFEM trial space degree. From Fig. 4.1 and Fig. 4.2, we expect that the choice of DFEM interpolation point will change the estimate of  $\rho$ , but will not cause a method to become unstable.

#### 4.5.1.1 S2SA Spectral Radius Sensitivity

In Fig. 4.3 and Fig. 4.4, we compute  $\rho$  for S2SA as a function of  $S_N$  order for linear SL Gauss and linear SL Lobatto, respectively. In both Figs. 4.3-4.4, the higher the  $S_N$  order, the larger  $\rho$ , across all cell optical thicknesses, though there is little

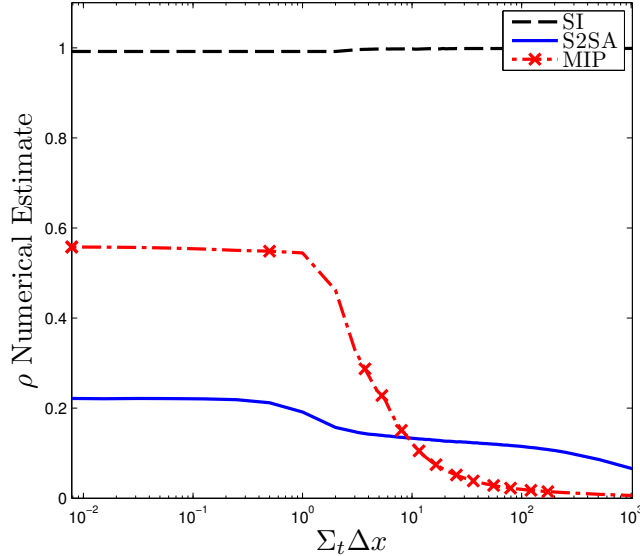


Figure 4.2: Estimates of  $\rho$  for different iterative techniques for  $S_8$ ,  $c = 0.999$ , linear SL Lobatto.

difference between  $S_8$  and  $S_{16}$ . Comparing our estimates of  $\rho$  of S2SA, as a function of  $c$ , for linear SL Gauss and SL Lobatto in Fig. 4.5 and Fig. 4.6, respectively, we conclude that the closer  $c$  is to unity, the larger,  $\rho$ , but there is negligible increase from  $c = 0.999$  to  $c = 0.9999$ , except in very optically thick cells, but  $\rho$  is not largest with the S2SA scheme for large values of  $\Sigma_t \Delta x$ . Finally, in Fig. 4.7 and Fig. 4.8, we compare  $\rho$  for  $S_8$ ,  $c = 0.999$  S2SA with SL Gauss and SL Lobatto differencing, respectively, as a function of DFEM trial space degree.  $\rho$  remains nearer the optically thin value for larger values of  $\Sigma_t \Delta x$  the higher the DFEM trial space degree, but S2SA remains stable for all  $P$ . Regardless of  $c$ ,  $P$ ,  $\Sigma_t \Delta x$ , and  $S_N$  order, we numerically verified that the S2SA matrix that must be inverted was neither symmetric or positive definite, requiring direct (Gaussian) elimination to invert the matrix.

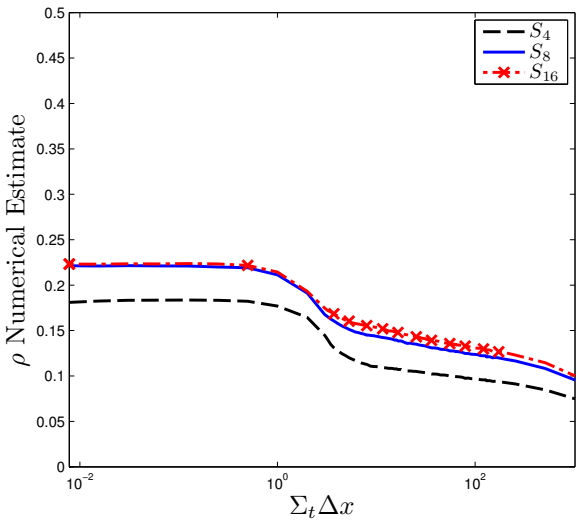


Figure 4.3: Estimate of  $\rho$  for S2SA as a function of  $S_N$  order for  $c = 0.999$  for linear SL Gauss.

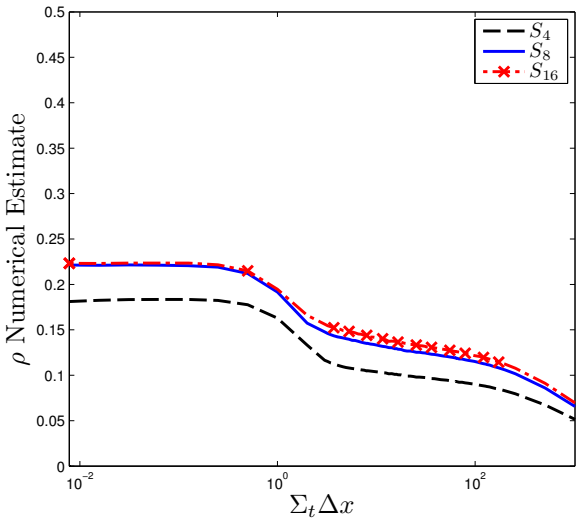


Figure 4.4: Estimate of  $\rho$  for S2SA as a function of  $S_N$  order for  $c = 0.999$  for linear SL Lobatto.

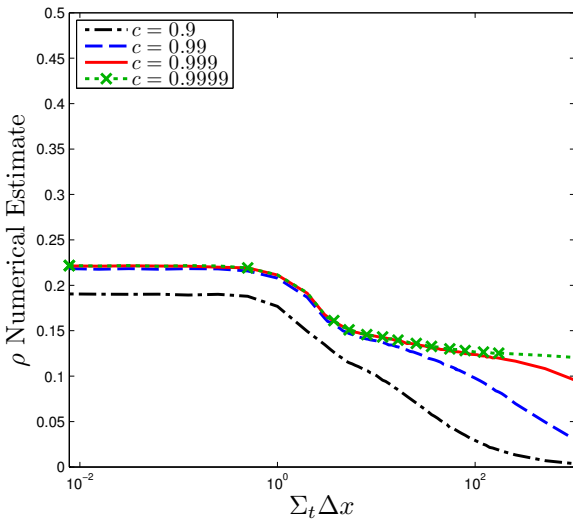


Figure 4.5: Estimates of  $\rho$  for S2SA as a function of  $c$  for  $S_8$  linear SL Gauss.

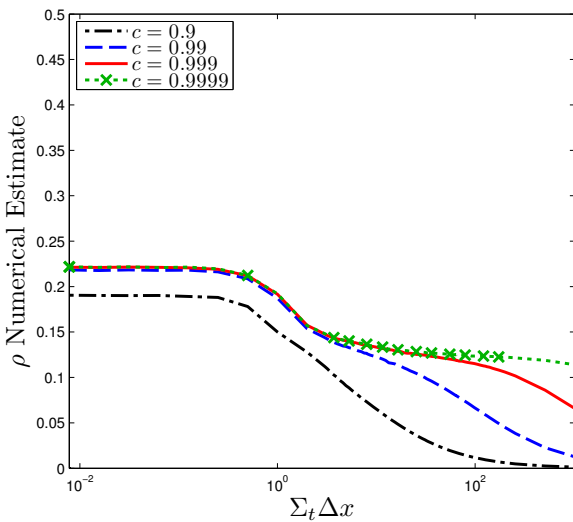


Figure 4.6: Estimates of  $\rho$  for S2SA as a function of  $c$  for  $S_8$  linear SL Lobatto.

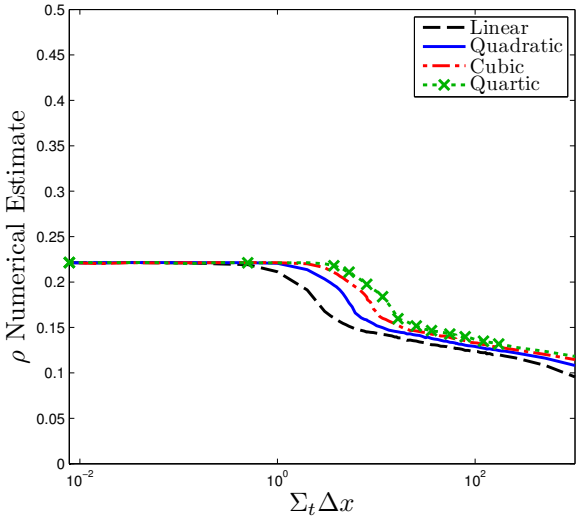


Figure 4.7: Estimates of  $\rho$  for S2SA with  $S_8$ ,  $c = 0.999$ , SL Gauss as a function of trial space degree.

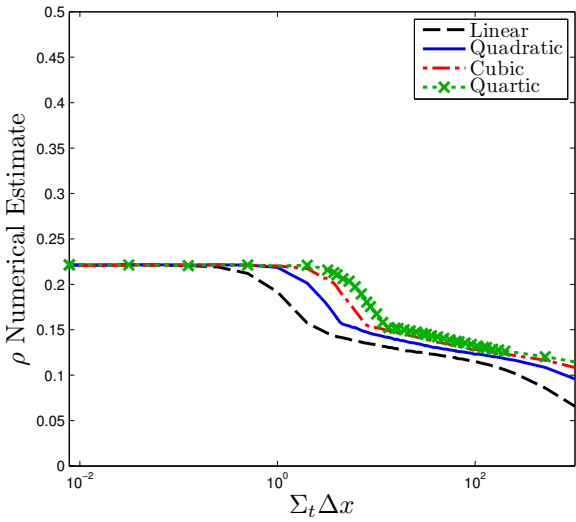


Figure 4.8: Estimates of  $\rho$  for S2SA with  $S_8$ ,  $c = 0.999$ , SL Lobatto as a function of trial space degree.

#### 4.5.1.2 MIP DSA Spectral Radius Sensitivity

In Fig. 4.9 and Fig. 4.10 we compare  $\rho$  for MIP DSA as a function of  $S_N$  order, for linear SL Gauss and linear SL Lobatto, respectively, with  $c = 0.999$ . As with S2SA, the higher  $S_N$  order, the larger  $\rho$  is for the MIP DSA scheme. However, the value of  $\rho$  obtained with  $S_8$  is only slightly smaller than the  $\rho$  of  $S_{16}$ , and as such we prefer the reduced computational work of  $S_8$  simulations to  $S_{16}$  in examining iterative effectiveness.

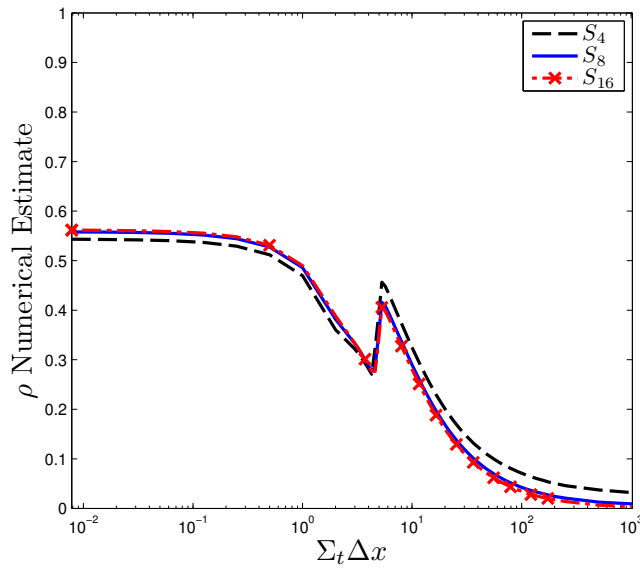


Figure 4.9: Estimate of  $\rho$  for MIP DSA as a function of  $S_N$  order for  $c = 0.999$  linear SL Gauss.

Figure 4.11 and Fig. 4.12 examine the effect of  $c$  on  $\rho$  for MIP DSA with the linear SL Gauss and SL Lobatto schemes. The general trend is that as  $c \rightarrow 1$ , the

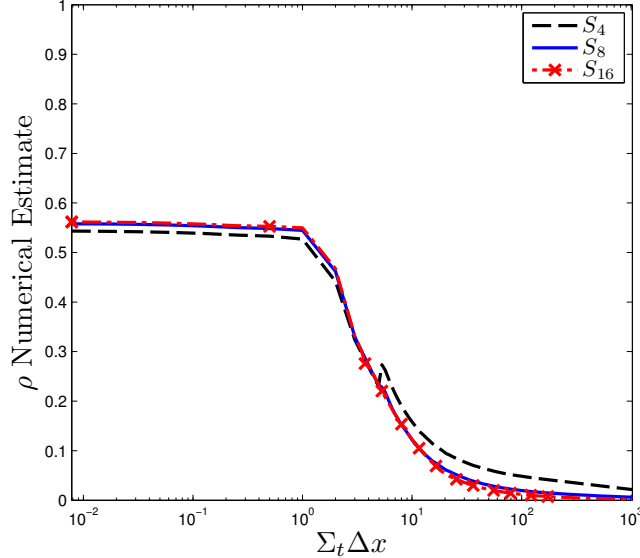


Figure 4.10: Estimate of  $\rho$  for MIP DSA as a function of  $S_N$  order for  $c = 0.999$  linear SL Lobatto.

larger the estimate of  $\rho$ , but both SL Gauss and SL Lobatto with MIP DSA remain iteratively stable.

It is as this point that we remember that the MIP DSA scheme uses a constant,  $\kappa_{IP}$ , which depends on a chosen constant. In all of the results that have presented to this point, we have assumed that  $Z_{MIP}$  of Eq. (4.53),  $Z_{MIP} = 2$ . Just as Wang did in his dissertation [42], we now consider  $Z_{MIP} = 4$ . Estimates of  $\rho$  for MIP DSA as a function of  $c$  for SL Gauss and SL Lobatto, with  $Z_{MIP} = 4$  are given in Fig. 4.13 and Fig. 4.14, respectively.

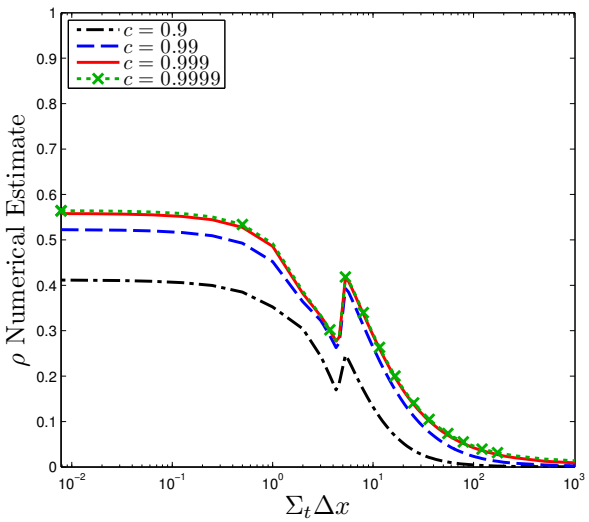


Figure 4.11: Estimate of  $\rho$  for MIP DSA as a function of  $c$  for  $S_8$  linear SL Gauss.

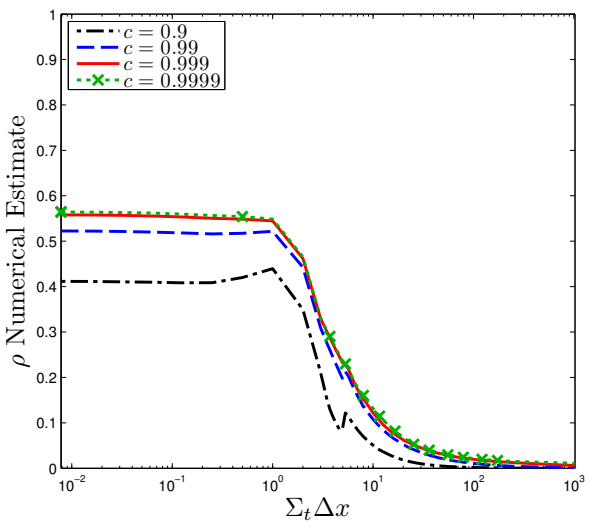


Figure 4.12: Estimate of  $\rho$  for MIP DSA as a function of  $c$  for  $S_8$  linear SL Lobatto.

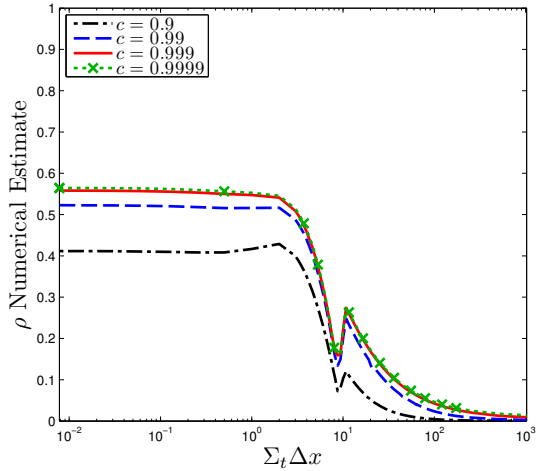


Figure 4.13:  $\rho$  for MIP DSA as a function of  $c$  for  $S_8$  linear SL Gauss, with  $Z_{MIP} = 4$ .

There are small differences between Figs. 4.11-4.12 and Figs. 4.13-4.14 . With  $Z_{MIP} = 4$  in Fig. 4.13 SL Gauss maintains a slightly higher value of  $\rho$  at small optical thicknesses than when  $Z_{MIP} = 2$ , and the the transitional drop from intermediate to larger rho at small optical thicknesses to smaller  $\rho$  for large cell optical thicknesses is more pronounced. With  $Z_{MIP} = 4$ , SL Lobatto displays a modest, smooth increase in  $\rho$  over a range of intermediate  $\Sigma_t \Delta x$  and exhibits a sharper drop in  $\rho$  as well. Currently, the choice of  $Z_{MIP} = 2$  or  $Z_{MIP} = 4$  seems to have negligible effect on  $\rho$ , but we will retain adjustments to  $Z_{MIP}$  as a tool should any combination of spatial discretization and MIP DSA appear unstable.

Having determined that  $c = 0.999$  and  $S_8$  will yield nearly maximal  $\rho$ , we calculate  $\rho$  as a function of  $P$  for MIP DSA acceleration of SL Gauss and SL Lobatto transport spatial discretizations in Fig. 4.15 and Fig. 4.16, respectively, using  $Z_{MIP} = 2$ .

As  $P$  increases, both SL Gauss and SL Lobatto accelerated with MIP DSA remain

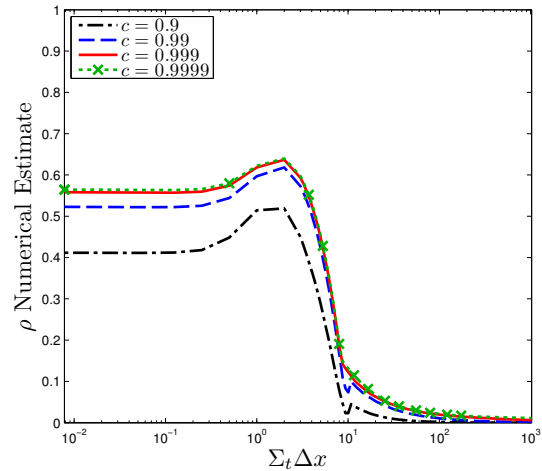


Figure 4.14:  $\rho$  for MIP DSA as a function of  $c$  for  $S_8$  linear SL Lobatto, with  $Z_{MIP} = 4$ .

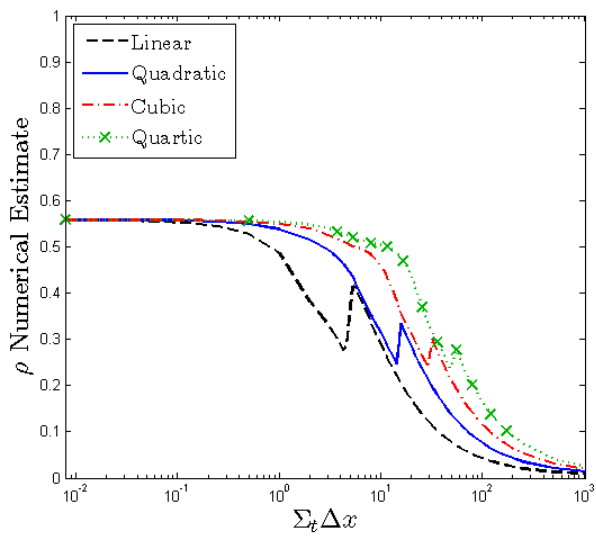


Figure 4.15: Estimate of  $\rho$  for MIP DSA as a function of  $P$  for  $S_8$ ,  $c = 0.999$ , SL Gauss with  $Z_{MIP} = 2$ .

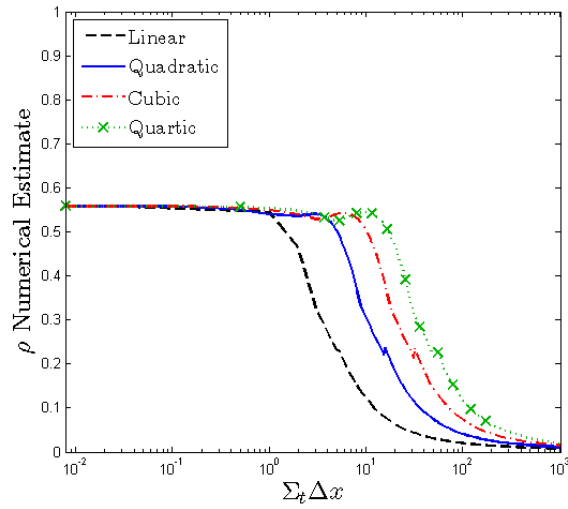


Figure 4.16: Estimate of  $\rho$  for MIP DSA as a function of  $P$  for  $S_8$ ,  $c = 0.999$ , SL Lobatto with  $Z_{MIP} = 2$ .

iteratively effecting. Similarly, if we consider  $Z_{MIP} = 4$ , both SL Gauss and SL Lobatto spatial differencing schemes remain stable.

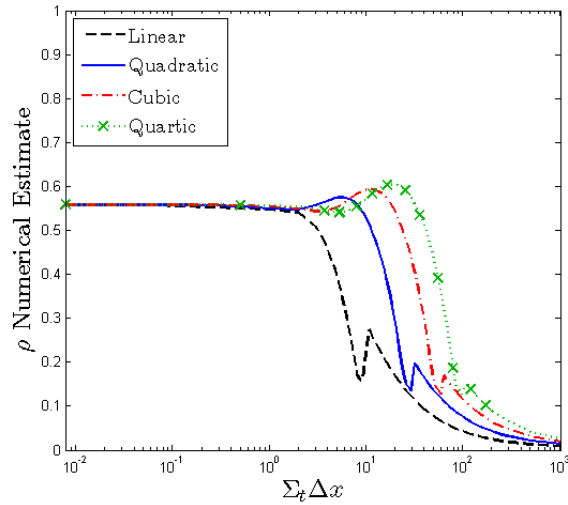


Figure 4.17:  $\rho$  for MIP DSA as a function of  $P$  for  $S_8$ ,  $c = 0.999$ , SL Gauss with  $Z_{MIP} = 4$ .

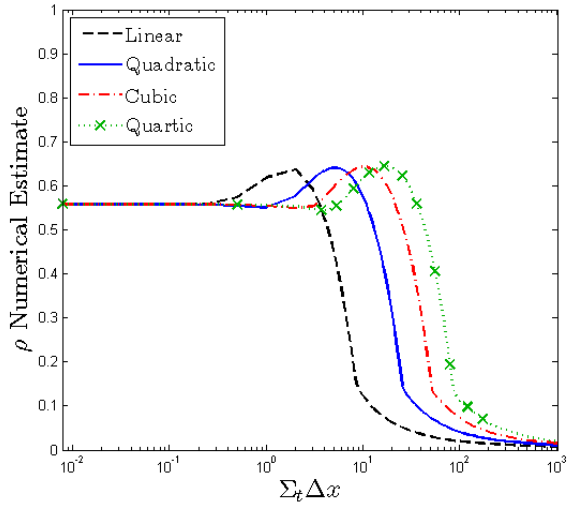


Figure 4.18: Estimates of  $\rho$  for MIP DSA as a function of  $P$  for  $S_8$ ,  $c = 0.999$ , SL Lobatto with  $Z_{MIP} = 4$ .

#### 4.5.2 Spatially Varying Cross Section Scattering Problem

To test the effectiveness of MIP DSA and S2SA for a problem with a spatially varying cross section, we again consider a slab  $x \in [0, 20[cm]]$ . We impose

$$\Sigma_t(x) = \Sigma_{t,0} \exp \left[ \frac{|(10-x)|}{2} \right]. \quad (4.71)$$

We hold  $c$  constant in space. We will estimate  $\rho$  as a function of  $\overline{\Sigma_t \Delta x}$ , the average optical thickness of each mesh cell. For values of  $\overline{\Sigma_t \Delta x} > 2$ , we will use 10 mesh cells, and adjust  $\Sigma_{t,0}$  to achieve the desired optical thickness. For values of  $\overline{\Sigma_t \Delta x} < 2$ , we will hold  $\Sigma_{t,0}$  constant, and increase the number of mesh cells. We wish to maintain a total slab optical thickness of at least 20 mean free paths. Since,

$$\text{Total Mean Free Path} = 2 \int_0^{10 \text{ cm}} \Sigma_{t,0} \exp \left[ \frac{10-x}{2} \right] dx \quad (4.72a)$$

$$\text{Total Mean Free Path} = 4 \Sigma_{t,0} (\exp[5] - 1), \quad (4.72b)$$

the minimum value of  $\Sigma_{t,0}$  is:

$$\Sigma_{t,0} = \frac{5}{\exp[5] - 1}. \quad (4.72c)$$

For values of  $\overline{\Sigma_t \Delta x} > 2$ ,

$$10\overline{\Sigma_t \Delta x} = 4\Sigma_{t,0}(\exp[5] - 1) \quad (4.72d)$$

$$\Sigma_{t,0} = \frac{5\overline{\Sigma_t \Delta x}}{2(\exp[5] - 1)}. \quad (4.72e)$$

#### 4.5.2.1 S2SA

In Fig. 4.19 and Fig. 4.20, we plot the estimate of  $\rho$  for the variable cross section problem, with  $c = 0.999$  and  $S_8$  angular quadrature for S2SA using SL Gauss and SL Lobatto schemes, respectively, as a function of trial space degree. S2SA remains

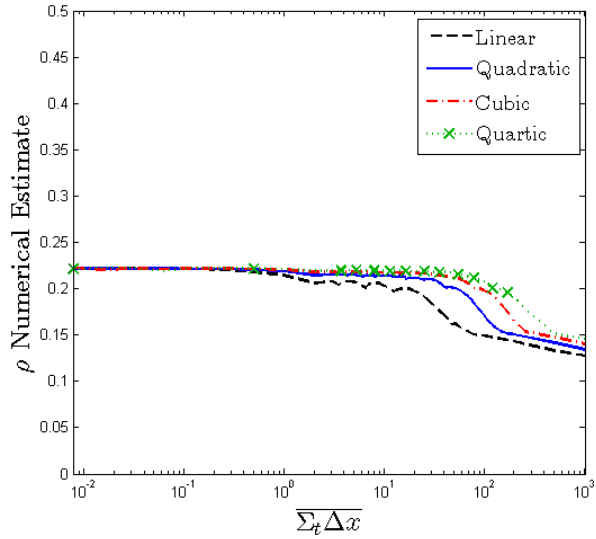


Figure 4.19: Estimate of  $\rho$  for S2SA as a function of  $\overline{\Sigma_t \Delta x}$  and  $P$ , with SLXS Gauss.

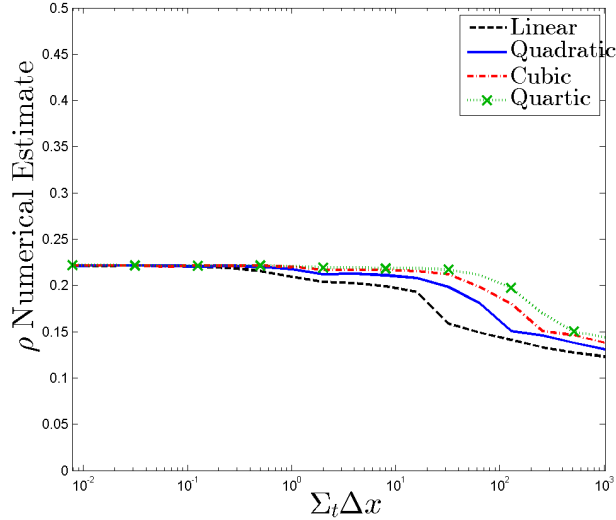


Figure 4.20: Estimate of  $\rho$  for S2SA as a function of  $\Sigma_t \Delta x$  and  $P$ , with SLXS Lobatto.

unconditionally stable for the case of a spatially varying cross section, for all  $P$  considered, for both SLXS Gauss and SLXS Lobatto schemes.

#### 4.5.2.2 MIP DSA

We now examine  $\rho$  for the MIP DSA scheme as a function of  $P$  for the variable cross section problem, with  $c = 0.999$ ,  $S_8$  angular quadrature, and  $Z_{MIP} = 4$ . Results for SLXS Gauss are given in Fig. 4.21 and  $\rho$  for MIP DSA with SLXS Lobatto scheme is given in Fig. 4.22. Since  $\rho < 1$  in Figs. 4.21-4.22, we conclude that MIP DSA remains a stable iterative scheme for SLXS Gauss and SLXS Lobatto, for all  $P$  considered when  $Z_{MIP} = 2$  for problems with spatially varying cross sections.

## 4.6 Conclusions

Both S2SA and MIP DSA are stable iterative acceleration techniques for problems with spatially constant and spatially varying cross section. We have verified our implementations of S2SA and MIP DSA by comparing to published, spatially

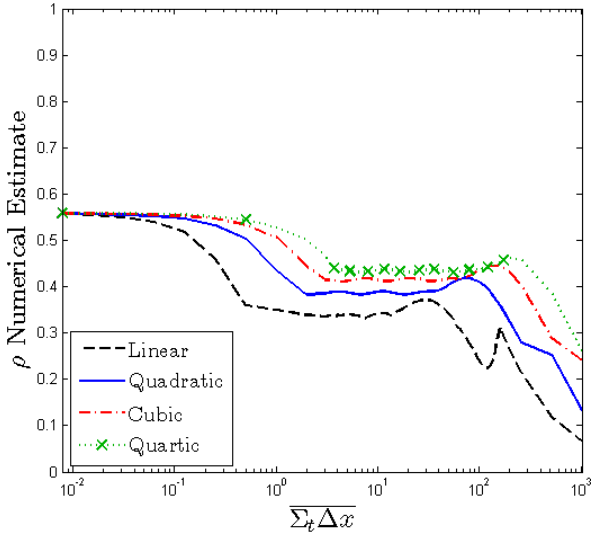


Figure 4.21: Estimate of  $\rho$  for MIP DSA with SLXS Gauss as a function of  $\overline{\Sigma_t \Delta x}$  and  $P$ .

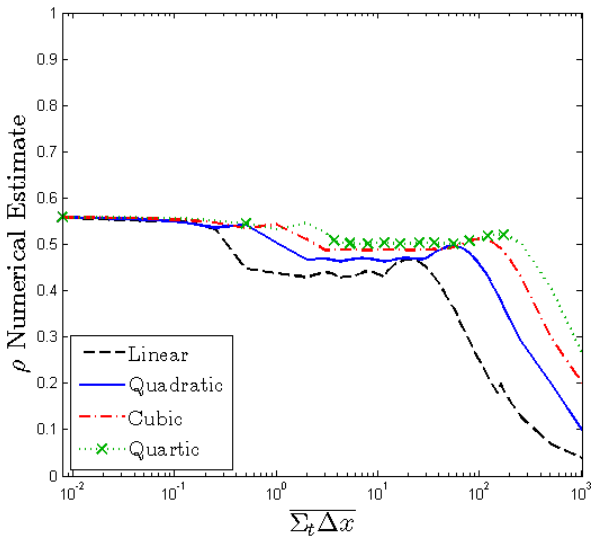


Figure 4.22: Estimate of  $\rho$  for MIP DSA with SLXS Lobatto as a function of  $\overline{\Sigma_t \Delta x}$  and  $P$ .

constant cross section results. While the S2SA technique is more effective than MIP DSA (smaller  $\rho$ ), the S2SA matrix that must be inverted is not symmetric or positive definite. Thus, S2SA requires direct matrix inversion which in general is not feasible for large systems of equations. Conversely, though MIP DSA is not as effective as S2SA, the MIP DSA matrix is SPD, thus it can be inverted much more efficiently (faster) [41] than the S2SA matrix can be inverted. As such, to demonstrate that self-lumping schemes that account for within cell spatial variation of quadrature can be used for more realistic problems, we first employ S2SA to accelerate neutron transport within a model fuel depletion problem in Chapter 5. However, since S2SA is really only practical for small, one dimensional problems, we will apply a variant of MIP DSA to accelerate the iterative process required for thermal radiative transfer problems in Section 6.

## 5. FUEL DEPLETION PROBLEM

We now consider a fuel depletion problem to illustrate that self-lumping DFEM schemes remain accurate for more complex physics than simply a purely absorbing medium. The depletion method we use [time stepping scheme, time step size, etc.] is chosen for its simplicity, not for its fidelity relative to state-of-the art depletion methodologies. Our goal is to assess the accuracy of spatial discretization methods for problems with spatially varying cross sections, not to propose a new depletion method. However, we stress that self-lumping methods can be implemented with any time depletion method or time stepping scheme since implementation of self-lumping only requires changes pertaining to the spatial discretization.

### 5.1 Problem Physical Description

We will consider a 1-D slab fuel depletion problem. The dimensions and layout of the fuel and moderator layers lattice is shown in Fig. 5.1.

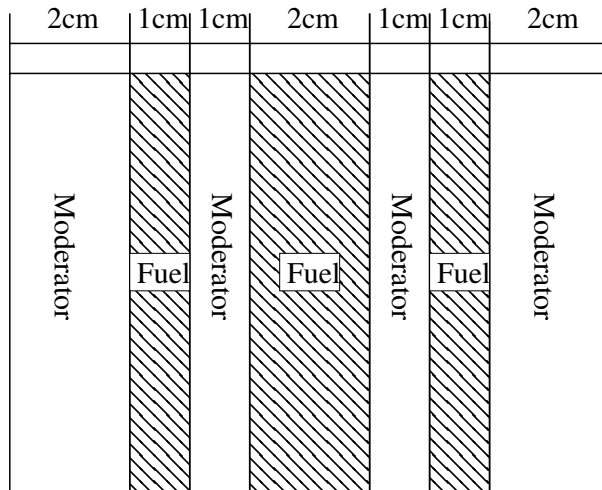


Figure 5.1: Depletion problem fuel/moderator lattice.

Initially, each fuel region is a homogeneous mixture containing only fissile  $^{235}U$  and fertile  $^{238}U$  nuclei, with compositions given in Table 5.1. As fuel depletion

Table 5.1: Fuel atom density data.

Fuel Density [ $g/cm^3$ ]	10.97
Atom Fraction $^{235}U$	0.05
Atom Fraction $^{238}U$	0.95
Fuel Molecular Weight [ $amu$ ]	270.03

progresses, the isotopic composition of fuel changes. The moderator is light water and its composition, given in Table 5.2, does not change with irradiation. We track

Table 5.2: Water atom density data.

Water Density [ $g/cm^3$ ]	1
Atom Fraction $^1H$	$\frac{2}{3}$
Atom Fraction $^{16}O$	$\frac{1}{3}$
Water Molecular Weight [ $amu$ ]	18.02

five nuclide types in the fuel during the fuel depletion problem: fissile, fertile, parasitic absorber fission product, scattering fission product, and inert, whose spatial nuclide densities, [ $atom/cm^3$ ], are respectively denoted as  $N_{FS}$ ,  $N_{FT}$ ,  $N_{FP-A}$ ,  $N_{FP-S}$ , and  $N_I$ .

We use a two-energy-group approximation with the standard numbering convention—the lower the group number, the faster the neutron. All neutrons are born fast, there is no thermal upscattering, and we assume all scattering and fission is isotropic in angle. We also assume that if neutron absorption leads to isotopic transmutation,

the transmutation occurs at the time of absorption, there are no radioactive decay chains. All possible transmutation paths are shown in Fig. 5.2.

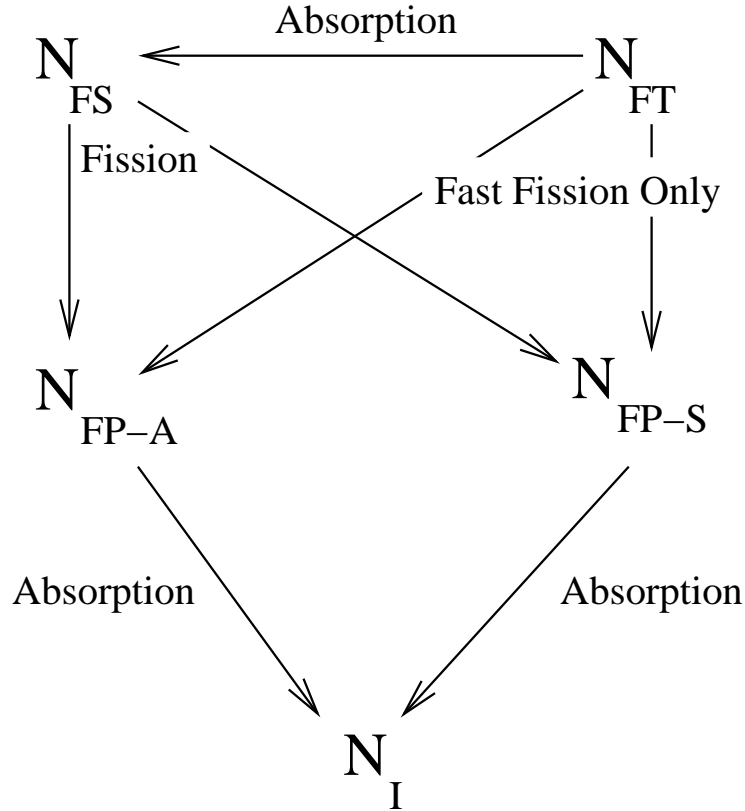


Figure 5.2: Depletion problem possible transmutation paths and mechanisms.

Under these assumptions, and given the transmutation paths given in Fig. 5.2, the fully analytic, nonlinear depletion equations are:

$$\mu \frac{\partial \psi_1}{\partial x} + \Sigma_{t,1} \psi_1 = \frac{\Sigma_{s,1 \rightarrow 1}}{4\pi} \phi_1 + \frac{1}{k} \left( \frac{\nu \Sigma_{f,1}}{4\pi} \phi_1 + \frac{\nu \Sigma_{f,2}}{4\pi} \phi_2 \right) \quad (5.1a)$$

$$\mu \frac{\partial \psi_2}{\partial x} + \Sigma_{t,2} \psi_2 = \frac{\Sigma_{s,2 \rightarrow 2}}{4\pi} \phi_2 + \frac{\Sigma_{s,1 \rightarrow 2}}{4\pi} \phi_1 \quad (5.1b)$$

$$\begin{aligned} \frac{\partial N_{FS}}{\partial t} = & -N_{FS} [(1 - \gamma_{FS,1})\sigma_{a,FS,1}\phi_1 + (1 - \gamma_{FS,2})\sigma_{a,FS,2}\phi_2] \\ & + N_{FT}[\gamma_{FT,1}\sigma_{a,FT,1}\phi_1 + \gamma_{FT,2}\sigma_{a,FT,2}\phi_2] \quad (5.1c) \end{aligned}$$

$$\frac{\partial N_{FT}}{\partial t} = -N_{FT}[\sigma_{a,FT,1}\phi_1 + \sigma_{a,FT,2}\phi_2] \quad (5.1d)$$

$$\begin{aligned} \frac{\partial N_{FP-S}}{\partial t} = & N_{FS} [(1 - p_{FS,1})y_{FS,1}\sigma_{a,FS,1}\phi_1 + (1 - p_{FS,2})y_{FS,2}\sigma_{a,FS,2}\phi_2] \\ & + N_{FT} [(1 - p_{FT,1})y_{FT}\sigma_{a,FT,1}\phi_1] - N_{FS} [\sigma_{a,FP-S,1}\phi_1 + \sigma_{a,FP-S,2}\phi_2] \quad (5.1e) \end{aligned}$$

$$\begin{aligned} \frac{\partial N_{FP-A}}{\partial t} = & N_{FS} [p_{FS,1}y_{FS,1}\sigma_{a,FS,1}\phi_1 + p_{FS,2}y_{FS,2}\sigma_{a,FS,2}\phi_2] \\ & + N_{FT}p_{FT,1}y_{FT,1}\sigma_{a,FT,1}\phi_1 \\ & - N_{FP-A} [(1 - \xi_{FP-A,1})\sigma_{a,FP-A,1}\phi_1 + (1 - \xi_{FP-A,2})\sigma_{a,FP-A,2}\phi_2] \quad (5.1f) \end{aligned}$$

$$\begin{aligned} \frac{\partial N_I}{\partial t} = & N_{FP-A} [\xi_{FP-A,1}\sigma_{a,FP-A,1}\phi_1 + \xi_{FP-A,2}\sigma_{a,FP-A,2}\phi_2] \\ & + N_{FP-S} [\sigma_{a,FP-S,1}\phi_1 + \sigma_{a,FP-S,2}\phi_2] . \quad (5.1g) \end{aligned}$$

In Eq. (5.1a) and Eq. (5.1b)  $\phi_g$  is the group  $g$  scalar flux [ $n/cm^2/sec$ ],  $\Sigma_{t,g}$  is the total macroscopic cross section [ $cm^{-1}$ ] of group  $g$ ,  $\Sigma_{s,g \rightarrow g'}$  [ $cm^{-1}$ ] is the macroscopic cross section for neutrons scattering from group  $g$  to group  $g'$ ,  $k$  is the system multiplication factor, and  $\nu\Sigma_{f,g}$  is the average number of neutrons released per fission ( $\nu$ ) for a fission induced by a neutron in group  $g$ , multiplied by the group  $g$  macroscopic fission cross section. The nuclide production destruction equations, Eqs. (5.1c) - (5.1g), use the following notation:  $\gamma_{m,g}$  is the probability that a neutron absorption

in nuclide  $m$  results in the production of a fissile isotope,  $y_{m,g}$  is the ratio of nuclide  $m$ 's fission cross section to total cross section for group  $g$ ,  $p_{m,g}$  is the probability that the fission of nuclide  $m$  yields a parasitic absorber fission produce, and  $\xi_g$  is the probability that when a parasitic absorber fission production absorbs a neutron, another parasitic absorber fission product is produced. Though not explicitly noted in Eqs. (5.1), all scalar fluxes  $\phi_g$ , macroscopic cross sections  $\Sigma_g$ , and nuclide densities  $N$ , are functions of position. We use Gauss-Legendre  $S_2$  angular quadrature, with weights that sum to 2, to approximate the scalar fluxes.

Macroscopic cross sections are generated from nuclide density and microscopic cross section data. As an example,  $\Sigma_{t,g}$  is calculated as shown in Eq. (5.2):

$$\begin{aligned} \Sigma_{t,g,i} = & N_{FS}\sigma_{t,FS,g} + N_{FT}\sigma_{t,FT,g} + N_{FP-A}\sigma_{t,FP-A,g} \\ & + N_{FP-S}\sigma_{t,FP-S,g} + N_I\sigma_{t,I,g}. \end{aligned} \quad (5.2)$$

Macroscopic fission cross section and average neutrons per fission products are found in a similar fashion, but we can limit our consideration to the fissile and fertile nuclide densities as shown in Eq. (5.3),

$$\nu\Sigma_{f,g,i} = N_{FS}\nu_{FS,g}\sigma_{f,FS,g} + N_{FT}\nu_{FT,g}\sigma_{f,FT,g}. \quad (5.3)$$

### 5.1.1 Microscopic Cross Section and Yield Data

We complete the specification of the depletion problem by giving the physical data used to solve the problem. Microscopic cross section data for the water is given in Table 5.3. Absorption and scattering cross sections for the fertile and fissile nuclides are given in Table 5.4, and fission cross sections and average neutrons per fission are given in Table 5.5. Radiative capture fractions and probability of an absorbed

neutron inducing fission are given in Table 5.6. Cross-section data for the fission products and inert nuclides are given in Table 5.7. Fission product yields and the parasitic absorber fission product regeneration fraction,  $\xi$ , are given in Table 5.8.

Table 5.3: Water microscopic cross section, in barns [ $10^{-24} \text{ cm}^2$ ]. Moderator is composed only of  $H_2O$ .

Nuclide	$\sigma_{a,1}$	$\sigma_{a,2}$	$\sigma_{s,1 \rightarrow 1}$	$\sigma_{s,2 \rightarrow 2}$	$\sigma_{s,1 \rightarrow 2}$
$^1H$	0	0.332	0	20.47	3.926
$^{16}O$	0	0	2.739	3.780	0

Table 5.4: Fuel microscopic cross sections, in barns [ $10^{-24} \text{ cm}^2$ ].

Nuclide	$\sigma_{a,1}$	$\sigma_{a,2}$	$\sigma_{s,1 \rightarrow 1}$	$\sigma_{s,2 \rightarrow 2}$	$\sigma_{s,1 \rightarrow 2}$
$^{235}_{92}U$	1.325	683.21	4.566	15.04	0
$^{238}_{92}U$	0.374	2.717	4.804	9.36	0

Table 5.5: Average neutron yield per fission, and fission microscopic cross section [ $10^{-24} \text{ cm}^2$ ].

Nuclide	$\nu_1$	$\nu_2$	$\sigma_{f,1}$	$\sigma_{f,2}$
$^{235}_{92}U$	2.6	2.4	1.235	584.4
$^{238}_{92}U$	2.8	N/A	0.308	0

Table 5.6: Radiative capture fraction, and fission probability for fissile and fertile nuclides.

Nuclide	$\gamma_1$	$\gamma_2$	$y_1$	$y_2$
$^{235}_{92}\text{U}$	$\frac{0.09}{1.325} = 0.068$	$\frac{98.81}{683.21} = 0.145$	$\frac{1.235}{1.325} = 0.932$	$\frac{584.4}{683.21} = 0.855$
$^{238}_{92}\text{U}$	$\frac{0.066}{0.374} = 0.177$	1	$\frac{0.308}{0.374} = 0.823$	0

Table 5.7: Parasitic absorber fission product, scattering fission product, and inert nuclide microscopic cross section data in barns [ $10^{-24} \text{ cm}^2$ ].

Nuclide	$\sigma_{a,1}$	$\sigma_{a,2}$	$\sigma_{s,1}$	$\sigma_{s,2}$	$\sigma_{s,1 \rightarrow 2}$
FP-A	15	1000	0.5	5	0
FP-S	0.5	5	15	100	0
Inert	1	5	1	5	0

Table 5.8: Fission product branch ratios and parasitic absorber fission product regeneration fraction.

$p_{FS,1}$	0.3
$p_{FS,2}$	0.3
$p_{FT,1}$	0.3
$p_{FT,2}$	0.3
$\xi_{FP-A,1}$	0.3
$\xi_{FP-A,2}$	0.5

### 5.1.2 Reactor Power Levels and Normalization

Vacuum boundary conditions are imposed on both sides of the slab. We normalize reactor scalar flux values so that the reactor produces a constant fission power level of 2000 [W] for the duration of the burn-up cycle. The burn-up cycle length consists of 600 full-power days and we use a time step of 10 days to update the scalar fluxes. A typical beginning-of-cycle flux profile is shown in Fig. 5.3 and an end-of-cycle scalar flux profile is shown in Fig. 5.4.

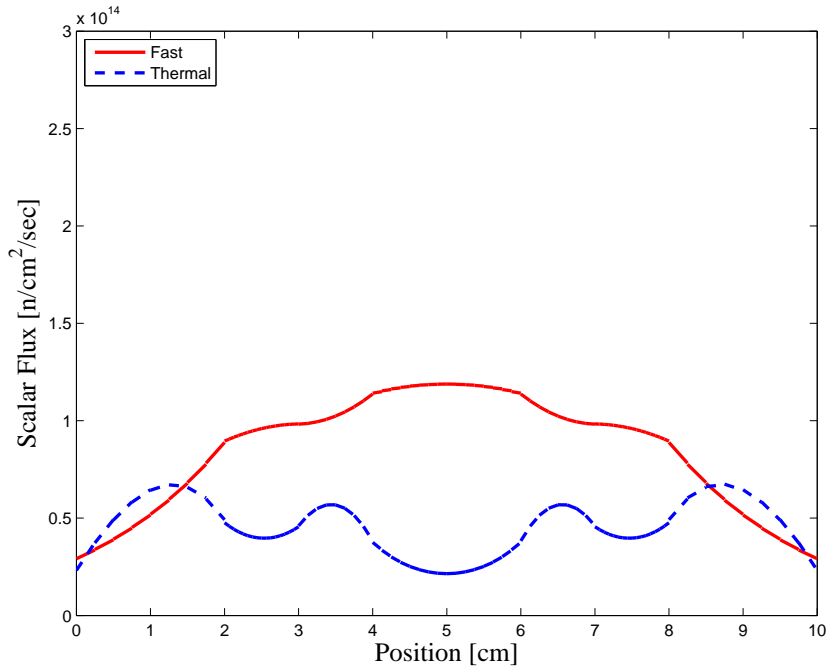


Figure 5.3: Example normalized scalar flux profiles at beginning of fuel burn-up cycle.

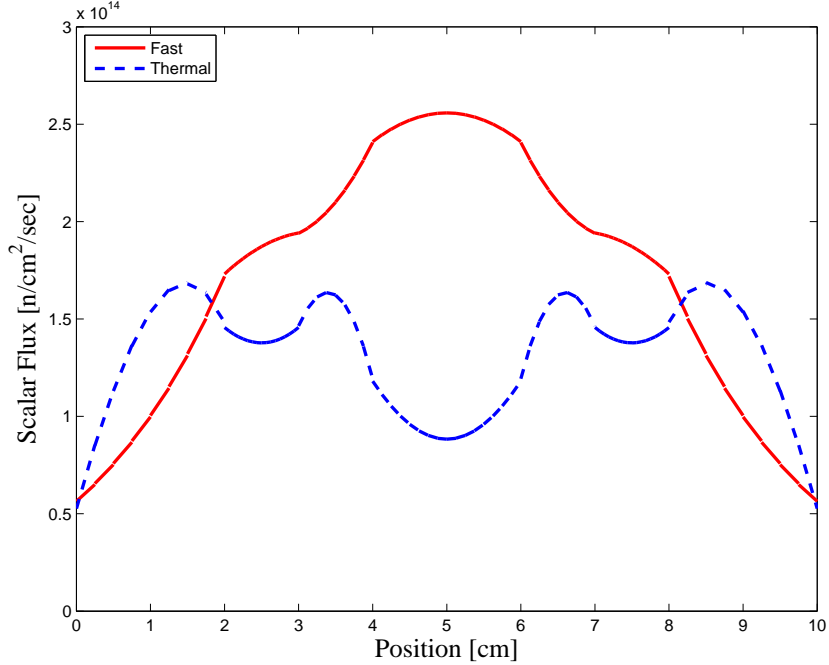


Figure 5.4: Example normalized scalar flux profiles at end of fuel burn-up cycle.

## 5.2 Spatial Discretization

We solve Eqs. (5.1) using a semi-static approach [33] assuming the flux distribution at the start of the time step remains constant throughout the time step. Nuclide densities are advanced in time using explicit Euler time differencing, then a corresponding radiation solution is found. We will consider three DFEM schemes to spatially discretize Eqs. (5.1).

1. AD DFEM: expands the angular flux in a  $P$  degree polynomial trial space using equally-spaced interpolation points, uses exact spatial integration, assumes cell-wise constant cross sections for solving the radiation equations, and tracks only cell average nuclide densities.
2. SL Collapse: expands both the angular flux and nuclide densities in a  $P$  degree

polynomial trial space, uses self-lumping quadrature to approximate integrals, and assumes cell-wise constant cross sections for solving the radiation equations. Lobatto quadrature is used as the DFEM interpolation points for odd degree trial spaces and Gauss quadrature as the DFEM interpolation points for even degree trial spaces.

3. SL Full: expands both the angular flux and nuclide densities in a  $P$  degree polynomial trial space, uses self-lumping quadrature to approximate integrals, and explicitly accounts for the variation of macroscopic cross section within each spatial cell. Lobatto quadrature is used as the DFEM interpolation points for odd degree trial spaces and Gauss quadrature as the DFEM interpolation points for even degree trial spaces.

### 5.2.1 Radiation Solution

Using the nomenclature developed in Section 2 and Section 3, the spatially discretized radiation equations are:

$$\begin{aligned} \mu_d \mathbf{G} \vec{\psi}_{d,1} - \mu_d \psi_{in,d,1} \vec{f} + \mathbf{R}_{\Sigma_{t,1}} \vec{\psi}_{d,1} &= \frac{1}{4\pi} \mathbf{R}_{\Sigma_{s,1 \rightarrow 1}} \vec{\phi}_1 \\ &\quad + \frac{1}{k_\tau} \frac{1}{4\pi} \left( \mathbf{R}_{\nu \Sigma_{f,1}} \vec{\phi}_1 + \mathbf{R}_{\nu \Sigma_{f,2}} \vec{\phi}_2 \right), \end{aligned} \quad (5.4)$$

and

$$\mu_d \mathbf{G} \vec{\psi}_{d,2} - \mu_d \psi_{in,d,2} \vec{f} + \mathbf{R}_{\Sigma_{t,2}} \vec{\psi}_{d,2} = \frac{1}{4\pi} \left( \mathbf{R}_{\Sigma_{s,2 \rightarrow 2}} \vec{\phi}_2 + \mathbf{R}_{\Sigma_{s,1 \rightarrow 2}} \vec{\phi}_1 \right). \quad (5.5)$$

In Eq. (5.4) and Eq. (5.5)  $k_\tau$  is the multiplication factor at time index  $\tau$  and  $\mathbf{R}_{\Sigma_{s,1 \rightarrow 1}}$ ,  $\mathbf{R}_{\Sigma_{s,1 \rightarrow 2}}$ ,  $\mathbf{R}_{\Sigma_{s,2 \rightarrow 2}}$ ,  $\mathbf{R}_{\nu \Sigma_{f,1}}$ , and  $\mathbf{R}_{\nu \Sigma_{f,2}}$  are defined analogously to  $\mathbf{R}_{\Sigma_t}$ , as in Eq. (3.3), replacing  $\Sigma_t(s)$  with  $\Sigma_{s,1 \rightarrow 1}(s)$ ,  $\Sigma_{s,1 \rightarrow 2}(s)$ ,  $\Sigma_{s,2 \rightarrow 2}(s)$ ,  $\Sigma_{f,1}(s)$ , and  $\Sigma_{f,2}(s)$ , respectively.

We solve Eq. (5.4) and Eq. (5.5) following the standard power iteration procedure, described for DFEM neutron transport in [43]. Convergence is checked after each power iteration. Using  $\ell$  as the iteration index, convergence after the  $\ell + 1$  iterate is said to occur when:

$$\delta_k = \left| \frac{k^{(\ell+1)} - k^{(\ell)}}{k^{(\ell)}} \right| < \epsilon_k, \quad (5.6)$$

and

$$\delta_\phi = \max_{g=1,2} \max_{i=1,\dots,N_{cell}} \max_{j=1,\dots,N_P} \left| \frac{\phi_{g,i,j}^{(\ell+1)} - \phi_{g,i,j}^{(\ell)}}{\phi_{g,i,j}^{(\ell)}} \right| < \epsilon_\phi. \quad (5.7)$$

In our computational results we use  $\epsilon_k = 10^{-12}$  and  $\epsilon_\phi = 10^{-10}$ . For each power iteration, the within group components of Eq. (5.4) and Eq. (5.5) are solved separately with a single transport sweep and S2SA iteration. Since we are using an  $S_2$  angular quadrature, a single source iteration with a single S2SA step exactly solves a given within group neutron transport problem.

The converged scalar flux is normalized such that the desired power level of  $P_{Total} = 2000$  [ $W/cm^2$ ], is achieved. All fission energy is assumed to be deposited only in the fuel. For the SL Full scheme, we calculate the normalization factor,  $F_P$ , as:

$$F_P = E_f \sum_{g=1}^2 \left[ \sum_{i=1}^{N_{Fuel}} \frac{\Delta x_i}{2} \sum_{j=1}^{N_P} w_j \Sigma_{f,g,i,j} \phi_{g,i,j} \right], \quad (5.8)$$

where in  $E_f$  is the energy released per fission, assumed to be 200 [ $MeV$ ],  $w_j$  is the quadrature weight associated with the  $j$ -th DFEM interpolation point, and  $N_{Fuel}$  is the total number of spatial cells in the fuel region. The SL Collapse and AD DFEM schemes calculate  $F_P$  as

$$F_P = E_f \sum_{g=1}^2 \left[ \sum_{i=1}^{N_{Fuel}} \frac{\Delta x_i \widehat{\Sigma}_{f,g,i}}{2} \sum_{j=1}^{N_P} w_j \Sigma_{f,g,i,j} \phi_{g,i,j} \right]. \quad (5.9)$$

$\tilde{\phi}^{(\ell+1)}$  is then scaled as:

$$\tilde{\phi}_g^{(\ell+1)} \leftarrow \frac{P_{Total}}{F_P} \tilde{\phi}_g^{(\ell+1)}. \quad (5.10)$$

### 5.2.2 Nuclide Density

We consider three spatial discretization schemes to solve the nuclide production/destruction components of Eqs. (5.1). The first, AD DFEM, tracks only cell average nuclide densities, approximating the true spatial distribution of nuclide  $m$ ,  $N_m(x, t)$ , as being a constant in each cell, equal to the cell average density of nuclide  $m$ . Denoting the average nuclide density in cell  $i$  for nuclide  $m$  as  $\bar{N}_{m,i}$  and the average group  $g$  scalar flux in cell  $i$  as  $\bar{\phi}_{g,i}$ , we give the fissile nuclide update equation for the AD DFEM scheme in Eq. (5.11):

$$\begin{aligned} \frac{\bar{N}_{FS,i}^{\tau+1} - \bar{N}_{FS,i}^{\tau}}{\Delta t} &= \bar{N}_{FT,i}^{\tau} [\gamma_{FT,1}\sigma_{a,FT,1}\bar{\phi}_{1,i}^{\tau} + \gamma_{FT,2}\sigma_{a,FT,2}\bar{\phi}_{2,i}^{\tau}] \\ &\quad - \bar{N}_{FS,i}^{\tau} ((1 - \gamma_{FS,1})\sigma_{a,FS,1}\bar{\phi}_{1,i}^{\tau} + (1 - \gamma_{FS,2})\sigma_{a,FS,2}\bar{\phi}_{2,i}^{\tau}) . \end{aligned} \quad (5.11)$$

In Eq. (5.11) superscript  $\tau$  denotes time index  $\tau$  quantities and  $\Delta t$  is the time step size. The update equations for  $N_{FT}$ ,  $N_{FP-A}$ ,  $N_{FP-S}$ , and  $N_I$  can be derived analogously to Eq. (5.11). AD DFEM calculates  $\bar{\phi}_{g,i}$  using closed Newton-Cotes quadrature with the quadrature points limited to the DFEM interpolation points:

$$\bar{\phi}_{g,i} = \frac{1}{2} \sum_{j=1}^{N_P} w_j \phi_{g,j} . \quad (5.12)$$

The averaging in Eq. (5.12) is exact since an  $N_P$  point closed Newton-Cotes quadrature can exactly integrate any  $P$  degree polynomial. Equation (5.11) locally updates all average nuclide densities,  $\bar{N}_{FS,i}$ ,  $\bar{N}_{FT,i}$ ,  $\bar{N}_{FP-A,i}$ ,  $\bar{N}_{FP-S,i}$ , and  $\bar{N}_{I,i}$ , simultaneously via a  $5 \times 5$  matrix-vector multiply.

The SL Full and SL Collapse schemes approximate the true spatial density of nuclide  $m$  as a  $P$  degree Lagrange polynomial,  $\tilde{N}_m(s)$ , in each cell:

$$\tilde{N}_m(s) = \sum_{j=1}^{N_P} N_{m,j} b_j(s), \quad (5.13)$$

where  $b_j$  are the  $N_P = P + 1$  Lagrange interpolatory polynomials in the interval  $s \in [-1, 1]$ . We require the set of nuclide density DFEM interpolation points to be the same set of  $N_P$  points as the angular flux DFEM interpolation points. Following a Galerkin procedure, we multiply each production/destruction nuclide equation of Eqs. (5.1) by basis function  $b_j$  and integrate generating  $5(P + 1)$  equations. The system of update equations for  $\vec{N}_{FS,i}$  is shown in Eqs. (5.14):

$$\begin{aligned} \frac{1}{\Delta t} \mathbf{M} \left( \vec{N}_{FS,i}^{\tau+1} - \vec{N}_{FS,i}^{\tau} \right) &= -(1 - \gamma_{FS,1}) \sigma_{a,FS,1} \widehat{\mathbf{M}}_{\phi_{1,i},\tau} \vec{N}_{FS,i}^{\tau} \\ &\quad - (1 - \gamma_{FS,2}) \sigma_{a,FS,2} \widehat{\mathbf{M}}_{\phi_{2,i},\tau} \vec{N}_{FS,i}^{\tau} \\ &\quad + \gamma_{FT,1} \sigma_{a,FT,1} \widehat{\mathbf{M}}_{\phi_{1,i}^{\tau}} \vec{N}_{FT,i}^{\tau} + \gamma_{FT,2} \sigma_{a,FT,2} \widehat{\mathbf{M}}_{\phi_{2,i}^{\tau}} \vec{N}_{FT,i}^{\tau}. \end{aligned} \quad (5.14)$$

The equations for  $\vec{N}_{FT,i}$ ,  $\vec{N}_{FP-A,i}$ ,  $N_{FP-S,i}$ , and  $N_{I,i}$  are derived in a similar fashion to Eq. (5.14). In Eq. (5.14) we have defined:

$$\widehat{\mathbf{M}}_{\phi_{g,i},jk} = \frac{\Delta x}{2} \int_{-1}^1 b_j(s) b_k(s) \tilde{\phi}_{g,\tau,i}(s) \, ds \quad , \text{ and} \quad (5.15)$$

$$\vec{N}_{m,i}^{\tau} = \begin{bmatrix} N_{m,1}^{\tau} \\ \vdots \\ N_{m,j}^{\tau} \\ \vdots \\ N_{m,P+1}^{\tau} \end{bmatrix}. \quad (5.16)$$

Given that we track five nuclides in the fuel region, each expanded in a  $P$  degree polynomial in each cell, there are  $5(P + 1)$  unknowns in each cell, thus Eq. (5.14) is a closed,  $5(P + 1) \times 5(P + 1)$  system of linear equations for the  $5(P + 1)$  unknown nuclide densities,  $N_{m,i,j}$  in each cell.

Using self-lumping quadrature to approximate Eq. (5.15) causes  $\widehat{\mathbf{M}}_{\phi_{g,i}^\tau}$  to be a diagonal matrix. Recalling that  $\widetilde{N}_m$  uses the same interpolation points as  $\widetilde{\phi}_g$ , approximating the integration of Eq. (5.15) with numerical quadrature restricted to the DFEM interpolating points, results in

$$\widehat{\mathbf{M}}_{\phi_{g,i}^\tau,jk} = \begin{cases} w_j \frac{\Delta x}{2} \phi_{g,\tau,i,j} & j = k \\ 0 & \text{otherwise} \end{cases}. \quad (5.17)$$

Macroscopic cross sections are generated from nuclide density and microscopic cross section data. For the AD DFEM scheme, each cell has a single macroscopic cross section (per reaction type), and a single value of nuclide density for each nuclide type. Thus, interaction cross sections are easily tabulated. As an example, the cell average total interaction cross section in cell  $i$  is calculated in Eq. (5.18):

$$\begin{aligned} \widehat{\Sigma}_{t,g,i} = & N_{FS,i} \sigma_{t,FS,g} + N_{FT,i} \sigma_{t,FT,g} + N_{FP-A,i} \sigma_{t,FP-A,g} \\ & + N_{FP-S,i} \sigma_{t,FP-S,g} + N_{I,i} \sigma_{t,I,g}. \end{aligned} \quad (5.18)$$

Macroscopic fission cross section and average neutrons per fission products are found in a similar fashion, but we can limit our consideration to the fissile and fertile nuclide densities as shown in Eq. (5.19),

$$\widehat{\nu\Sigma}_{f,g,i} = N_{FS,i} \nu_{FS,g} \sigma_{f,FS,g} + N_{FT,i} \nu_{FT,g} \sigma_{f,FT,g}. \quad (5.19)$$

The SL Full and SL Collapse schemes calculate macroscopic cross sections in a similar fashion to Eq. (5.18) and Eq. (5.19), but instead of calculating a cell average,  $\widehat{\Sigma}_{g,i}$ , they calculate macroscopic values at each DFEM interpolation point. SL Collapse then averages the macroscopic cross section at each DFEM interpolation point to estimate the cell average cross section, as shown in Eq. (5.20) for  $\widehat{\Sigma}_{t,i}$ :

$$\widehat{\Sigma}_{t,i} = \frac{1}{2} \sum_{j=1}^{N_P} w_j \Sigma_{t,g,i,j}. \quad (5.20)$$

### 5.3 Numerical Results

Since an analytic solution to this depletion problem is not available we employ a fine spatial mesh to obtain the reference solution. We use a fine mesh of 10,240 cells and the SL Full scheme with a quartic polynomial trial space as our reference numerical solution. We present  $L_2$  spatial error measures for

1. the total scalar flux ( $E_\phi$ ),
2. the fissile nuclide density ( $E_{N_{FS}}$ ),
3. the fertile nuclide density ( $E_{N_{FT}}$ ), and
4. the parasitic absorber fission product ( $E_{N_{FP-A}}$ ).

To allow for easier comparison, we normalize each error to the reference solution quantity. We define  $E_\phi$  as:

$$E_\phi = \frac{\sqrt{\sum_{g=1}^2 \sum_{i=1}^{N_{ref}} \frac{\Delta x_i}{2} \sum_{q=1}^{N_{qf}} w_q \left( \tilde{\phi}_{ref,i,g}(s_q) - \tilde{\phi}_{num,i,g}(s_q) \right)^2}}{\sqrt{\sum_{g=1}^2 \sum_{i=1}^{N_{ref}} \frac{\Delta x_i}{2} \sum_{q=1}^{N_{qf}} w_q \tilde{\phi}_{ref,i,g}(s_q)^2}}, \quad (5.21)$$

where  $N_{ref}$  is the number of reference cells,  $\tilde{\phi}_{ref,i,g}(s)$  is the reference solution group  $g$  scalar flux in cell  $i$ , and  $\tilde{\phi}_{num,i,g}(s)$  is the coarse mesh numerical scheme's approximation of the group  $g$  scalar flux in cell  $i$ . Error measures for  $N_{FS}$ ,  $N_{FT}$ , and  $N_{FP-A}$  are derived similarly.

Convergence of  $E_\phi$  is shown in Figs. 5.5-5.8 as a function of DFEM trial space degree and DFEM scheme.

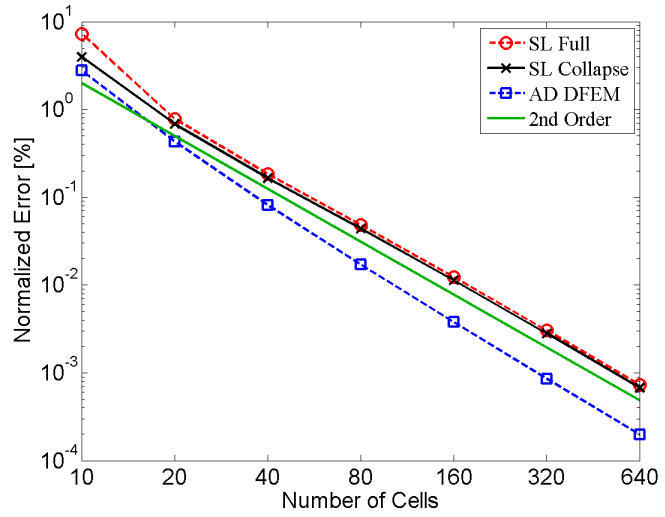


Figure 5.5: Normalized total scalar flux error for the depletion problem at end of cycle, for linear DFEM.

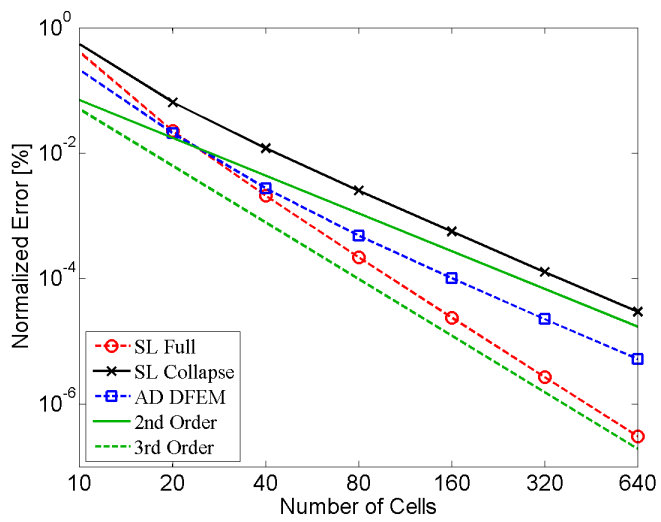


Figure 5.6: Normalized total scalar flux error for the depletion problem at end of cycle, for quadratic DFEM.

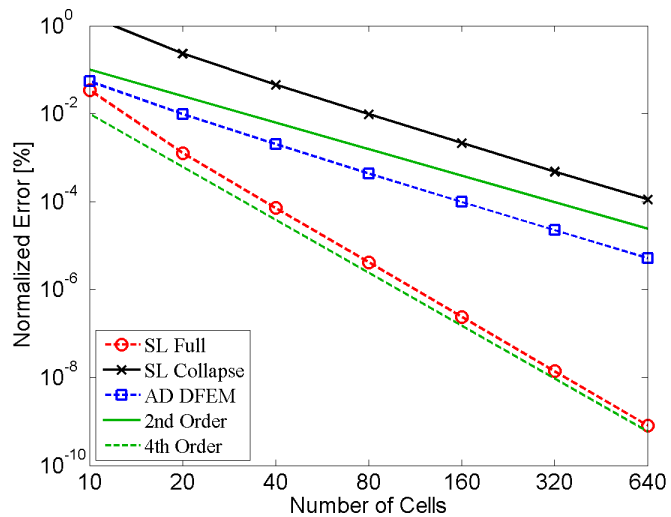


Figure 5.7: Normalized total scalar flux error for the depletion problem at end of cycle, for cubic DFEM.

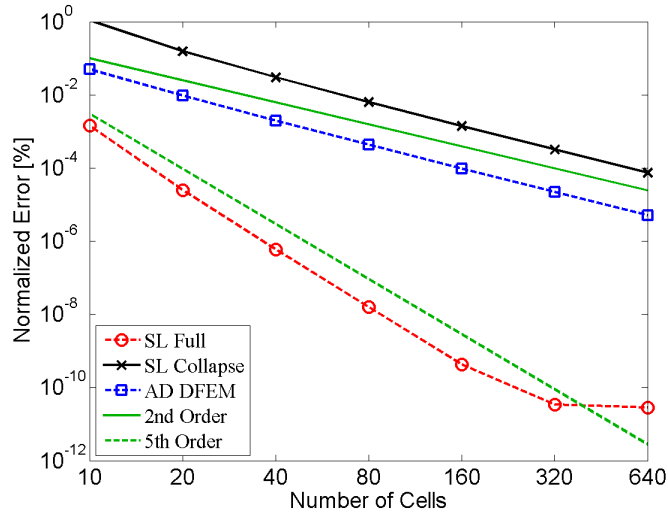


Figure 5.8: Normalized total scalar flux error for the depletion problem at end of cycle, for quartic DFEM.

Figures 5.5-5.8 re-emphasize two key results observed in the case of a pure absorber. First, when employing cell-wise constant cross sections, angular / scalar flux convergence is at most second order in space, regardless of the DFEM trial space polynomial degree. Second, exact integration of the interaction terms in the DFEM moment equations is not required to achieve high-order accuracy. In the depletion term, the DFEM interaction term is a degree  $3P$  polynomial, and self-lumping schemes using Gauss or Lobatto quadrature only integrate  $2P + 1$  and  $2P - 1$  degree polynomials, respectively.

Convergence of  $E_{N_{FS}}$ ,  $E_{N_{FT}}$ , and  $E_{N_{FP-A}}$  are given in Figs. 5.9-5.12, Figs. 5.13-5.16, and Figs. 5.17-5.20, respectively for linear through quartic trial space degrees.

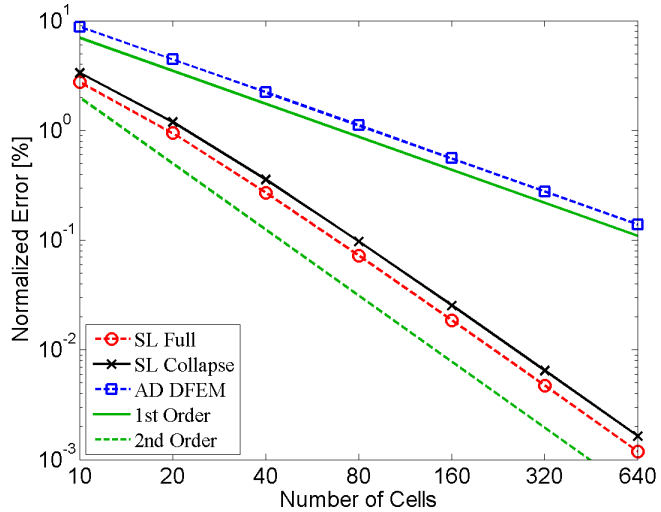


Figure 5.9: Normalized fissile nuclide density error for the depletion problem at end of cycle, for linear DFEM

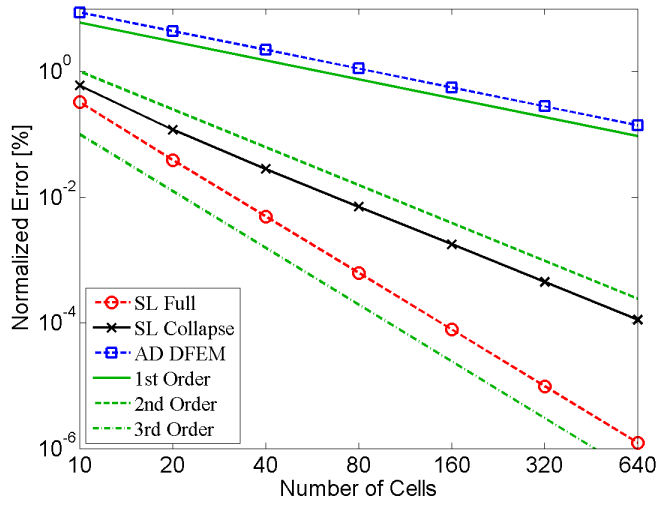


Figure 5.10: Normalized fissile nuclide density error for the depletion problem at end of cycle, for quadratic DFEM.

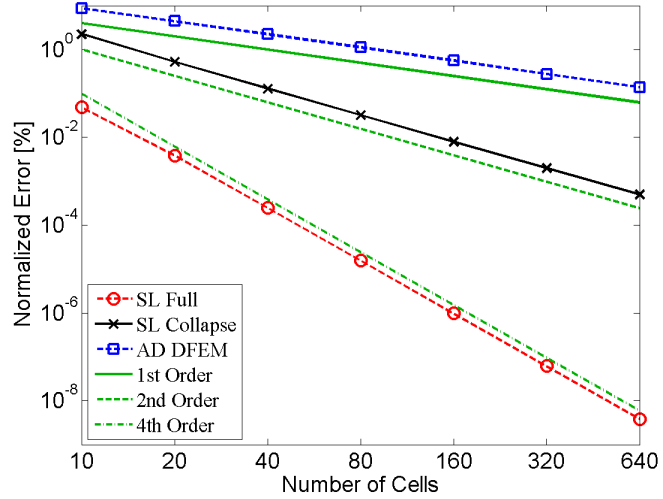


Figure 5.11: Normalized fissile nuclide density error for the depletion problem at end of cycle, for cubic DFEM.

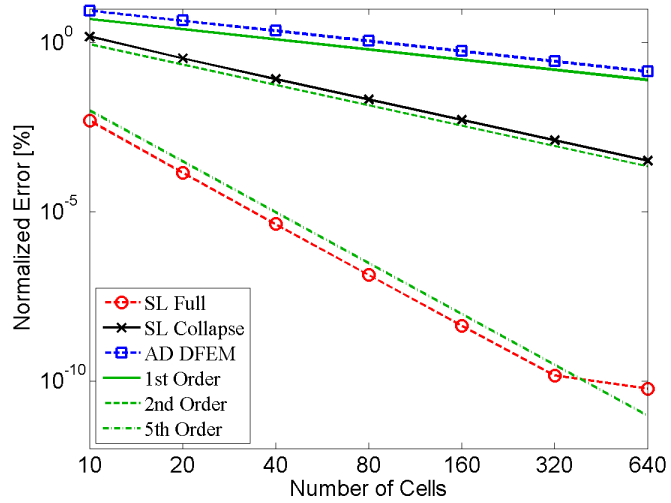


Figure 5.12: Normalized fissile nuclide density error for the depletion problem at end of cycle, for quartic DFEM.

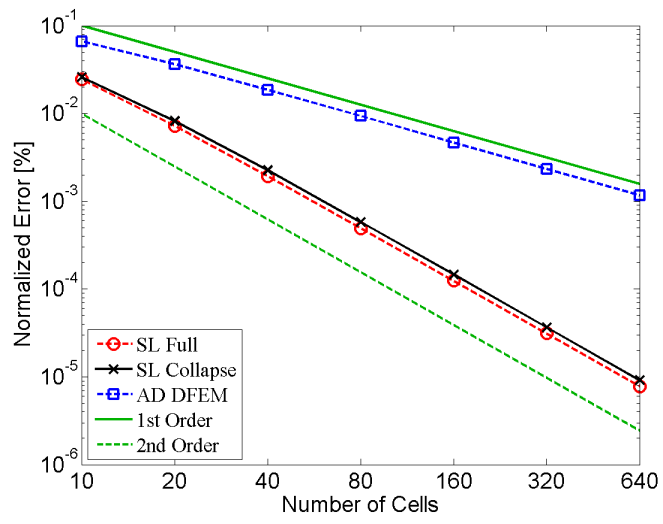


Figure 5.13: Normalized fertile nuclide density error for the depletion problem at end of cycle, for linear DFEM.

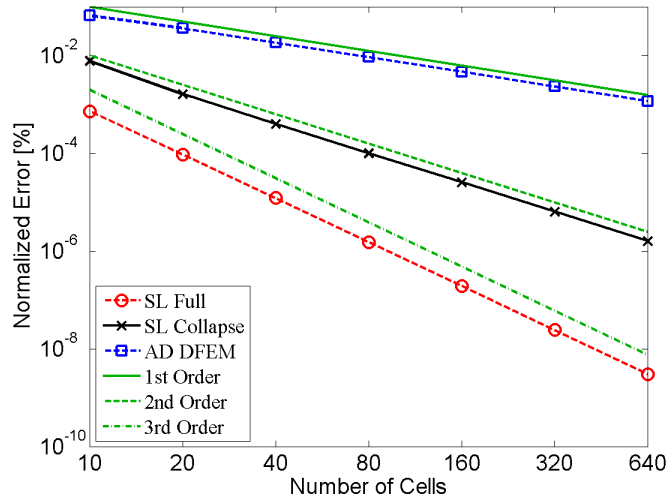


Figure 5.14: Normalized fertile nuclide density error for the depletion problem at end of cycle, for quadratic DFEM..

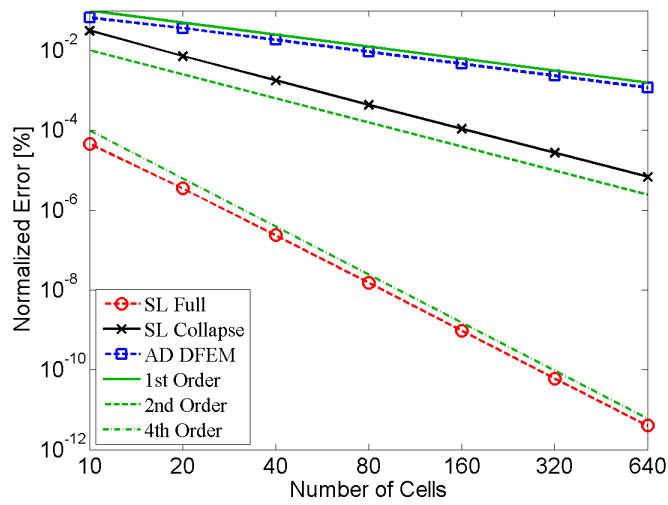


Figure 5.15: Normalized fertile nuclide density error for the depletion problem at end of cycle, for cubic DFEM.

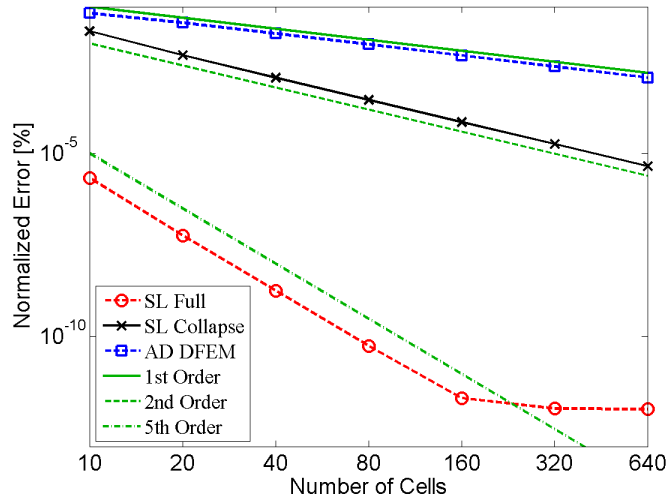


Figure 5.16: Normalized fertile nuclide density error for the depletion problem at end of cycle, for quartic DFEM.

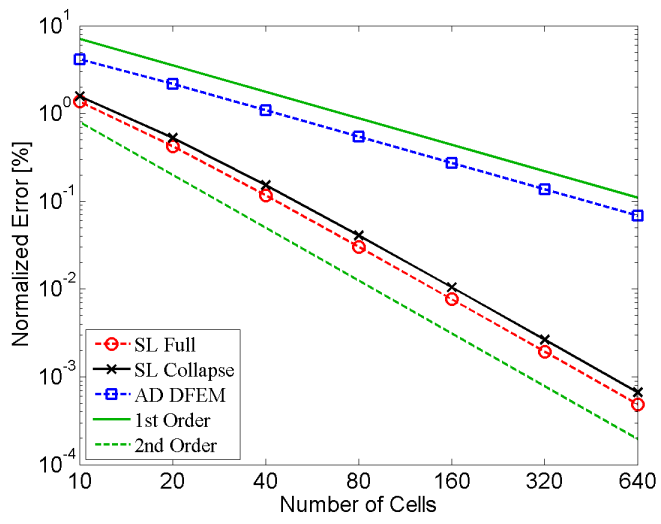


Figure 5.17: Normalized parasitic absorber fission product error for the depletion problem at end of cycle, for linear DFEM.

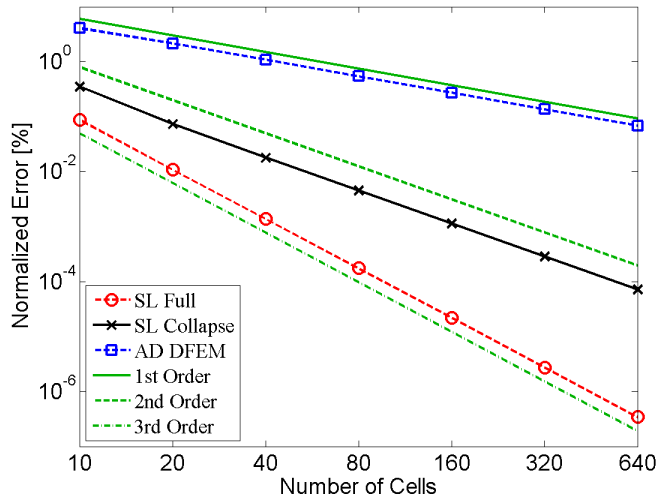


Figure 5.18: Normalized parasitic absorber fission product error for the depletion problem at end of cycle, for quadratic DFEM.

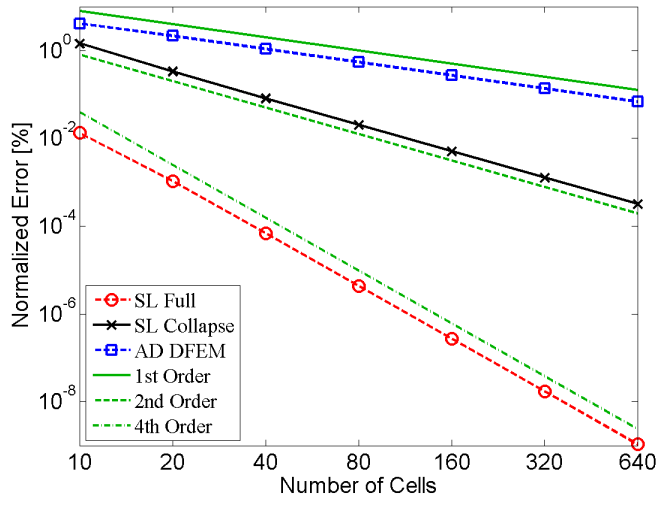


Figure 5.19: Normalized parasitic absorber fission product error for the depletion problem at end of cycle, for cubic DFEM.

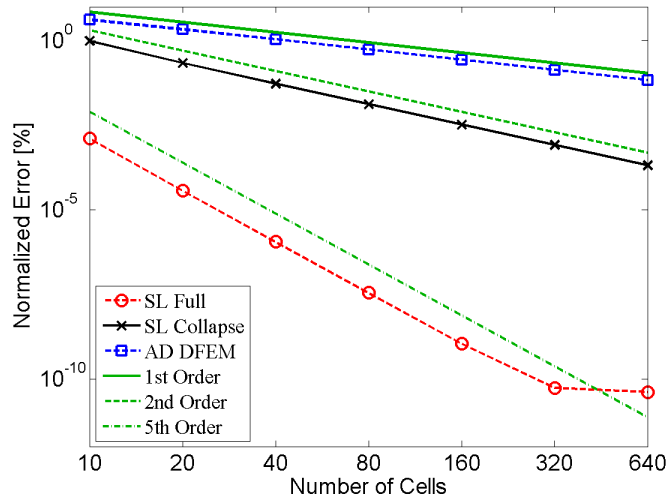


Figure 5.20: Normalized parasitic absorber fission product error for the depletion problem at end of cycle, for quartic DFEM.

Examining the spatial convergence in nuclide densities, we make several observations. First, we note that the AD DFEM scheme (cell-wise average cross section, cell average nuclide density) achieves at most first-order convergence for all spatial nuclide density errors, regardless of the angular flux trial space degree. The AD DFEM scheme is limited to at most first-order convergence of the error in the spatial distribution of nuclides because the scalar flux is updated using only a cell-wise average cross section and only the cell average nuclide density is tracked. Second, though the SL Collapse scheme expands nuclide density in a  $P$  degree polynomial DFEM trial space, it achieves at most second-order  $L^2$  convergence of the error in nuclides spatial distribution, for all trial space polynomial degrees. SL Collapse is limited to at most second-order convergence of the spatial nuclide density solely because the scheme assumes a constant cross section in each cell when updating the scalar flux. The respective first-order and second-order convergence of the error in nuclide spatial distribution of the AD DFEM and SL Collapse scheme verifies the result observed in the pure absorber problem: assuming a cell-wise average cross section for coupled radiation transport problems limits the order of convergence of any quantity that depends on an interaction rate. SL Full achieves  $P+1$  order convergence of the error in spatial nuclide density for the fuel depletion problem, showing that coupled systems of equations involving radiation transport can be solved with arbitrary order of accuracy using high-order DFEM polynomial trial spaces and self-lumping numerical quadrature that explicitly accounts for the spatial variation of cross section within each cell.

## 6. GREY THERMAL RADIATIVE TRANSFER- THEORY

We now apply our self-lumping DFEM methodology to the grey thermal radiative transfer equations. Our framework shares important characteristics of the work presented by Morel, Wareing, and Smith [6]

1. linearization of the Planckian about an arbitrary temperature,
2. expansion of the angular intensity and temperature in a  $P$  degree trial space,  
and
3. expansion of the spatial dependence of the Planckian in a  $P$  degree trial space.

However, there are several differences between the work we present here and that of [6]. First, we derive our method for arbitrary DFEM polynomial trial space degree, not only a linear polynomial trial space. Second, [6] used a DFEM scheme equivalent to traditional lumping, whereas we primarily consider quadrature based self-lumping discretizations. However, the equations we derive are applicable to any DFEM scheme that uses polynomial trial space and test functions. Additionally, we consider arbitrary order (and stage count) SDIRK time integration, not only implicit Euler time integration. The two most important differences between our work here and that of [6] are:

1. we assume opacity and heat capacity can vary within each spatial cell and
2. we fully converge the Planckian linearization in temperature.

As shown by Larsen, Kumar, and Morel, failure to fully converge the Planckian linearization in temperature can result in non-physical solutions that violate the maximum principle [44].

The remainder of this section is divided into three parts. Section 6.1 describes our linearization and discretization of the grey thermal radiative transfer (TRT) equations. We describe the time marching and nested iteration process we follow while solving the TRT in Section 6.2 In Section 6.3 we describe necessary modifications to physical quantities handle negative angular intensities and temperatures and in Section 6.4 we describe some adaptive time step selection techniques. We conclude with a brief description of our computer code implementation in Section 6.5

## 6.1 Linearization and Discretization of Grey TRT Equations

We begin our discussion of how to linearize the Planckian of the grey thermal radiative transfer in temperature by first briefly outlining SDIRK temporal integration in Section 6.1.1. A more complete explanation can be found in [2]

### 6.1.1 SDIRK Time Integration

SDIRK time integration schemes are one of many options available for solving initial value problems of the form:

$$g(0) = g_0 \tag{6.1}$$

$$\frac{\partial g}{\partial t} = f(t, g), \tag{6.2}$$

where  $t$  is time, and  $g_0$  is the initial value of  $g$  at time  $t = 0$ . Depending on the literary source, SDIRK stands for Single-Diagonally Implicit Runge-Kutta, S-stable Diagonally Implicit Runge-Kutta, or one of many other expansions of the SDIRK acronym. The coefficients,  $a_i$ ,  $b_i$ , and  $c_i$  that describe any Runge-Kutta time integration are typically given in formatted tables called Butcher tableaux. Due to the stiff nature of the TRT equations, we limit ourselves to SDIRK time integration schemes. The Butcher tableaux of an SDIRK scheme with  $N_{stage}$  stages is given in

Eq. (6.3)

Stage	$c_i$	$a$					
1	$c_1$	$a_{11}$	0	$\dots$	0		
2	$c_2$	$a_{21}$	$a_{22}$	0	$\vdots$		
$i$	$c_i$	$a_{i1}$	$a_{i2}$	$\ddots$	0		
$N_{stage}$	$c_{N_{stage}}$	$a_{N_{stage}1}$	$a_{N_{stage}2}$	$\dots$	$a_{N_{stage}N_{stage}}$		
		$b_1$	$b_2$	$\dots$	$b_{N_{stage}}$		

(6.3)

To illustrate how SDIRK is used to advance time-dependent quantities, let us consider a time-dependent scalar function,  $g(t)$ . Given an initial value at time (or time step)  $t^n$ ,  $g(t^n) = g_n$ , then  $g(t^{n+1})$  is:

$$g_{n+1} = g_n + \Delta t \sum_{i=1}^{N_{stage}} b_i k_i, \quad (6.4)$$

where  $\Delta t = t^{n+1} - t^n$ , and  $k_i$  is defined as:

$$k_i = f \left( t_n + c_i \Delta t, g_n + \Delta t \sum_{j=1}^i a_{ij} k_j \right). \quad (6.5)$$

Equation 6.5 can also be interpreted as meaning:

$$g_i = g_n + \Delta t \sum_{j=1}^i a_{ij} f(t_j, g_j), \quad (6.6)$$

where  $g_i$  is the intermediate value of  $g$  at the time of stage  $i$  and  $t_j = t^n + \Delta t c_j$ .

We consider three different SDIRK schemes in our work, implicit Euler (IE); a two stage, second order S-stable scheme (SDIRK 2-2); and a three stage, third order S-stable scheme (SDIRK 3-3). Both multi-stage schemes were taken from [2]. The

Butcher tableaux for the implicit Euler scheme can be written as:

$$\begin{array}{c|cc|c} & & & \\ \hline & 1 & 1 & 1 \\ \hline & & & 1 \\ \hline \end{array} . \quad (6.7)$$

The SDIRK 2-2 scheme of Alexander has the following Butcher tableaux,

$$\begin{array}{c|cc|cc} \hline & & & & \\ \hline 1 & 1 - \frac{\sqrt{2}}{2} & 1 - \frac{\sqrt{2}}{2} & 0 & \\ \hline 2 & 1 & \frac{\sqrt{2}}{2} & 1 - \frac{\sqrt{2}}{2} & , \\ \hline & & \frac{\sqrt{2}}{2} & 1 - \frac{\sqrt{2}}{2} & \\ \hline \end{array} \quad (6.8)$$

and the SDIRK 3-3 scheme's Butcher tableaux is:

$$\begin{array}{c|cc|ccc} \hline & & & & & & \\ \hline 1 & \gamma & & \gamma & & & \\ \hline 2 & \frac{1+\gamma}{2} & & \frac{1-\gamma}{2} & \gamma & & , \\ \hline 3 & 1 & & \delta & \beta & \gamma & \\ \hline & & & \delta & \beta & \gamma & \\ \hline \end{array} \quad (6.9)$$

with

$$\gamma = 0.435866521508459 \quad (6.10)$$

$$\delta = \frac{-6\gamma^2 + 16\gamma - 1}{4} \quad (6.11)$$

$$\beta = \frac{6\gamma^2 - 20\gamma + 5}{4} . \quad (6.12)$$

### 6.1.2 Spatially Analytic Linearization

We now linearize Planckian of the spatially analytic, 1-D slab, grey, discrete ordinates TRT equations with SDIRK time integration. The spatially and temporally

analytic grey discrete ordinates TRT are given in Eqs. (6.13),

$$\frac{1}{c} \frac{\partial I}{\partial t} + \mu_d \frac{\partial I}{\partial x} + \sigma_t I = \frac{1}{4\pi} \sigma_s \phi + \sigma_a B + S_I \quad (6.13a)$$

$$C_v \frac{\partial T}{\partial t} = \sigma_a (\phi - 4\pi B) + S_T. \quad (6.13b)$$

In Eqs. (6.13), we have assumed all scattering and material photon emission is isotropic, defined that  $I$  is the photon intensity with directional cosine  $\mu_d$  (relative to the  $x$ -axis),  $S_I$  is a driving radiation source intensity source in the direction of  $\mu_d$ ,  $S_T$  is a driving temperature source, and the frequency integrated (grey) Planck function,  $B$ , is:

$$B(T) = \frac{1}{4\pi} acT^4, \quad (6.14)$$

where  $c$  is the speed of light and  $a$  is the Planck radiation constant. To use SDIRK to advance  $I$  and  $T$  in time, we must first define the time derivatives of  $I$  and  $T$ :

$$\frac{\partial I}{\partial t} = c \left[ \frac{1}{4\pi} \sigma_s \phi + \sigma_a B + S_I - \mu_d \frac{\partial I}{\partial x} - \sigma_t I \right] \quad (6.15)$$

and

$$\frac{\partial T}{\partial t} = \frac{1}{C_v} [\sigma_a (\phi - 4\pi B) + S_T]. \quad (6.16)$$

We evaluate  $k_{I,s}$  and  $k_{T,s}$ , the SDIRK  $k$  values (Eq. (6.5)), for intensity and temperature for stage  $s$  as:

$$k_{I,s} = c \left[ \frac{1}{4\pi} \sigma_s(T_s) \phi_s + \sigma_a(T_s) B(T_s) + S_I(t_s) - \mu_d \frac{\partial I_s}{\partial x} - \sigma_t(T_s) I_s \right] \quad (6.17)$$

and

$$k_{T,s} = \frac{1}{C_v(T_s)} [\sigma_a(T_s) (\phi_s - 4\pi B(T_s)) + S_T(t_s)], \quad (6.18)$$

where  $\phi_s$ ,  $I_s$ , and  $T_s$  are the angle integrated intensity, angular intensity, and temperature at time  $t_s$ , and  $t_s$  is the time of stage  $s$ .

#### 6.1.2.1 SDIRK Stage 1

With the definitions of Eq. (6.6), Eq. (6.17), and Eq. (6.18), we now seek to find

$I_1$

$$I_1 = I_n + a_{11} \Delta t k_{I,1}. \quad (6.19)$$

Substituting in the definition of Eq. (6.17) into Eq. (6.19), for the intensity in stage 1, we have,

$$I_1 = I_n + a_{11} \Delta t c \left[ \frac{1}{4\pi} \sigma_s \phi_1 + \sigma_a B + S_I - \mu_d \frac{\partial I_1}{\partial x} - \sigma_t I_1 \right]. \quad (6.20)$$

Similarly, for  $T_1$ , we have

$$T_1 = T_n + \frac{a_{11} \Delta t}{C_v} [\sigma_a (\phi_1 - 4\pi B) + S_T]. \quad (6.21)$$

In Eq. (6.20) and Eq. (6.21), we have assumed that unless otherwise noted, all material properties and sources are evaluated at time  $t_s$  and temperature  $T_s$ .

We now introduce the linearization of the Planckian in temperature. For an arbitrary temperature iterate,  $T_*$ , we approximate  $B(T_s)$  as:

$$B(T) \approx B(T_*) + \frac{\partial B}{\partial T} \Big|_{T=T_*} (T - T_*) \quad (6.22a)$$

$$B(T) \approx B_* + D_* (T - T_*) \quad (6.22b)$$

$$B_* = \frac{1}{4\pi} a c T_*^4 \quad (6.22c)$$

$$D_* = \frac{1}{\pi} a c T_*^3. \quad (6.22d)$$

Equation 6.20 has a strong non-linear dependence on  $T_1$  due to the Planckian term,  $\sigma_a B$ , and a weak non-linear dependence on  $T_1$  if the material opacities are temperature dependent. If we could remove the dependence of  $T_1$  from Eq. (6.20), we could solve Eq. (6.20) using the same techniques that have been developed to solve the discrete ordinates neutron transport equation. We attempt to remove the strong non-linear dependence on  $T_1$  from Eq. (6.20) by linearizing the Planckian term. We neglect the non-linear dependence material opacities and heat capacities on temperature. To linearize the Planckian we first apply the linearization of Eq. (6.22) to Eq. (6.21) and manipulate. Inserting the linearization, we begin with Eq. (6.23)

$$T_1 = T_n + \frac{a_{11}\Delta t}{C_v} [\sigma_a (\phi_1 - 4\pi (B_* + D_* (T_1 - T_*))) + S_T] , \quad (6.23)$$

then move all  $T_1$  terms to the left hand side,

$$\left(1 + \frac{4\pi a_{11}\Delta t}{C_v} \sigma_a D_*\right) T_1 = T_n + \frac{a_{11}\Delta t}{C_v} [\sigma_a (\phi_1 - 4\pi B_* + 4\pi D_* T_*) + S_T] . \quad (6.24)$$

In Eq. (6.23), we have made the assumption that all material properties are evaluated at  $T_*$ , but we neglect to denote this for streamlined notation. Next, we divide by the coefficient in front of  $T_1$  on the left hand side:

$$\begin{aligned} T_1 &= \left(1 + \frac{4\pi a_{11}\Delta t}{C_v} \sigma_a D_*\right)^{-1} T_n + \dots \\ &\quad \left(1 + \frac{4\pi a_{11}\Delta t}{C_v} \sigma_a D_*\right)^{-1} \frac{a_{11}\Delta t}{C_v} [\sigma_a (\phi_1 - 4\pi B_*) + S_T] + \dots \\ &\quad \left(1 + \frac{4\pi a_{11}\Delta t}{C_v} \sigma_a D_*\right)^{-1} \frac{4\pi a_{11}\Delta t}{C_v} \sigma_a D_* T_* , \end{aligned} \quad (6.25)$$

and then add “nothing”,

$$\left(1 + \frac{4\pi a_{11}\Delta t}{C_v} \sigma_a D_*\right)^{-1} (T_* - T_*) , \quad (6.26)$$

to the right hand side,

$$\begin{aligned} T_1 = & \left(1 + \frac{4\pi a_{11}\Delta t}{C_v} \sigma_a D_*\right)^{-1} T_n + \dots \\ & \left(1 + \frac{4\pi a_{11}\Delta t}{C_v} \sigma_a D_*\right)^{-1} \frac{a_{11}\Delta t}{C_v} [\sigma_a (\phi_1 - 4\pi B_*) + S_T] + \dots \\ & \left(1 + \frac{4\pi a_{11}\Delta t}{C_v} \sigma_a D_*\right)^{-1} \left(1 + \frac{4\pi a_{11}\Delta t}{C_v} \sigma_a D_*\right) T_* \dots \\ & - \left(1 + \frac{4\pi a_{11}\Delta t}{C_v} \sigma_a D_*\right)^{-1} T_* . \end{aligned} \quad (6.27)$$

Noting that

$$\left(1 + \frac{4\pi a_{11}\Delta t}{C_v} \sigma_a D_*\right)^{-1} \left(1 + \frac{4\pi a_{11}\Delta t}{C_v} \sigma_a D_*\right) = 1 , \quad (6.28)$$

and condensing, we finally have:

$$T_1 = T_* + \left(1 + \frac{4\pi a_{11}\Delta t}{C_v} \sigma_a D_*\right)^{-1} \left(T_n - T_* + \frac{a_{11}\Delta t}{C_v} [\sigma_a (\phi_1 - 4\pi B_*) + S_T]\right) . \quad (6.29)$$

We occasionally refer to Eq. (6.29), and subsequent, similar equations, as a temperature update, as Eq. (6.29) is the non-linear iteration for temperature we must converge in order to solve the grey TRT.

We now linearize the Planck term of Eq. (6.20) in temperature,

$$I_1 = I_n + a_{11}\Delta t c \left[ \frac{1}{4\pi} \sigma_s \phi_1 + \sigma_a (B_* + D_*(T_1 - T_*)) + S_I - \mu_d \frac{\partial I_1}{\partial x} - \sigma_t I_1 \right] . \quad (6.30)$$

We then insert Eq. (6.29) into Eq. (6.30),

$$I_1 = I_n + a_{11}\Delta tc \left[ \frac{1}{4\pi} \sigma_s \phi_1 + S_I - \mu_d \frac{\partial I_1}{\partial x} - \sigma_t I_1 + \sigma_a \left( B_* + D_* \left( 1 + \frac{4\pi a_{11}\Delta t}{C_v} \sigma_a D_* \right)^{-1} \left( T_n - T_* + \frac{a_{11}\Delta t}{C_v} [\sigma_a (\phi_1 - 4\pi B_*) + S_T] \right) \right) \right]. \quad (6.31)$$

Next, we divide by  $a_{11}\Delta tc$ , and move the interaction and gradient terms to the left hand side:

$$\begin{aligned} \mu_d \frac{\partial I_1}{\partial x} + \sigma_t I_1 + \frac{1}{a_{11}\Delta tc} I_1 &= \frac{1}{a_{11}\Delta tc} I_n + \frac{1}{4\pi} \sigma_s \phi_1 + S_I \dots \\ + \sigma_a \left( B_* + D_* \left( 1 + \frac{4\pi a_{11}\Delta t}{C_v} \sigma_a D_* \right)^{-1} \left( T_n - T_* + \frac{a_{11}\Delta t}{C_v} [\sigma_a (\phi_1 - 4\pi B_*) + S_T] \right) \right) &. \end{aligned} \quad (6.32)$$

We now manipulate the right hand side,

$$\begin{aligned} \mu_d \frac{\partial I_1}{\partial x} + \sigma_t I_1 + \frac{1}{a_{11}\Delta tc} I_1 &= \frac{1}{a_{11}\Delta tc} I_n + \frac{1}{4\pi} \sigma_s \phi_1 \dots \\ + \sigma_a D_* \left( 1 + \frac{4\pi a_{11}\Delta t}{C_v} \sigma_a D_* \right)^{-1} \frac{a_{11}\Delta t}{C_v} \sigma_a \phi_1 \dots & \\ + S_I + \sigma_a B_* + \sigma_a D_* \left( 1 + \frac{4\pi a_{11}\Delta t}{C_v} \sigma_a D_* \right)^{-1} \left( T_n - T_* + \frac{a_{11}\Delta t}{C_v} [S_T - 4\pi \sigma_a B_*] \right), & \end{aligned} \quad (6.33)$$

and define

$$\sigma_{\tau,1} = \sigma_t + \frac{1}{a_{11}\Delta tc}, \quad (6.34)$$

giving

$$\begin{aligned}
\mu_d \frac{\partial I_1}{\partial x} + \sigma_{\tau,1} I_1 &= \frac{1}{a_{11}\Delta tc} I_n + \frac{1}{4\pi} \sigma_s \phi_1 \dots \\
&\quad + \sigma_a D_* \left( 1 + \frac{4\pi a_{11}\Delta t}{C_v} \sigma_a D_* \right)^{-1} \frac{a_{11}\Delta t}{C_v} \sigma_a \phi_1 \dots \\
&\quad + S_I + \sigma_a B_* + \sigma_a D_* \left( 1 + \frac{4\pi a_{11}\Delta t}{C_v} \sigma_a D_* \right)^{-1} \left( T_n - T_* + \frac{a_{11}\Delta t}{C_v} [S_T - 4\pi \sigma_a B_*] \right).
\end{aligned} \tag{6.35}$$

Focusing on the second  $\phi_1$  term on the right hand side,

$$\sigma_a D_* \left( 1 + \frac{4\pi a_{11}\Delta t}{C_v} \sigma_a D_* \right)^{-1} \frac{a_{11}\Delta t}{C_v} \sigma_a \phi_1, \tag{6.36}$$

we first simplify the terms in front of  $\sigma_a \phi_1$

$$\sigma_a D_* \left( 1 + \frac{4\pi a_{11}\Delta t}{C_v} \sigma_a D_* \right)^{-1} \frac{a_{11}\Delta t}{C_v} = \frac{\sigma_a D_* a_{11}\Delta t}{C_v + 4\pi a_{11}\Delta t \sigma_a D_*}, \tag{6.37}$$

then multiply by  $\frac{4\pi}{4\pi}$  and arrange, yielding:

$$\frac{1}{4\pi} \frac{\sigma_a D_* a_{11}\Delta t}{C_v + 4\pi a_{11}\Delta t \sigma_a D_*} \sigma_a \phi_1. \tag{6.38}$$

Defining a constant,  $\nu_1$ ,

$$\nu_1 = (4\pi a_{11}\Delta t \sigma_a D_*) (C_v + 4\pi a_{11}\Delta t \sigma_a D_*)^{-1}, \tag{6.39}$$

we arrive at an equation for intensity  $I_1$  that is similar in form to the discrete ordinates neutron transport equations with isotropic scattering, fission, and a fixed

source:

$$\mu_d \frac{\partial I_1}{\partial x} + \sigma_{\tau,1} I_1 = \frac{1}{4\pi} \sigma_s \phi_1 + \frac{1}{4\pi} \nu_1 \sigma_a \phi_1 + \xi_1, \quad (6.40)$$

where

$$\begin{aligned} \xi_1 &= \frac{1}{a_{11}\Delta t c} I_n + S_I + \sigma_a B_* + \dots \\ &\quad \sigma_a D_* \left( 1 + \frac{4\pi a_{11}\Delta t}{C_v} \sigma_a D_* \right)^{-1} \left( T_n - T_* + \frac{a_{11}\Delta t}{C_v} [S_T - 4\pi \sigma_a B_*] \right). \end{aligned} \quad (6.41)$$

The similarity of Eq. (6.40) to the neutron transport equation is especially apparent if we define pseudo total interaction and scattering cross sections,  $\widetilde{\Sigma}_t$  and  $\widetilde{\Sigma}_s$ , to be

$$\widetilde{\Sigma}_t = \sigma_{\tau,1} \quad (6.42a)$$

$$\widetilde{\Sigma}_s = \sigma_s + \nu_1 \sigma_a. \quad (6.42b)$$

By definition,  $\widetilde{\Sigma}_s < \widetilde{\Sigma}_t$ . This can be seen by considering the definition of Eq. (6.39), and realizing that  $\nu_1 < 1$ . Since  $\widetilde{\Sigma}_t > \sigma_t$ , and  $\widetilde{\Sigma}_s < \sigma_t$ , it follows that  $\widetilde{\Sigma}_s < \widetilde{\Sigma}_t$ .

Inserting Eqs. (6.42) into Eq. (6.40) yields

$$\mu_d \frac{\partial I_1}{\partial x} + \widetilde{\Sigma}_t I_1 = \frac{1}{4\pi} \widetilde{\Sigma}_s \phi_1 + \xi_1. \quad (6.43)$$

If we define a pseudo absorption interaction cross section as,

$$\widetilde{\Sigma}_a = \widetilde{\Sigma}_t - \widetilde{\Sigma}_s, \quad (6.44)$$

then it appears that all of the methodology, including DSA, developed for discrete ordinates neutron transport might be applicable for solving the discrete ordinates thermal radiative transfer equations using SDIRK time integration. The next step

in examining the possibility of applying neutron transport methods to solve the TRT equations is to attempt to form a pseudo neutron transport equation for stage  $i$  of any SDIRK time integration scheme.

#### 6.1.2.2 SDIRK Stage $i$

The intensity at stage  $i$ , is given by:

$$I_i = I_n + \Delta t \sum_{j=1}^{i-1} a_{ij} k_{I,j} + a_{ii} \Delta t c \left[ \frac{1}{4\pi} \sigma_s \phi_i + \sigma_a [B_* + D_*(T_i - T_*)] + S_I - \mu_d \frac{\partial I_i}{\partial x} - \sigma_t I_i \right]. \quad (6.45)$$

Likewise for  $T_i$ , we have

$$T_i = T_n + \Delta t \sum_{j=1}^{i-1} a_{ij} k_{T,j} + \frac{a_{ii} \Delta t}{C_v} [\sigma_a (\phi_i - 4\pi [B_* + D_*(T_i - T_*)]) + S_T]. \quad (6.46)$$

The only difference between Eq. (6.45) and Eq. (6.30) is the addition of

$$\Delta t \sum_{j=1}^{i-1} a_{ij} k_{I,j}. \quad (6.47)$$

Likewise, the only difference between Eq. (6.46) and Eq. (6.23) is the additional term

$$\Delta t \sum_{j=1}^{i-1} a_{ij} k_{T,j}. \quad (6.48)$$

For brevity, we omit the manipulation of Eq. (6.46) to form a temperature update equation, and instead give the final result:

$$T_i = T_* + \left( 1 + \frac{4\pi a_{ii}\Delta t}{C_v} \sigma_a D_* \right)^{-1} \left( T_n - T_* + \Delta t \sum_{j=1}^{i-1} a_{ij} k_{T,j} + \frac{a_{ii}\Delta t}{C_v} [\sigma_a (\phi_i - 4\pi B_*) + S_T] \right), \quad (6.49)$$

where we have highlighted that the stage  $i$  SDIRK temperature equation differs from the stage 1 SDIRK temperature update equation, Eq. (6.29), by only an additional term. This result is significant because Eq. (6.29) could be thought of as being unique to the implicit Euler discretization which is only first order accurate in time. Modifying Eq. (6.29) by the addition of only a single term, or alternatively, by thinking in terms of arbitrary stage count SDIRK time integration schemes rather than deriving the thermal radiative transfer equations for a single time discretization (implicit Euler), allows for arbitrary order accuracy time integration. Similarly, we omit the manipulation of Eq. (6.45) into a pseudo-fission form, and instead give the final result,

$$\mu_d \frac{\partial I_i}{\partial x} + \sigma_{\tau,i} = \frac{1}{4\pi} \sigma_s \phi_i + \frac{1}{4\pi} \nu_i \sigma_a \phi_i + \xi_i, \quad (6.50)$$

where we have defined the following:

$$\nu_i = 4\pi \sigma_a D_* \left( 1 + \frac{4\pi a_{ii}\Delta t}{C_v} \sigma_a D_* \right)^{-1} \frac{a_{ii}\Delta t}{C_v} = \frac{4\pi a_{ii}\Delta t \sigma_a D_*}{C_v + 4\pi a_{ii}\Delta t \sigma_a D_*}, \quad (6.51a)$$

$$\sigma_{\tau,i} = \frac{1}{a_{ii}\Delta t c} + \sigma_t, \text{ and} \quad (6.51b)$$

$$\xi_i = \sigma_a B_* + S_I + \frac{1}{a_{ii}\Delta tc} I_n + \frac{1}{a_{ii}c} \sum_{j=1}^{i-1} a_{ij} k_{I,j} + \dots$$

$$\sigma_a D_* \left( 1 + \frac{4\pi a_{ii}\Delta t}{C_v} \sigma_a D_* \right)^{-1} \left( T_n - T_* + \Delta t \sum_{j=1}^{i-1} a_{ij} k_{T,j} + \frac{a_{ii}\Delta t}{C_v} (S_T - 4\pi\sigma_a B_*) \right) .$$
(6.51c)

Again, we have highlighted in Eqs. (6.51) the only structural changes that result by considering arbitrary order accuracy SDIRK time integration of the thermal radiative transfer equations instead of limiting oneself to implicit Euler time integration of the thermal radiative transfer equations.

In the spatially analytic case, the grey TRT equations, with Planck linearization and arbitrary stage count SDIRK time integration can be put into a pseudo neutron transport form. This suggests that we may techniques such as spatial discretization and acceleration methods, can be used to solve the grey TRT equations. To verify this, we go through the linearization procedure again with the spatially discretized grey TRT equations that explicitly account for the spatial variation of material properties in the next section.

If we could solve the spatially discretized equations efficiently through source iteration alone, it would be redundant to go through the entire linearization process with the spatially analytic and spatially discretized TRT equations. However, iterative acceleration is essential for efficient solution of the TRT equations due to the Planckian absorption/re-emission terms in the linearized radiation intensity equation creating a situation analogous to a scattering dominated medium in neutron transport. As we will see, the problem with accelerating the spatially discretized TRT equations is that we need a pseudo diffusion coefficient,  $\tilde{D}$ , both at quadrature integration points and cell edges for MIP DSA acceleration, but do not have a physical definition of

that quantity.

### 6.1.3 Spatially Discretized Linearization

Now we attempt to derive a pseudo fission form of the spatially discretized grey TRT equations. First, we must define a spatially discretized  $k_I$  and  $k_T$ . To do this, we apply the standard Galerkin procedure outlined in Section 2 and Section 3 to the spatially analytic forms of  $k_I$  and  $k_T$  given in Eq. (6.17) and Eq. (6.18), respectively. For  $\vec{k}_I$ , we have:

$$\vec{k}_I = c\mathbf{M}^{-1} \left[ \frac{1}{4\pi} \mathbf{R}_{\sigma_s} \vec{\phi} + \mathbf{R}_{\sigma_a} \vec{B} - \mathbf{R}_{\sigma_t} \vec{I} - \mu_d \mathbf{G} \vec{I} + \mu_d I_{in} \vec{f} + \vec{S}_I \right], \quad (6.52)$$

where we have approximated the true angular intensity, angle integrated intensities, and temperatures in every spatial cell as  $P$  degree polynomials:

$$I(s) \approx \tilde{I}(s) \quad (6.53)$$

$$\tilde{I}(s) = \sum_{i=1}^{N_P} I_i b_i(s) \quad (6.54)$$

$$\phi(s) \approx \tilde{\phi}(s) \quad (6.55)$$

$$\tilde{\phi}(s) = \sum_{i=1}^{N_P} \phi_i b_i(s) \quad (6.56)$$

$$T(s) \approx \tilde{T}(s) \quad (6.57)$$

$$\tilde{T}(s) = \sum_{i=1}^{N_P} T_i b_i(s), \quad (6.58)$$

with

$$\vec{I} = [I_1 \dots I_{N_P}]^T \quad (6.59)$$

$$\vec{\phi} = [\phi_1 \dots \phi_{N_P}]^T \quad (6.60)$$

$$\vec{T} = [T_1 \dots T_{N_P}]^T \quad (6.61)$$

$$\vec{B} = \frac{1}{4\pi} [B(T_1) \dots B(T_{N_P})]^T, \quad (6.62)$$

and

$$\vec{S}_{I,j} = \frac{\Delta x}{2} \int_{-1}^1 b_j(s) S_I(s) ds. \quad (6.63)$$

Additionally,  $\mathbf{R}_{\sigma_t}$ ,  $\mathbf{R}_{\sigma_a}$ , and  $\mathbf{R}_{\sigma_s}$ , are defined analogously to the  $\mathbf{R}_\Sigma$  defined for neutron transport, as are  $\mathbf{G}$ ,  $\mathbf{M}$ , and  $\vec{f}$ . Defining  $\vec{k}_T$ :

$$\vec{k}_T = \mathbf{R}_{C_v}^{-1} \left[ \mathbf{R}_{\sigma_a} \left( \vec{\phi} - 4\pi \vec{B} \right) + \vec{S}_T \right], \quad (6.64)$$

with

$$\vec{S}_{T,j} = \frac{\Delta x}{2} \int_{-1}^1 b_j(s) S_T(s) ds, \quad (6.65)$$

and

$$\mathbf{R}_{C_v,ij} = \frac{\Delta x}{2} \int_{-1}^1 C_v(s) b_i(s) b_j(s) ds. \quad (6.66)$$

Before proceeding, it is critical to note that in Eq. (6.52) and Eq. (6.64) we approximate the “true” spatial dependence of the Planckian,

$$B(s) = B(\tilde{T}(s)), \quad (6.67)$$

as

$$B(s) \approx \sum_{i=1}^{N_P} b_i(s) B(T_i). \quad (6.68)$$

Additionally, since we assume the Planckian is a  $P$  degree polynomial in space, it follows that:

$$B(\tilde{T}(s)) \approx \sum_{i=1}^{N_P} b_i(s) \left[ B(T_{i,*}) + (T_i - T_{i,*}) \frac{dB}{dT} \Big|_{T=T_{i,*}} \right], \quad (6.69)$$

where  $T_{i,*}$  is an arbitrary temperature at DFEM interpolation point  $i$ .

#### 6.1.3.1 SDIRK Stage $i$

As we showed with the spatially analytic case, the  $i$ -th SDIRK stage is only slightly different than the first SDIRK stage. Thus, we omit the first stage derivation for the spatially discretized case, and begin with SDIRK stage  $i$ , first writing the equation for  $\vec{I}_i$  and  $\vec{T}_i$ :

$$\begin{aligned} \vec{I}_i &= \vec{I}_n + \Delta t \sum_{j=1}^{i-1} a_{ij} k_{I,j} + \\ &\Delta t a_{ii} c \mathbf{M}^{-1} \left[ \frac{1}{4\pi} \mathbf{R}_{\sigma_s} \vec{\phi}_i + \mathbf{R}_{\sigma_a} \left( \vec{B}_* + \mathbf{D}_* \left( \vec{T}_i - \vec{T}_* \right) \right) - \mathbf{R}_{\sigma_t} \vec{I}_i - \mu_d \mathbf{G} \vec{I}_i + \mu_d I_{in,i} \vec{f} + \vec{S}_I \right] \end{aligned} \quad (6.70)$$

$$\vec{T}_i = \vec{T}_n + \Delta t \sum_{j=1}^{i-1} a_{ij} k_{T,j} + \Delta t a_{ii} \mathbf{R}_{C_v}^{-1} \left[ \mathbf{R}_{\sigma_a} \left( \vec{\phi}_i - 4\pi \vec{B}_* - 4\pi \mathbf{D}_* \left( \vec{T}_i - \vec{T}_* \right) \right) + \vec{S}_T \right]. \quad (6.71)$$

In Eq. (6.70), Eq. (6.71), and all of the equations that follow, we evaluate all material properties ( $\sigma$ ,  $C_v$ ) at  $\tilde{T}_*$ , but fail to denote this with  $*$ , to improve equation readability. The diagonal matrix  $\mathbf{D}_*$  is defined as

$$\mathbf{D}_{*,ii} = \frac{dB}{dT} \Big|_{T=T_{i,*}}. \quad (6.72)$$

We now solve Eq. (6.71) for  $\vec{T}_i$ , by first moving all  $\vec{T}_i$  terms to the left hand side:

$$\begin{aligned} \vec{T}_i + 4\pi\Delta t a_{ii} \mathbf{R}_{Cv}^{-1} \mathbf{R}_{\sigma_a} \mathbf{D}_* \vec{T}_i = \\ \vec{T}_n + \Delta t \sum_{j=1}^{i-1} a_{ij} k_{T,j} + \Delta t a_{ii} \mathbf{R}_{Cv}^{-1} \left[ \mathbf{R}_{\sigma_a} \left( \vec{\phi}_i - 4\pi \vec{B}_* + 4\pi \mathbf{D}_* \vec{T}_* \right) + \vec{S}_T \right], \end{aligned} \quad (6.73)$$

and consolidate the  $\vec{T}_i$  coefficient matrices,

$$\begin{aligned} [\mathbf{I} + 4\pi\Delta t a_{ii} \mathbf{R}_{Cv}^{-1} \mathbf{R}_{\sigma_a} \mathbf{D}_*] \vec{T}_i = \\ \vec{T}_n + \Delta t \sum_{j=1}^{i-1} a_{ij} k_{T,j} + \Delta t a_{ii} \mathbf{R}_{Cv}^{-1} \left[ \mathbf{R}_{\sigma_a} \left( \vec{\phi}_i - 4\pi \vec{B}_* + 4\pi \mathbf{D}_* \vec{T}_* \right) + \vec{S}_T \right]. \end{aligned} \quad (6.74)$$

Multiplying the inverse of the coefficient matrix,

$$\begin{aligned} \vec{T}_i = [\mathbf{I} + 4\pi\Delta t a_{ii} \mathbf{R}_{Cv}^{-1} \mathbf{R}_{\sigma_a} \mathbf{D}_*]^{-1} \left[ \vec{T}_n + \Delta t \sum_{j=1}^{i-1} a_{ij} k_{T,j} \right] \dots \\ + \Delta t a_{ii} [\mathbf{I} + 4\pi\Delta t a_{ii} \mathbf{R}_{Cv}^{-1} \mathbf{R}_{\sigma_a} \mathbf{D}_*]^{-1} \mathbf{R}_{Cv}^{-1} \left[ \mathbf{R}_{\sigma_a} \left( \vec{\phi}_i - 4\pi \vec{B}_* + 4\pi \mathbf{D}_* \vec{T}_* \right) + \vec{S}_T \right], \end{aligned} \quad (6.75)$$

Isolating the  $\vec{T}_*$  term on the right hand side,

$$\begin{aligned} \vec{T}_i = [\mathbf{I} + 4\pi\Delta t a_{ii} \mathbf{R}_{Cv}^{-1} \mathbf{R}_{\sigma_a} \mathbf{D}_*]^{-1} \left[ \vec{T}_n + \Delta t \sum_{j=1}^{i-1} a_{ij} k_{T,j} \right] \dots \\ + \Delta t a_{ii} [\mathbf{I} + 4\pi\Delta t a_{ii} \mathbf{R}_{Cv}^{-1} \mathbf{R}_{\sigma_a} \mathbf{D}_*]^{-1} \mathbf{R}_{Cv}^{-1} \left[ \mathbf{R}_{\sigma_a} \left( \vec{\phi}_i - 4\pi \vec{B}_* \right) + \vec{S}_T \right] \dots \\ + 4\pi\Delta t a_{ii} [\mathbf{I} + 4\pi\Delta t a_{ii} \mathbf{R}_{Cv}^{-1} \mathbf{R}_{\sigma_a} \mathbf{D}_*]^{-1} \mathbf{R}_{Cv}^{-1} \mathbf{R}_{\sigma_a} \mathbf{D}_* \vec{T}_*, \end{aligned} \quad (6.76)$$

adding nothing,

$$\begin{aligned}
\vec{T}_i &= [\mathbf{I} + 4\pi\Delta t a_{ii} \mathbf{R}_{C_v}^{-1} \mathbf{R}_{\sigma_a} \mathbf{D}_*]^{-1} \left[ \vec{T}_n + \Delta t \sum_{j=1}^{i-1} a_{ij} k_{T,j} \right] \dots \\
&\quad + \Delta t a_{ii} [\mathbf{I} + 4\pi\Delta t a_{ii} \mathbf{R}_{C_v}^{-1} \mathbf{R}_{\sigma_a} \mathbf{D}_*]^{-1} \mathbf{R}_{C_v}^{-1} \left[ \mathbf{R}_{\sigma_a} (\vec{\phi}_i - 4\pi \vec{B}_*) + \vec{S}_T \right] \dots \\
&\quad + [\mathbf{I} + 4\pi\Delta t a_{ii} \mathbf{R}_{C_v}^{-1} \mathbf{R}_{\sigma_a} \mathbf{D}_*]^{-1} \left[ 4\pi\Delta t a_{ii} \mathbf{R}_{C_v}^{-1} \mathbf{R}_{\sigma_a} \mathbf{D}_* \vec{T}_* \right] \dots \\
&\quad + [\mathbf{I} + 4\pi\Delta t a_{ii} \mathbf{R}_{C_v}^{-1} \mathbf{R}_{\sigma_a} \mathbf{D}_*]^{-1} (\vec{T}_* - \vec{T}_*) , \quad (6.77)
\end{aligned}$$

and noting that

$$\left[ 4\pi\Delta t a_{ii} \mathbf{R}_{C_v}^{-1} \mathbf{R}_{\sigma_a} \mathbf{D}_* \vec{T}^* \right]^{-1} \left[ 4\pi\Delta t a_{ii} \mathbf{R}_{C_v}^{-1} \mathbf{R}_{\sigma_a} \mathbf{D}_* \vec{T}^* \right] = \mathbf{I}, \quad (6.78)$$

we reach the stage  $i$  temperature update equation,

$$\begin{aligned}
\vec{T}_i &= \vec{T}_* + [\mathbf{I} + 4\pi\Delta t a_{ii} \mathbf{R}_{C_v}^{-1} \mathbf{R}_{\sigma_a} \mathbf{D}_*]^{-1} \left[ \vec{T}_n - \vec{T}_* + \Delta t \sum_{j=1}^{i-1} a_{ij} k_{T,j} \right] \dots \\
&\quad + \Delta t a_{ii} [\mathbf{I} + 4\pi\Delta t a_{ii} \mathbf{R}_{C_v}^{-1} \mathbf{R}_{\sigma_a} \mathbf{D}_*]^{-1} \mathbf{R}_{C_v}^{-1} \left[ \mathbf{R}_{\sigma_a} (\vec{\phi}_i - 4\pi \vec{B}_*) + \vec{S}_T \right]. \quad (6.79)
\end{aligned}$$

Multiplying Eq. (6.70) by  $\frac{1}{c\Delta t a_{ii}} \mathbf{M}$ :

$$\begin{aligned}
\frac{1}{c\Delta t a_{ii}} \mathbf{M} \vec{I}_i &= \frac{1}{c\Delta t a_{ii}} \mathbf{M} \vec{I}_n + \frac{1}{ca_{ii}} \mathbf{M} \sum_{j=1}^{i-1} a_{ij} k_{I,j} \dots \\
&\quad + \frac{1}{4\pi} \mathbf{R}_{\sigma_s} \vec{\phi}_i + \mathbf{R}_{\sigma_a} (\vec{B}_* + \mathbf{D}_* (\vec{T}_i - \vec{T}_*)) - \mathbf{R}_{\sigma_t} \vec{I}_i - \mu_d \mathbf{G} \vec{I}_i + \mu_d I_{in,i} \vec{f} + \vec{S}_I, \quad (6.80)
\end{aligned}$$

moving the gradient terms and  $\frac{1}{a_{ii}c\Delta}\mathbf{M}\vec{I}_i$  to the left hand side and inserting the result of Eq. (6.79) into Eq. (6.80), we have:

$$\begin{aligned}
& \mu_d \mathbf{G}\vec{I}_i + \left( \frac{1}{c\Delta t a_{ii}} \mathbf{M} + \mathbf{R}_{\sigma_t} \right) \vec{I}_i = \frac{1}{c\Delta t a_{ii}} \mathbf{M}\vec{I}_n + \frac{1}{ca_{ii}} \mathbf{M} \sum_{j=1}^{i-1} a_{ij} k_{I,j} + \frac{1}{4\pi} \mathbf{R}_{\sigma_s} \vec{\phi}_i + \mathbf{R}_{\sigma_a} \vec{B}_* \dots \\
& + \mathbf{R}_{\sigma_a} \mathbf{D}_* \left\{ [\mathbf{I} + 4\pi \Delta t a_{ii} \mathbf{R}_{C_v}^{-1} \mathbf{R}_{\sigma_a} \mathbf{D}_*]^{-1} \left[ \vec{T}_n - \vec{T}_* + \Delta t \sum_{j=1}^{i-1} a_{ij} k_{T,j} \right] \dots \right. \\
& \left. + \Delta t a_{ii} [\mathbf{I} + 4\pi \Delta t a_{ii} \mathbf{R}_{C_v}^{-1} \mathbf{R}_{\sigma_a} \mathbf{D}_*]^{-1} \mathbf{R}_{C_v}^{-1} \left[ \mathbf{R}_{\sigma_a} (\vec{\phi}_i - 4\pi \vec{B}_*) + \vec{S}_T \right] \right\} + \mu_d I_{in,i} \vec{f} + \vec{S}_I . 
\end{aligned} \tag{6.81}$$

Re-arranging Eq. (6.81) to isolate  $\vec{\phi}_i$  terms on the right hand side, we have:

$$\begin{aligned}
& \mu_d \mathbf{G}\vec{I}_i + \left( \frac{1}{c\Delta t a_{ii}} \mathbf{M} + \mathbf{R}_{\sigma_t} \right) \vec{I}_i = \frac{1}{4\pi} \mathbf{R}_{\sigma_s} \vec{\phi}_i \dots \\
& + \Delta t a_{ii} \mathbf{R}_{\sigma_a} \mathbf{D}_* [\mathbf{I} + 4\pi \Delta t a_{ii} \mathbf{R}_{C_v}^{-1} \mathbf{R}_{\sigma_a} \mathbf{D}_*]^{-1} \mathbf{R}_{C_v}^{-1} \mathbf{R}_{\sigma_a} \vec{\phi}_i \dots \\
& + \mu_d \vec{f} I_{in,i} + \vec{S}_I + \frac{1}{c\Delta t a_{ii}} \mathbf{M}\vec{I}_n + \frac{1}{ca_{ii}} \mathbf{M} \sum_{j=1}^{i-1} a_{ij} k_{I,j} + \mathbf{R}_{\sigma_a} \vec{B}_* \dots \\
& + \mathbf{R}_{\sigma_a} \mathbf{D}_* [\mathbf{I} + 4\pi \Delta t a_{ii} \mathbf{R}_{C_v}^{-1} \mathbf{R}_{\sigma_a} \mathbf{D}_*]^{-1} \left[ \vec{T}_n - \vec{T}_* + \Delta t \sum_{j=1}^{i-1} a_{ij} k_{T,j} \right] \dots \\
& + \Delta t a_{ii} \mathbf{R}_{C_v}^{-1} [\mathbf{I} + 4\pi \Delta t a_{ii} \mathbf{R}_{C_v}^{-1} \mathbf{R}_{\sigma_a} \mathbf{D}_*]^{-1} \left[ \vec{S}_T - 4\pi \mathbf{R}_{\sigma_a} \vec{B}_* \right] . 
\end{aligned} \tag{6.82}$$

Making the following definitions:

$$\begin{aligned}
\bar{\xi}_{d,i} &= \frac{1}{c\Delta t a_{ii}} \mathbf{M}\vec{I}_n + \frac{1}{ca_{ii}} \mathbf{M} \sum_{j=1}^{i-1} a_{ij} k_{I,j} + \mathbf{R}_{\sigma_a} \vec{B}_* + \vec{S}_I \dots \\
& + \mathbf{R}_{\sigma_a} \mathbf{D}_* [\mathbf{I} + 4\pi \Delta t a_{ii} \mathbf{R}_{C_v}^{-1} \mathbf{R}_{\sigma_a} \mathbf{D}_*]^{-1} \left\{ \vec{T}_n - \vec{T}_* + \Delta t \sum_{j=1}^{i-1} a_{ij} k_{T,j} \right. \\
& \left. + \Delta t a_{ii} \mathbf{R}_{C_v}^{-1} [\vec{S}_T - 4\pi \mathbf{R}_{\sigma_a} \vec{B}_*] \right\} 
\end{aligned} \tag{6.83a}$$

$$\bar{\bar{\nu}}_i = 4\pi \Delta t a_{ii} \mathbf{R}_{\sigma_a} \mathbf{D}_* [\mathbf{I} + 4\pi \Delta t a_{ii} \mathbf{R}_{C_v}^{-1} \mathbf{R}_{\sigma_a} \mathbf{D}_*]^{-1} \mathbf{R}_{C_v}^{-1} \quad (6.83b)$$

$$\bar{\bar{\mathbf{R}}}_{\sigma_t,i} = \mathbf{R}_{\sigma_t} + \frac{1}{c \Delta t a_{ii}} \mathbf{M}, \quad (6.83c)$$

and inserting into Eq. (6.83a) gives our final equation for the radiation intensity:

$$\mu_d \mathbf{G} \vec{I}_i + \bar{\bar{\mathbf{R}}}_{\sigma_t,i} \vec{I}_i = \frac{1}{4\pi} \mathbf{R}_{\sigma_s} \vec{\phi}_i + \frac{1}{4\pi} \bar{\bar{\nu}}_i \mathbf{R}_{\sigma_a} \vec{\phi}_i + \bar{\bar{\xi}}_{d,i} + \mu_d \vec{f} I_{in,i}. \quad (6.84)$$

Given the form of Eq. (6.84), it appears that we can apply MIP DSA to accelerate the iterative solution of Eq. (6.84), but we still wish to verify that definition of  $\tilde{\Sigma}_t$  and  $\tilde{\Sigma}_a$  is consistent between both the spatially discretized and spatially analytic cases.

#### 6.1.4 Consistency of Pseudo Cross Sections

In Section 4, we used MIP DSA to accelerate a spatially analytic problem of the form

$$\mu_d \frac{d\psi}{dx} + \Sigma_t \psi = \frac{1}{4\pi} \Sigma_s \phi + Q_d, \quad (6.85)$$

with spatially discretized analog

$$\mu_d \frac{d\psi}{dx} \mathbf{R}_{\Sigma_t} \psi = \frac{1}{4\pi} \mathbf{R}_{\Sigma_s} \phi + \vec{Q}_d. \quad (6.86)$$

In the neutron transport problem,  $\Sigma_t$ ,  $\Sigma_s$ , and  $\Sigma_a$  are physically meaningful quantities, the total macroscopic interaction cross section, macroscopic scattering cross section, and absorption macroscopic cross section are inherent physical properties of a material, and by definition

$$\Sigma_a + \Sigma_s = \Sigma_t. \quad (6.87)$$

Likewise for the spatially discretized case, it is true that

$$\mathbf{R}_{\Sigma_a} = \mathbf{R}_{\Sigma_t} - \mathbf{R}_{\Sigma_s}, \quad (6.88)$$

since we have defined

$$\mathbf{R}_{\Sigma_a,ij} = \frac{\Delta x}{2} \int_{-1}^1 \Sigma_a(s) b_i(s) b_j(s) ds \quad (6.89a)$$

$$\mathbf{R}_{\Sigma_s,ij} = \frac{\Delta x}{2} \int_{-1}^1 \Sigma_s(s) b_i(s) b_j(s) ds \quad (6.89b)$$

$$\mathbf{R}_{\Sigma_t,ij} = \frac{\Delta x}{2} \int_{-1}^1 \Sigma_t(s) b_i(s) b_j(s) ds. \quad (6.89c)$$

Equation 6.88 can be verified by inserting the definitions of Eqs. (6.89) into Eq. (6.88),

$$\mathbf{R}_{\Sigma_a,ij} \stackrel{?}{=} \frac{\Delta x}{2} \int_{-1}^1 \Sigma_t(s) b_i(s) b_j(s) ds - \frac{\Delta x}{2} \int_{-1}^1 \Sigma_s(s) b_i(s) b_j(s) ds, \quad (6.90)$$

and obviously,

$$\mathbf{R}_{\Sigma_a,ij} = \frac{\Delta x}{2} \int_{-1}^1 (\Sigma_t(s) - \Sigma_s(s)) b_i(s) b_j(s) ds = \frac{\Delta x}{2} \int_{-1}^1 \Sigma_a(s) b_i(s) b_j(s) ds. \quad (6.91)$$

However, though the forms of Eq. (6.50) and Eq. (6.84) appear analogous to neutron transport, it is not obvious that the linearized, pseudo interaction cross sections (Eq. (6.50)) and their spatially discretized analogs, (Eq. (6.84)) are equivalent. That is, if we started with the spatially analytic linearization, Eq. (6.50), re-cast as,

$$\mu_d \frac{dI}{dx} + \tilde{\Sigma}_t I = \frac{1}{4\pi} \tilde{\Sigma}_s \phi + \xi_{d,i} \quad (6.92)$$

with

$$\widetilde{\Sigma}_t = \sigma_{\tau,i} \quad (6.93)$$

$$\widetilde{\Sigma}_s = \sigma_s + \nu_i \sigma_a, \quad (6.94)$$

then applied the Galerkin procedure, yielding,

$$\mu_d \mathbf{G} \vec{I} + \mathbf{R}_{\widetilde{\Sigma}_t} \vec{I} = \frac{1}{4\pi} \mathbf{R}_{\widetilde{\Sigma}_s} \vec{\phi} + \vec{\xi}_{d,i}, \quad (6.95)$$

with

$$\mathbf{R}_{\widetilde{\Sigma}_t,jk} = \frac{\Delta x}{2} \int_{-1}^1 \widetilde{\Sigma}_t(s) b_j(s) b_k(s) ds \quad (6.96a)$$

$$\mathbf{R}_{\widetilde{\Sigma}_s,jk} = \frac{\Delta x}{2} \int_{-1}^1 \widetilde{\Sigma}_s(s) b_j(s) b_k(s) ds \quad (6.96b)$$

$$\vec{\xi}_{d,j} = \frac{\Delta x}{2} \int_{-1}^1 b_j(s) \xi_{d,i} ds, \quad (6.96c)$$

would the definitions of Eqs. (6.96) be equivalent to

$$\mathbf{R}_{\widetilde{\Sigma}_t} \stackrel{?}{=} \overline{\overline{\mathbf{R}}}_{\sigma_{\tau,i}} \quad (6.97a)$$

$$\mathbf{R}_{\widetilde{\Sigma}_s} \stackrel{?}{=} \mathbf{R}_{\sigma_s} + \bar{\nu}_i \mathbf{R}_{\sigma_a} ? \quad (6.97b)$$

In Eqs. (6.96), we use  $i$  subscript to denote SDIRK stage  $i$ ,  $j$  to denote matrix row, and  $k$  to denote matrix column. We continue this notation for the remainder of this section.

We first consider the equivalence of  $\overline{\overline{\mathbf{R}}}_{\sigma_{\tau,i}}$  to  $\mathbf{R}_{\widetilde{\Sigma}_t}$ . By definition,

$$\overline{\overline{\mathbf{R}}}_{\sigma_{\tau,i}} = \frac{1}{a_{ii} c \Delta t} \mathbf{M} + \mathbf{R}_{\sigma_t}. \quad (6.98)$$

It follows that,

$$\overline{\overline{\mathbf{R}}}_{\sigma_{\tau,i},jk} = \frac{1}{a_{ii}c\Delta t} \frac{\Delta x}{2} \int_{-1}^1 b_j(s)b_k(s) ds + \frac{\Delta x}{2} \int_{-1}^1 \sigma_t(s)b_j(s)b_k(s) ds \quad (6.99)$$

$$\overline{\overline{\mathbf{R}}}_{\sigma_{\tau,i},jk} = \frac{\Delta x}{2} \int_{-1}^1 \left( \frac{1}{a_{ii}c\Delta t} + \sigma_t(s) \right) b_j(s)b_k(s) ds. \quad (6.100)$$

From Eqs. (6.96),

$$\mathbf{R}_{\widetilde{\Sigma}_t,jk} = \frac{\Delta x}{2} \int_{-1}^1 \left( \frac{1}{a_{ii}\Delta tc} + \sigma_t(s) \right) b_j(s)b_k(s) ds, \quad (6.101)$$

and we conclude that  $\overline{\overline{\mathbf{R}}}_{\sigma_{\tau,i}} = \mathbf{R}_{\widetilde{\Sigma}_t}$ . This is a very important result because it implies that we have a consistent definition of  $\widetilde{\Sigma}_t$ , that in turn allows us to define a diffusion coefficient for MIP DSA,

$$D(s) = \frac{1}{3\widetilde{\Sigma}_t(s)} = \frac{1}{3 \left( \frac{1}{a_{ii}c\Delta t} + \sigma_t(s) \right)}. \quad (6.102)$$

We now attempt to determine if

$$\mathbf{R}_{\widetilde{\Sigma}_s} = \mathbf{R}_{\sigma_s} + \bar{\nu}_i \mathbf{R}_{\sigma_a}. \quad (6.103)$$

First, we expand the definition of  $\mathbf{R}_{\widetilde{\Sigma}_s}$  from Eqs. (6.96), with the definition of TRT pseudo cross sections,

$$\mathbf{R}_{\widetilde{\Sigma}_s,jk} = \frac{\Delta x}{2} \int_{-1}^1 b_j(s)b_k(s) ds \left( \sigma_s + \frac{4\pi a_{ii}\Delta t \sigma_a D_*}{C_v + 4\pi a_{ii}\Delta t \sigma_a D_*} \sigma_a \right). \quad (6.104)$$

Obviously, we may split Eq. (6.104) into separate components:

$$\begin{aligned}\mathbf{R}_{\widetilde{\Sigma}_s,jk} &= \frac{\Delta x}{2} \int_{-1}^1 \sigma_s b_j(s) b_k(s) \, ds + \dots \\ &\quad \frac{\Delta x}{2} \int_{-1}^1 b_j(s) b_k \left( \frac{4\pi a_{ii} \Delta t \sigma_a D_*}{C_v + 4\pi a_{ii} \Delta t \sigma_a D_*} \sigma_a \right) ds.\end{aligned}\quad (6.105)$$

Clearly

$$\frac{\Delta x}{2} \int_{-1}^1 \sigma_s b_j(s) b_k(s) \, ds = \mathbf{R}_{\sigma_s}, \quad (6.106)$$

so we are left to determine whether

$$\frac{\Delta x}{2} \int_{-1}^1 b_j(s) b_k \left( \frac{4\pi a_{ii} \Delta t \sigma_a D_*}{C_v + 4\pi a_{ii} \Delta t \sigma_a D_*} \sigma_a \right) ds = \bar{\nu}_i \mathbf{R}_{\sigma_a}. \quad (6.107)$$

Using the definition of  $\bar{\nu}_i$  from Eqs. (6.83), we expand  $\bar{\nu}_i \mathbf{R}_{\sigma_a}$ ,

$$\bar{\nu}_i \mathbf{R}_{\sigma_a} = 4\pi \Delta t a_{ii} \mathbf{R}_{\sigma_a} \mathbf{D}_* \left[ \mathbf{I} + 4\pi \Delta t a_{ii} \mathbf{R}_{C_v}^{-1} \mathbf{R}_{\sigma_a} \mathbf{D}_* \right]^{-1} \mathbf{R}_{C_v}^{-1} \mathbf{R}_{\sigma_a}. \quad (6.108)$$

In the general case, when  $\mathbf{R}_{\sigma_a}$  and  $\mathbf{R}_{C_v}$  are dense, Eq. (6.108) will not yield a matrix with elements

$$[\bar{\nu}_i \mathbf{R}_{\sigma_a}]_{jk} \neq \frac{\Delta x}{2} \int_{-1}^1 b_j(s) b_k \left( \frac{4\pi a_{ii} \sigma_a D_*}{C_v + 4\pi a_{ii} \Delta t \sigma_a D_*} \sigma_a \right) ds. \quad (6.109)$$

Though we have showed in the general case,  $\mathbf{R}_{\sigma_s} + \bar{\nu}_i \mathbf{R}_{\sigma_a} \neq \mathbf{R}_{\widetilde{\Sigma}_s}$ , we wish to investigate whether self-lumping DFEM schemes may be better suited for the solution of the TRT equations. Consider an arbitrary, linear DFEM self-lumping scheme, with

the following matrices,

$$\mathbf{R}_{C_v} = \begin{bmatrix} \frac{\Delta x}{2} w_l C_{v,l} & 0 \\ 0 & \frac{\Delta x}{2} w_r C_{v,r} \end{bmatrix} \quad (6.110a)$$

$$\mathbf{R}_{\sigma_a} = \begin{bmatrix} \frac{\Delta x}{2} w_l \sigma_{a,l} & 0 \\ 0 & \frac{\Delta x}{2} w_r \sigma_{a,r} \end{bmatrix} \quad (6.110b)$$

$$\mathbf{D}_* = \begin{bmatrix} D_{*,l} & 0 \\ 0 & D_{*,r} \end{bmatrix} \quad (6.110c)$$

$$D_{*,l} = \left. \frac{dB}{dT} \right|_{T=\tilde{T}_{*,l}} \quad (6.110d)$$

$$D_{*,r} = \left. \frac{dB}{dT} \right|_{T=\tilde{T}_{*,r}} \quad (6.110e)$$

with the  $l$  and  $r$  subscripts denoting values at the two quadrature points,  $s_l$  and  $s_q$ . Since  $\mathbf{R}_{C_v}$  is diagonal,

$$\mathbf{R}_{C_v}^{-1} = \begin{bmatrix} \frac{2}{\Delta x w_l C_{v,l}} & 0 \\ 0 & \frac{2}{\Delta x w_r C_{v,r}} \end{bmatrix}, \quad (6.111)$$

we have

$$[\mathbf{I} + 4\pi\Delta t a_{ii} \mathbf{R}_{C_v}^{-1} \mathbf{R}_{\sigma_a} \mathbf{D}_*]_{11} = 1 + 4\pi\Delta t a_{ii} \left( \frac{2}{\Delta x w_l C_{v,l}} \right) \left( \frac{\Delta x w_l \sigma_{a,l}}{2} \right) D_{*,l} \quad (6.112)$$

$$[\mathbf{I} + 4\pi\Delta t a_{ii} \mathbf{R}_{C_v}^{-1} \mathbf{R}_{\sigma_a} \mathbf{D}_*]_{22} = 1 + 4\pi\Delta t a_{ii} \left( \frac{2}{\Delta x w_r C_{v,r}} \right) \left( \frac{\Delta x w_r \sigma_{a,r}}{2} \right) D_{*,r} \quad (6.113)$$

$$[\mathbf{I} + 4\pi\Delta t a_{ii} \mathbf{R}_{C_v}^{-1} \mathbf{R}_{\sigma_a} \mathbf{D}_*]_{12} = [\mathbf{I} + 4\pi\Delta t a_{ii} \mathbf{R}_{C_v}^{-1} \mathbf{R}_{\sigma_a} \mathbf{D}_*]_{21} = 0. \quad (6.114)$$

Completing the definition of  $\bar{\nu}_i \mathbf{R}_{\sigma_a}$ ,

$$\begin{aligned} \bar{\nu}_i \mathbf{R}_{\sigma_a} &= 4\pi a_{ii} \Delta t \begin{bmatrix} \frac{\Delta x w_l \sigma_{a,l}}{2} & 0 \\ 0 & \frac{\Delta x w_l \sigma_{a,r}}{2} \end{bmatrix} \begin{bmatrix} D_{*,l} & 0 \\ 0 & D_{*,r} \end{bmatrix} \times \dots \\ &\quad \begin{bmatrix} \frac{1}{1+4\pi\Delta a_{ii}\frac{\sigma_{a,l}}{C_{v,l}}} & 0 \\ 0 & \frac{1}{1+4\pi\Delta a_{ii}\frac{\sigma_{a,r}}{C_{v,r}}} \end{bmatrix} \begin{bmatrix} \frac{2}{\Delta x w_l C_{v,l}} & 0 \\ 0 & \frac{2}{\Delta x w_r C_{v,r}} \end{bmatrix} \begin{bmatrix} \frac{\Delta x w_l \sigma_{a,l}}{2} & 0 \\ 0 & \frac{\Delta x w_l \sigma_{a,r}}{2} \end{bmatrix} \end{aligned} \quad (6.115)$$

$$\bar{\nu}_i \mathbf{R}_{\sigma_a} = 4\pi a_{ii} \Delta t \frac{\Delta x}{2} \begin{bmatrix} \frac{w_l \sigma_{a,l} D_{*,l} \frac{\sigma_{a,l}}{C_{v,l}}}{1+4\pi\Delta a_{ii}\frac{\sigma_{a,l}}{C_{v,l}}} & 0 \\ 0 & \frac{w_r \sigma_{a,r} D_{*,r} \frac{\sigma_{a,r}}{C_{v,r}}}{1+4\pi\Delta a_{ii}\frac{\sigma_{a,r}}{C_{v,r}}} \end{bmatrix} \quad (6.116)$$

For some quantity  $f$ , we note that  $\mathbf{R}_f$  with our linear, self-lumping quadrature would be:

$$\mathbf{R}_f = \begin{bmatrix} \frac{\Delta x}{2} w_l f_l & 0 \\ 0 & \frac{\Delta x}{2} w_r f_r \end{bmatrix}. \quad (6.117)$$

Considering Eq. (6.116), and thinking about  $\bar{\nu}_i \mathbf{R}_{\sigma_a} = \mathbf{R}_f$

$$f_l = 4\pi a_{ii} \Delta t \frac{\sigma_{a,l} D_{*,l}}{C_{v,l} + 4\pi\Delta a_{ii}\sigma_{a,l}} \sigma_{a,l} \quad (6.118)$$

$$f_r = 4\pi a_{ii} \Delta t \frac{\sigma_{a,r} D_{*,r}}{C_{v,r} + 4\pi\Delta a_{ii}\sigma_{a,r}} \sigma_{a,r} \quad (6.119)$$

$$f = 4\pi a_{ii} \Delta t \frac{\sigma_a D_*}{C_v + 4\pi\Delta a_{ii}\sigma_a} \sigma_a = \nu_i \sigma_a \quad (6.120)$$

$$\mathbf{R}_{\nu_i \sigma_a} = \bar{\nu}_i \mathbf{R}_{\sigma_a}. \quad (6.121)$$

Thus, when accounting for the within cell spatial variation of material properties, only when using self-lumping DFEM schemes would it be equivalent to

1. linearize the Planckian of the spatially analytic grey TRT and then spatially

discretize, or

2. spatially discretize the grey TRT equations then linear the Planckian.

Given this information, in the most general case, when using MIP DSA to accelerate grey radiative transfer, we define the integration in cell  $k$  (Eq. (4.54) ) as:

$$(\Sigma_a \Delta\phi, b_*) = \mathbf{R}_{\sigma_{\tau,i}} - (\mathbf{R}_{\sigma_s} + \bar{\nu}_i \mathbf{R}_{\Sigma_a}) \vec{\Delta\phi}_k, \quad (6.122)$$

where  $\Delta\phi$  is the low order approximation of the angle integrated intensity error, not the neutron transport scalar flux error. Likewise, we define the MIP DSA driving source, the difference between two successive iterates, as

$$(\Sigma_s(\phi^{(\ell+1/2)} - \phi^{(\ell)}), b_*) = (\mathbf{R}_{\sigma_s} + \bar{\nu}_i \mathbf{R}_{\Sigma_a}) (\vec{\phi}^{(\ell+1)} - \vec{\phi}^{(\ell)}). \quad (6.123)$$

Since we have shown that

$$\mathbf{R}_{\sigma_{\tau,i},jk} = \frac{\Delta x}{2} \int_{-1}^1 ds \left( \frac{1}{a_{ii}c\Delta t} + \sigma_t \right) b_j(s)b_k(s), \quad (6.124)$$

we use the point-wise definition of Eq. (6.102) to evaluate  $\mathbf{S}$  and MIP DSA edge integrals requiring knowledge of a point-wise diffusion coefficient.

## 6.2 Iterative Solution Process

To solve the time-dependent, grey TRT equations, we use a time marching loop with two levels of nested iteration, as detailed through the pseudo-code shown in Listing 6.1.

Listing 6.1: TRT iteration pseudo-code

```

time = t_start; t_step = 0
while !end_of_time
{
    t_step += 1; dt = calculate_dt(t_step, dt_old, time, t_end)
    t_star = t_old
    for stage = 1:1:n_stage
    {
        time_stage = time + dt*c_sdirk[stage]
        damping = 1; thermal_iter = 0; thermal_converged = false
        while !thermal_converged
        {
            thermal_iter += 1; intensity_converged = false; phi_new = 0
            while !intensity_converged
            {
                phi_new = calculate_new_intensity_iterate(t_star)
                change_phi = normalized_diff(phi_new, phi_old)
                intensity_converged = change_phi < epsilon_phi
                phi_old = phi_new
            }
            [t_star, change_t] = update_temperature(t_star, phi_new, damping)
            thermal_converged = change_t < epsilon_temperature
            damping = check_if_damping_needed(thermal_iter)
        }
        k_I[stage] = calculate_k_I(t_star, phi_new)
        k_T[stage] = calculate_k_T(t_star, phi_new)
    }
    advance_intensity(i_old, k_I)
    advance_temperature(t_old, k_T)
    time += dt; end_of_time = time < t_end
}

```

We terminate the thermal iteration using a point-wise relative change criterion. However, we only store two objects of temperature unknowns, each of size  $N_{cell} \times N_P$ , corresponding to  $\vec{T}_n$  and  $\vec{T}_*$ .  $\vec{T}_n$  is modified only after the completion of a time step. This is not a problem, as we already have the point-wise change in temperature,  $\Delta\vec{T} = \vec{T}_*^{(\ell+1)} - \vec{T}_*^{(\ell)}$ , from Eq. (6.79):

$$\begin{aligned}\vec{\Delta T} &= [\mathbf{I} + 4\pi\Delta t a_{ii} \mathbf{R}_{C_v}^{-1} \mathbf{R}_{\sigma_a} \mathbf{D}_*]^{-1} \left[ \vec{T}_n - \vec{T}_* + \Delta t \sum_{j=1}^{i-1} a_{ij} k_{T,j} \right] \dots \\ &\quad + \Delta t a_{ii} [\mathbf{I} + 4\pi\Delta t a_{ii} \mathbf{R}_{C_v}^{-1} \mathbf{R}_{\sigma_a} \mathbf{D}_*]^{-1} \mathbf{R}_{C_v}^{-1} \left[ \mathbf{R}_{\sigma_a} \left( \vec{\phi}_i - 4\pi\vec{B}_* \right) + \vec{S}_T \right], \quad (6.125)\end{aligned}$$

and

$$\text{change\_t} = \max_{c=1}^{N_{cell}} \left[ \max_{j=1}^{N_P} \left[ \left| \frac{\Delta T_j}{T_{j,*}} \right| \right] \right]. \quad (6.126)$$

Likewise, we terminate the intensity update iteration using a point-wise relative change criterion:

$$\text{change\_phi} = \max_{c=1}^{N_{cell}} \left[ \max_{j=1}^{N_P} \left[ \left| \frac{\phi_{c,j}^{(\ell+1)} - \phi_{c,j}^{(\ell)}}{\phi_{c,j}^{(\ell+1)}} \right| \right] \right]. \quad (6.127)$$

Unless otherwise noted, we use an angle integrated intensity convergence criteria  $\epsilon_\phi = 10^{-13}$  and a temperature criteria of  $\epsilon_T = 10^{-11}$ .

Since MIP DSA requires two iterates of the angle integrated radiation energy density,  $\phi^{(\ell+1)}$  and  $\phi^{(\ell)}$ , both of size  $N_{cell} \times N_P$ , we store at least two objects of the same dimensionality as  $\phi$ . We use one of these objects, `phi_new` in Listing 6.1, to update  $\vec{T}^*$ , while the other is local only to the intensity update. Our code is designed to use only a single intensity data object of size  $N_{cell} \times N_P \times N_{dir}$ ,  $\vec{I}_N$ . Limiting ourselves to a single `i_old` requires our intensity update convergence to be based upon the angle integrated intensity and to perform one additional sweep

while calculating  $\vec{k}_I$ . The SDIRK time integration technique requires that we save data objects  $k_T$  and  $k_I$  with,  $N_{stage} \times N_{cell} \times N_P$  and  $N_{stage} \times N_{cell} \times N_P \times N_{dir}$  unknowns, respectively. For all significant values of  $N_{dir}$ , the need to store  $\vec{I}_n$  and  $\vec{k}_I$  dominates the memory footprint of our implementation, and a reasonable upper bound on memory usage is  $(1 + N_{stage}) \times N_{dir} \times N_{cell} \times N_P$ .

### 6.3 Methods for Tolerating Negative Solutions

As shown in Section 3, only linear SLXS Lobatto schemes yield strictly positive angular flux outflows from pure absorbers with arbitrarily spatial variation of cross section. However, we wish to use higher trial space DFEM methods to improve solution accuracy. Since opacity will vary by orders of magnitude within single mesh cells near the Marshak wave front, we expect that we may generate negative angular intensity solutions, which may then generate negative temperature solutions. Though we would prefer to have strictly non-negative angular intensities and temperatures, we must alter our definitions of the Planck function, derivative of the Planck with respect to temperature, and opacities that are temperature dependent, to enable the continued solution of our non-linear thermal radiative transfer simulations in the presence of negative solutions.

We will use the same techniques given by Morel et al. [45] for self-adjoint angular intensity forms of the thermal radiative transfer equations. First, we require that all temperature dependent material properties,  $\sigma_a$ ,  $\sigma_s$ , and  $C_v$  remain positive, despite negative temperature values. In particular, we will  $\sigma_a$  to be

$$\sigma_a(T) = \begin{cases} \sigma_a(T_{cold}) & T < T_{cold} \\ \sigma_a(T) & \text{otherwise} \end{cases}. \quad (6.128)$$

On the basis that:

*a negative intensity contributes to a negative time derivative of the temperature, the Planck function at negative temperatures should similarly contribute to a negative time derivative of the intensity. This implies that the Planck function at negative temperatures should be negative,*

Morel et al. [45] argued that for an arbitrary positive temperature  $\bar{T}$ ,

$$B(-\bar{T}) = -B(\bar{T}) \quad (6.129)$$

$$\left. \frac{dB}{dT} \right|_{T=-\bar{T}} = - \left. \frac{dB}{dT} \right|_{T=\bar{T}}. \quad (6.130)$$

For grey thermal radiative transfer, we define this to be

$$B(-\bar{T}) = \frac{|\bar{T}|}{\bar{T}} \frac{ac\bar{T}^4}{4\pi} \quad (6.131)$$

$$\left. \frac{dB}{dT} \right|_{T=-\bar{T}} = \frac{|\bar{T}|}{\bar{T}} \frac{ac\bar{T}^3}{\pi}. \quad (6.132)$$

## 6.4 Adaptive Time Stepping Methods

To be as efficient as possible, we would like to take as large of time steps as we can while still maintaining some measure of accuracy for our time dependent thermal radiative transfer simulations. Additionally, after a time step, we would like to verify that the solution did not change too rapidly over a single time step. We achieve these goals by using adaptive time stepping algorithms. For those problems that are too large to be clearly over resolved in time, adaptive time stepping algorithms, in general, compare differences in the solution at different time steps. Comparisons can take the form of a high-order/low-order adaptive quadrature to predict error or

may be as simple as permitting only a certain level of relative change per time step. We elect to use relative change time step controllers, taken from and inspired by the work of Edwards, Morel, and Knoll for radiative diffusion [46].

As in [46], given the current time step,  $\Delta t^n$ ,  $\Delta t^n = t^n - t^{n-1}$ , the next time step,  $\Delta t^{n+1}$ ,  $\Delta t^{n+1} = t^{n+1} - t^n$ , is predicted as:

$$\Delta t^{n+1} = \frac{\Delta T_{goal}}{\Delta T} \Delta t^n, \quad (6.133)$$

where  $\Delta T_{goal}$  and  $C_{max}$  are user prescribed values and  $\Delta T$  is a measure of the change in temperature that occurred over  $\Delta t^n$ . Typical values of  $\Delta T_{goal}$  would be on the order of  $\Delta T_{goal} = 0.01$ , corresponding to approximately a 1% increase in temperature across a time step. In addition to also choosing  $\Delta t^{n+1}$  so that we end the simulation at the desired time, we also prescribe a maximum time step size,  $\Delta t_{max}$ , and a maximum allowable increase factor,  $C_{max}$ , so that

$$\Delta t^{n+1} = \min(\Delta t^{n+1}, C_{max} \Delta t^n, \Delta t_{max}). \quad (6.134)$$

We use the adaptive criterion to verify that in advancing the solution from  $t^{n-1}$  to  $t^n$  the solution has not changed too rapidly by enforcing

$$\Delta T < 1.2 \Delta T_{goal}. \quad (6.135)$$

If a given  $\Delta t^n$  has caused Eq. (6.135) to be false, the time step is restarted using a time step that is  $\frac{1}{2}$  the size of the time step that violated our change tolerance.

We will consider three different methods for calculating  $\Delta T$ . Regardless of how we calculate  $\Delta T$ , we will select our next time step according to Eq. (6.133) and Eq. (6.134). In [46], a point-wise formula is prescribed to calculate the adaptive time

criterion  $\Delta T$ ,

$$\Delta T = 2 \max_{i=1,\dots,N_{cell}} \left[ \max_{j=1,\dots,N_P} \left[ \frac{|T_j^n - T_j^{n-1}|}{T_j^n + T_j^{n-1}} \right] \right]. \quad (6.136)$$

If calculating  $\Delta T$  according to Eq. (6.136), we say that we are using the *point-wise* adaptive criterion. In our testing, using Eq. (6.136) resulted in taking extremely small time steps, in particular when considering higher order DFEM spatial discretizations of the thermal radiative transfer equations. We believe this is because the denominator does not account for the possibility of point-wise temperature solutions than the physical limits of the problem. To account for the possibility of lower, possibly even negative temperatures, we also consider a *modified point-wise* temperature criterion:

$$\Delta T = 2 \max_{i=1,\dots,N_{cell}} \left[ \max_{j=1,\dots,N_P} \left[ \frac{|T_j^{n+1} - T_j^n|}{\max(|T_j^{n+1}| + |T_j^n|, T_{offset})} \right] \right], \quad (6.137)$$

where  $T_{offset}$  is a user selected temperature. In practice, Eq. (6.137) with  $T_{offset} = 0$  works for problems in where Eq. (6.136) fails, but still chooses very small time steps. To achieve reasonable time step sizes for higher order DFEM, reasonable being defined as time step sizes comparable against the reported time step sizes of [46] for the same test problem, we often needed to use  $T_{offset}$  on the order of  $50 \times T_{cold}$ , where  $T_{cold}$  is the initial slab temperature for a Marshak wave problem. We refer to our final time adaptive criterion as the *volumetric* adaptive criterion. The volumetric adaptive criterion is inspired by Eq. (6.136). Dividing the spatial mesh into  $N_{groups}$  contiguous groupings of cells, each grouping with  $N_{cg}$  cells, such that  $N_{cell} = N_{groups} \times N_{cg}$ , the volumetric adaptive criterion defines  $\Delta T$  as:

$$\Delta T = 2 \max_{N_{groups}} \left[ \frac{\|\tilde{T}^{n+1} - \tilde{T}^n\|_{2,g}}{\|\tilde{T}^{n+1}\|_{2,g} + \|\tilde{T}^n\|_{2,g}} \right], \quad (6.138)$$

where  $\|\tilde{T}_{g,2}\|$  is an  $L_2$  norm of  $\tilde{T}$  over the space covered by grouping  $g$ :

$$\|\tilde{T}\|_{g,2} = \sqrt{\int_{x_{g-1/2}}^{x_{g+1/2}} (\tilde{T})^2 dx}, \quad (6.139)$$

$x_{g-1/2} = x_{N_{cg}(g-1)+1/2}$ , and  $x_{g+1/2} = x_{N_{cg}g+1/2}$ . We exactly integrate Eq. (6.139) using a  $2P$  point Gauss quadrature.  $N_{cg}$  is user defined, and can range from one to  $N_{cell}$ . When  $N_{cg} = 1$ , the volumetric adaptive criterion is most like the point-wise adaptive criteria. However, increasing  $N_{cg}$  has the same effect as increasing  $T_{offset}$  in Eq. (6.137), thus we will investigate the effect of  $N_{cg}$  on the time step sizes chosen by the volumetric adaptive criterion. We elect to use sum of norms in the denominator of Eq. (6.138) to avoid any cancellation that could occur if either  $\tilde{T}^n$  or  $\tilde{T}^{n+1}$  are negative. Additionally since

$$\|a + b\| \leq \|a\| + \|b\|, \quad (6.140)$$

for any quantities  $a$  and  $b$ , separating the norms results in a larger magnitude denominator, thus making it more likely that larger step sizes will be taken. As will be seen in Section 7, the main drawback of the point-wise and modified point-wise adaptive time criterion is that they select prohibitively small  $\Delta t^{n+1}$ .

## 6.5 Software Implementation

We have implemented our grey radiative transfer equations in a C++ 11 computer code. All attempts have been made to incorporate the best practices of modern, C++ programming and software design[47, 48]. We have made extensive use of the object-oriented programming paradigm of virtual base classes with concrete instantiations. For example, we have compared the effects of different methods of DFEM

mass matrix construction. Regardless of whether we use exact matrix construction, traditional lumping, or self lumping integration, solution of the radiative transfer equations requires access to a mass matrix, for example when calculating  $\vec{k}_I$  in Eq. (6.52). To shelter other portions of our code and programming logic from the particulars of a given simulation’s choice of mass matrix construction, in our radiative transfer implementation, we declared a virtual base class, `V_Matrix_Construction` with pure virtual member function `construct_dimensionless_mass_matrix()`. The concrete instantiations of `V_Matrix_Construction`: `Matrix_Construction_Exact`, `Matrix_Construction_Trad_Lumping`, and `Matrix_Construction_Self_Lumping`, each exhibit the object-oriented programming inheritance “is a” relationship with base class `V_Matrix_Construction`. Then, through the use of C++ 11’s smart pointers, in particular the `std::shared_ptr`, at program run-time we declare, once during the entire program’s execution, the particular instantiation of base class `V_Matrix_Construction` we wish our smart pointer, named `matrix_construction`, to point to/possess. From this point forward, anytime a mass matrix is needed, we simply call `matrix_construction->construct_dimensionless_mass_matrix()`, and, regardless of our choice of DFEM integration strategy, the appropriate mass matrix is returned.

Where possible we have used third party software to prevent duplication of efforts. All Gauss-Legendre, Gauss-Lobatto, and closed Newton-Cotes quadrature functions are derived from the QUADRULE [49] package, with minor modifications including: use C++ `std::vectors` rather than arrays and encapsulation of the QUADRULE functions into a QUADRULE class to limit access and contamination of the global name space. We have directly implemented all of the matrix/vector based equations in this section, as written, using the Eigen linear algebra package [50]. To invert the MIP DSA matrix used to accelerate the iterative solution of the grey TRT equations, we use

the PETSc package[51] preconditioned with algebraic multigrid[41] via the BoomerAMG package of Hypre [52]. We document our code using inline comments and Doxygen [53]. To build and test the components of our grey thermal radiative transfer code, we use the CMake and CTest packages from Kitware[54]. By using CTest to verify and test the code, we have created a set (greater than 50) of unit tests that can be performed every time the code is changed or compiled. Tests range in size from single component to full simulations using the method of manufactured solutions[55] testing for convergence. Though requiring more additional work than simply using `std::cout` to test components as added then commenting out the output statements, CTest allows for continuous testing to find bugs that the programmer would not otherwise suspect. Finally, input parameters for the code are input an XML file, which we read using TinyXML [56].

## 7. GREY THERMAL RADIATIVE TRANSFER- NUMERICAL RESULTS

We now consider several test problems to verify and demonstrate the capability of the self-lumping DFEM spatial discretizations we have developed to solve the grey TRT equations. First, in Section 7.1 we will consider problems with analytic solutions to verify and demonstrate the asymptotic convergence rates of our DFEM and SDIRK discretizations of the grey thermal radiative transfer equations. In Section 7.2, we will consider two Marshak wave problems. A Marshak wave test problem consists of an initially cold slab that is heated by a strong, incident photon source, and is characteristic of several thermal radiative transfer problems of interest, such as inertial confinement fusion. Finally, we summarize the effectiveness of the modified interior penalty diffusion synthetic acceleration operator in accelerating the iterative convergence of the grey TRT equations in Section 7.3.

We present numerical results for several DFEM schemes:

1. TL: traditional mass matrix lumping using equally-spaced interpolation points with cell-wise constant material properties,
2. SL Lobatto: self-lumping quadrature using Lobatto interpolation points with cell-wise constant material properties,
3. SL Gauss: self-lumping quadrature using Gauss interpolation points with cell-wise constant material properties,
4. SLXS Lobatto: self-lumping quadrature using Lobatto interpolation points with approximate integration of spatially varying  $\mathbf{R}$ , and
5. SLXS Gauss: self-lumping quadrature using Gauss interpolation points with approximate integration of spatially varying  $\mathbf{R}$ .

In problems where opacities and heat capacities are constant functions of temperature, SL Lobatto is equivalent to SLXS Lobatto and SL Gauss is equivalent to SLXS Gauss. However, for problems with temperature dependent material properties, SL Lobatto and SL Gauss will approximate the within cell variation of material properties assuming a cell-wise constant equal to the volumetric average of each material property, whereas SLXS Gauss and SLXS Lobatto will explicitly account for the within cell variation of material properties following the example of Eq. (3.8).

Accuracy comparisons will be based upon the discrete  $L_2$  norm of the error in angle integrated intensity,  $E_\phi = \|\tilde{\phi}(x) - \phi(x)\|_{L^2}$ , and the  $L_2$  error in temperature,  $E_T = \|\tilde{T}(x) - T(x)\|_{L^2}$ . We calculate  $E_\phi$  as

$$E_\phi = \sqrt{\sum_{c=1}^{N_{cell}} \frac{\Delta x_c}{2} \sum_{q=1}^{N_{qf}} w_q (\tilde{\phi}(s_q, t_{end}) - \phi(s_q, t_{end}))^2}, \quad (7.1)$$

where  $w_q$ ,  $s_q$  are Gauss quadrature points and  $N_{qf} = 2P + 7$ , and  $P$  is the DFEM trial space degree.  $E_T$  is calculated analogously to  $E_\phi$ . Additionally, we will consider  $L^2$  like norms of the cell average angle integrated intensity,  $E_{\phi_A}$ , and cell average temperature error,  $E_{T_A}$ .  $E_{\phi_A}$  is approximated as:

$$E_{\phi_A} = \sqrt{\sum_{c=1}^{N_{cell}} \frac{\Delta x}{2} \left( \frac{1}{2} \sum_{q=1}^{N_{qf}} w_q \tilde{\phi}(s_q, t_{end}) - \frac{1}{2} \sum_{q=1}^{N_{qf}} w_q \phi(s_q, t_{end}) \right)^2}, \quad (7.2)$$

with  $N_{qf}$  defined as in Eq. (7.1).  $E_{T_A}$  is estimated in a similar fashion.

## 7.1 Problems with Analytic Solutions

### 7.1.1 Su-Olson Problem

The Su-Olson problem [57] is an analytic benchmark that consists of an initially cold (initial radiation energy density and temperature conditions are identically absolute zero) half-space slab, heated for a finite amount of time by a volumetric, isotropic radiation source. The slab's scattering and absorption opacities are constant in space and temperature and  $C_v \propto T^3$ . Assuming  $C_v = \alpha T^3$  is critical; as Long, et al. [58] noted, the assumption regarding  $C_v$  is not physical, but is required to make the thermal radiative transfer equations linear in  $I$  and  $T^4$ , or conversely linear in  $I$  and material energy density. After a series of transformations, Su and Olson derived an analytic solution to the thermal radiative transfer equations under these conditions; their solution is more accurately described as being semi-analytic. While the radiation energy density and material temperature at every point can be expressed as a closed form integral, evaluation of each integral requires numerical estimation. Further, the integral is a 2-D, indefinite integral (in both variables) of a trigonometric function with a slowly decaying exponential argument. However, [57] provides several radiation energy density and material energy density points in space, and thus the Su-Olson problem is beneficial as a benchmark problem to verify the physics of a given radiative transfer implementation.

Given the initial temperature condition is explicitly zero, this implies the initial  $C_v$  is also zero. This is problematic when solving explicitly for temperature and not material energy. A near-zero heat capacity would result in the material rapidly heating, but a zero heat capacity implies a material that cannot accept heat, and thus can never be heated up. To prevent this problem, we modify the definition of

$C_v$ :

$$C_v = 10^{-8} + \alpha T^3. \quad (7.3)$$

Alternatively, we could set an initial temperature to be a non absolute zero value.

Since [57] presents results in a non-dimensional format, we elect to define  $a = c = 1$ ,  $\sigma_a = 1$ ,  $\sigma_s = 0$ ,  $\alpha = 4$ , truncate the full half space to  $x \in [0, 5]$ , and define the reference temperature,  $T_H = 1$ . We solve the problem using 200 spatial mesh cells, linear SLXS Lobatto, the SDIRK 2-2 time differencing scheme, an initial time step size of  $\Delta t = 10^{-5}$ , and increase the time step size by a factor of 1.1 until a maximum time step size of  $\Delta t = 10^{-3}$  is reached.

In Fig. 7.1 we present the radiation energy density solution, ( $W(x)$  in the notation on [57]) for  $S_2$  angular differencing plotted against the analytic diffusion and transport solutions. Likewise, in Fig. 7.2, we plot the material energy density ( $V(x)$  in the notation on [57]) for  $S_2$  angular differencing. Solutions at non-dimensional times  $\tau = 1$  and  $\tau = 10$  are given in both plots. As expected, the  $S_2$  solution is nearly identical to diffusion, but skews slightly in the direction of the full transport solution.

Increasing the number of discrete ordinates, the radiation energy density profile and material energy density profiles are given in Fig. 7.3 and Fig. 7.4 for  $S_8$  angular differencing. By adding a few discrete directions to the quadrature set, our numerical solution becomes indistinguishable from published results of [57], and we conclude that our TRT equation implementation is valid.

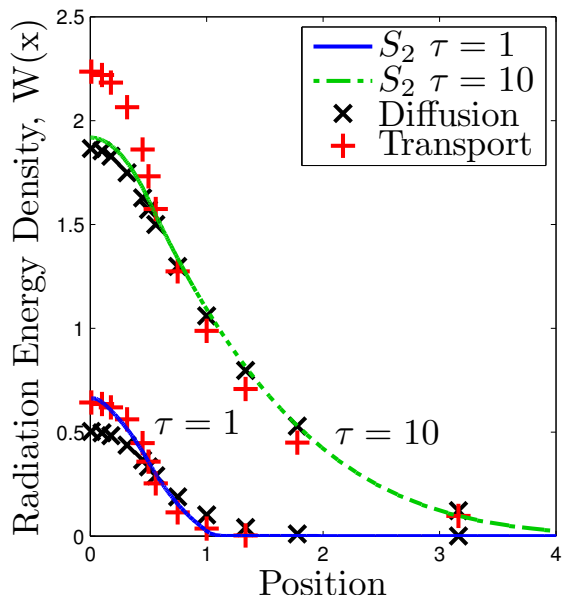


Figure 7.1:  $S_2$  radiation energy density profile for Su-Olson problem.

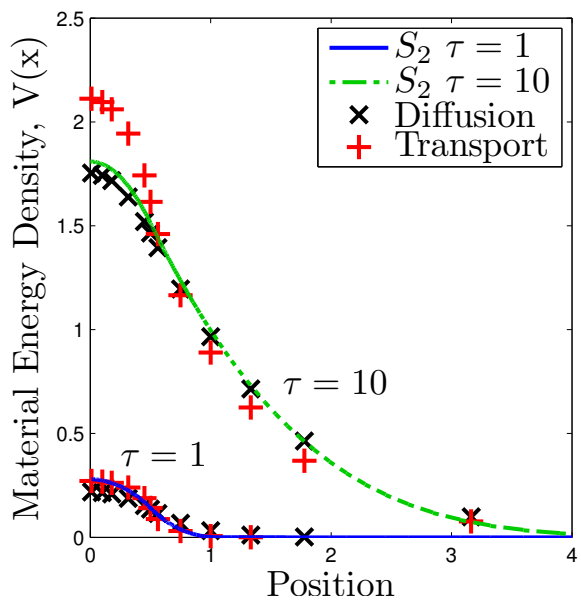


Figure 7.2:  $S_2$  material energy density profile for Su-Olson problem.

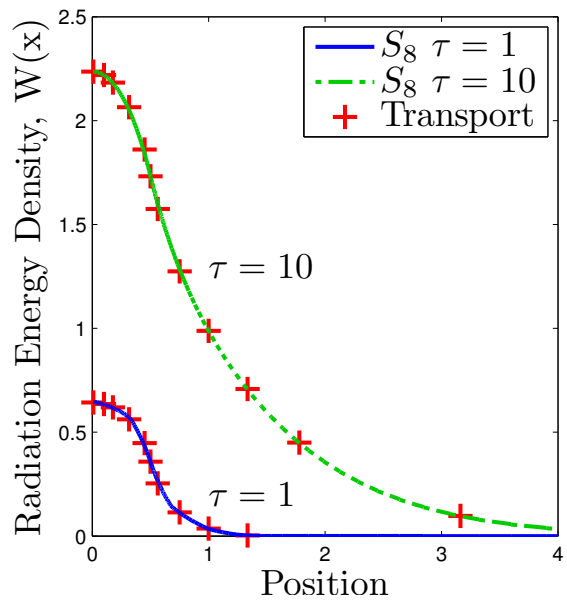


Figure 7.3:  $S_8$  radiation energy density profile for Su-Olson problem.

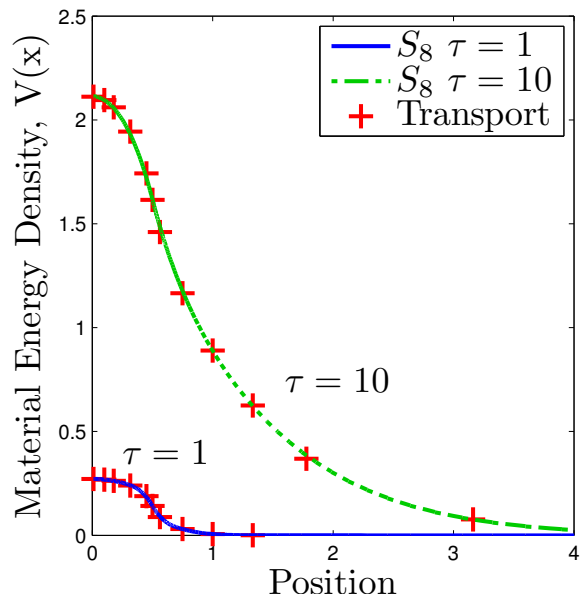


Figure 7.4:  $S_8$  material energy density profile for Su-Olson problem.

### 7.1.2 Method of Manufactured Solutions

The method of manufactured solutions, MMS, consists of choosing an analytic solution, then defining the driving source necessary to achieve that solution [55]. Though MMS solutions are derived, they are excellent for testing the convergence of numerical methods devised to solve complex physics phenomena. While analytic solutions that do not use exotic source terms are more appealing for verification purposes, these types of solutions are difficult to devise for complex physics phenomena, especially for coupled physical phenomena like radiative transfer. For those multi-physics problems for which an analytic solution does exist, the solutions are usually semi-analytic, and cannot be used effectively as a reference solution for a convergence study because the semi-analytic solution has numerical errors of the same magnitude (or greater) than the numerical simulations we are attempting to verify.

We elect to choose separable manufactured solutions of the form:

$$I_d(x, \mu_d, t) = M(\mu_d)F(t)W_I(x) \quad (7.4a)$$

$$T(x) = F(t)W_T(x) \quad (7.4b)$$

$$\phi(x) = C_M F(t)W_I(x) \quad (7.4c)$$

$$C_M = \sum_{d=1}^{N_{dir}} w_d M(\mu_d). \quad (7.4d)$$

where  $M(\mu_d)$  is as angular component of the intensity solution desired,  $I_d(x, \mu_d, t)$ ;  $F(t)$  is the time component of the manufactured solution, chosen to be the same for the angular intensity, angle integrated intensity, and temperature;  $W_I(x)$  is the spatial component of the angular intensity; and  $W_T(x)$  is the spatial component of the temperature solutions. The definition of  $C_M$  given in Eqs. (7.4) and  $W_I(x)$  being the spatial component of  $\phi$  is required for the  $S_N$  approximation to be true.

For all MMS simulations, our initial conditions are

$$I(x, \mu_d, t_0) = M(\mu_d)W_I(x)F(t_0) \quad (7.5)$$

$$T(x, t_0) = W_T(x)F(t_0) \quad (7.6)$$

$$\phi(x, t_0) = \left[ \sum_{d=1}^{N_{dir}} w_d M(\mu_d) \right] W_I(x)F(t_0). \quad (7.7)$$

Likewise, we always use an incident flux intensity boundary condition, for  $\mu_d > 0$ :

$$I_{in}(\mu_d, t) = M(\mu_d)W_I(x_{1/2})F(t), \quad (7.8)$$

and for  $\mu_d < 0$

$$I_{in}(\mu_d, t) = M(\mu_d)W_I(x_{N_{cell}+1/2})F(t), \quad (7.9)$$

where  $x_{1/2}$  is the left domain boundary and  $x_{N_{cell}+1/2}$  is the right domain boundary. We do not impose, and no boundary conditions are required for the material temperature. We evaluate  $\vec{S}_I$  and  $\vec{S}_T$  using the spatially analytic definitions of  $S_I$  and  $S_T$  respectively, and numerically integrate the source moments using a  $N_q$  Gauss-Legendre quadrature points, with  $N_q = 2N_P + 5$ , and  $N_P$  is the number of DFEM interpolation points, as defined previously.

#### 7.1.2.1 Linear in Time - Trigonometric in Space

In our first method of manufactured solutions problem, MMS1, we design a source whose radiation and temperature solutions is a cosine in space and linear in time. We use a non-dimensional form of the TRT, assume that  $a = c = 1$ , and that material opacities and heat capacities are constant functions of space and temperature. We

impose the solution:

$$M(\mu_d) = \frac{1}{4\pi} \quad (7.10)$$

$$W_I(x) = 10 \cos\left(\frac{\pi x}{10} - \frac{\pi}{2}\right) + 15 \quad (7.11)$$

$$W_T(x) = 25 \cos\left(\frac{\pi x}{10} - \frac{\pi}{2}\right) + 30 \quad (7.12)$$

$$F(t) = 1 + .02t. \quad (7.13)$$

Physically,  $x \in [0, 10]$ ,  $C_v = 0.1$ ,  $\sigma_a = 100.0$ ,  $\sigma_s = 0.5$ , we start the simulation at  $t_0 = 0$ , end the simulation at  $t_{end} = 1$ , taking 100 equal time steps of length  $\Delta t = 0.01$ , with the SDIRK 2-2 scheme.

Figure 7.5, Fig. 7.6, and Fig. 7.7 plot the order of convergence of  $E_\phi$  for the TL, SL Lobatto, and SL Gauss schemes, respectively, as a function of trial space degree and cell size. Analogous data for  $E_T$  is given in Figs. 7.8-7.10.

We make several observations regarding Figs. 7.5-7.10. First, the TL scheme does not necessarily increase in accuracy with an increase in trial space degree. TL convergence of  $E_\phi$  is limited to second order in space for odd degree trial space DFEM and third order spatial convergence for even degree trial space schemes, behavior identical to that demonstrated in our neutron transport testing. A similar limit exists for TL convergence of  $E_T$ ; TL converges  $E_T$  at most first order for odd trial space DFEM and second order for even trial space degree DFEM. Second, SL Lobatto converges the  $L^2$  norm of the angle integrated intensity  $\propto P + 1$ , the same order of convergence achieved in our neutron transport test problems for the convergence of  $L^2$  error of the angular and scalar fluxes. However, SL Lobatto only converges  $E_T \propto P$ , not  $P + 1$ , as was the case for the neutron transport interaction rate. Finally, SL Gauss converges  $E_\phi$  and  $E_T \propto P + 1$ , the same order of convergence as seen with neutron transport.

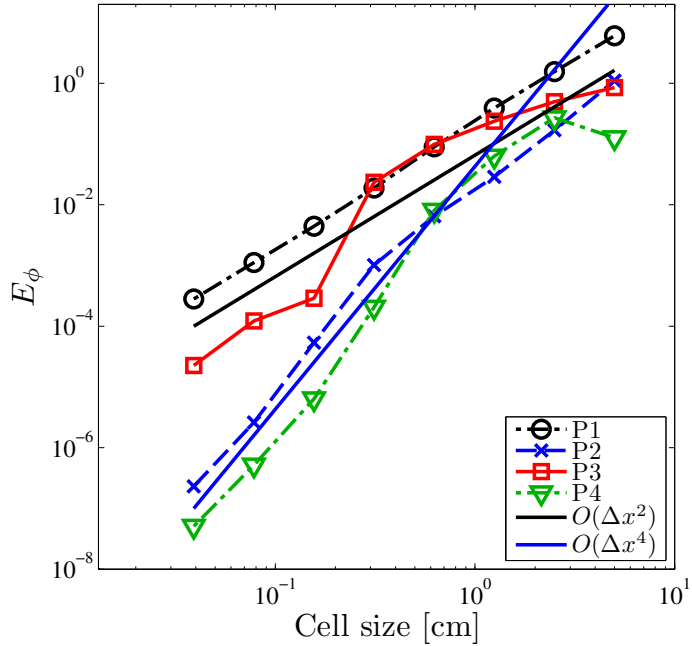


Figure 7.5: Convergence of  $E_\phi$  for the TL scheme in problem MMS1.

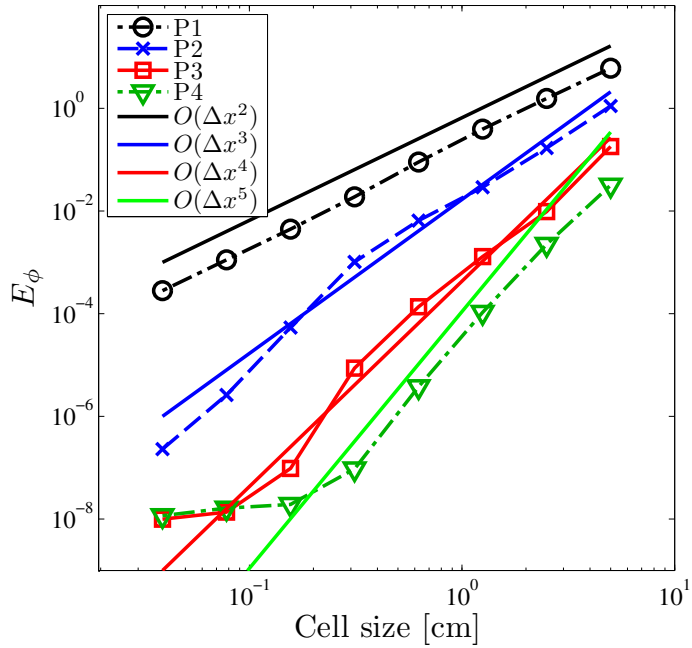


Figure 7.6: Convergence of  $E_\phi$  for the SL Lobatto scheme in problem MMS1.

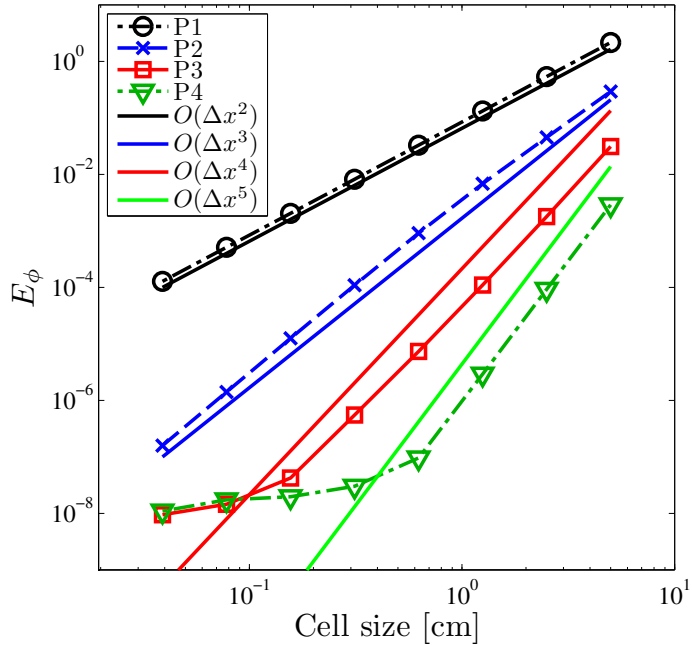


Figure 7.7: Convergence of  $E_\phi$  for the SL Gauss scheme in problem MMS1.

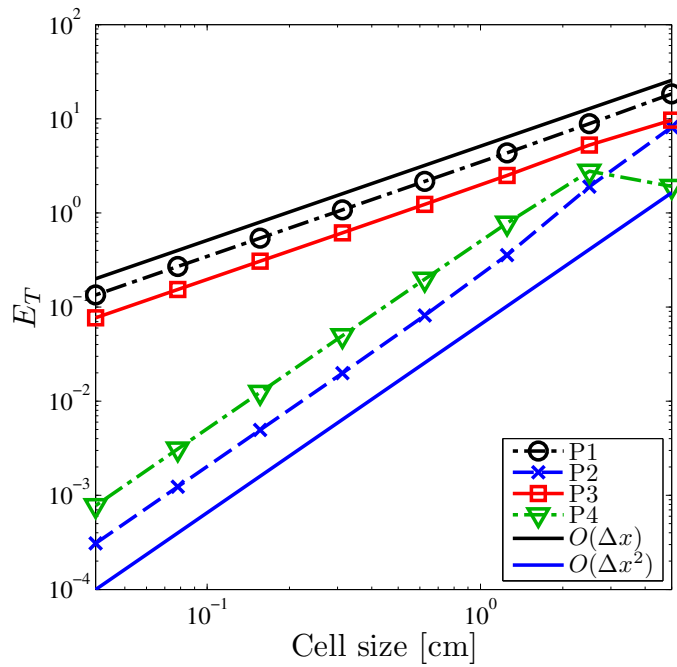


Figure 7.8: Convergence of  $E_T$  for the TL scheme in problem MMS1.

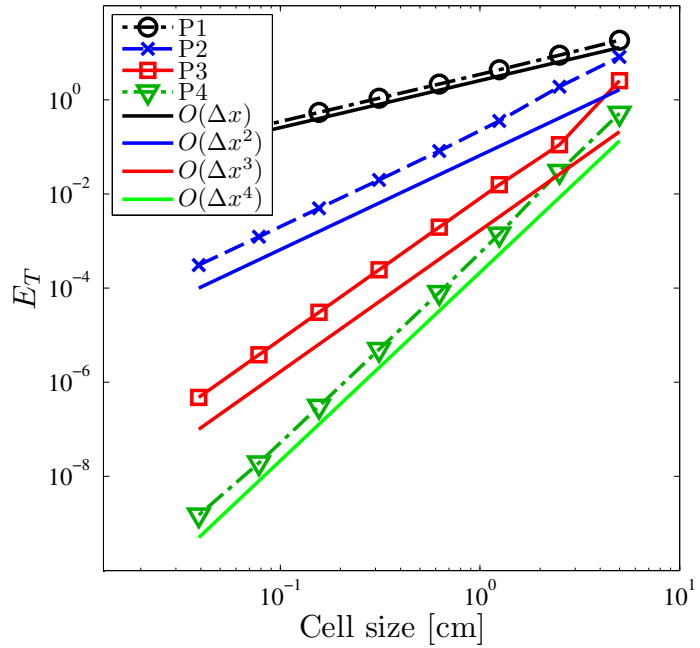


Figure 7.9: Convergence of  $E_T$  for the SL Lobatto scheme in problem MMS1.

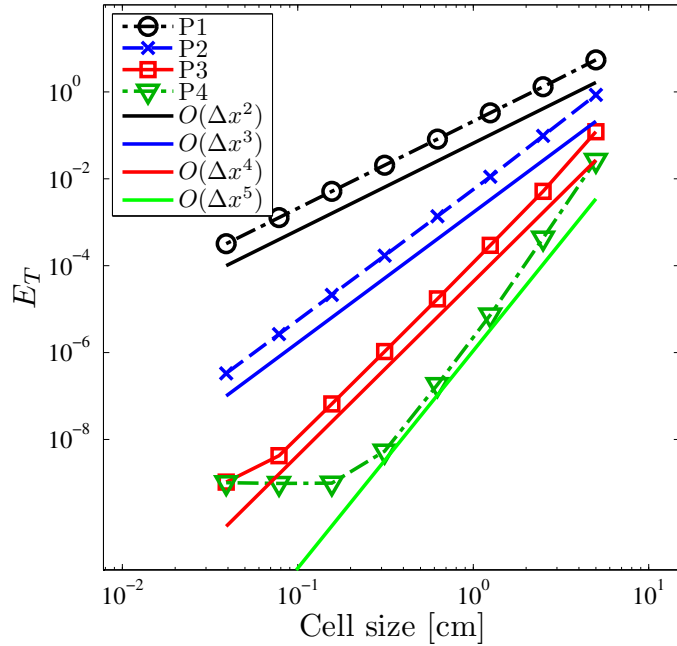


Figure 7.10: Convergence of  $E_T$  for the SL Gauss scheme in problem MMS1.

Convergence of  $E_{\phi_A}$  is given in Fig. 7.11 for SL Lobatto and Fig. 7.12 for SL Gauss. Convergence of  $E_{T_A}$  is given in Figs. 7.13-7.14 for SL Lobatto and SL Gauss, respectively. No definitive pattern emerges in the convergence of  $E_{\phi_A}$  as a function of  $P$  for SL Lobatto in Fig. 7.11 when considering linear through quartic polynomial trial spaces, though SL Lobatto convergence of  $E_{\phi_A}$  looks to be  $\propto 2P$  or slightly less. SL Lobatto's apparent order of convergence for  $E_{\phi_A}$  for TRT problems as shown in Fig. 7.11 is less than SL Lobatto convergence of  $E_{\psi_A}$  for neutron transport (Figs. 2.17-2.20), but not significantly. Similarly, the radiative transfer variant of SL Gauss does not converge  $E_{\phi_A}$  for TRT simulations consistently  $\propto 2P + 1$  as SL Gauss converged  $E_{\psi_A}$  neutron transport problems, but it is close. Interestingly, the observed decreases in the convergence of  $E_{\phi_A}$  for SL Lobatto and SL Gauss when applied to TRT relative to neutron transport convergence of  $E_{\psi_A}$  does not hold when considering the convergence of  $E_{T_A}$ . SL Lobatto converges  $E_{T_A}$  for TRT with the same order as SL Lobatto converges  $E_{\psi_A}$  and  $E_{IR_A}$  for neutron transport,  $\propto 2P$ . SL Gauss actually exhibits an  $E_{T_A}$  order of convergence that appears to exceed its neutron transport analog, converging  $E_{T_A} \propto 2P + 2$ .

It is our hypothesis that the apparent super convergence demonstrated by SL Gauss in converging  $E_T$  is related to how we expand the Planckian in the same trial space as the DFEM temperature and radiation solutions. That is to say that we suspect the  $N_P$  quadrature points of a given trial space degree SL Gauss scheme are significantly more accurate at integrating

$$b_i(s)B(\tilde{T}), \quad (7.14)$$

a degree  $5P$  polynomial, than an  $N_P$  Lobatto quadrature. Though the  $N_P$  point Gauss quadrature only exactly integrates polynomials of degree  $2P + 1$ , it may be

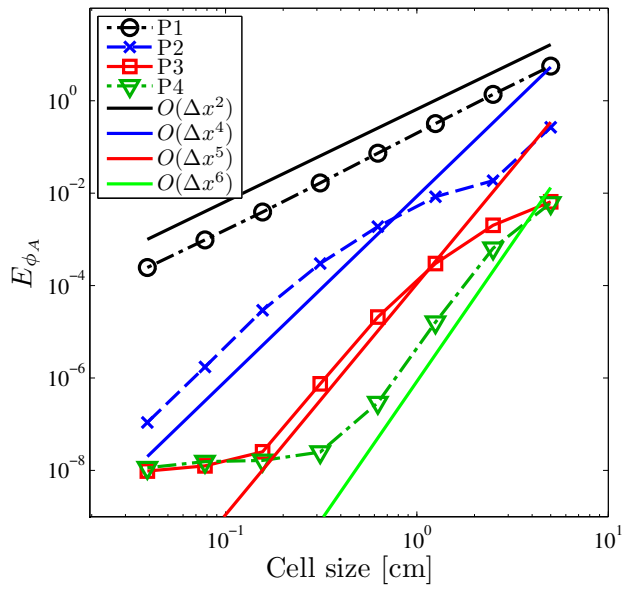


Figure 7.11: Convergence of  $E_{\phi_A}$  for the SL Lobatto scheme in problem MMS1.

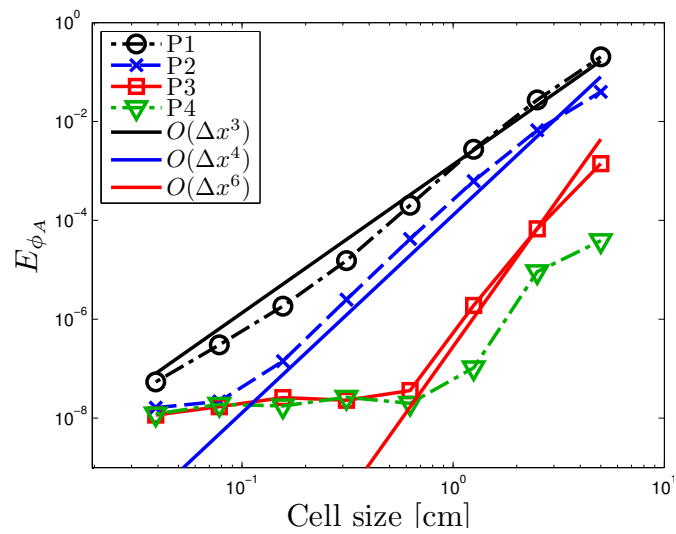


Figure 7.12: Convergence of  $E_{\phi_A}$  for the SL Gauss scheme in problem MMS1.

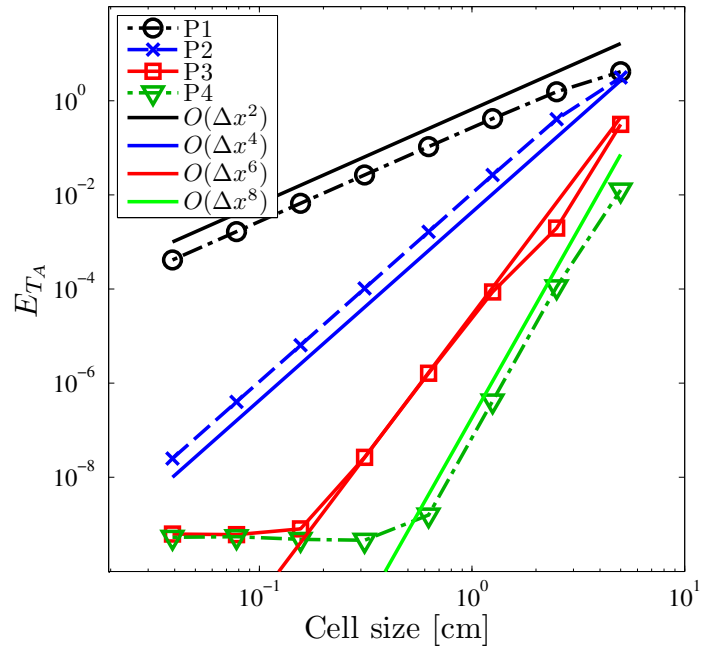


Figure 7.13: Convergence of  $E_{T_A}$  for the SL Lobatto scheme in problem MMS1.

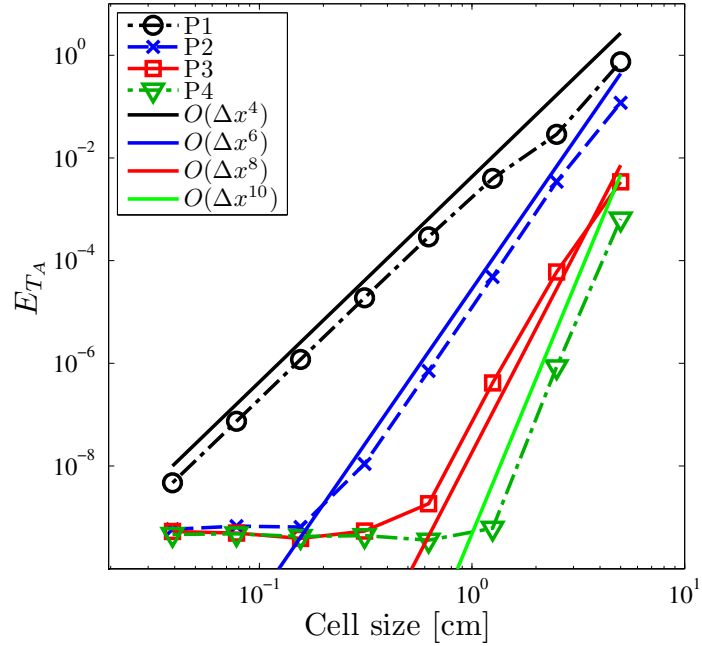


Figure 7.14: Convergence of  $E_{T_A}$  for the SL Gauss scheme in problem MMS1.

that the remaining terms are coincidentally very small in magnitude for a degree  $5P$  polynomial of the particular nature of Eq. (7.14).

### 7.1.2.2 Trigonometric in Space - Linear in Time - with Temperature Dependent Material Properties

We now consider a problem with temperature dependent material properties, MMS2. We impose the following solution:

$$M(\mu_d) = \frac{1}{4\pi} \quad (7.15)$$

$$W_I(x) = 9 \cos\left(\frac{\pi x}{10} - \frac{\pi}{2}\right) + 3, \quad (7.16)$$

$$W_T(x) = 5 \cos\left(\frac{\pi x}{10} - \frac{\pi}{2}\right) + 5, \quad (7.17)$$

$$F(t) = 1 + .02t, \quad (7.18)$$

and define the following material properties:

$$C_v = 0.2 + 0.01T^3 \quad (7.19)$$

$$\sigma_a = \frac{10^4}{T^3} \quad (7.20)$$

$$\sigma_s = 0.5. \quad (7.21)$$

In our problem,  $x \in [0, 10]$ ,  $t \in [0, 2]$  and we discretize in time using the SDIRK 3-3 scheme with  $\Delta t = 0.001$ . In total , we consider four different DFEM schemes for this problem, SL Lobatto, SL Gauss, SLXS Lobatto, and SLXS Gauss. To reiterate, methods denoted SL assume cell-wise constant opacities and heat capacities, equal to the cell-wise volumetric average of that quantity; SLXS schemes explicitly account for the within cell variation of temperature dependent material properties by evaluating  $\mathbf{R}$  as in Eq. (3.8).  $E_\phi$  convergence for the SL Lobatto and SL Gauss schemes is

plotted in Fig. 7.15 and Fig. 7.16, respectively.

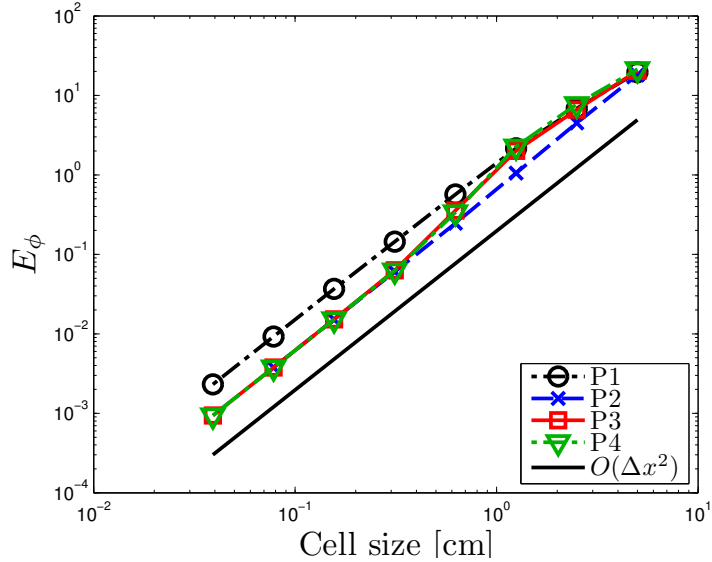


Figure 7.15: Convergence of  $E_\phi$  for the SL Lobatto scheme in problem MMS2.

Regardless of DFEM interpolation point type or trial space degree, assuming cell-wise constant material properties limits spatial convergence of  $E_\phi$  to at most second order. Confirming our suspicion that assuming cell-wise constant material properties limit the convergence of  $E_T$  as well, we plot the convergence of  $E_T$  for the SL Lobatto scheme in Fig. 7.17 and for the SL Gauss scheme in Fig. 7.18. Figures 7.17-7.18 verify the hypothesis we developed while discussing our neutron transport results: assuming a cell-wise constant opacity limits  $L^2$  convergence of temperature to at most first order in space, regardless of DFEM trial space degree.

Recalling that in Section 3, assuming a cell-wise constant cross section equal to the volumetric average cross section in a neutron transport pure absorber problem resulted in a scheme that converged the cell average interaction rate,  $E_{IR_A} \propto 2P+1$ ,

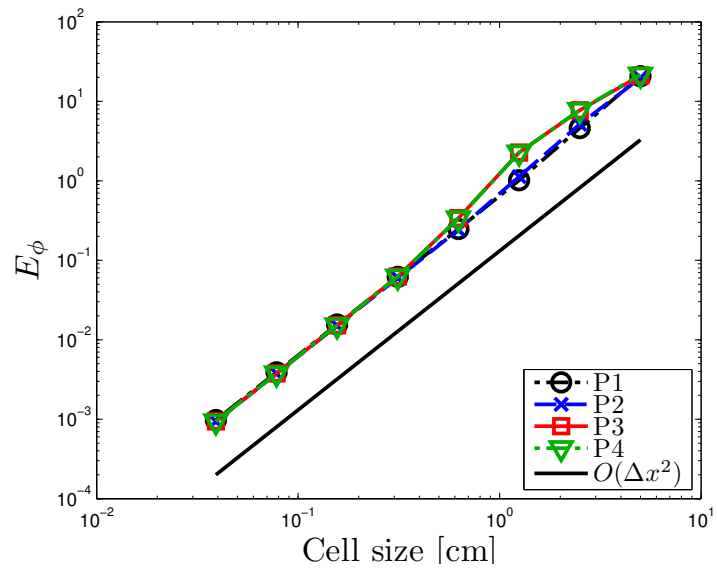


Figure 7.16: Convergence of  $E_\phi$  for the SL Gauss scheme in problem MMS2.

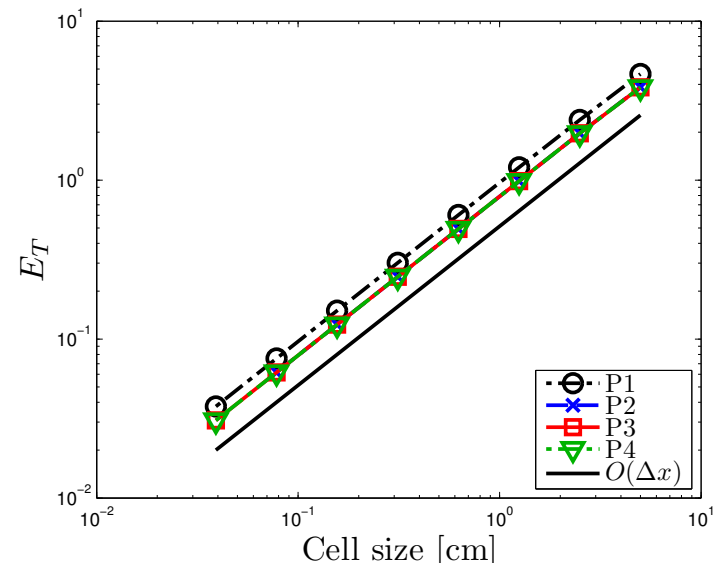


Figure 7.17: Convergence of  $E_T$  for the SL Lobatto scheme in problem MMS2.

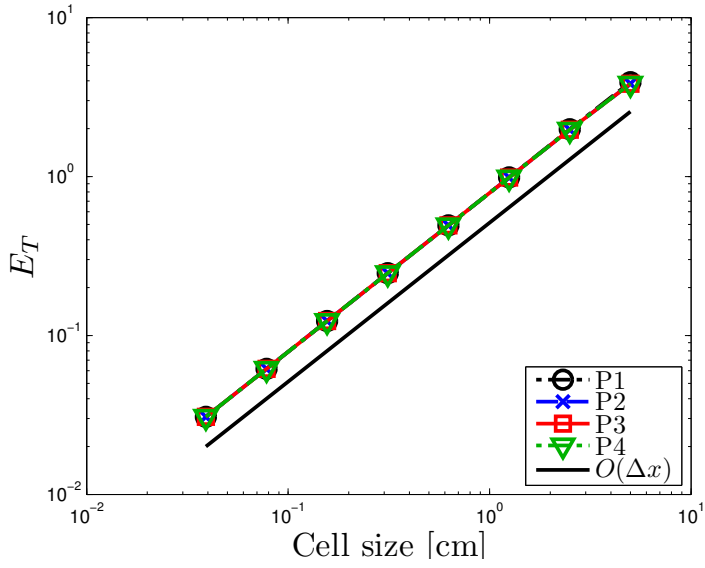


Figure 7.18: Convergence of  $E_T$  for the SL Gauss scheme in problem MMS2.

we now consider convergence of  $E_{T_A}$ , a quantity controlled by cell average interaction rates. in Fig. 7.19 and Fig. 7.20. Figure 7.19 verifies that regardless of trial space degree, the SL Lobatto scheme assuming a cell-wise constant opacity for a problem with temperature or spatially varying opacities converges  $E_{T_A}$  second order in space. Likewise, Fig. 7.20 demonstrates the same is true for the SL Gauss scheme.

We now consider the convergence of SLXS Lobatto and SLXS Gauss. First, we see that in Fig. 7.21, SLXS Lobatto converges  $E_\phi \propto P + 1$ , and in Fig. 7.22, SLXS Gauss converges  $E_\phi \propto P + 1$  as well. Moving on to the convergence of  $E_T$ , in Fig. 7.23 SLXS Lobatto converges  $E_T \propto P$ , the same rate SL Lobatto converged  $E_T$  for the TRT problem with constant material properties. In Fig. 7.24 SLXS Gauss converges  $E_T$  very rapidly, and only the asymptotic convergence rate of linear and quadratic DFEM can be estimated, though both suggest SLXS Gauss converges  $E_T \propto P + 2$ .

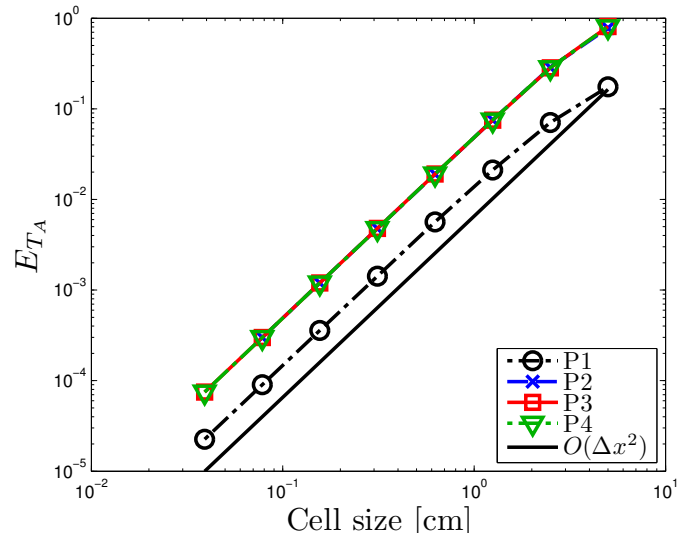


Figure 7.19: Convergence of  $E_{TA}$  for the SL Lobatto scheme in problem MMS2.

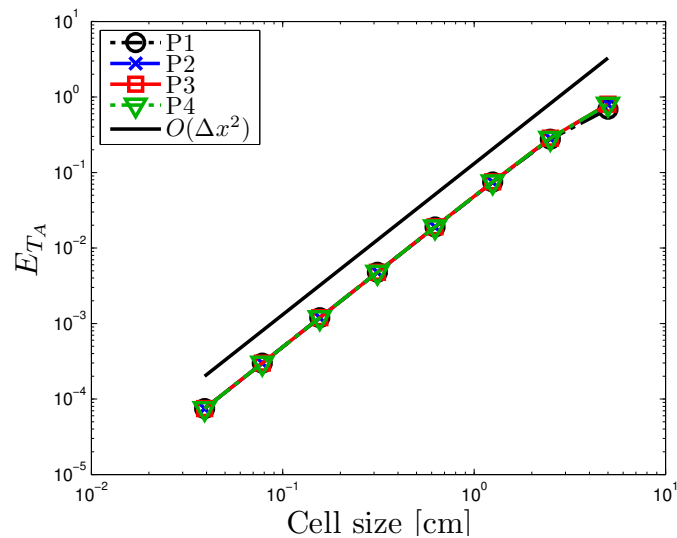


Figure 7.20: Convergence of  $E_{TA}$  for the SL Gauss scheme in problem MMS2.

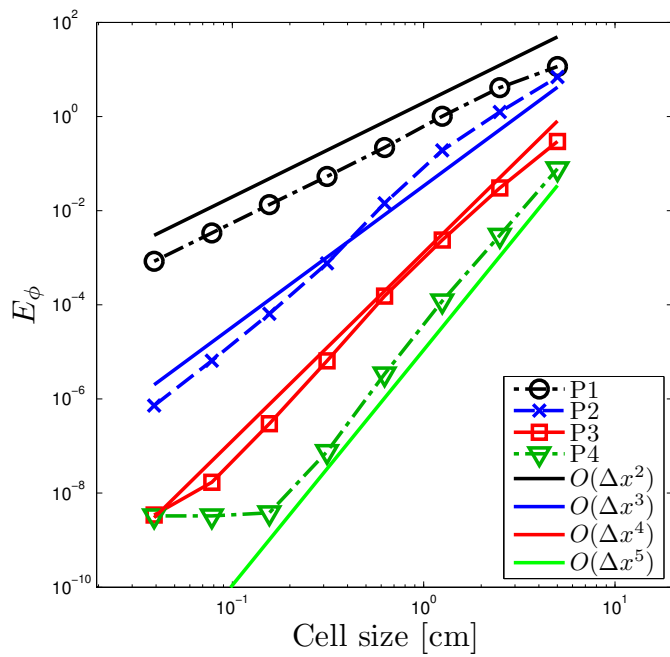


Figure 7.21: Convergence of  $E_\phi$  for the SLXS Lobatto scheme in problem MMS2.

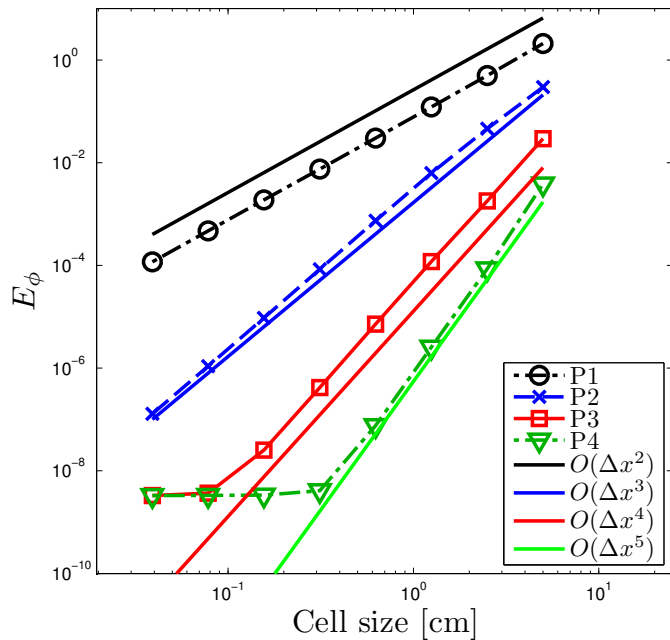


Figure 7.22: Convergence of  $E_\phi$  for the SLXS Gauss scheme in problem MMS2.

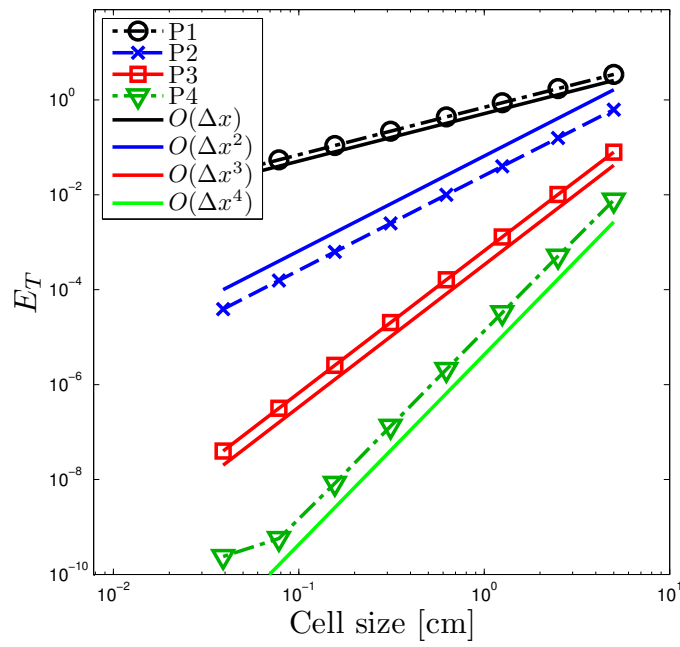


Figure 7.23: Convergence of  $E_T$  for the SLXS Lobatto scheme in problem MMS2.

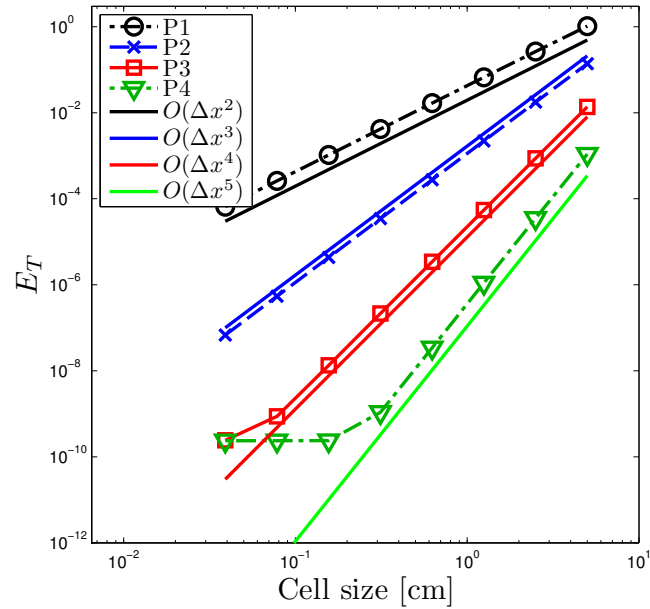


Figure 7.24: Convergence of  $E_T$  for the SLXS Gauss scheme in problem MMS2.

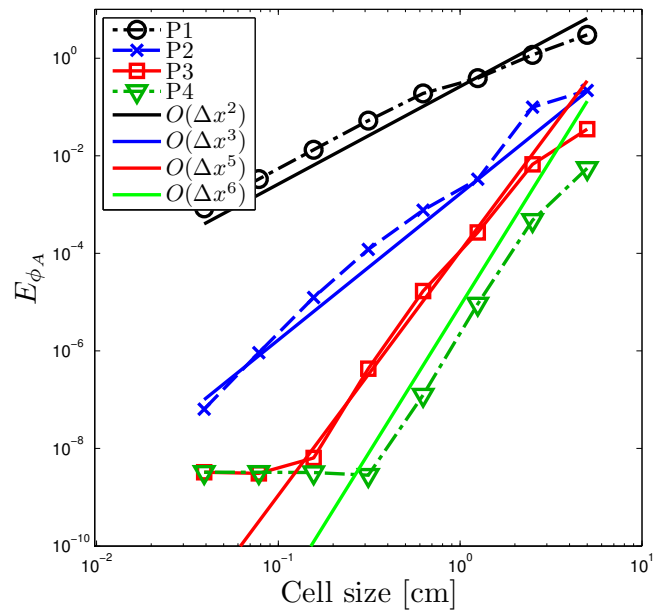


Figure 7.25: Convergence of  $E_{\phi_A}$  for the SLXS Lobatto scheme in problem MMS2.

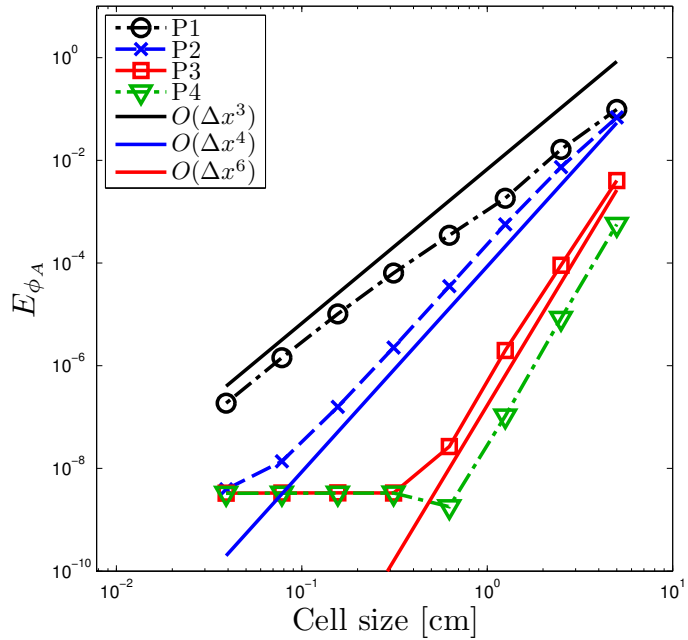


Figure 7.26: Convergence of  $E_{\phi_A}$  for the SLXS Gauss scheme in problem MMS2.

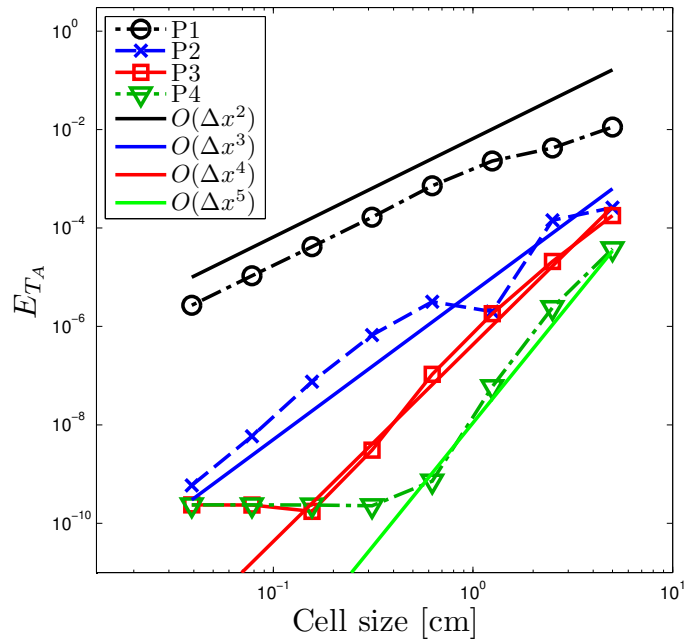


Figure 7.27: Convergence of  $E_{TA}$  for the SLXS Lobatto scheme in problem MMS2.

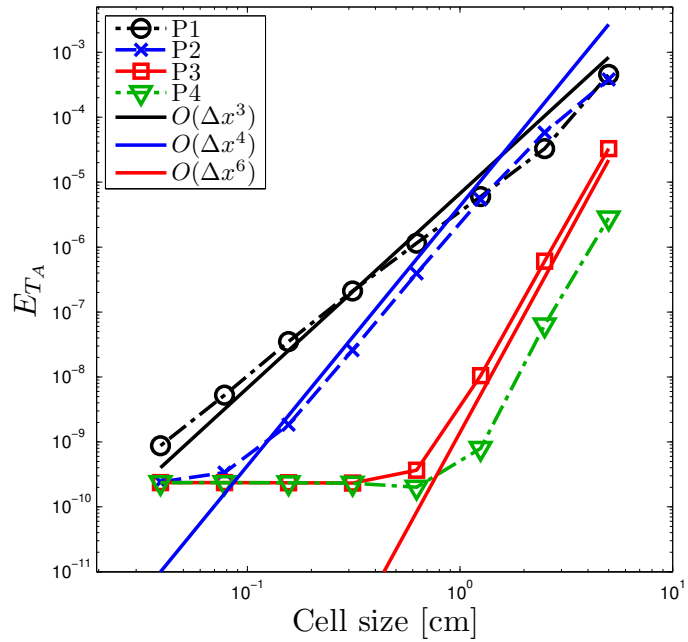


Figure 7.28: Convergence of  $E_{TA}$  for the SLXS Gauss scheme in problem MMS2.

Focusing now on the convergence of cell average error quantities, we first consider  $E_{\phi_A}$  for SLXS Lobatto and SLXS Gauss in Fig. 7.25 and Fig. 7.26, respectively. Both SLXS Lobatto and SLXS Gauss converge  $E_{\phi_A}$  at an order less than or at most equal to the order that their respective neutron transport analogs converged  $E_{\psi_A}$ . However, since both methods require only a small amount of mesh refinement to reach an error level approximately equal to our temperature tolerance, it is difficult to establish with certainty the order of convergence of either method for higher  $P$ . For completeness, we include convergence plots of  $E_{T_A}$  for SLXS Lobatto and SLXS Gauss respectively in Fig. 7.27 and Fig. 7.28. All we can definitively conclude from Figs. 7.27-7.28 is that both SLXS Lobatto and SLXS Gauss experience increases in convergence of  $E_{T_A}$  with increases in trial space degree.

In Figs. 7.5-7.28, the plateauing of errors that appears in some plots is a result of our relative convergence tolerances for both temperature and angle integrated intensity. Given our convergence criteria, we might expect a plateau,  $E_{T,min}$  of approximately

$$E_{T,min} \int_{x_{1/2}}^{x_{N_{cell}+1/2}} \epsilon_T [F_t(t_{end})W_T(x)] dx. \quad (7.22)$$

Applying Eq. (7.22) to MMS1,  $E_{T,min} = 4.6 \times 10^{-8}$ , which is consistent with the location of the  $E_T$  error plateau. In Eq. (7.22), we are implicitly assuming that the error in  $\phi$  is significantly less than the error in temperature. Alternatively, we could consider results generated with less stringent  $\epsilon_T$  and  $\epsilon_\phi$ . In Fig. 7.29 and Fig. 7.30, we give the results for  $E_T$  convergence for the SLXS Gauss scheme and  $E_\phi$  convergence for the SLXS Lobatto scheme for MMS2, but use  $\epsilon_T = 10^{-8}$  and  $\epsilon_\phi = 10^{-10}$ . Comparing the  $E_T$  plateau in Fig. 7.29 of  $\approx 5 \times 10^{-7}$  we see a factor of roughly 1000 increase compared to the plateau observed in Fig. 7.24 for the same quantity, equivalent to the relative relaxations of  $\epsilon_T$  and  $\epsilon_\phi$ . Likewise, the  $E_\phi$  plateau

of  $\approx 10^{-5}$  in Fig. 7.30 is roughly 1000 times greater than the same plateau observed in Fig. 7.21.

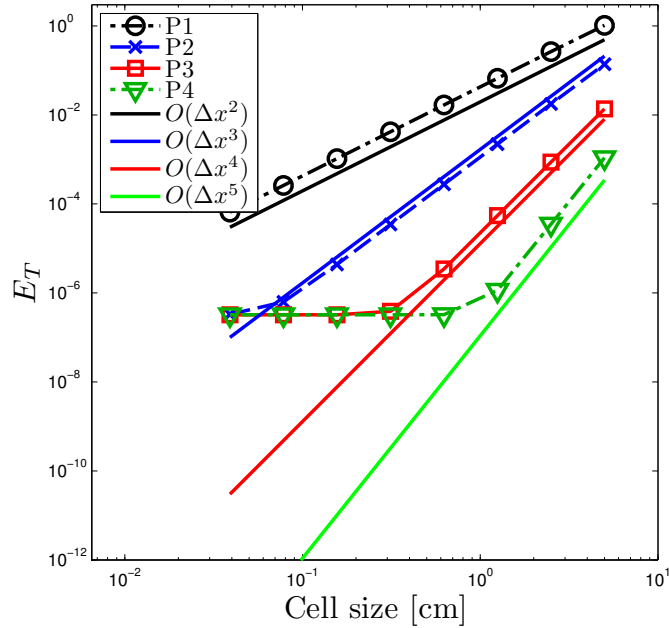


Figure 7.29: Convergence of  $E_T$  for the SLXS Gauss scheme in problem MMS2 using  $\epsilon_T = 10^{-8}$  and  $\epsilon_\phi = 10^{-10}$ .

### 7.1.2.3 Constant in Time - Trigonometric in Space - with Temperature Dependent Material Properties

We now consider a problem that is constant in time and varies as a cosine in space with temperature dependent material properties. Though very similar to MMS2, we hope that by considering a truly steady state problem, we can study the spatial error of our DFEM schemes without temporal error interference. We impose a solution of

the form:

$$M(\mu_d) = \frac{1}{4\pi} \quad (7.23)$$

$$W_I(x) = 19 \cos\left(\frac{\pi x}{2}\right) + 20, \quad (7.24)$$

$$W_T(x) = 15 \cos\left(\frac{\pi x}{2}\right) + 20, \quad (7.25)$$

$$F(t) = 10 \quad (7.26)$$

and define the following material properties:

$$C_v = 0.1 + 0.2T^2 \quad (7.27)$$

$$\sigma_a = \frac{5}{T^2} \quad (7.28)$$

$$\sigma_s = 0.01. \quad (7.29)$$

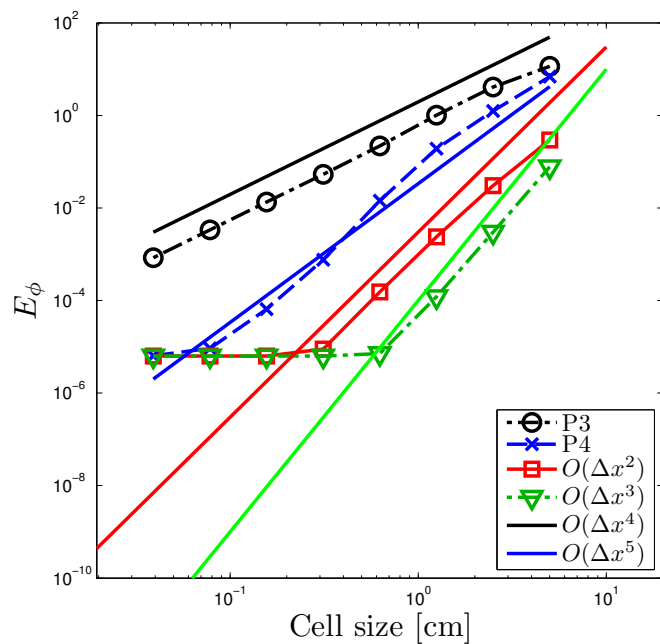


Figure 7.30: Convergence of  $E_\phi$  for the SLXS Lobatto scheme in problem MMS2 using  $\epsilon_T = 10^{-8}$  and  $\epsilon_\phi = 10^{-10}$ .

Repeating as we have before, we first consider the convergence of  $E_\phi$  for SLXS Lobatto and SLXS Gauss in Fig. 7.31 and Fig. 7.32. As before, SLXS Lobatto

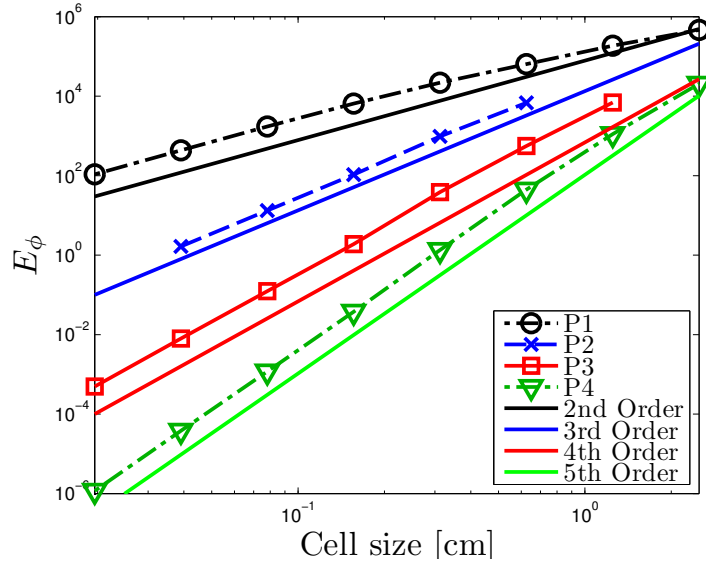


Figure 7.31: Convergence of  $E_\phi$  for SLXS Lobatto scheme for steady state test problem.

converges  $E_\phi \propto P + 1$ . However, SLXS Gauss appears to converges  $E_\phi \propto P + 2$ . It is not clear why SLXS Gauss convergence of  $E_\phi$  increases when moving from the time dependent MMS1 and MMS2 problems to the steady-state test problem.

Now considering the convergence of  $E_T$ , the steady-state problem confirms SLXS Lobatto converges  $E_T \propto P$ , shown in Fig. 7.33, and SLXS Gauss converges  $E_T \propto P + 2$ , as shown in Fig. 7.34.

We now examine the convergence of  $E_{\phi_A}$ . The estimated order of convergence of  $E_{\phi_A}$  in Fig. 7.35 for SLXS Lobatto, appears to be  $\propto 2P$ , greater than the results from MMS1 and MMS2, but equal to what we would have hypothesized from neutron

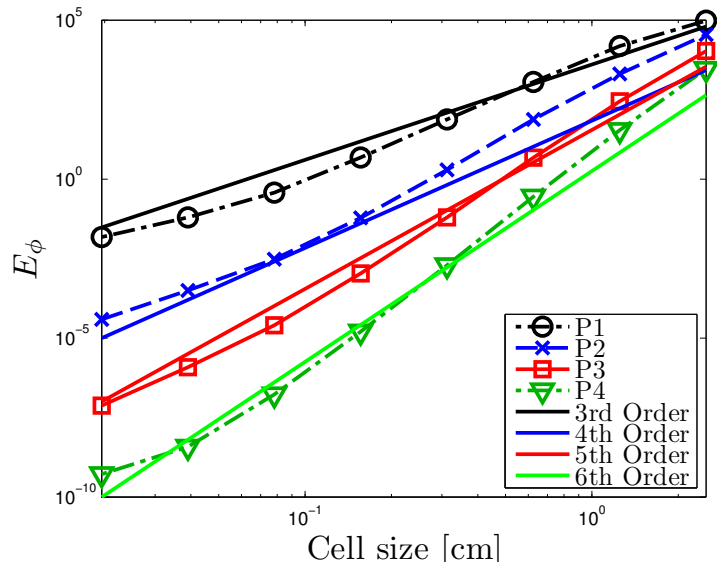


Figure 7.32: Convergence of  $E_\phi$  for SLXS Gauss scheme, for steady state test problem.

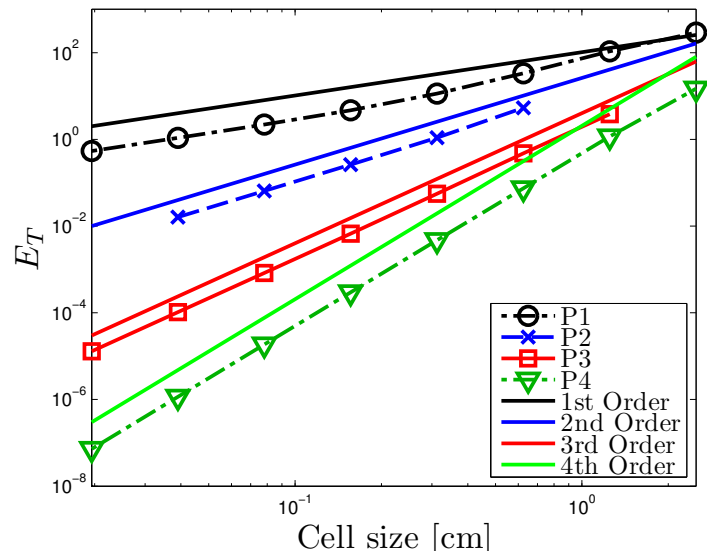


Figure 7.33: Convergence of  $E_T$  for SLXS Lobatto scheme, for steady state test problem.

transport. Similarly the convergence of  $E_{\phi_A}$  for SLXS Gauss estimated in Fig. 7.36 appears to be greater,  $\propto 2P + 2$ , than the SLXS Gauss order of convergence for  $E_{\phi_A}$ ,  $< 2P + 1$ , given in Fig. 7.26.

Finally, we consider the convergence of  $E_{T_A}$ . In Fig. 7.37 SLXS Lobatto converges  $E_{T_A} \propto 2P$ , and in Fig. 7.38 SLXS Gauss converges  $E_{T_A} \propto 2P + 2$ . Both of these convergence rates are higher than those observed in any of our previous MMS test problems. The SLXS Lobatto  $E_{T_A}$  convergence rate is equal to the SLXS Lobatto convergence rates for  $E_{\psi_A}$  and  $E_{IR_A}$ , whereas the SLXS Gauss  $E_{T_A}$  convergence rate is greater than any convergence rate observed for SLXS Gauss for neutron transport.

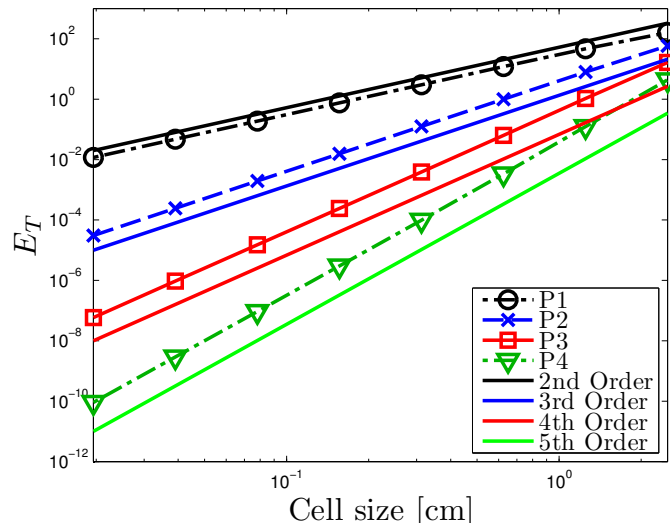


Figure 7.34: Convergence of  $E_T$  for SLXS Gauss scheme, for steady state test problem.

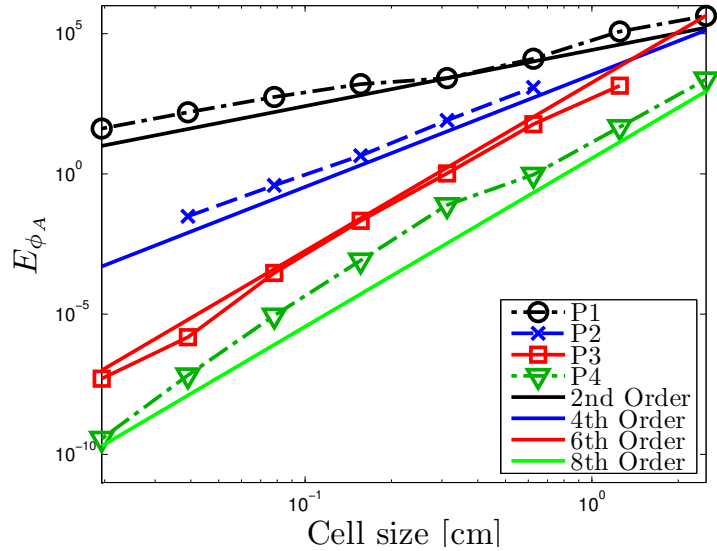


Figure 7.35: Convergence of  $E_{\phi_A}$  for SLXS Lobatto scheme, for steady state test problem.

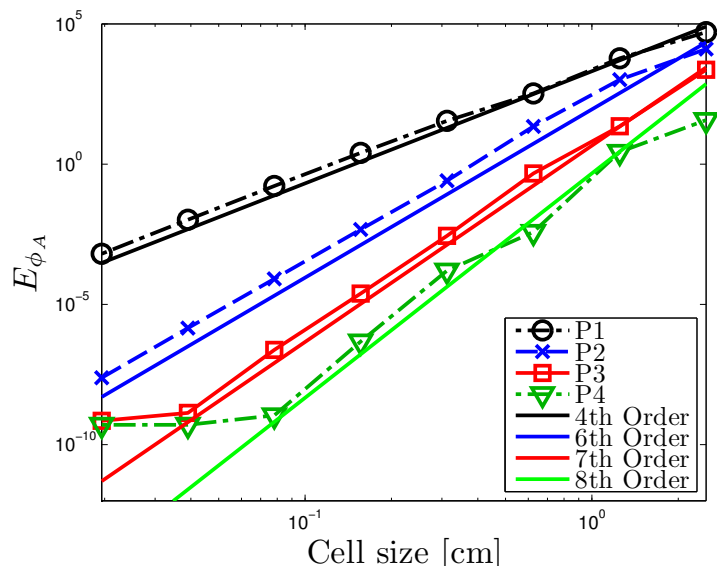


Figure 7.36: Convergence of  $E_{\phi_A}$  for SLXS Gauss scheme, for steady state test problem.

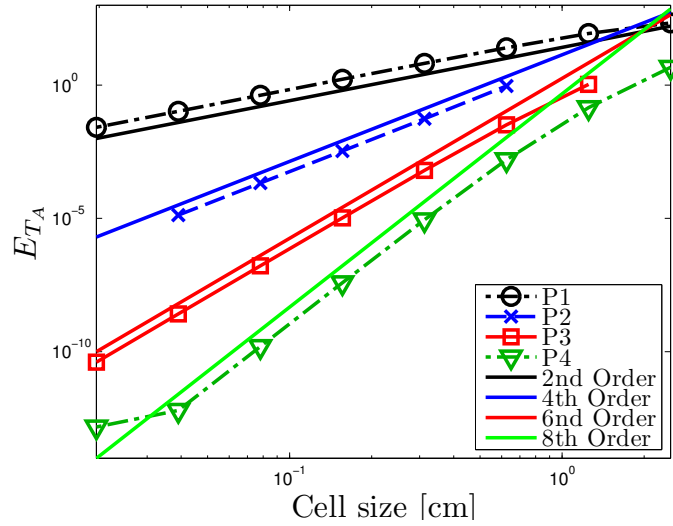


Figure 7.37: Convergence of  $E_{TA}$  for SLXS Lobatto scheme, for steady state test problem.

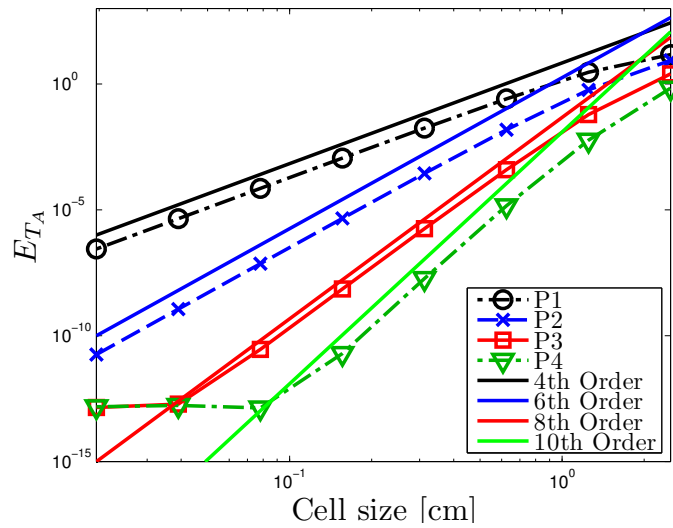


Figure 7.38: Convergence of  $E_{TA}$  for SLXS Gauss scheme, for steady state test problem.

#### 7.1.2.4 Constant in Space - Trigonometric in Time

We now verify the asymptotic order of convergence of each SDIRK scheme: IE, SDIRK 2-2, and SDIRK 3-3, as a function of time step size. To simplify the process, we consider a problem with constant spatial dependence:

$$M(\mu_d) = \frac{1}{4\pi} \quad (7.30)$$

$$W_I(x) = \frac{10}{4\pi} \quad (7.31)$$

$$W_T(x) = 10 \quad (7.32)$$

$$F(t) = 45 \cos(\pi t) + 46, \quad (7.33)$$

$t \in [0, 1]$ ,  $\sigma_s = 0.1$ ,  $\sigma_a = 2.5$ ,  $C_v = 0.2$ ,  $x \in [0, 10]$  discretized with 10 equally spaced cells. Convergence of  $E_\phi$  as a function of  $\Delta t$  for the IE, 2-2, and 3-3 time differencing schemes is given in Fig. 7.39. As expected, IE converges 1st order in time, SDIRK 2-2 converges second order, and SDIRK 3-3 converges third order in time. The same data for temperature is given in Fig. 7.40. Though the SDIRK 2-2 and SDIRK 3-3 schemes are always more accurate than IE, much smaller time steps were required for SDIRK 2-2 and SDIRK 3-3 to demonstrate their respective asymptotic orders of convergence for  $E_T$  than were required to reach asymptotic convergence of  $E_\phi$  with respect to time step size.

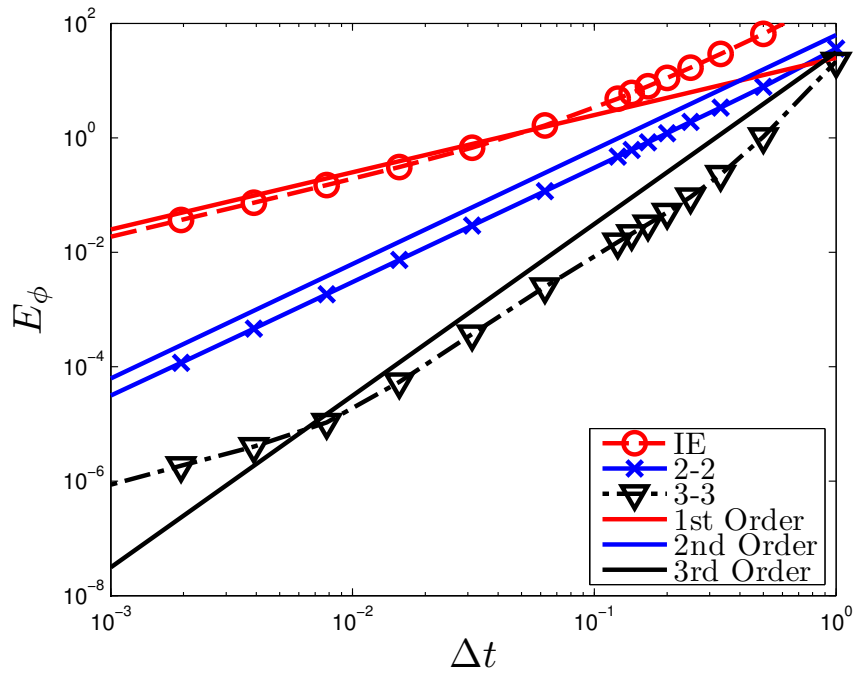


Figure 7.39: Convergence of  $E_\phi$  for different time integrators as a function of  $\Delta t$ .

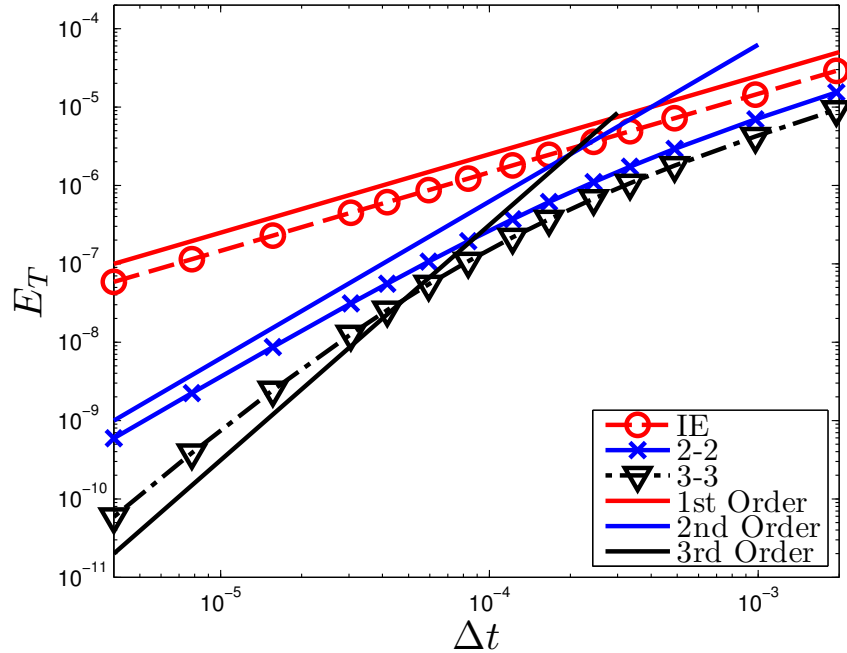


Figure 7.40: Convergence of  $E_T$  for different time integrators as a function of  $\Delta t$ .

## 7.2 Thermal Radiative Transfer Simulations Without Analytic Solutions

We now consider two Marshak wave test problems. In thermal radiative transfer problems, at low temperatures, materials are generally optically thick and emit very few photons, behaving like pure absorbers. However, as the material heats up, its optical thickness decreases, photon emission increases, and the problem becomes very diffusive. Marshak wave test problems, problems that begin with a cold material that is heated by an incident photon beam, are extremely challenging for discrete ordinates transport spatial discretizations, requiring methods that are accurate in both transport effects (cold material) and diffusive (heated material) regimes, and that can handle rapid variations in material properties.

The first problem, originally described by Ober and Shadid for radiative diffusion [9], arbitrarily sets  $a = c = C_v = 1$ , and as such, we will refer to it as the “unity” Marshak wave problem. Originally proposed in 1960 by Petschek and Williamson [59], but considered more recently in [45, 46], our second Marshak wave problem has a similar opacity dependence,  $\sigma_a \propto T^{-3}$ , as the unity Marshak wave problem, but uses physical units. We thus refer to the second Marshak wave problem as the physical Marshak wave problem.

### 7.2.1 Unity Marshak Wave Problem

Given as a radiative diffusion problem, we adapt the radiative diffusion problem of [9] to discrete ordinates thermal radiative transfer by interpreting the left boundary to be a unit isotropic incident current. The physical domain is  $x \in [0, 1]$  and we advance the solution from  $t = 0$  to  $t = 1$ . Initially, the slab is in thermal equilibrium, and  $T = (10^{-5})^{1/4}$ . There is no scattering,  $\sigma_s = 0$ , and the absorption opacity is temperature dependent,  $\sigma_a = \frac{1}{T^3}$ . Like most thermal radiative transfer problems, no analytic solution exists. As such, we focus on qualitative comparisons of how DFEM

trial space degree, mesh refinement, and time step refinement affect the radiation energy density and material temperature solutions.

We use an initial mesh of 20 cells, but also consider results using meshes of 80, 320, and 1280 cells. Unless otherwise noted, for all simulations we use the SDIRK 2-2 time discretization. We begin with a minimum time step of  $\Delta t = 5 \times 10^{-4}$  and increase the time step size by 10% until we reach a maximum time step size of  $\Delta t = 10^{-2}$ . For our time refinement studies, we divide the minimum and maximum time step sizes both by a factor of 4, 16, or 64. We consider linear, quadratic, cubic and quartic SLXS Lobatto and SLXS Gauss schemes. To demonstrate that assuming a cell-wise constant opacity results in a bladed TRT temperature solution, we also consider linear SL Lobatto with a cell-wise volumetric average opacity.

We first investigate the effect of assuming a cell-wise constant opacity. Figure 7.41 shows the linear SL Lobatto radiation energy density solution at  $t = 1.0$ . Except for the effects of a very coarse spatial mesh when using 20 cells, the radiation energy density solution is effectively smooth, and comparable to the results published in [9]. The full temperature solution is shown in Fig. 7.42. Clearly, the large, non-monotonic discontinuities (blading) observed in the neutron transport interaction rate profile are present in the TRT temperature profile. In Fig. 7.42, mesh refinement reduces the magnitude of the temperature solution blading but does not eliminate the phenomena. To emphasize that blading is not eliminated with mesh refinement, consider Fig. 7.43, that zooms in on the material temperature solution near the Marshak wavefront. Clearly, Fig. 7.42 and Fig. 7.43, in addition to the limited order of convergence results of Fig. 7.17 and Fig. 7.18 demonstrate that the assumption of a cell-wise constant opacity is not appropriate for thermal radiative transfer simulations with temperature dependent material properties.

For comparison, consider the linear SLXS Lobatto radiation energy density solu-

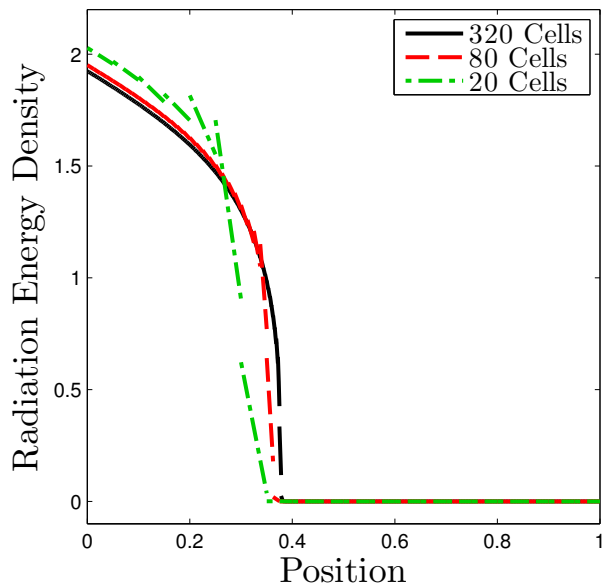


Figure 7.41: Linear SL Lobatto radiation solution for the unity Marshak wave problem assuming cell-wise constant volumetric averaged opacities.

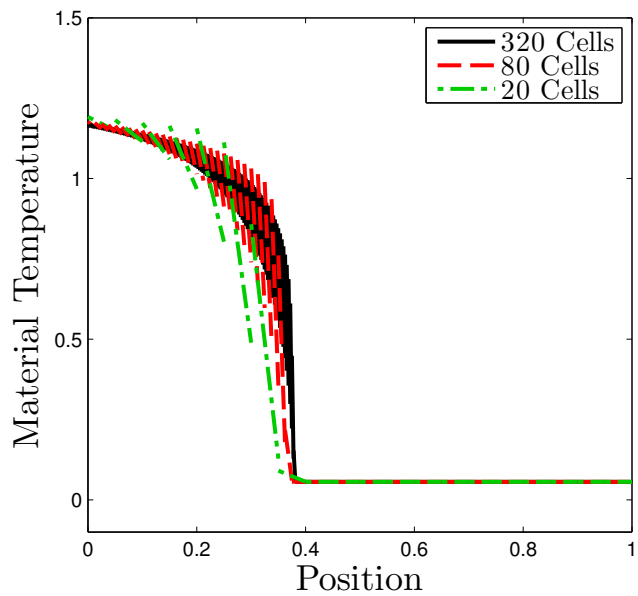


Figure 7.42: Linear SL Lobatto temperature solution for the unity Marshak wave problem assuming cell-wise constant volumetric averaged opacities.

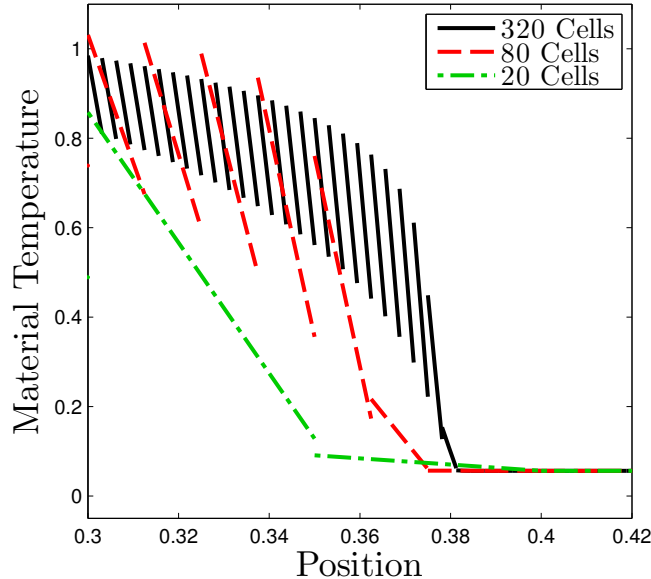


Figure 7.43: Linear SL Lobatto temperature solution for the unity Marshak wave problem near the wavefront.

tion in Fig. 7.44 and the temperature solution in Fig. 7.45, computed using 80 mesh cells. Visually, there is little difference between the SL Lobatto and SLXS Lobatto angle integrated intensity solutions. However, this is not the case when examining the material temperature solutions. Unlike Fig. 7.42, Fig. 7.45 does not exhibit any blading.

We now consider the effects of spatial mesh refinement on the unity Marshak wave problem. We first consider the linear SLXS Lobatto scheme, looking at a zoom in near the wavefront of the radiation profile in Fig. 7.46 and the material temperature profile in Fig. 7.47. Though the changes are subtle, we can see that mesh refinement actually changes the location of both the radiation and temperature profile wavefront, with the changes more prominent in the material temperature profile,

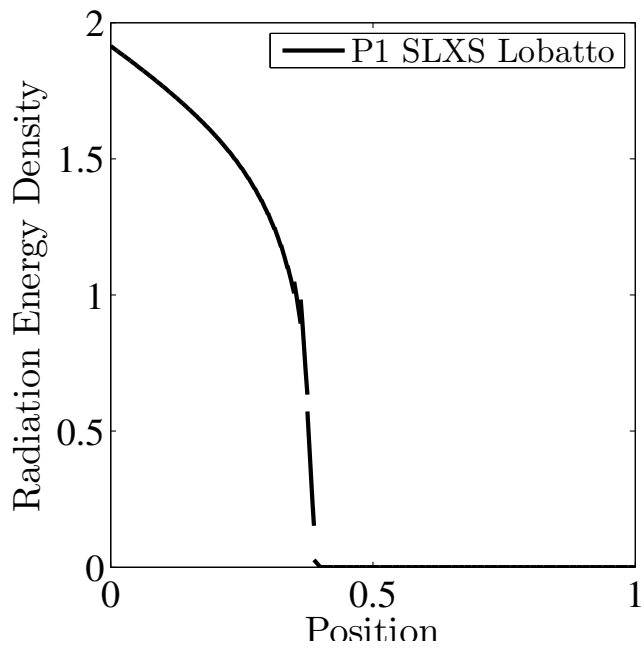


Figure 7.44: Linear SLXS Lobatto angle integrated intensity solution with 80 cells.

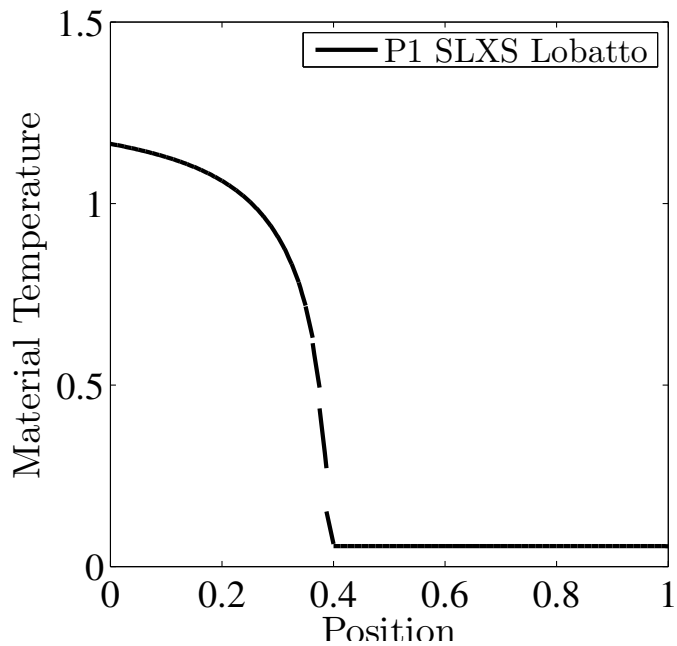


Figure 7.45: Linear SLXS Lobatto temperature solution with 80 cells.

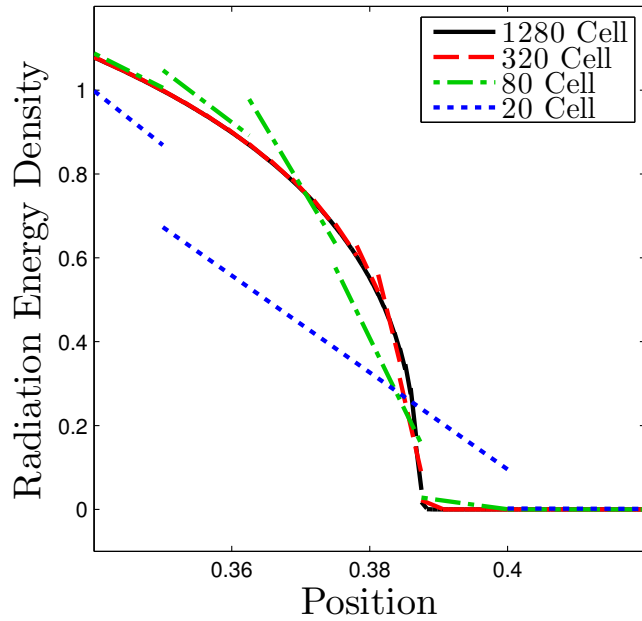


Figure 7.46: Linear SLXS Lobatto radiation solution near wavefront with increasing spatial mesh refinement.

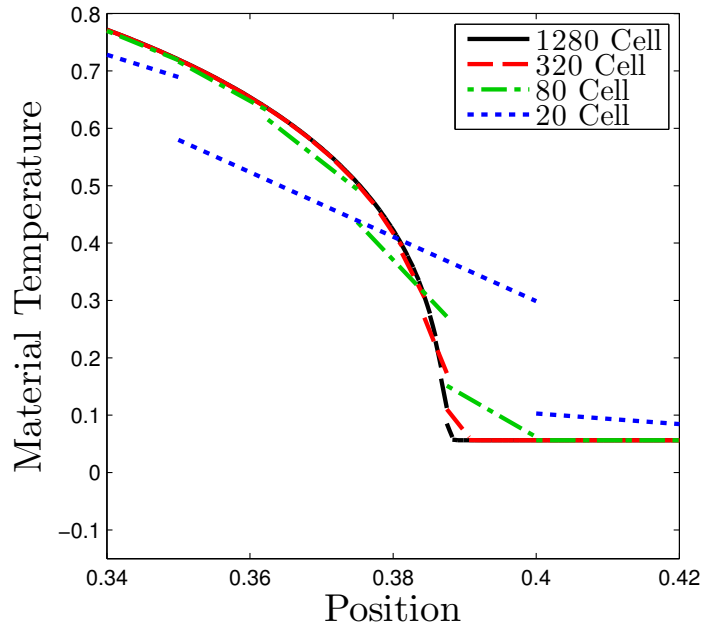


Figure 7.47: Linear SLXS Lobatto temperature solution near wavefront with increasing spatial mesh refinement.

Fig. 7.47. The changes in the material temperature profile are more pronounced than in the radiation profile because linear SLXS Lobatto more accurately calculates the radiation intensity than the material temperature, converging  $E_\phi \propto 2$  and  $E_T \propto 1$ . Equivalent plots to Fig. 7.46 and Fig. 7.47 are provided in Fig. 7.48 and Fig. 7.49, respectively for the quartic SLXS Gauss scheme. Due to the SLXS Gauss' high order

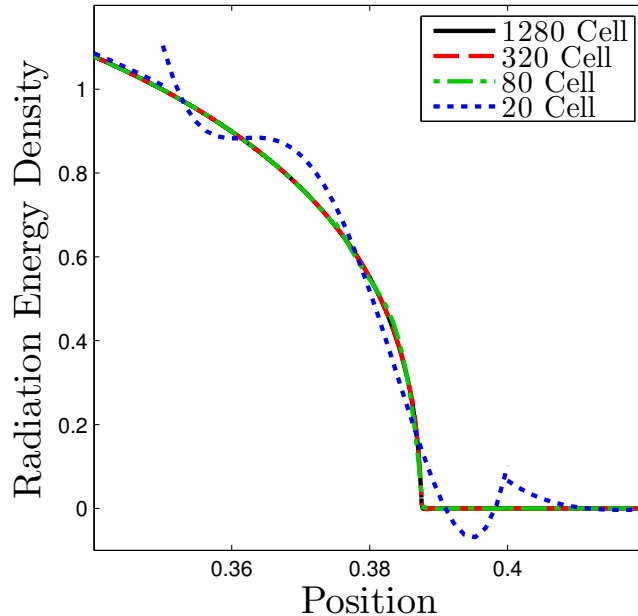


Figure 7.48: Quartic SLXS Gauss radiation solution near wavefront with increasing spatial mesh refinement.

of spatial convergence, few changes are noticeable with mesh refinement, except when moving from 20 to 80 cells. However, when moving from 20 to 80 cells, the Gibbs' phenomena near the solution discontinuity are no longer visible, except for a very small negativity in the temperature solution. All solutions for this spatial mesh refinement study use  $\Delta t = 1.5625 \times 10^{-4}$ .

We now examine the effect of increasing DFEM trial space degree, on a fixed mesh

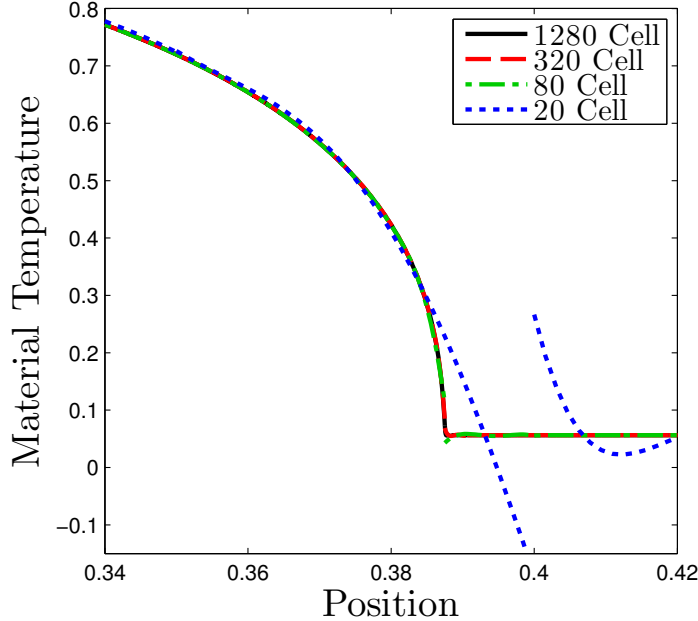


Figure 7.49: Quartic SLXS Gauss temperature solution near wavefront with increasing spatial mesh refinement.

of 320 spatial cells using SLXS Lobatto, focusing on the region near the Marshak wavefront. In Fig. 7.50 we plot the angle integrated intensity profile and plot the temperature profile in Fig. 7.51. Increasing  $P$  make the wavefront in the radiation profile sharper, but at a resolution of 320 cells, none of the  $P$  considered result in a visually continuous solution. The most notable changes with increase  $P$  come in the temperature profile, where linear SLXS Lobatto does not form a sharp interface, whereas all of the higher  $P$  schemes capture the non-smooth transition more accurately.

Before looking at very high spatial resolution solutions, we first consider the effect of time step refinement on the unity Marshak wave problem in Fig. 7.52 for the angle integrated intensity and in Fig. 7.53 for the material temperature solution. Both Fig. 7.52 and Fig. 7.53 use a quartic SLXS Gauss spatial discretization with

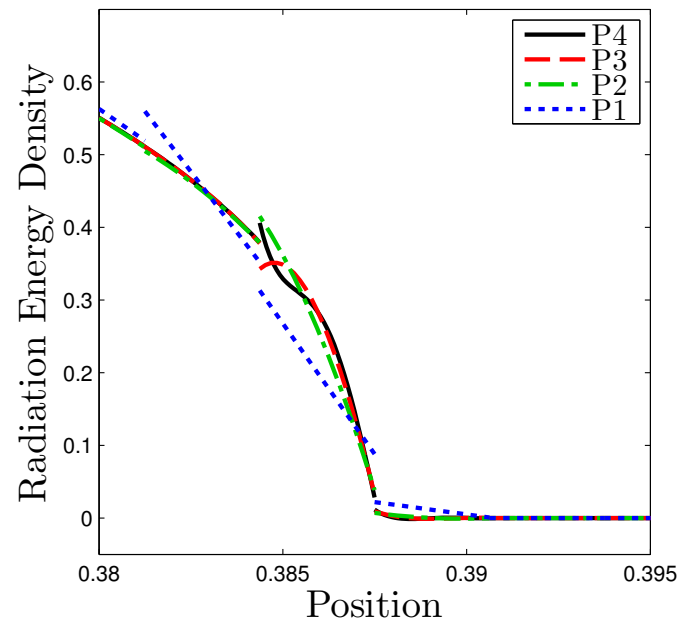


Figure 7.50: SLXS Lobatto radiation energy density solution with 320 cells for different  $P$  near Marshak wavefront.

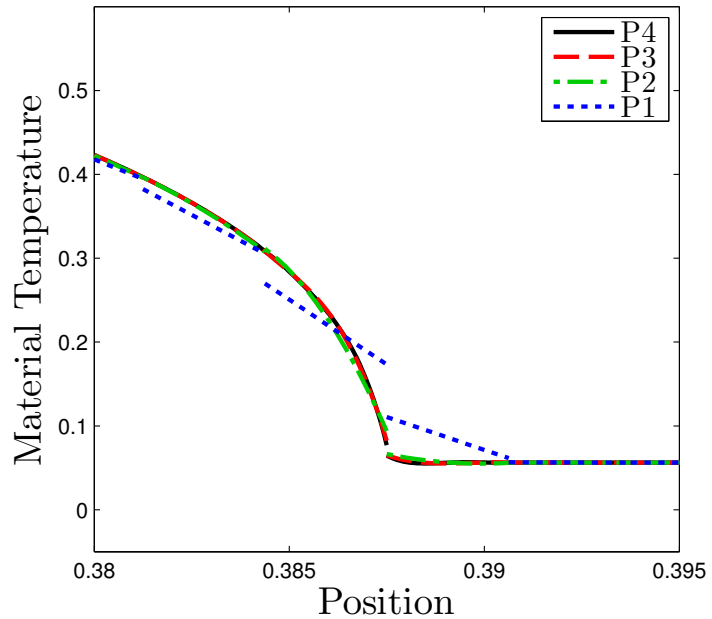


Figure 7.51: SLXS Lobatto material temperature solution with 320 cells for different  $P$  near Marshak wavefront.

1280 cells. The effects of decreasing time step size are non-trivial near the wavefront. As seen in Fig. 7.52, at lower time resolutions,  $\Delta t$  and  $\frac{\Delta t}{4}$ , the wavefront is visibly not uniform concave down, with several “wiggles” in the radiation profile in the heated region of the slab. Additionally, increased temporal resolution causes the discontinuity at the leading edge of the wavefront to sharpen. In Fig. 7.53, the effects of increased time resolution are the same as in Fig. 7.52. However, increased time resolution more noticeably sharpens the discontinuity in the temperature profile than it eliminates wavefront wiggles, though in Fig. 7.53 the  $\Delta t$  curve is not strictly concave down in the heated region of the slab near the wavefront.

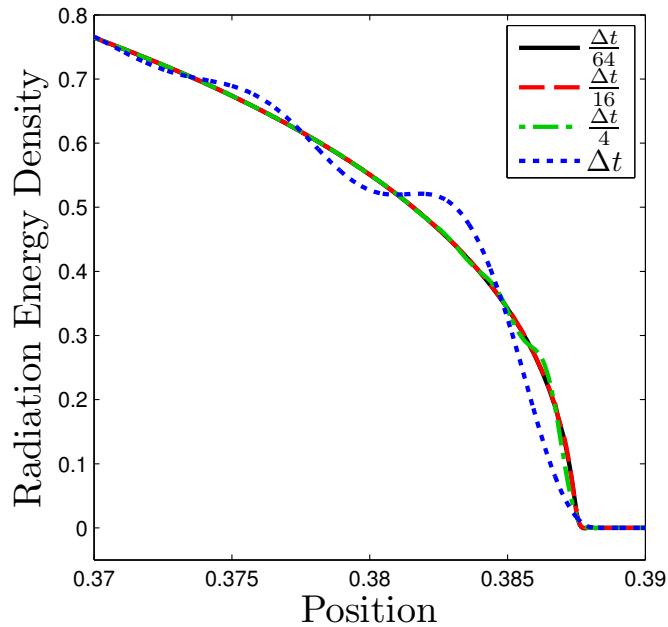


Figure 7.52: Quartic SLXS Lobatto radiation energy density solution with 1280 cells for different time refinements near the Marshak wavefront.

We now discuss highly resolved  $S_2$  solutions to the Marshak wave problem. Our hope is that with sufficient spatial resolution and higher order DFEM, we are able to resolve transport boundary layers. Our highest resolution simulation uses ten thousand spatial mesh cells. Given the initial, cold temperature of the slab is roughly  $T = 0.056$ ,  $\sigma_t = \sigma_a = \frac{1}{T^3}$ , then the total slab optical thickness is roughly 5700 MFP thick, and when using ten thousand cells, each mesh cell is roughly 0.57 MFP thick. As noted by Larsen, Morel, and Miller [60], this type of mesh spacing is neither optically thick nor thin. To answer whether ten thousand mesh cells is sufficient, we first consider Fig. 7.54 where we compare the results of cubic SLXS Lobatto schemes that use

1. ten thousand spatial cells, with ten thousand time steps and the SDIRK 3-3 scheme,

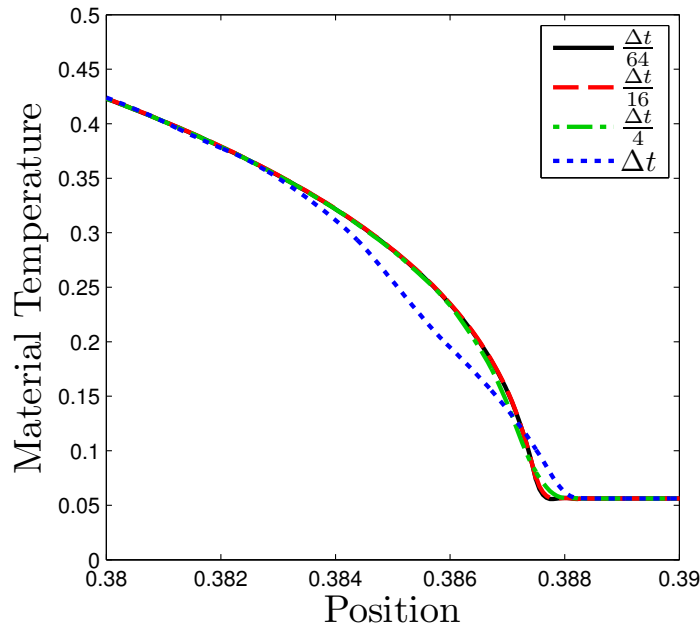


Figure 7.53: Quartic SLXS Lobatto temperature solution with 1280 cells for different time refinements near the Marshak wavefront.

2. ten thousand spatial cells, with one thousand time steps and the SDIRK 3-3 scheme, and
3. 1280 spatial cells, with six thousand time steps of the SDIRK 3-3 scheme.

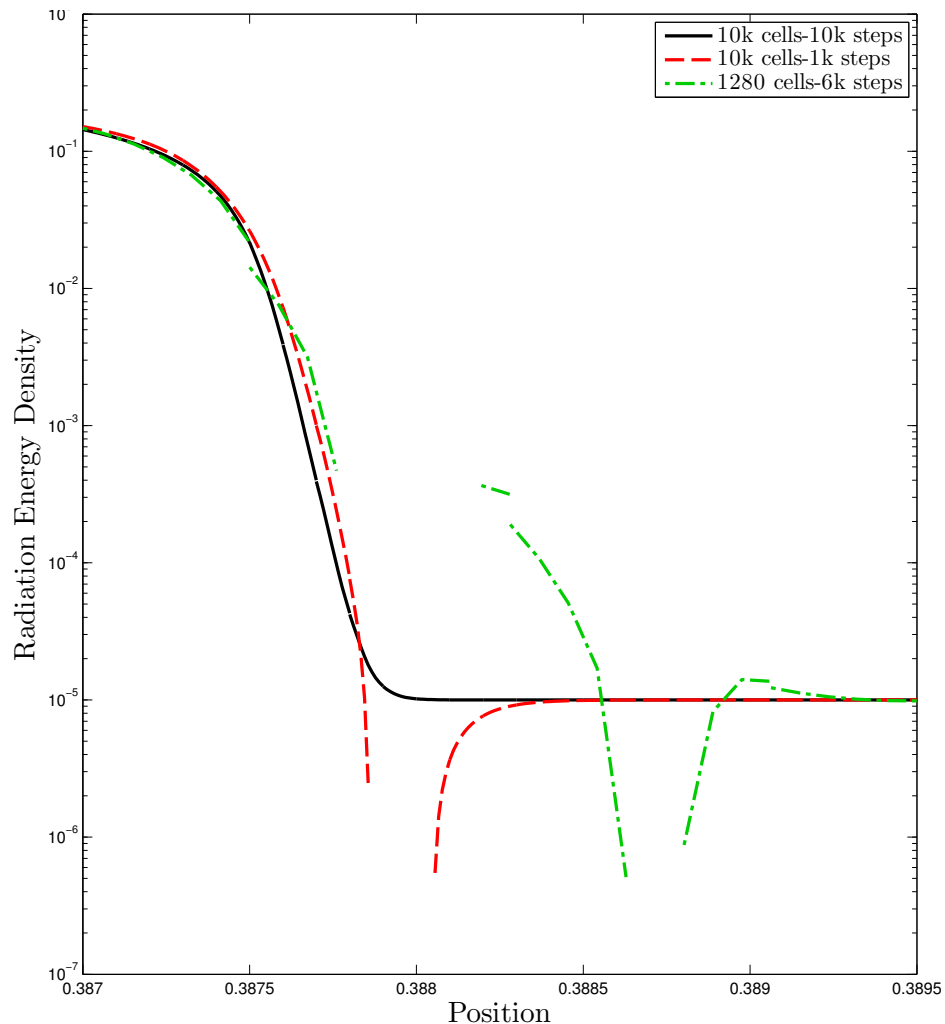


Figure 7.54: Plot of the radiation energy density on a logarithmic scale for different high resolution simulations near the Marshak wavefront.

Missing' segments in Fig. 7.54 are caused by negative angle integrated intensity

solutions. The 1280 cell simulation has only 1 negative node. The ten thousand cell simulation that uses one thousand time steps has a total of 8 negative nodes; one entire cell has a negative radiation energy density, and two other cells have at least one node with a negative radiation energy density. Since the ten thousand cell simulation with ten thousand time steps does not have any negative radiation energy densities, it is clear then that accurate TRT simulations require both space and time refinement.

In Fig. 7.55, we plot the angular intensities for  $\mu = \pm \frac{1}{\sqrt{3}}$  of the ten thousand cell, ten thousand time step simulation. Clearly the radiation traveling from the hot

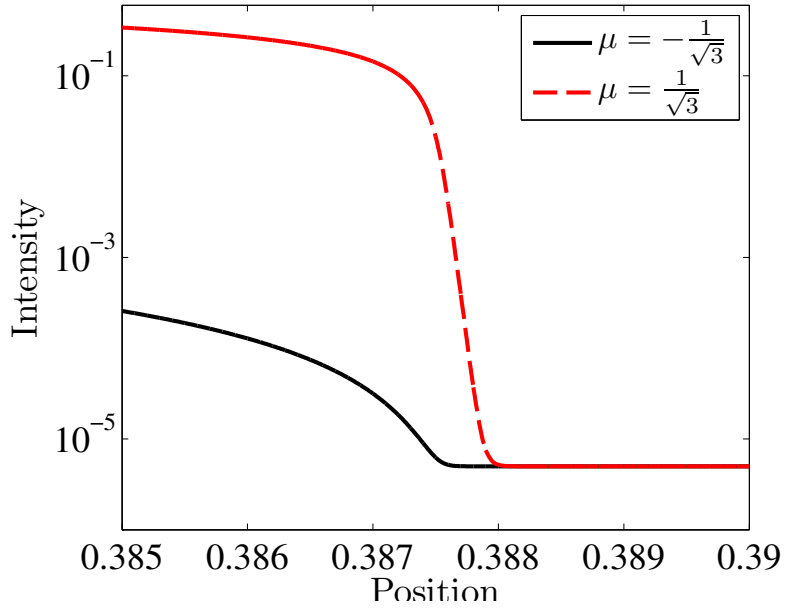


Figure 7.55: Plot of the angular intensity on a logarithmic scale near the transport boundary layer at the Marshak wave front.

to cold region,  $I_d(\mu_d = \frac{1}{\sqrt{3}}, x)$  has a large boundary layer near the thermal, but the

rapid rise in angular intensity appears to be smooth, suggesting we have resolved the radiation boundary layer. Unfortunately, to obtain high resolution everywhere at all times in the simulation requires a uniform spatial mesh, and using ten thousand total cells leaves only ten cells available to resolve the transport boundary layer present at  $x \in [0.3870.388]$  at  $t = 1.0$ .

We conclude our discussion of the unity Marshak wave problem by considering higher  $S_N$  solutions to the Marshak wave problem. First, we compare the  $S_8$  solution to the  $S_2$  solution for material temperature in Fig. 7.56 and for radiation energy density in Fig. 7.57. The  $S_8$  solution in Figs. 7.56-7.57 was generated using quartic SLXS Gauss with five thousand spatial cells, the SDIRK 2-2 scheme, and approximately ten thousand time steps. The  $S_2$  solution is the same solution as plotted in Fig. 7.55. The  $S_8$  solution exhibits many of the qualitative features we would expect

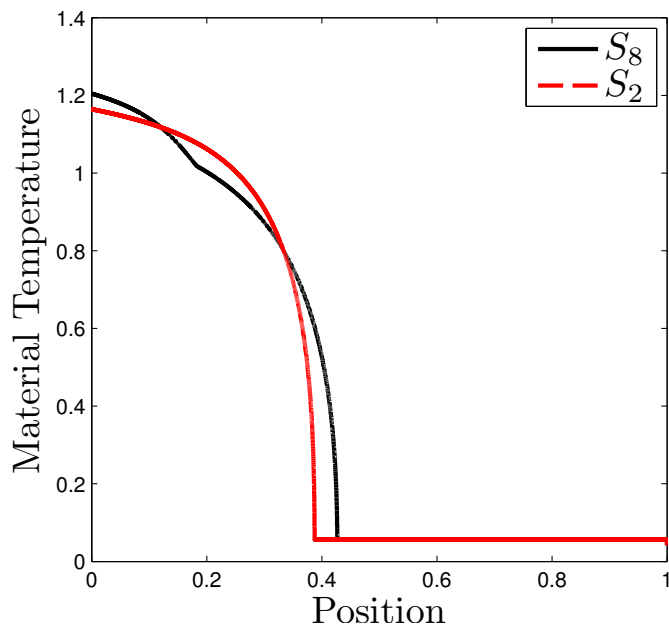


Figure 7.56:  $S_8$  and  $S_2$  material temperature profiles.

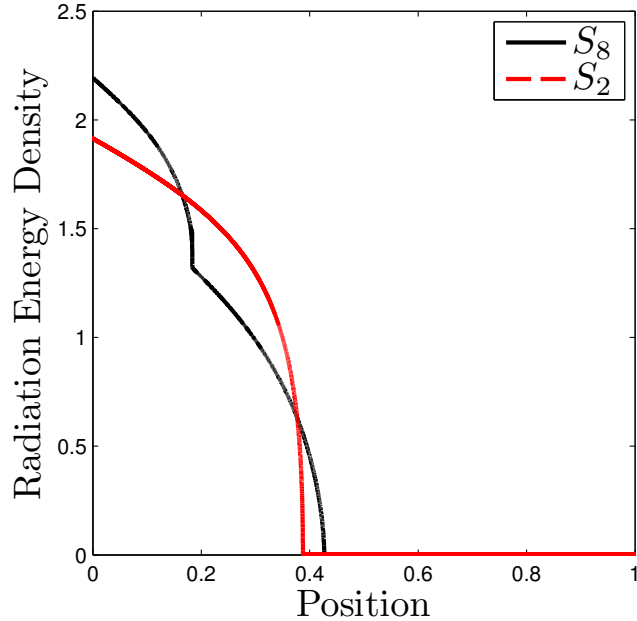


Figure 7.57:  $S_8$  and  $S_2$  radiation energy density profiles.

a transport solution to exhibit. For example, we expect the transport solution to have a higher temperature solution near the problem boundary, with a more rapid drop in both the material temperature and radiation energy density/angle integrated intensity solutions relative to a diffusion solution. Additionally, we expect the transport material temperature and radiation energy density solution to penetrate farther into the slab than the diffusion solution, but with a less steep gradient. Figures 7.57-7.56 both exhibit these behaviors, caused by the transport solution becoming more and more like  $\delta(\mu - 1)$  in optically thick regions. However, we did not expect the non-smooth features near  $x = 0.2$ . We suspect the kinks in the temperature and radiation energy density profiles is caused by the transition of the most glancing  $\mu_d > 0$  from being dominated by boundary contributions to being dominated by photon re-emission. To verify this, we plot the  $S_8$  intensity solution in Fig. 7.58.

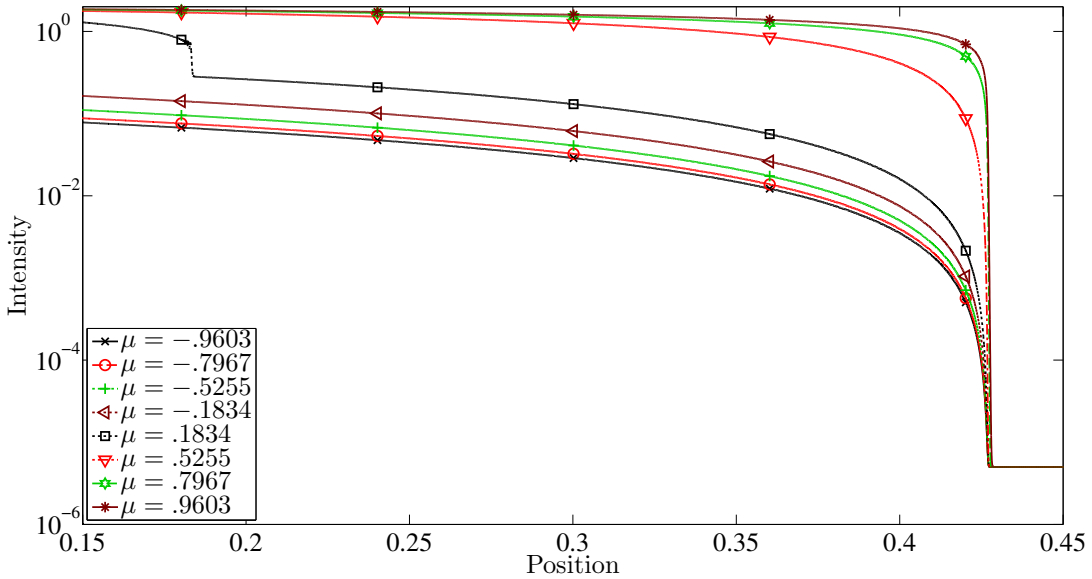


Figure 7.58: Logarithmic plot of  $S_8$  intensities for the unity Marshak wave problem.

We now zoom in to the boundary layer intensities near  $x = 0.2$  and near the thermal wave front. In Fig. 7.59, it is clear that the intensity in the direction of  $\mu = +0.1834$  experiences a rapid variation as the incident flux from the boundary is attenuated, and the isotropic emission from the heated regions of the slabs becomes the main contributor to  $I(\mu_d = +0.1834)$ . It is also clear that despite having 25 cells with quartic DFEM in the region  $x \in [.18, .185]$ , the factor  $\approx 7\times$  step drop in  $I(\mu_d = +0.1834)$  cannot be fully resolved. The more glancing  $\mu_d$ , the sooner the transition, relative to the left boundary.

Near the hot/cold material interface, all angular intensities experience a boundary layer transition. Using higher order DFEM and high spatial resolution, it appears that we are able to resolve these boundary layers, given the smooth profile of angular intensity for every direction in the quadrature set.

Next we investigate the structure of an  $S_{32}$  solution with 1000 spatial cells, quartic SLXS Gauss, and five thousand time steps using the SDIRK 2-2 time integration

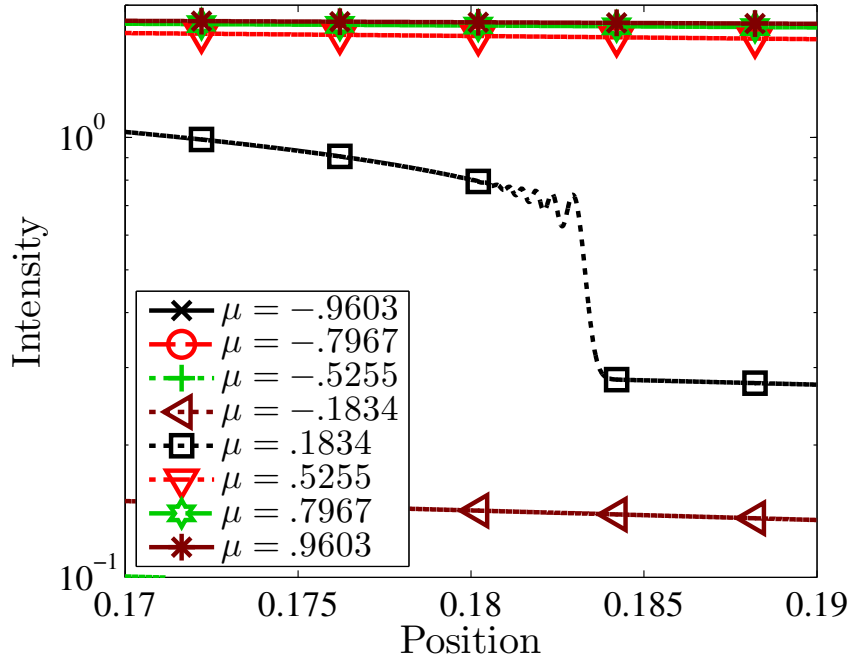


Figure 7.59: Logarithmic plot of intensity near glancing  $\mu = +0.1834$  boundary layer.

scheme. The material temperature solution is plotted in Fig. 7.61 against the  $S_8$  solution that uses quartic SLXS Gauss, five thousand spatial cells, and ten thousand SDIRK time integration steps. Likewise, the angle integrated intensity solutions are compared in Fig. 7.62. Even with  $S_{32}$  Gauss quadrature, we continue to see non-smooth dips in both the material temperature and angle integrated intensity profiles, however the dips are significantly smaller for the  $S_{32}$  solution as compared to the  $S_8$  solution, particularly for the material temperature profile. In Fig. 7.62, the  $S_{32}$  exhibits four smaller dips as compared to the single, larger dip associated with  $S_8$ . Suspecting these are caused by glancing incidence angles in the quadrature set, we plot the angular intensity for all  $\mu_d > 0$  in Fig. 7.63. As with the  $S_8$  solution, the dips in  $\phi$  are associated with corresponding dips in  $I_d$  for glancing  $\mu_d > 0$ .

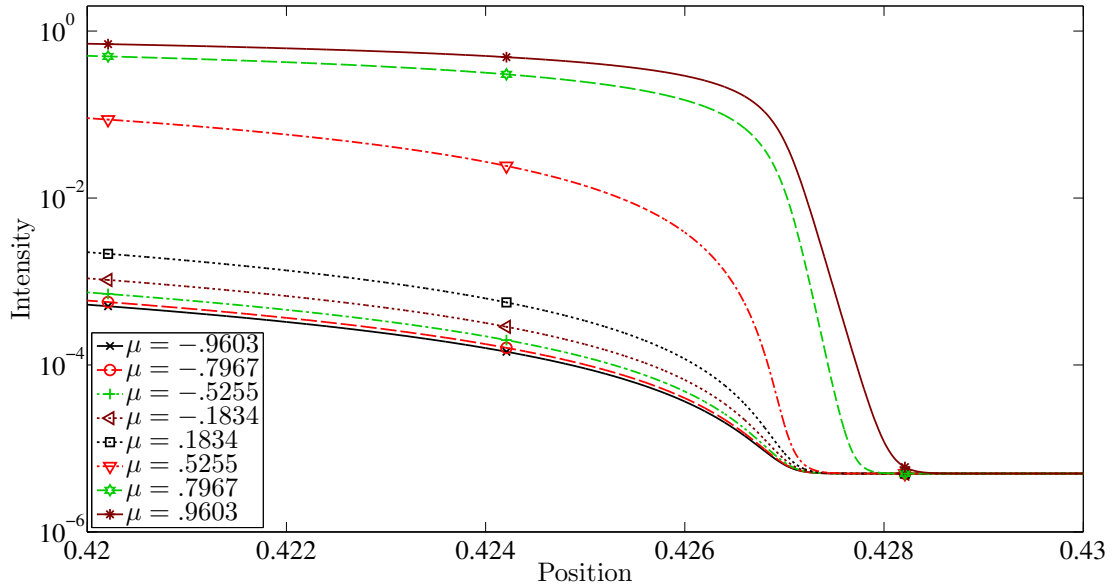


Figure 7.60: Logarithmic plot of intensity boundary layers near thermal wavefront.

The discontinuity associated with  $\mu_d = 0.3319$  is obscured in Fig. 7.62 as the dip occurs just as the  $S_{32}$  angle integrated intensity cross over the  $S_8$  angle integrated intensity solution. The  $\mu_d = 0.0483$  intensity jump in Fig. 7.63 causes the greatest effect in Fig. 7.62 for two reasons. First, the most glancing quadrature angle is attenuated the most rapidly and as such would be expected to have the greatest drop in value. Second, Gauss angular quadrature assigns the greatest weight to the quadrature points most near  $\mu_d = 0$ . Surprisingly, the  $S_8$  and  $S_{32}$  calculations have nearly identical positions and values of the temperature and angle integrated intensity solution near the problem boundary and the hot/cold interface. If however, the goal is a smooth transport solution, the value of  $N$  required to create a smooth  $S_N \phi$  solution appears to be much higher than  $S_{32}$ , due to the presence of time ray effects [1].

The kinks observed in the higher order  $S_N$  solutions for the Marshak wave problem

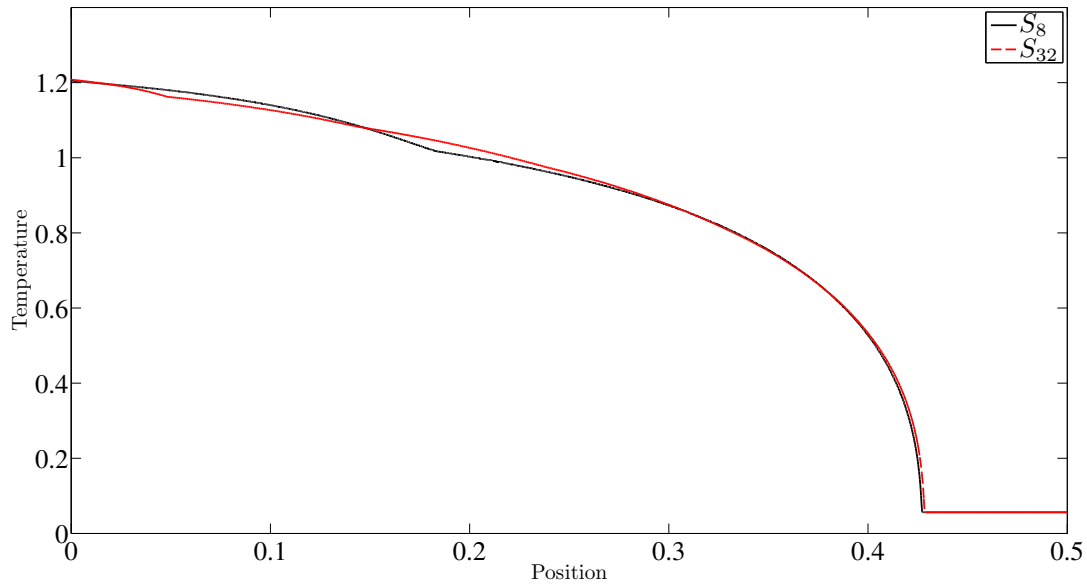


Figure 7.61: Comparison of  $S_8$  and  $S_{32}$  material temperature profiles for the unity Marshak wave problem.

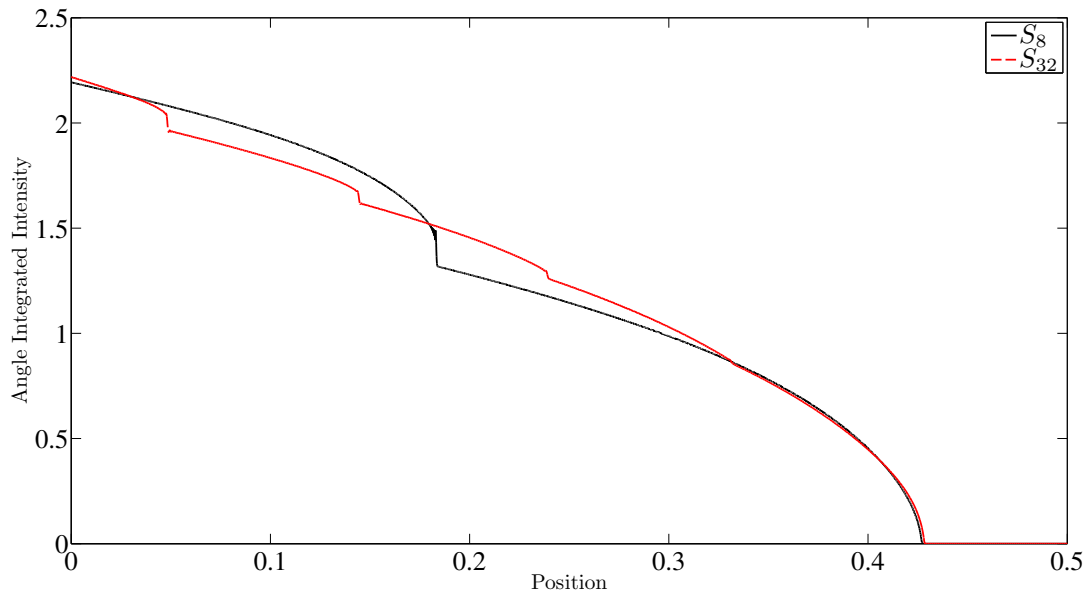


Figure 7.62: Comparison of  $S_8$  and  $S_{32}$  angle integrated intensity solutions for the unity Marshak wave problem.

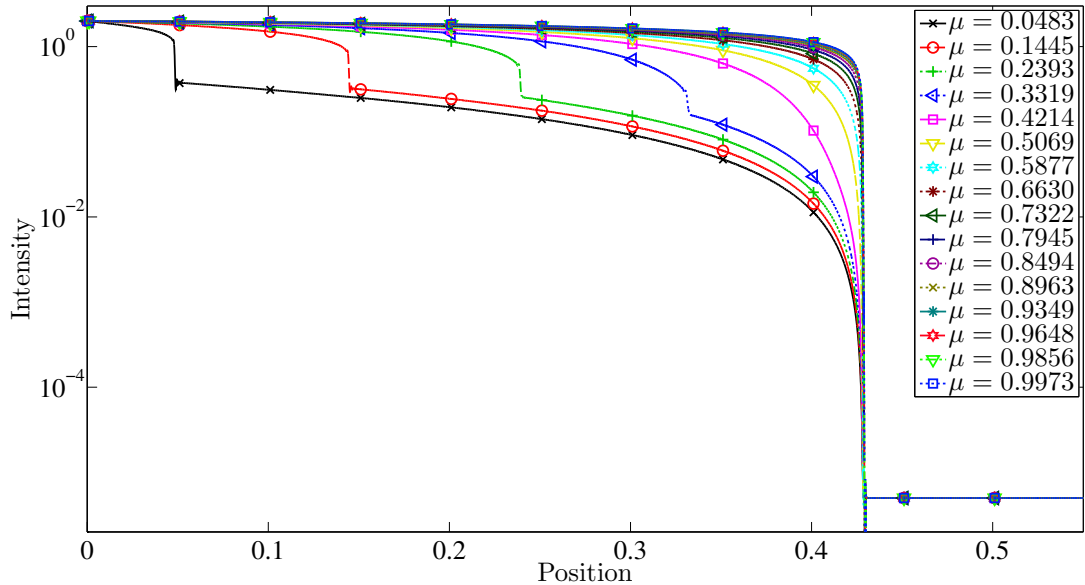


Figure 7.63:  $S_{32}$  intensity solutions for all  $\mu_d > 0$ , for the unity Marshak wave problem.

are examples of time ray effects. Typically these are not observed in thermal radiative transfer simulations, because as the material heats up, the magnitude of photon re-emission sources quickly becomes comparable to and surpasses the rapidly attenuated incident photon contribution to the angular intensity. If the observed kinks are time ray effects, they will be worse at earlier times and less pronounced at later times, due to the attenuation of the incident intensity contribution over a greater distance (as the wave front advances) and photon re-emission from the increased material temperature. To verify that the observed kinks are indeed time ray effects, consider Fig. 7.64 and Fig. 7.65 which show the  $S_{32}$  Marshak wave radiation energy density and material temperature at different points in time, computed using 1000 spatial cells, cubic SLXS Lobatto,  $\Delta t_{max} = 2 \times 10^{-4}$ , and the SDIRK 2-2 time scheme. While the earliest time material temperature solution does not have visually large kinks due

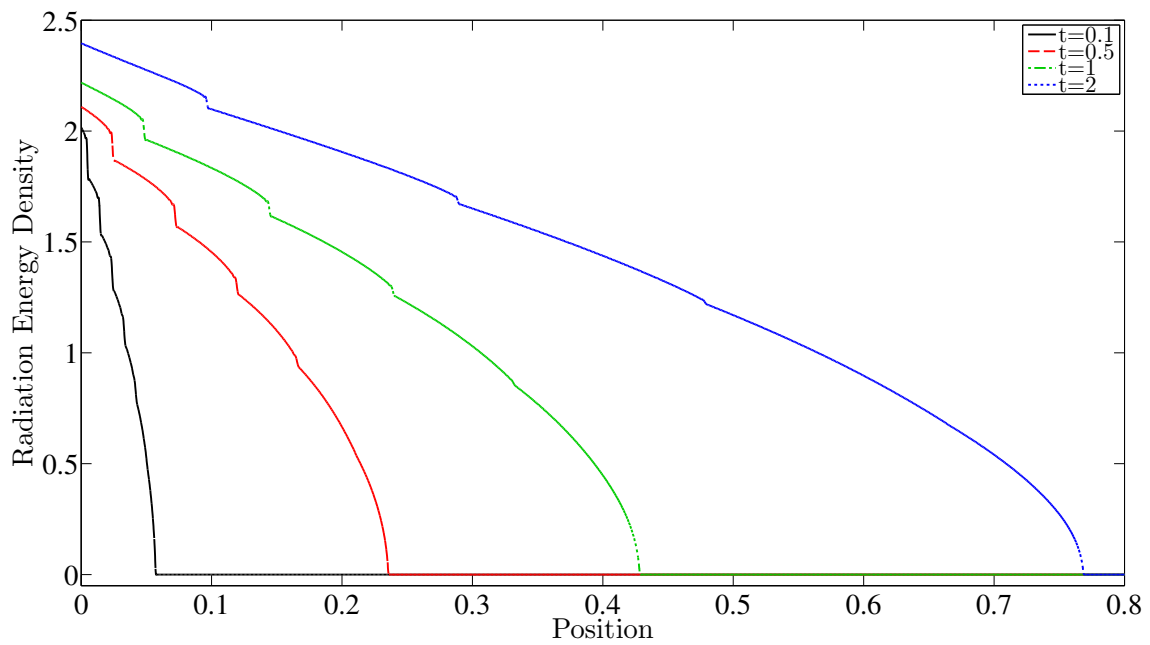


Figure 7.64:  $S_{32}$  radiation energy density at different times for the unity Marshak wave problem.

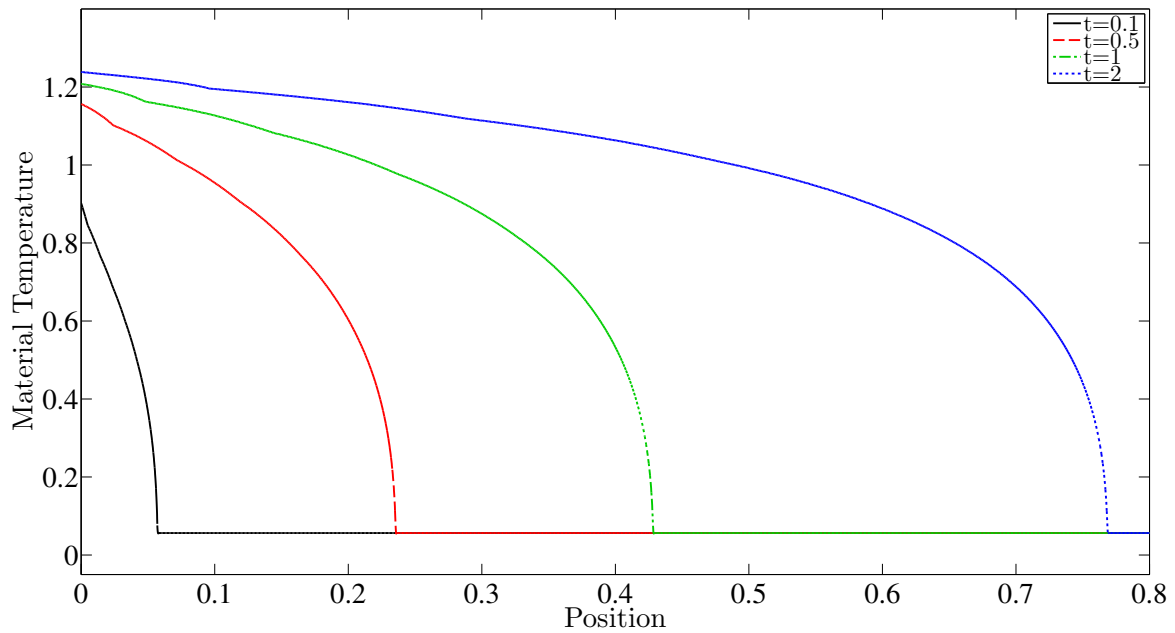


Figure 7.65:  $S_{32}$  material temperature solution at different times for the unity Marshak wave problem.

to ray effects, ray effects can be seen in the radiation energy density solution at all times considered. To observe that the radiation energy density ray effects decrease in magnitude at later times, first consider the radiation energy density at  $t = 0.1$ , given in Fig. 7.66, and then compare to the radiation energy density at  $t = 2.0$  given in Fig. 7.67. Figure 7.66 and Fig. 7.67 use the same  $y$ -axis scaling. Comparing Figs. 7.66-7.67, it is clear that the radiation energy drops associated with ray effects are significantly larger at  $t = 0.1$  than at  $t = 2.0$ . The  $\mu$  labels in Figs. 7.66-

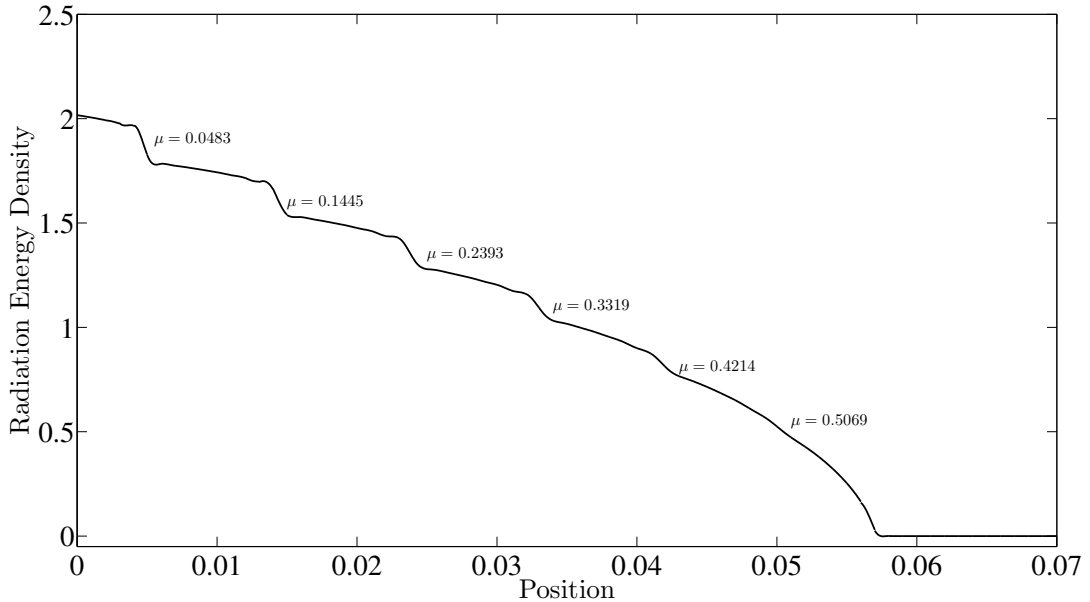


Figure 7.66:  $S_{32}$  radiation energy density at  $t = 0.1$  for the unity Marshak wave problem.

7.67 correspond to the directional cosines of angular intensities that experience a significant drop at those locations. as shown in Fig. 7.68 and Fig. 7.69 for  $t = 0.1$  and  $t = 2$ , respectively. Comparing Fig. 7.68 to Fig. 7.69 clearly shows that as time progresses, ray effects decrease, in Fig. 7.68, there are six angular intensities that

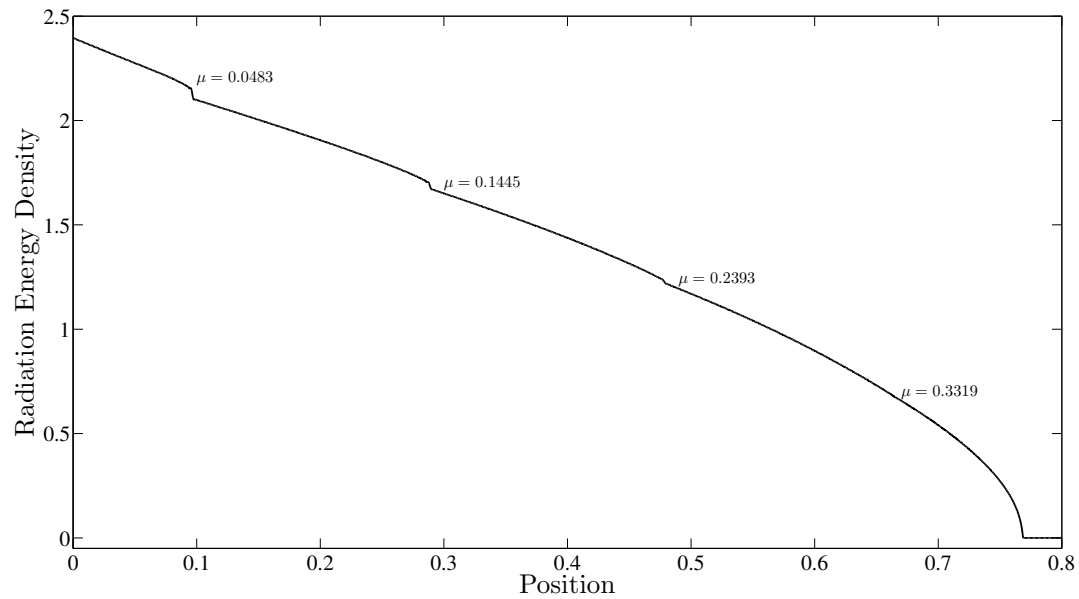


Figure 7.67:  $S_{32}$  radiation energy density at  $t = 2$  for the unity Marshak wave problem.

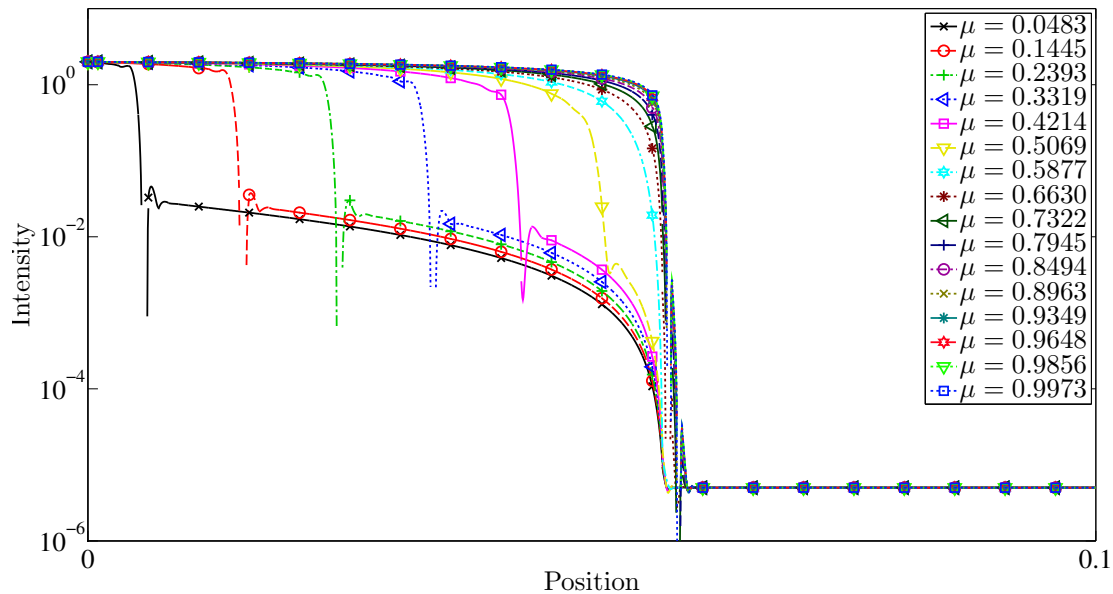


Figure 7.68:  $S_{32}$  angular intensity for  $\mu_d > 0$  at  $t = 0.1$  for the unity Marshak wave problem.

have a discontinuous jump from being dominated by incident boundary conditions and heated material photon re-emission whereas in Fig. 7.69, at most 4 directions experience a non-smooth transition from being dominated by incident boundary contributions to being dominated by photon re-emission.

Though ray effects are inherent to discrete ordinates calculations, the severe time ray effects observed in the unity Marshak wave problem are more a function of problem parameters than of a fundamental flaw with discrete ordinates methods applied to thermal radiative transfer. The choice to define  $a = c = C_v = 1$  and  $\sigma_t = \sigma_a = \frac{1}{T^3}$  was chosen by previous authors, and did not correspond to a physical scaling of typical physical material properties. This can easily be seen by considering an alternative simulation, where we define  $\sigma_t = \sigma_a = \frac{1000}{T^3}$ . Under this assumption, even the heated material is optically thick, and photon re-emission quickly becomes

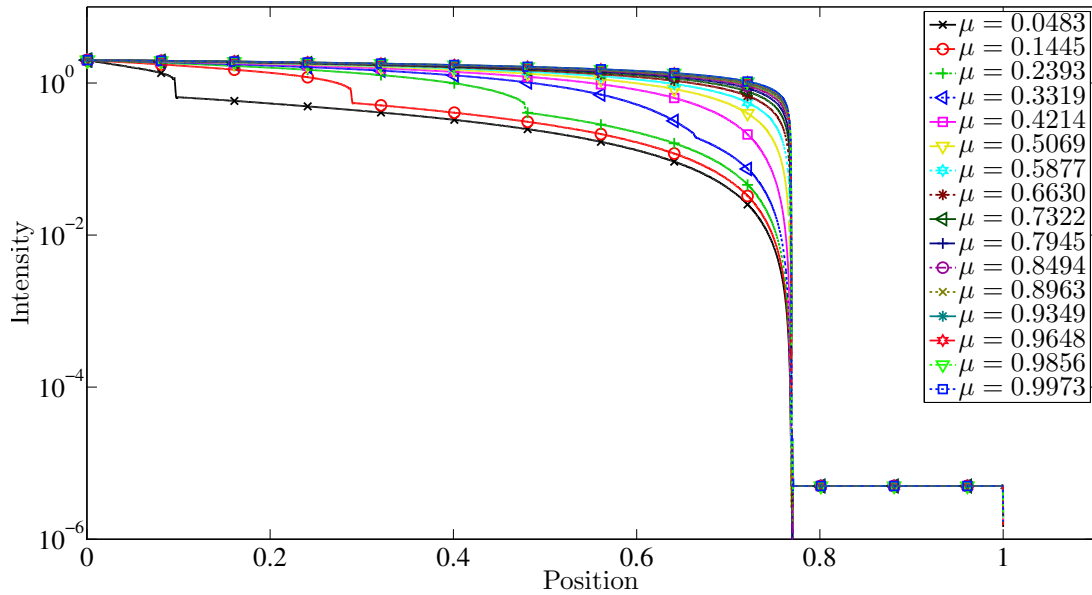


Figure 7.69:  $S_{32}$  angular intensity for  $\mu_d > 0$  at  $t = 2$  for the unity Marshak wave problem.

the more dominant contributor to angular intensity than incident photon energy. In Fig. 7.70, radiation energy density solutions for the modified unity Marshak wave problem at different times are given for a simulation using 1000 spatial cells,  $x \in [0, 1]$ , linear SLXS Lobatto, and SDRIK 2-2 time differencing. Figures 7.70-7.71 make

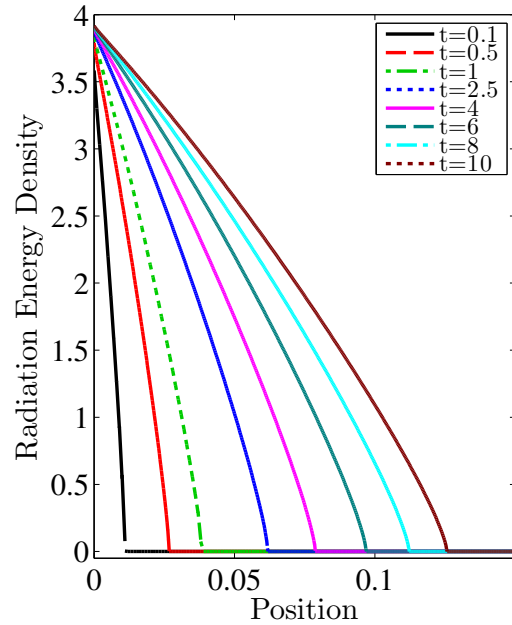


Figure 7.70:  $S_8$  radiation energy density solutions for the modified unity Marshak wave problem with  $\sigma_a = \frac{1000}{T^3}$  at different times using linear SLXS Lobatto, and 1000 spatial cells for  $x \in [0, 1]$ .

it clear that changing  $\sigma_a$  fundamentally alters the “unity” Marshak wave problem. The thermal wave does not penetrate nearly as far in the modified unity Marshak wave problem, but also does not exhibit any time ray effects as compared to the original unity Marshak wave problem. The apparent gaps in Fig. 7.70 and Fig. 7.71 are discontinuities in the solution representation at cell edges. Though Fig. 7.70 and Fig. 7.71 use 1000 spatial cells, the 1000 spatial cells are equally distributed for

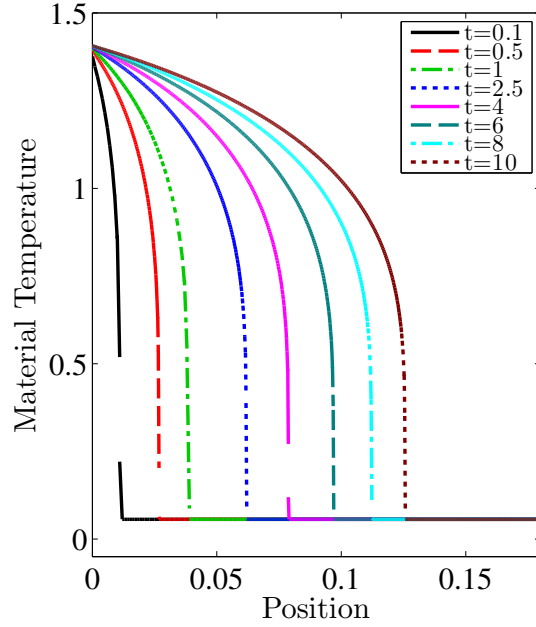


Figure 7.71:  $S_8$  material temperature solutions for modified unity Marshak wave problem with  $\sigma_a = \frac{1000}{T^3}$  at different times using linear SLXS Lobatto, and 1000 spatial cells for  $x \in [0, 1]$ .

$x \in [0, 1]$ , whereas, thermal wave travels only to  $x < 0.15$ . Ideally, we could use time adaptive mesh refinement to refine the mesh only near the Marshak wavefront at the current simulation time, refining in the area immediately in front of the wavefront, and coarsening after the steepest gradient of the wavefront has passed. However, such adaptivity is computationally challenging to implement, and beyond the scope of this work.

### 7.2.2 Physical Marshak Wave Problem

We now consider a Marshak wave problem that uses physical units. The problem has been considered repeatedly in the literature [45, 46, 59] and consists of a 0.05 [cm] slab at an initial temperature of 1 [eV], heated from the left with an isotropic 1 [keV] photon source. After 0.1 [sh],  $1 [sh] = 10^{-8} [sec]$ , the thermal

wave will have nearly passed through the entire domain. The material heat capacity is temperature independent,  $C_v = 0.3 \left[ \frac{jerks}{cm^3 \text{ keV}} \right]$ ,  $\sigma_a = \frac{300}{T^3} [cm^{-1}]$ , with  $T$  in keV, and  $\sigma_s = 0$ . Representative angle integrated intensity and temperature solutions at various times are given in Fig. 7.72 and Fig. 7.73. The representative solutions are generated using 100 spatial cells with cubic SLXS Lobatto and  $S_8$  Gauss angular quadrature. We note that Fig. 7.72 does not exhibit any time ray effects. This

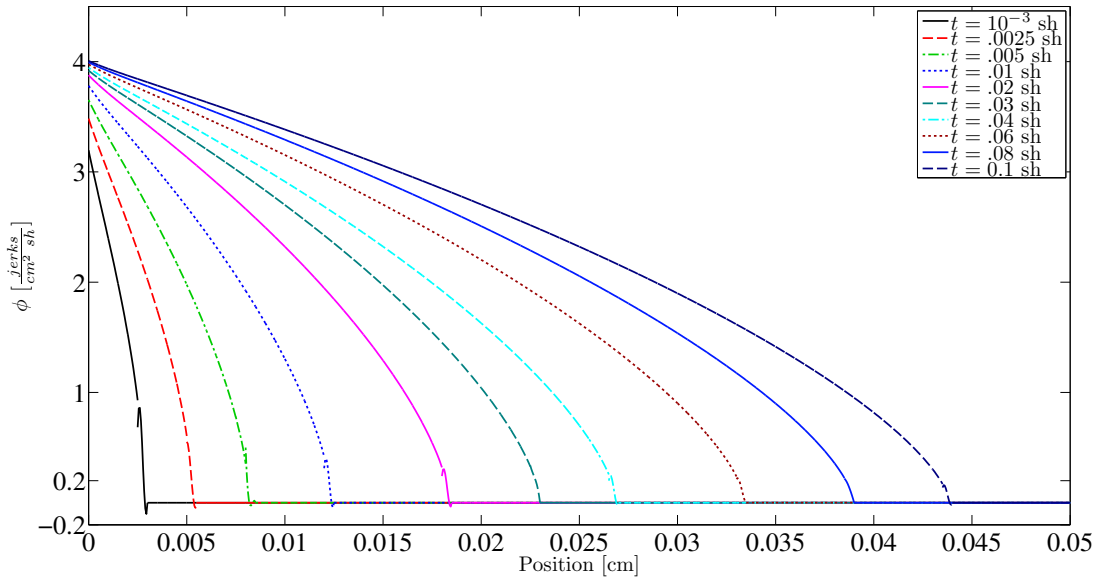


Figure 7.72:  $S_8$  angle integrated intensity solutions at various times for physical Marshak wave problem generated using 100 spatial cells and cubic SLXS Lobatto.

problem description, given in the cm-sh-keV unit system, has a heat capacity on the same order as  $C_v = 1$  in the unity Marshak wave problem. In addition the product of the radiation constant,  $a = 0.01372 \left[ \frac{jerks}{cm^3 (keV)^4} \right]$ , and speed of light,  $c = 299.792 [cm/sh]$ ,  $ac = 4.113 \left[ \frac{jerks}{cm^2 sh (keV)^4} \right]$ , is on the same order as  $a = c = 1$  from the unity Marshak wave problem. The only thing that is significantly different in this

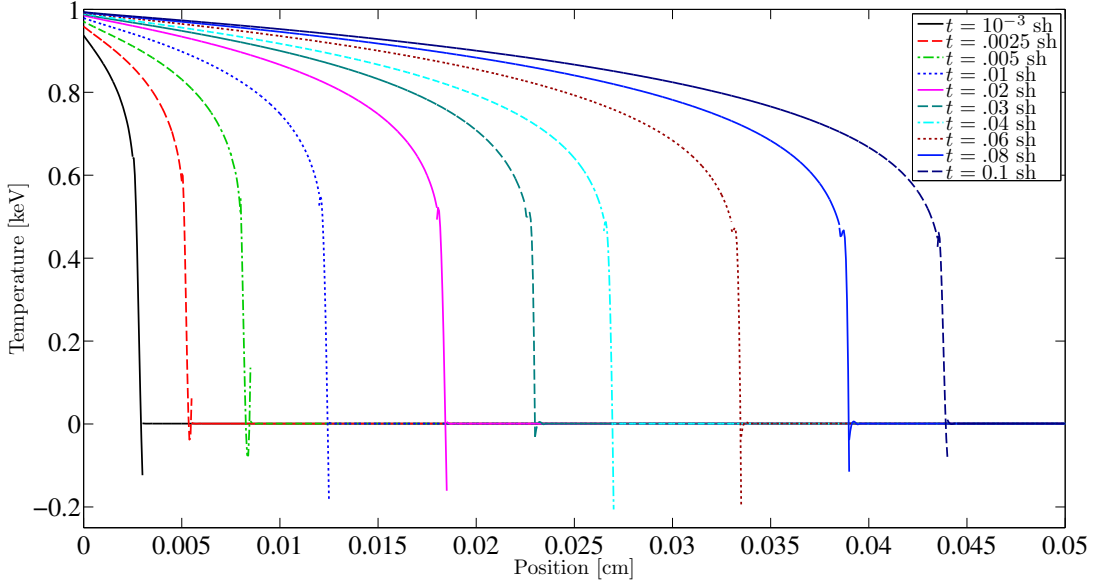


Figure 7.73: Temperature solutions at various times for physical Marshak wave problem generated using 100 spatial cells and cubic SLXS Lobatto.

problem is that the numerator in the definition of  $\sigma_a$  is a factor of 300 larger in this physical Marshak wave problem than the unity Marshak wave problem, reaffirming that the time ray effects observed in the unity Marshak wave problem are atypical of discrete ordinate solutions applied to the thermal radiative transfer equations, and a function more of the optically thin nature of the unity Marshak wave problem at higher temperatures. The apparent discontinuities and overshoots in Figs. 7.72-7.73 are the tails of the cubic finite element in some mesh cells. The discontinuities would be resolved with increased mesh refinement.

Our main interest in the physical Marshak wave problem is to test our different adaptive time criteria. Using the notation of Eq. (6.133), in all of the results that follow, we will assume  $\Delta T_{goal} = 0.01$ , unless otherwise stated. We first apply each adaptive method to a linear SLXS discretization of the physical Marshak wave using

50 spatial cells and  $S_2$  Gauss quadrature in angle. These discretization choices will yield the most direct comparison possible to the radiative diffusion results of [46]. Time step size selection as function of the simulated time is given for each method in Fig. 7.74. For this particular problem, the point-wise adaptive criterion taken from

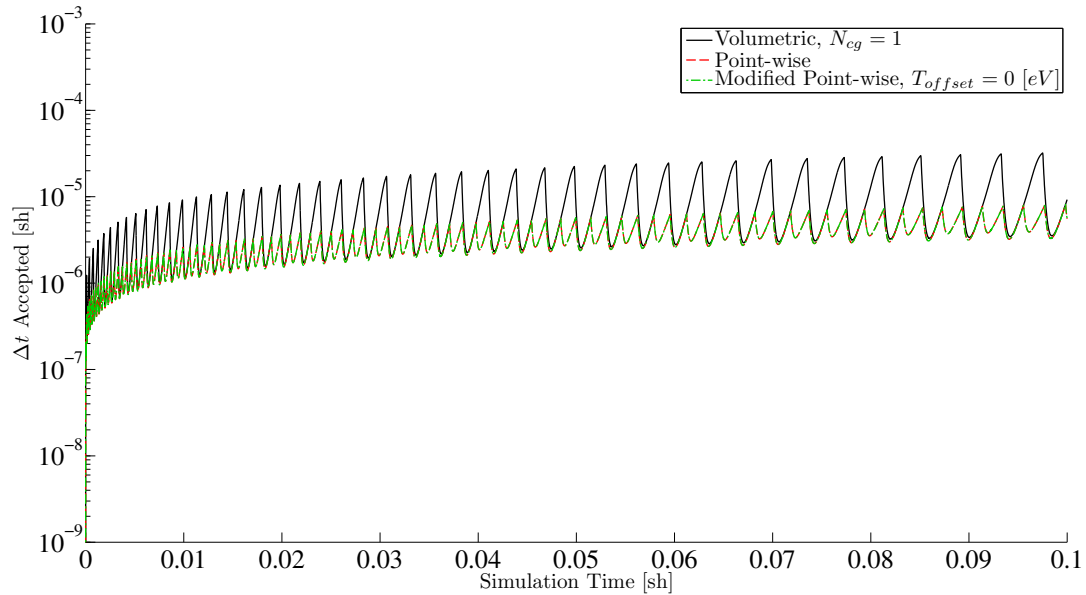


Figure 7.74: Time step sizes selected for different adaptive criterion applied to a linear SLXS Lobatto discretization of the physical Marshak wave problem with  $S_2$  angular quadrature and 50 spatial cells.

[46], yields the same time step selection at every time step as the modified point-wise criterion with  $T_{offset} = 0$  [eV] because no negative temperature solutions are generated with a linear SLXS Lobatto discretization of this problem. The volumetric scheme with  $N_{cg} = 1$  chooses larger time step sizes than the point-wise adaptive criterion as expected, since a 1% change over a volume permits a much larger increase in temperature than a 1% increase maximum at any one point. We also note the large

number of sharps peaks and valleys present in all traces of time step size in Fig. 7.74. Each peak and valley is related to the location of the thermal wave passing through an individual mesh cell. The point-wise and modified point-wise schemes choose larger  $\Delta t$  when the thermal wave is in the middle of a mesh cell. The volumetric scheme chooses larger  $\Delta t$  as the thermal wave crosses a cell boundary. The logic behind both point-wise schemes choosing larger  $\Delta t$  when the thermal wave (localized increase in temperature) is in the middle of the cell is that the increased heating is distributed amongst two points rather than heating a single point. Conversely, the volumetric scheme chooses larger  $\Delta t$  as the thermal wave crosses cell boundaries because the increase in temperature is distributed amongst two cells rather than 1. Additionally, we note that since the speed of the thermal front slows as time progresses, the peaks occur at a greater frequency at earlier times in the simulation than near the end of the simulation. The slowing of the wave can be more clearly visualized by viewing Fig. 7.73. At  $t = 0.01$  [sh], the wave is at approximately  $x = 0.0125$  [cm]. If the thermal wave propagated at a constant speed, then at  $t = 0.08$  [sh], we would expect the thermal wave to be near  $x = .1$  [cm]. However, the thermal wave is only located at approximately  $x < 0.04$  [cm] in Fig. 7.73. The number of time steps each adaptive method took, as well as the number of time steps that were rejected are given in Table 7.1. Rejected time steps are those  $\Delta t^n$ , that after computing  $\Delta T$  using  $\tilde{T}^{n+1}$  and  $\tilde{T}^n$ ,  $\Delta T > 1.2\Delta T_{goal}$ , thus indicating  $\Delta t^n$  was too large, requiring a repeat of the time step from  $t^n$  to  $t^{n+1}$ . The point-wise and modified point-wise results in Table 7.1 are comparable to the results reported in [46], where the point-wise adaptive scheme was applied to a 50 cell linear DFEM radiative diffusion discretization, reported to take about 33,000 time steps when using  $\Delta T_{goal} = 0.01$ .

We now examine the performance of each adaptive time criterion applied to a cubic SLXS Lobatto discretization of the physical Marshak wave problem using 100

Table 7.1: Time steps taken for different adaptive time stepping criterion for physical Marshak wave problem using  $S_2$  angular quadrature, spatially discretized with linear SLXS Lobatto, 50 cells, and  $\Delta T_{goal} = 0.01$ .

	Total Steps	Rejected Steps
Point-wise	40900	0
Modified Point-wise, $T_{offset} = 0 [eV]$	40900	0
Volumetric, $N_{cg} = 1$	26214	0

spatial cells. As seen in Fig. 7.73, negative temperature solutions are present at the thermal wavefront. Table 7.2 gives the total number of time steps a given adaptive scheme takes to solve the Physical Marshak wave problem discretized with cubic SLXS Lobatto, and confirms that negative temperature solutions cause the simplest point-wise adaptive criterion, Eq. (6.136), to fail. By fail, we mean that the point-wise adaptive scheme attempts to take unacceptably and vanishingly small time steps.

To show that it is only the challenging nature of an under resolved Marshak wave problem causes the point-wise adaptive criterion to fail, we consider an alternative to the physical Marshak wave problem. Using the same spatial domain, temporal domain, and material properties as the physical Marshak wave problem, we heat the slab heated with a distributed volumetric radiation source equivalent to a black body material radiating energy at a temperature of 1 keV, rather than heating the slab with an incident 1 keV temperature source. In this volumetric source driven problem,

1. the solution is constant in space,
2. opacities do not vary spatially,
3. the radiation solution is strictly non-negative,

Table 7.2: Time steps taken for different adaptive time stepping criterion for physical Marshak wave problem discretized with cubic SLXS Lobatto and 100 cells.

	Total Steps	Rejected Steps
Modified Point-wise, $T_{offset} = 0 [eV]$	Failed	
Modified Point-wise, $T_{offset} = 1 [eV]$	558495	3
Modified Point-wise, $T_{offset} = 5 [eV]$	397608	2
Modified Point-wise, $T_{offset} = 50 [eV]$	184033	0
Volumetric, $N_{cg} = 1$	1320259	976
Volumetric, $N_{cg} = 2$	68182	1252
Volumetric, $N_{cg} = 5$	29607	1346
Volumetric, $N_{cg} = 10$	16657	1449
Volumetric, $N_{cg} = 25$	9716	1631
Volumetric, $N_{cg} = 50$	7124	1736
Volumetric, $N_{cg} = 100$	5936	1808

- 4. negative temperatures are not generated, and
- 5. the point-wise adaptive criterion does not fail.

A trace of  $\Delta t$  selected at each time step, normalized by dividing the time step number  $n$  by the total number of time steps,  $n_{final}$ , required by a given adaptive criterion to complete the problem is given in Fig. 7.75 for a simulation of the source driven problem using cubic SLXS Lobatto and 1000 spatial cells. Figure 7.75 shows that for a spatially constant solution all three adaptive criteria yield the same time step size, as might be expected, and demonstrates that adaptive time step selection criteria may be used for higher order DFEM TRT simulations, but they must be designed in a sufficiently sophisticated way to be applicable to challenging simulations of interest.

Comparing the number of steps taken in Table 7.2 to the number of steps taken

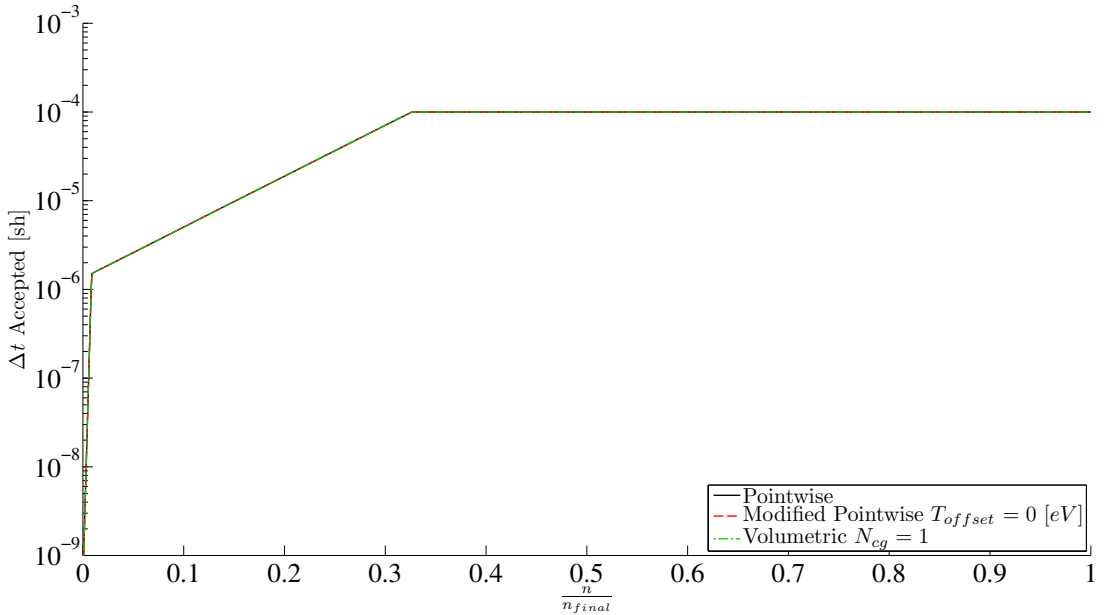


Figure 7.75: Time step sizes selected for adaptive criteria for volumetric radiation source driven problem.

in Table 7.1 makes it clear that higher order DFEM methods applied to TRT simulations challenge the performance of simple time adaptive criteria. Indeed, the modified point-wise scheme struggles, requiring  $T_{floor}$  to be artificially high to yield reasonable time step sizes. Interestingly though, using an artificially high  $T_{floor}$  did not yield significantly larger maximum time step sizes. As seen in Fig. 7.76, the largest time step size chosen with the modified point-wise adaptive scheme is the same regardless whether  $T_{offset} = 1$  [ev] or  $T_{offset} = 50$  [eV]. This can be seen more clearly by considering a zoom in if time step selection, as given in Fig. 7.77.

The increased numbers of peaks and valleys in Fig. 7.76 as compared to Fig. 7.74 is a result of increased spatial cell count and moving from linear to cubic DFEM. Consider Fig. 7.78 that plots the time step trace of linear SLXS Lobatto simulations using 50 and 100 spatial cells for  $S_8$  angular differencing with the point-wise adaptive

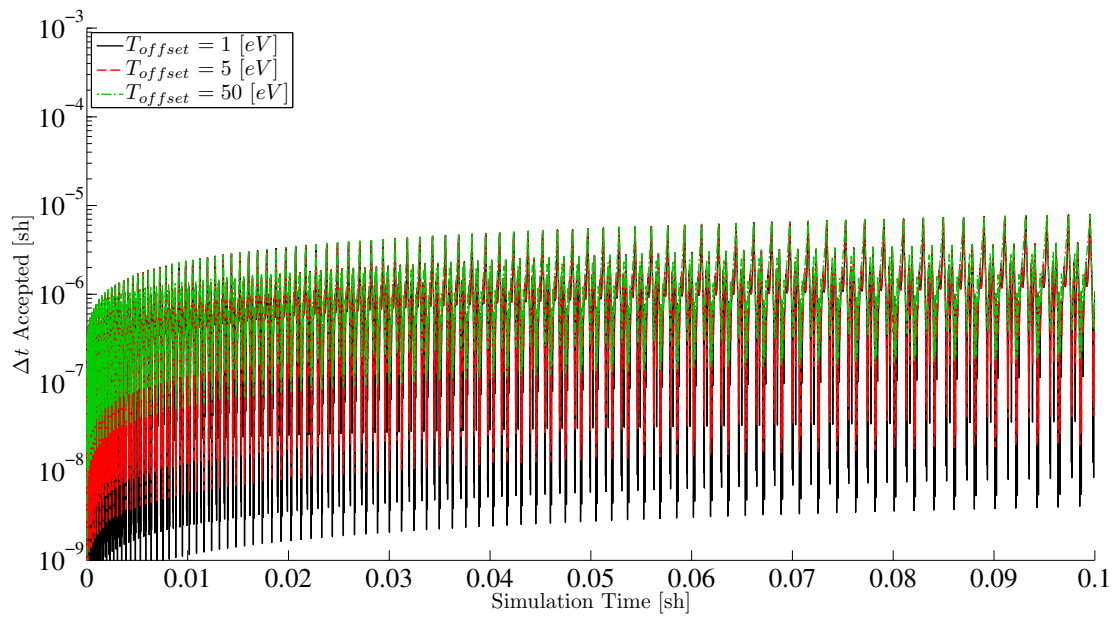


Figure 7.76: Time step sizes for modified point-wise adaptive criteria for cubic SLXS Lobatto discretization of the physical Marshak wave problem with different  $T_{offset}$ .

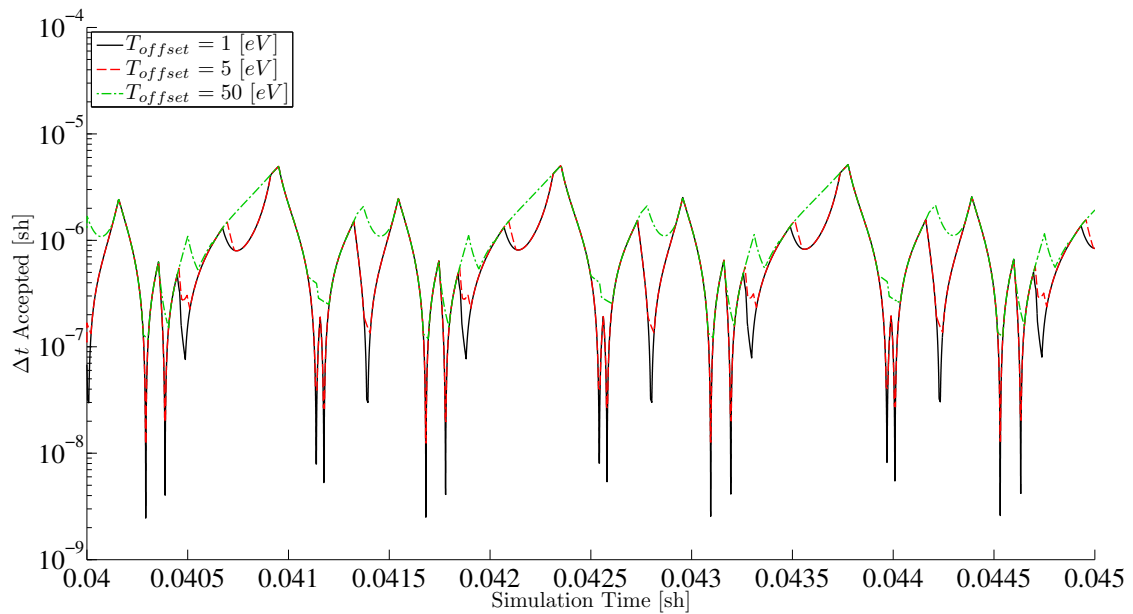


Figure 7.77: Time step sizes for modified point-wise adaptive criteria for cubic SLXS Lobatto discretization of the physical Marshak wave problem with different  $T_{offset}$ .

criteria. At early times, such as those considered in Fig. 7.78, the accumulation of

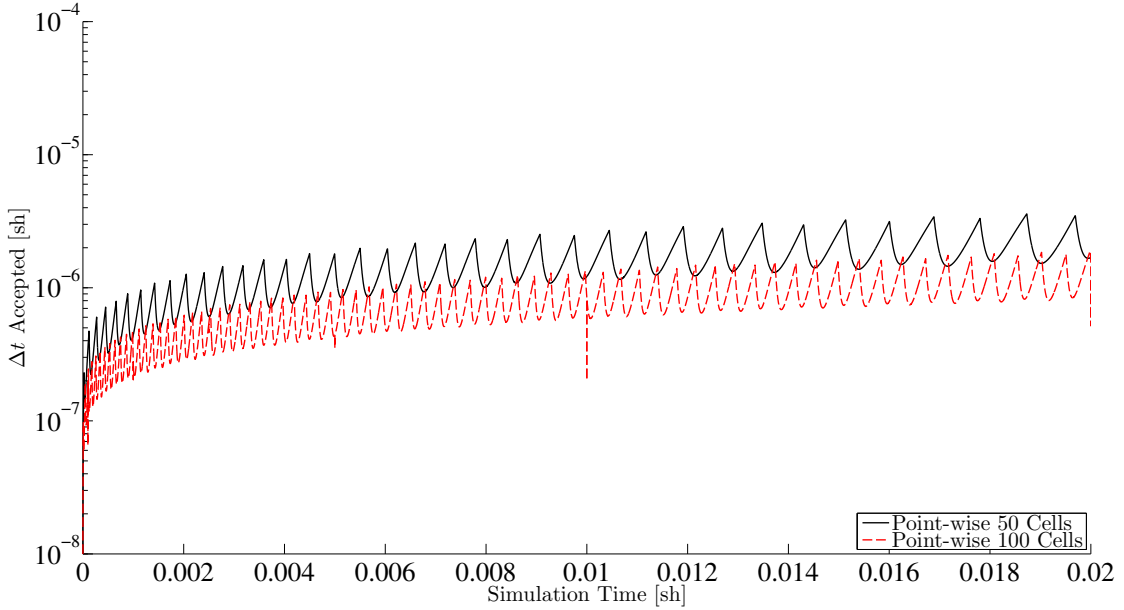


Figure 7.78: Zoom in of  $\Delta t$  trace for the modified point-wise adaptive criteria using linear SLXS Lobatto discretizations of the physical Marshak wave problem with 50 and 100 cells.

temporal errors is minimal, and despite the different spatial resolutions affecting wavefront location, for our purposes here, we assume the thermal waves are at the same position in the simulation. Under this assumption, it is clear that there are twice as many  $\Delta t$  spikes with the 100 cell scheme than there are with the 50 cell scheme. It is worth noting that even after 20% of the simulation,  $t = 0.02$  [sh], the  $\Delta t$  traces of the different spatial resolution begin to move out of phase. We note that the apparent ratio of the 50 cell maximum and minimum  $\Delta t$  to the 100 cell maximum and minimum  $\Delta t$  at identical simulation times is roughly equal to two. Figure 7.79 plots the time trace of simulations that use linear and cubic SLXS Lobatto, each

with 100 cells. Clearly the cubic DFEM scheme has significantly more features. The cubic DFEM time trace retains the same periodicity at the cell level, but within each cell there is a complex structure associated with the thermal wave advancing across individual degrees of freedom within each cell.

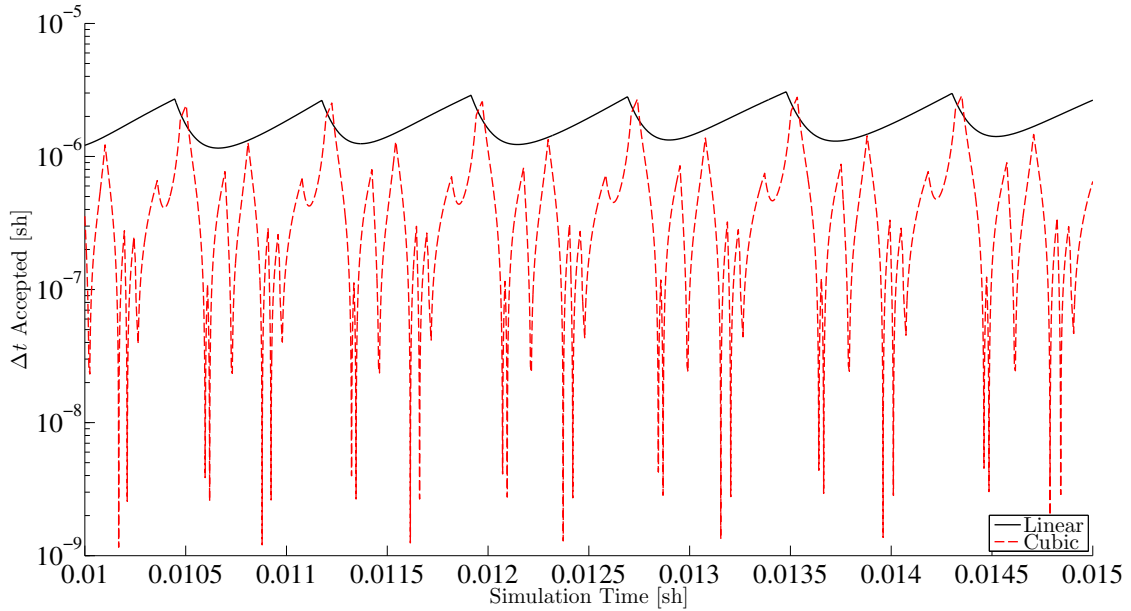


Figure 7.79: Time step traces for the modified point-wise adaptive scheme with  $T_{offset} = 1 \text{ [eV]}$  for linear and cubic SLXS Lobatto with 100 spatial cells.

Though the volumetric adaptive criterion with  $N_{cg} = 1$  requires more than twice as many time steps to solve the same Marshak wave problem with cubic rather than linear DFEM, the modified point-wise scheme requires more than  $7\times$  time steps to solve the same problem with cubic rather than linear DFEM. Additionally, the modified point-wise adaptive criterion is not universally applicable without sufficient  $T_{offset}$ , as evidenced by the failure the modified point-wise adaptive criterion for  $T_{offset} = 0 \text{ [eV]}$ , and exceedingly high number of time steps required with  $T_{offset} =$

$1 [eV]$ . Consider now the trace of  $\Delta t$  selection as a function of time in the simulation in Fig. 7.80 for the modified point-wise scheme with  $T_{offset} = 5 [eV]$  to the volumetric adaptive criterion with  $N_{cg} = 1$ . Using the volumetric adaptive scheme, we see the

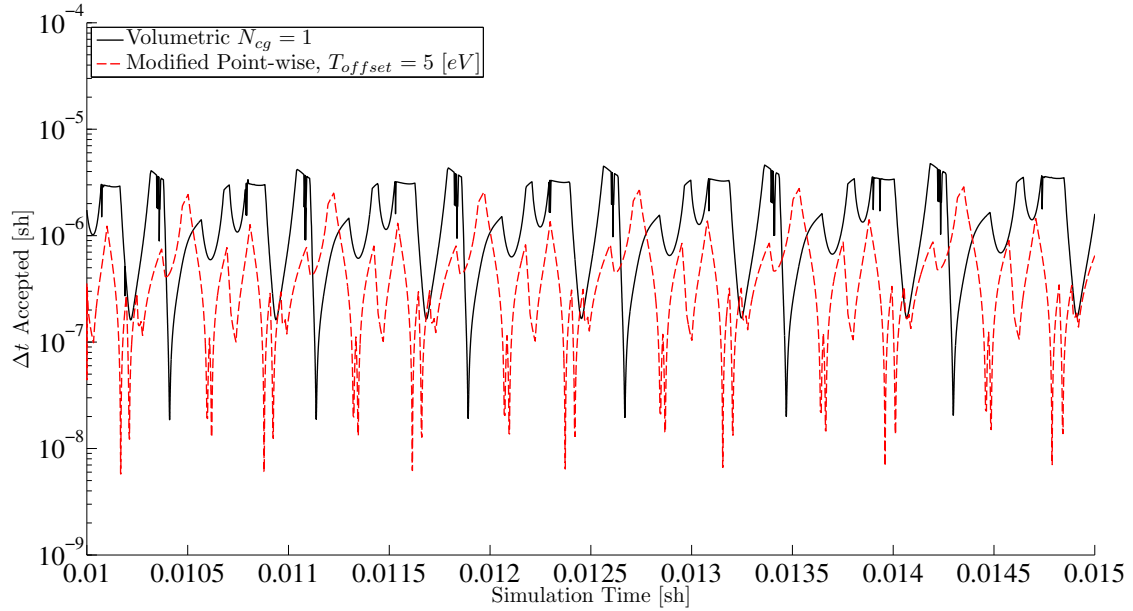


Figure 7.80: Time step sizes for volumetric and modified point-wise adaptive criteria for cubic SLXS Lobatto discretization of the physical Marshak wave problem.

same types of features in the time step size trace as we observed with the modified point-wise scheme: peak/valley pairs as the thermal wave through the mesh, as well as a complex structure of dips and peaks associated with the higher order spatial discretization. However the volumetric scheme, smooths corresponding modified point-wise  $\Delta t$  trace structures significantly; several of the very large dips in  $\Delta t$  taken by the modified point-wise scheme do not appear, or are averaged out by the volumetric adaptive criteria with  $N_{cg} = 1$ . Given that the maximum and minimum  $\Delta t$  chosen by each adaptive criterion are of the same order, we conclude that the

volumetric adaptive scheme with  $N_{cg} = 1$  takes approximately a quarter of the time steps taken by the modified point-wise adaptive scheme with  $T_{offset} = 5$  [eV] because the volumetric adaptivity scheme minimizes and smooths a number of very rapid transients the modified point-wise  $\Delta t$  trace takes.

Table 7.2 demonstrates that larger values of  $N_{cg}$  take significantly larger average time steps, but how does  $\Delta t$  selection vary for different  $N_{cg}$  as a function of time? In Fig. 7.81, the two extrema of  $N_{cg}$  for this particular spatial discretization, there appear to be no significant differences between the trend in time of the different values of  $N_{cg}$ , with the exception that for  $N_{cg} = 100$ ,  $\Delta t$  is chosen approximately  $10 \times - 100 \times$  larger than  $\Delta t$  for  $N_{cg} = 1$ . Both  $N_{cg} = 1$  and  $N_{cg} = 100$  have the peaks and valleys associated with the thermal wave passing through the spatial mesh.

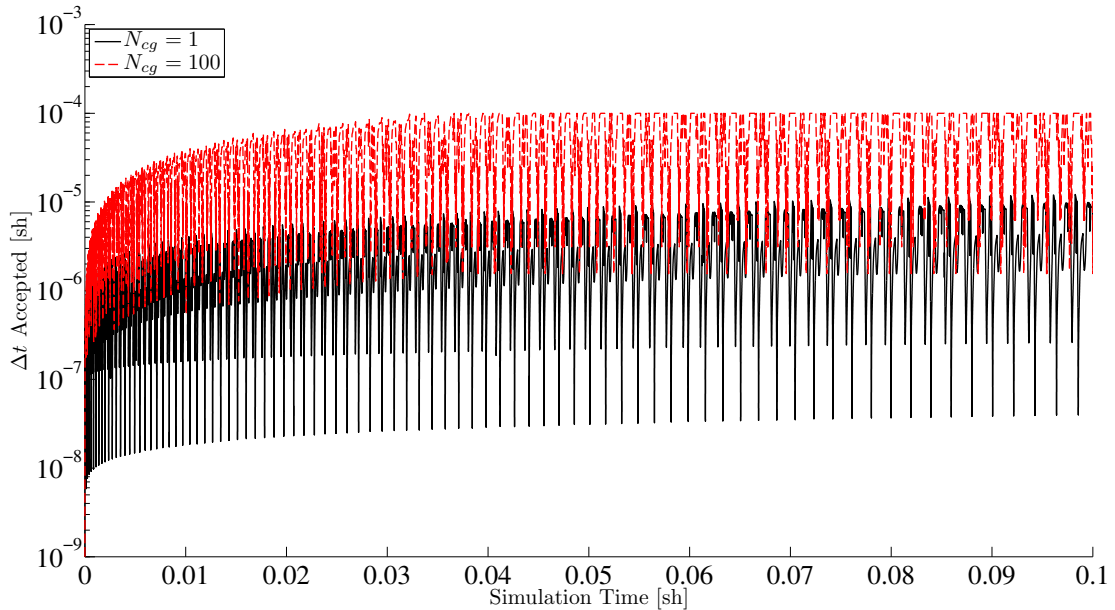


Figure 7.81: Time step sizes for volumetric adaptive criteria with  $N_{cg} = 1$  and  $N_{cg} = 100$  for cubic SLXS Lobatto in 100 cell physical Marshak wave problem.

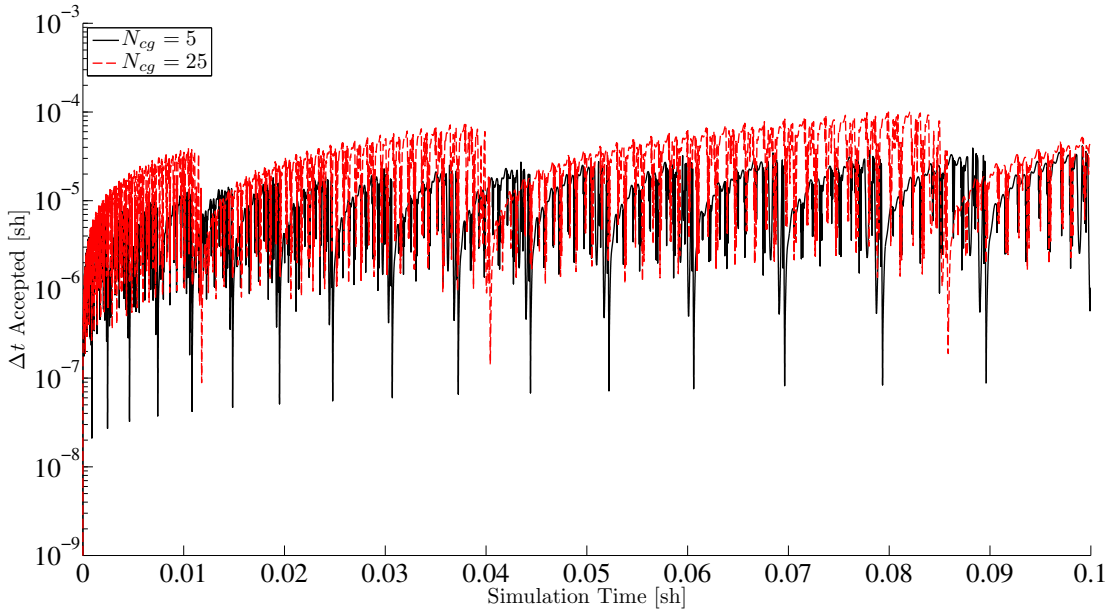


Figure 7.82: Time step sizes for volumetric adaptive criteria with  $N_{cg} = 1$  and  $N_{cg} = 100$  for cubic SLXS Lobatto in 100 cell physical Marshak wave problem.

This is not the case for intermediate values of  $N_{cg}$ . Consider Fig. 7.82 that plots  $\Delta t$  selected during the simulation for the volumetric adaptive criterion using  $N_{cg} = 5$  and  $N_{cg} = 25$ . The dips we have thus far seen and associated with the thermal wave crossing individual mesh cells are present, but in Fig. 7.82, there are additional lower frequency dips in  $\Delta t$ . These slower, periodic drops in  $\Delta t$  are associated with the thermal wave crossing from one volumetric adaptive grouping into another. If a problem was run until the slab was at a uniform temperature, i.e. the thermal wave has passed entirely through the slab, there would be  $N_{groups} - 1$  repetitive groupings.

Finally, we wish to examine whether the vastly different values of time steps taken by the different adaptive criteria result in significant differences in solution representation. As no analytic solution exists, we must simply compare the results of simulations that use different adaptive criteria at some selected time value. Assum-

ing that any temporal introduced by taking too large of a time step accumulates, we look at the angle integrated intensity and temperature solutions at  $t = 0.1$  [sh]. Further, assuming that the largest differences occur between the simulation that took the most time steps and the simulation that took the fewest time steps, in Figs. 7.83-7.84 we compare the angle integrated intensity and temperature solutions of simulations that use either the modified point-wise adaptive criterion with  $T_{offset} = 1$  [eV] or the volumetric adaptive criterion with  $N_{cg} = 100$ . Despite the modified point-wise

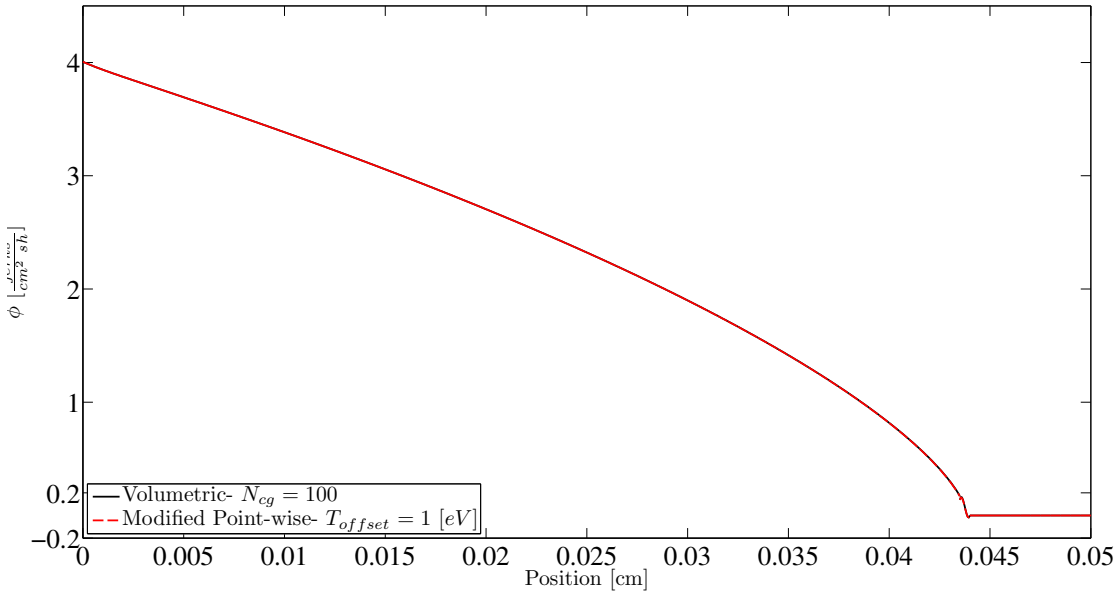


Figure 7.83: Comparison of angle integrated intensity for different adaptive criteria at  $t = 0.1$  [sh].

scheme with  $T_{offset} = 1$  [eV] using nearly  $95\times$  more time steps than the volumetric criterion with  $N_{cg} = 100$ , with this level of spatial accuracy, there is no appreciable visual difference between the two solutions when considering the problem as a whole, suggesting that the volumetric adaptive criteria is more efficient than the modified

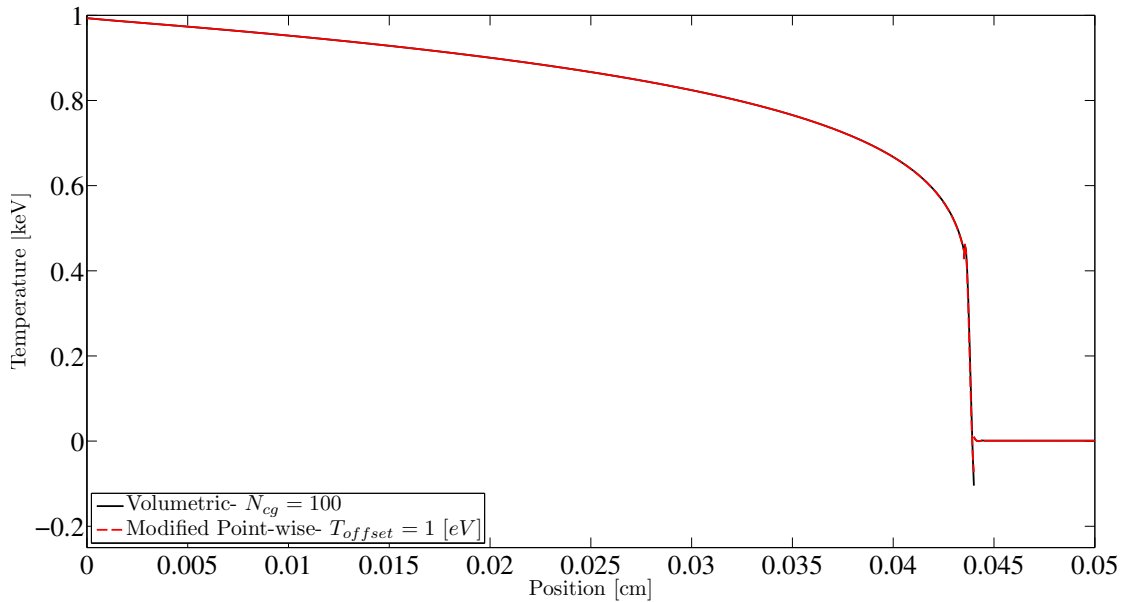


Figure 7.84: Comparison of temperature for different adaptive criteria at  $t = 0.1$  [sh].

point-wise criteria when applied to higher order DFEM TRT simulations. Even when focusing in on the Marshak wavefront, as in Fig. 7.85 and Fig. 7.86, the difference between the cubic physical Marshak wave simulations with different adaptive time criteria is small when compared against the difference between a cubic physical Marshak wave problem cubic result and a linear SLXS Lobatto result that uses the same number of mesh cells, and the point-wise adaptive criteria.

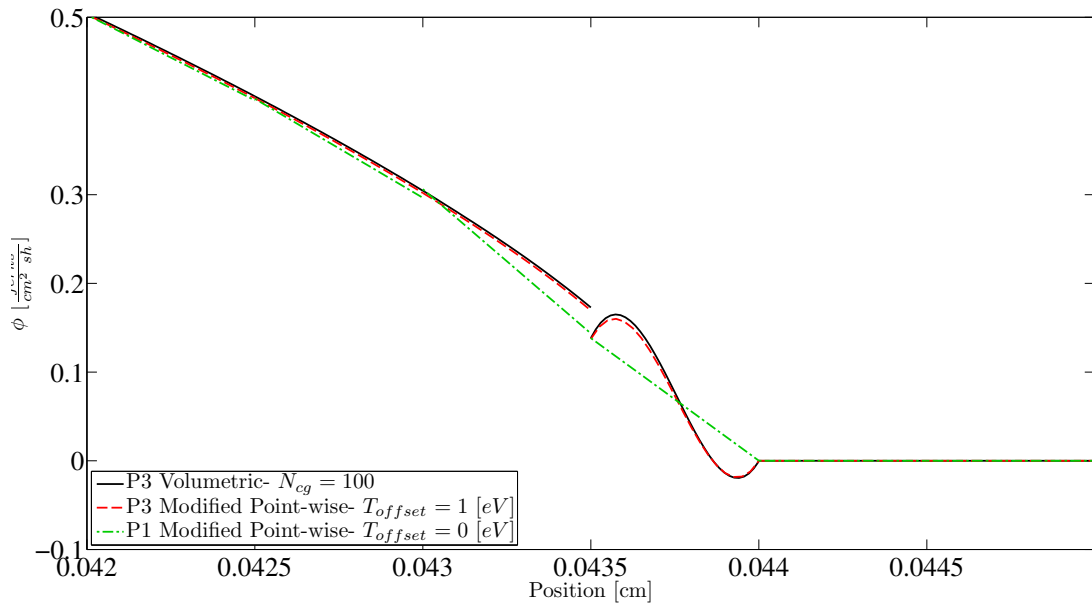


Figure 7.85: Comparison of angle integrated intensity for different adaptive criteria at  $t = 0.1$  [sh] with cubic SLXS Lobatto using 100 cells vs. linear SLXS Lobatto using 100 cells and the point-wise adaptive criteria.

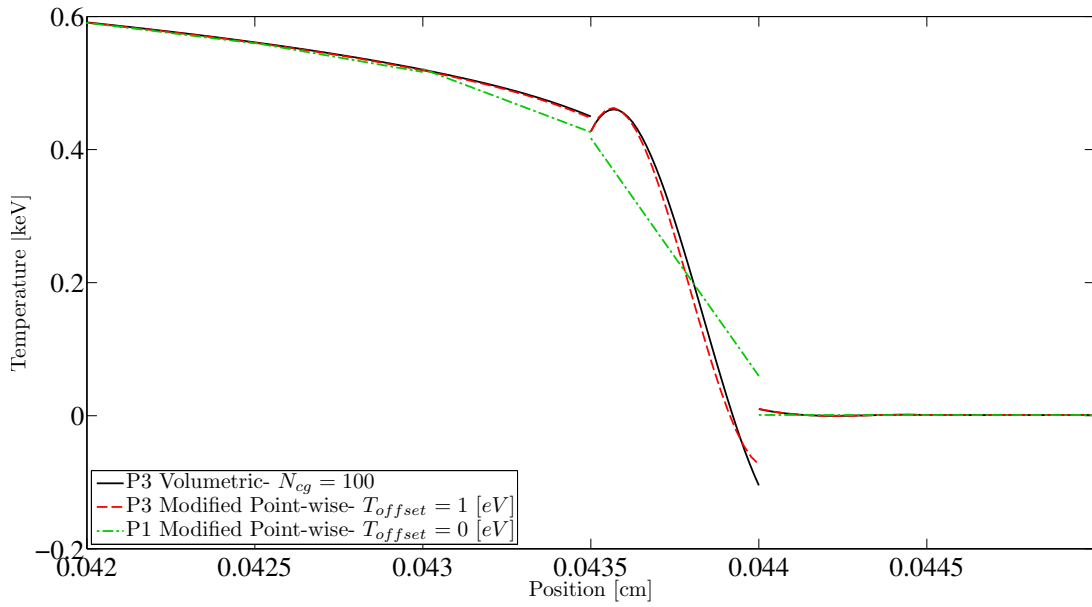


Figure 7.86: Comparison of temperature for different adaptive criteria at  $t = 0.1$  [sh] with cubic SLXS Lobatto using 100 cells vs. linear SLXS Lobatto using 100 cells and the point-wise adaptive criteria.

### 7.3 Effectiveness of MIP DSA for TRT Iterative Acceleration

As of yet, we have failed to discuss the iterative performance of the modified interior penalty diffusion synthetic operator (MIP DSA) applied to the grey thermal radiative transfer equations. Though the problems we have considered are not necessarily optically thick or diffusive, we have used MIP DSA to iteratively solve all problems. A large number of the problems we have considered are not optically thick, in part because we were interested in spatial error convergence. In Table 7.3, we give a sampling of the average number of iterations required to update the intensity for a given thermal iteration for different MMS and unity Marshak wave simulations. Iteration counts for a designed optically thick and diffusive problem are given in Table 7.4.

Several observations can be made regarding the data in Table 7.3. Most importantly, MIP DSA applied to the grey TRT is a stable iterative scheme and at worst requires as many iterations as source iteration alone. Also, the number of iterations for MIP DSA and SI are nearly equal only for most of the problems we have considered. Finally, MIP DSA is compatible with the self-lumping DFEM schemes we have developed that explicitly account for the within cell variation of opacity and heat capacity.

To demonstrate the iterative effectiveness of MIP DSA we now present a problem designed solely to be optically thick and diffusive. We again define a dimensionless problem,  $a = c = 1$ . We assume a constant  $C_v = 0.05$ , define  $x \in [0, 100]$ ,  $t \in [0, 5]$ ,  $\sigma_s = 0$ , and  $\sigma_a = \frac{5000}{T^2}$ . We are motivated to choose  $\sigma_a \propto \frac{1}{T^2}$  to ensure that as the problem heats up,  $\nu \rightarrow 1$ . In the cases where  $\sigma_a \propto \frac{1}{T^3}$ , the  $\sigma_a D_*$  components of  $\nu$  cancel one another out, in terms of functional temperature dependence. Initially, the slab is in thermodynamic equilibrium at a temperature of  $T = 0.5$ , and is heated

Table 7.3: Iteration count for different TRT model problems.

Problem Description	Scheme	Average DSA+SI Iterations	Average SI Iterations
MMS Constant Time 4 cells	Linear SLXS Lobatto	1.4	2.4
MMS Constant Time 8 cells	Cubic SLXS Lobatto	1.6	2.3
MMS Constant Time 128 cells	Cubic SLXS Lobatto	1.8	1.8
MMS1 2 cells	Quadratic SLXS Gauss	2.0	13.5
MMS1 32 cells	Quadratic SLXS Gauss	3.0	13.6
MMS1 128 cells	Quadratic SLXS Gauss	4.0	13.5
MMS1 256 cells	Quadratic SLXS Gauss	4.2	13.5
MMS2 2 cells	Linear SLXS Gauss	1.0	2.7
MMS Constant Space Alexander 3-3, $\Delta t = 1$	Quartic SLXS Lobatto	17.0	39.0
MMS Constant Space Alexander 3-3, $\Delta t = \frac{1}{8}$	Quartic SLXS Lobatto	6.6	11.7
MMS Constant Space Alexander 3-3, $\Delta t = \frac{1}{128}$	Quartic SLXS Lobatto	2.3	4.9
Unity Marshak Wave 20 cells, largest $\Delta t$	Linear SLXS Lobatto	2.1	2.9

with an incident current of 100 on the left hand side of the slab. We discretize the problem with linear SLXS Lobatto using 50 spatial cells, implicit Euler in time differencing, and a maximum time step size of  $\Delta t_{max} = 0.1$ . The average number of transport iterations per thermal iteration is given in Table 7.4. Clearly, MIP DSA

Table 7.4: Iteration count for a very optically thick TRT problem.

Intensity Iterative Strategy	Average Intensity Iterations Per Thermal Iteration
DSA	10
SI	18378

can significantly reduce the iterative work required to solve the grey TRT equations, but the majority of problems we have considered are not very optically thick.

In optically thick and diffusive problems such as this, the traditional convergence condition of

$$\frac{\|\phi^{(\ell+1)} - \phi^{(\ell)}\|}{\|\phi^{(\ell+1)}\|} < \epsilon_\phi, \quad (7.34)$$

can lead to false convergence [61]. Noting that our chosen point-wise convergence condition `change_phi < epsilon_phi`, repeated here from Eq. (6.127)

$$\text{change\_phi} = \max_{c=1}^{N_{cell}} \left[ \max_{j=1}^{N_P} \left[ \left| \frac{\phi_{c,j}^{(\ell+1)} - \phi_{c,j}^{(\ell)}}{\phi_{c,j}^{(\ell+1)}} \right| \right] \right]. \quad (7.35)$$

is not a true mathematical norm, we would still like to investigate the issue of false convergence. To do so, we use the  $L^1$  norm variant of Eq. (7.34):

$$\frac{\|\phi^{(\ell+1)} - \phi^{(\ell)}\|_{L^1}}{\|\phi^{(\ell+1)}\|_{L^1}} < \epsilon_\phi. \quad (7.36)$$

As shown in [61], we may eliminate false convergence by normalizing our convergence condition with  $1 - \rho$ ,

$$\frac{\|\phi^{(\ell+1)} - \phi^{(\ell)}\|_{L^1}}{(1 - \rho) \|\phi^{(\ell+1)}\|_{L^1}} < \epsilon_\phi, \quad (7.37)$$

where  $\rho$  is the spectral radius, which we estimate as:

$$\rho \approx \frac{\|\phi^{(\ell+1)} - \phi^{(\ell)}\|_{L^1}}{\|\phi^{(\ell)} - \phi^{(\ell-1)}\|_{L^1}}. \quad (7.38)$$

In Table 7.5, we plot the average number of iterations required to converge  $\phi$  for each time step for our optically thick and diffusive test problem. For all methods, we used  $\epsilon_\phi = 10^{-10}$ . Table 7.5 clearly indicates that for optically thick, diffusive problems,

Table 7.5: Average number of inner iterations per thermal iteration using different convergence criteria.

	change_phi < $\epsilon_\phi$	$\frac{\ \phi^{(\ell+1)} - \phi^{(\ell)}\ _{L^1}}{\ \phi^{(\ell+1)}\ _{L^1}} < \epsilon_\phi$	$\frac{\ \phi^{(\ell+1)} - \phi^{(\ell)}\ _{L^1}}{(1-\rho)\ \phi^{(\ell+1)}\ _{L^1}} < \epsilon_\phi$
SI	18378	6382	22563
DSA	10	7	7

the near unity spectral radius can lead to false iterative convergence, and as such should be accounted for explicitly via Eq. (7.37). We also remark that our choice of using  $\|\phi^{(\ell+1)}\|_{L^1}$  as a physical scaling constant could possibly be improved upon, as  $\|\phi^{(\ell+1)}\|_{L^1}$  is dominated by the already heated region, whereas the greatest changes in  $\phi$  are occurring near the thermal wavefront.

## 8. SUMMARY AND CONCLUSIONS

### 8.1 Summary

In this dissertation we have developed a new family of interpolatory DFEM spatial discretizations for discrete ordinates radiation transport. This set of DFEM schemes is unique in that it is not limited to equally-spaced DFEM interpolation points, automatically generates diagonal mass matrices, can be used with DFEM trial spaces of arbitrary degree, and can explicitly account for the within cell variation of material properties such as interaction cross section. We have tested this new family of DFEM techniques in a variety of slab geometry radiation transport applications including steady-state neutron transport, criticality, and time dependent thermal radiative transfer simulations.

Additionally, we have demonstrated that some canonical methods of discrete ordinates radiation transport do not always behave as expected. First, we showed that the traditional method of mass matrix lumping limits solution accuracy for higher degree polynomial trial spaces and is robust with a linear DFEM trial space. Later, we demonstrated that the usual assumption of a cell-wise constant interaction cross section has several negative effects in problems with spatially varying interaction cross sections. Across all application areas considered, the assumption of a cell-wise constant cross section for problems that had cross section variation within individual mesh cells resulted in a fundamental limit on spatial order of convergence, and generated non-smooth interaction rates. The non-smooth neutron transport interaction rates manifested themselves in our thermal radiative transfer results as a material temperature solution that contained large, non-monotonic discontinuities. Mesh refinement can reduce the severity of the thermal radiative transfer tempera-

ture solution discontinuities, but cannot eliminate the discontinuities. Not only are the discontinuities non-physical and a sign of limited spatial order of convergence, they also complicate and can inhibit the non-linear temperature iteration required to solve the thermal radiative transfer equations.

## 8.2 Conclusions

There are two main conclusions to be made from this dissertation.

1. Self-lumping DFEM schemes using Gauss-Legendre (SL Gauss) or Gauss-Lobatto-Legendre (SL Lobatto) quadrature as the DFEM interpolation points are well suited to discrete ordinates radiation transport calculations.
2. Self-lumping schemes are easily modified to explicitly account for the within cell variation of material properties, resulting in methods that are significantly more accurate for problems with spatially varying material properties than those that assume cell-wise constant material properties.

In neutron transport, criticality, and thermal radiative transfer simulations, both SL Gauss and SL Lobatto converge the  $L^2$  norm of the angular flux error  $\propto P + 1$  for problems with cell-wise constant cross section. SL Lobatto is robust for all odd degree DFEM trial spaces, and SL Gauss is robust for all even degree trial spaces, assuming cell-wise constant cross section. Further, SL Lobatto is equivalent to traditional lumping for linear DFEM, but unlike traditional lumping DFEM schemes, SL Lobatto increases in spatial order of convergence with increased trial space degree.

Self-lumping DFEM schemes easily account for the variation of interaction cross or other material properties. A  $P$  degree self-lumping scheme using Gauss or Lobatto quadrature only requires  $P + 1$  material property evaluations to obtain schemes that converge the  $L^2$  norm of the angular flux or radiation intensity  $\propto P + 1$ . This is

in contrast to DFEM schemes that assume a cell-wise constant cross yielding only second order spatial convergence, regardless of trial space degree, for problems with spatially varying interaction cross sections. In our neutron transport test problems, SLXS Lobatto and SLXS Gauss (the variants of SL Lobatto and SL Gauss that explicitly account for within cell variation of material properties), converged interaction rate and interaction rate dependent quantities  $\propto P + 1$ . However, in our thermal radiative transfer MMS testing SLXS Lobatto converged the  $L^2$  error of temperature, a quantity driven by an interaction rate,  $\propto P$ . Though not  $P + 1$  as we had hoped, given the non-linear nature of the thermal radiative transfer equations, and necessity to integrate much higher order polynomials, e.g. the Planckian term that is a  $P^4$  degree polynomial, order  $P$  convergence is still promising, as it still allows for increased accuracy with increasing DFEM trial space degree. More surprising is that SLXS Gauss applied to the grey TRT appears to converge the  $L^2$  error of temperature  $\propto P + 2$ . It should be noted though that the orders of convergence we have given here are effectively only experimental observations, and there was some disagreement between the apparent orders of convergence for certain error quantities between test problems.

### 8.2.1 Future Work

There are several exciting avenues for continued study and advancement if the topics and methods covered in this dissertation. Clearly the extension of this slab geometry work to multiple spatial dimensions is required for problems of greater scientific and engineering interest and complexity. Additionally, MIP DSA appeared to be an effective iterative acceleration technique for the grey TRT equations, and as such we would like to see how it performs as the diffusion operator for linear multi-frequency grey acceleration of the multi-group/multi-frequency thermal radiative

transfer equations.

Topics of research beyond simply extending our methodology are abundant as well. A non-exhaustive list includes:

1. developing a theory to explain and apriori predict whether a given matrix lumping technique will yield a robust solution,
2. explaining the apparent super convergence of SLXS Gauss for the TRT temperature solution,
3. conducting a diffusion limit analysis of higher order trial space DFEM, and
4. developing additional TRT manufactured solutions that challenge spatial discretization more completely and are closer to real-world applications in both nature and scaling.

## REFERENCES

- [1] E. E. Lewis and W. F. Miller. *Computational Methods of Neutron Transport*. American Nuclear Society, La Grange Park, IL, 1993.
- [2] R. Alexander. Diagonally implicit Runge-Kutta methods for stiff O.D.E.'s. *SIAM Journal of Numerical Analysis*, 14(6):1006–1021, 1977.
- [3] W. H. Reed, T. R. Hill, F. W. Brinkley, and K. D. Lathrop. TRIPLET: A two-dimensional, multigroup, triangular mesh, planar geometry, explicit transport code. Technical Report LA-5428-MS, Los Alamos Scientific Lab, 1973.
- [4] E. W. Larsen and P. Nelson. Finite-difference approximations and superconvergence for the discrete ordinates equations in slab geometry. *SIAM Journal of Numerical Analysis*, 19(2):334–348, 1982.
- [5] E. W. Larsen and J. E. Morel. Asymptotic solutions of numerical transport problems in optically thick, diffusive regimes II. *Journal of Computational Physics*, 83:212–236, 1989.
- [6] J. E. Morel, T. A. Wareing, and K. Smith. A linear-discontinuous spatial differencing scheme for  $S_N$  radiative transfer calculations. *Journal of Computational Physics*, 128:445–462, 1996.
- [7] M. L. Adams. Subcell balance methods for radiative transfer on arbitrary grids. *Transport Theory and Statistical Physics*, 26(4 &5):385–431, 1997.
- [8] M. L. Adams and P. F. Nowak. Asymptotic analysis of a computational method for time- and frequency- dependent radiative transfer. *Journal of Computational Physics*, 46:366–403, 1998.

- [9] C. C. Ober and J. N. Shadid. Studies on the accuracy of time-integration methods for the radiation-diffusion equations. *Journal of Computational Physics*, 195:743–772, 2004.
- [10] P. G. Maginot, J. C. Ragusa, and J. E. Morel. Characterization of high order spatial discretizations and lumping techniques for discontinuous finite element  $S_N$  transport. In *International Conference on Mathematics and Computational methods, Applied to Nuclear Science and Engineering*, Sun Valley, Idaho, May 2013.
- [11] P. G. Maginot, J. C. Ragusa, and J. E. Morel. Lumping techniques for DFEM transport in  $S_N$  transport in slab geometry. *Nuclear Science and Engineering*, 179(2):148–163, 2015.
- [12] E. W. Larsen and W. F. Miller. Convergence rates of spatial difference equations for the discrete-ordinates neutron transport equations in slab geometry. *Nuclear Science and Engineering*, 73:76–83, 1980.
- [13] S. Hamilton, M. Benzi, and J. S. Warsa. Negative flux fixups in discontinuous finite element  $S_N$  transport. In *International Conference on Mathematics, Computational Methods & Reactor Physics*, Saratoga Springs, New York, May 2009.
- [14] P. G. Maginot, J. E. Morel, and J. C. Ragusa. A non-negative moment preserving spatial discretization scheme for the linearized boltzmann transport equation in 1-D and 2-D cartesian geometries. *Journal of Computational Physics*, 231(20):6801–6826, 2012.
- [15] M. L. Adams. Discontinuous finite element transport solutions in thick diffusive problems. *Nuclear Science and Engineering*, 137:298–333, 2001.

- [16] W. F. Walters. The relation between finite element methods and nodal methods in transport theory. *Progress in Nuclear Energy*, 18:21–26, 1986.
- [17] J. P. Hennart and E. del Valle. A generalized nodal finite element formalism for discrete ordinate equations in slab geometry: Part II theory in the discontinuous moment case. *Transport Theory and Statistical Physics*, 24:479–504, 1995.
- [18] J. P. Hennart and E. del Valle. A generalized nodal finite element formalism for discrete ordinate equations in slab geometry: Part III numerical results. *Transport Theory and Statistical Physics*, 24:505–533, 1995.
- [19] J. S. Warsa and A. K. Prinja. p-adaptive numerical methods for particle transport. *Transport Theory and Statistical Physics*, 28(3):229–270, 1999.
- [20] Y. Wang and J. C. Ragusa. On the convergence of DGFEM applied to the discrete ordinates transport equation for structured and unstructured triangular meshes. *Nuclear Science and Engineering*, 163:56–72, 2009.
- [21] Y. Wang and J. C. Ragusa. A high-order discontinuous Galerkin method for the  $S_N$  transport equations on 2D unstructured triangular meshes. *Annals of Nuclear Energy*, 36(7):931–939, 2009.
- [22] K. D. Lathrop. Spatial differencing of the transport equation: Positivity vs. accuracy. *Journal of Computational Physics*, 4:475–498, 1969.
- [23] P. A. Raviart. The use of numerical integration in finite element methods for solving parabolic equations. In *Conference on Numerical Analysis, RIANA 1972*, pages 233–264, August 1972.
- [24] M. Abramowitz and I. A. Stegun. *Handbook of Mathematical Functions with Formulas, Graphs, and Mathematical Tables*. United States Department of Commerce, Washington, D.C., 1972.

- [25] V. Thomée. *Galerkin Finite Element Methods for Parabolic Problems*. Springer, New York, 1997.
- [26] The MathWorks. MATLAB 2011b, 2011.
- [27] W. M. Stacey. *Nuclear Reactor Physics*. John-Wiley & Sons Inc., 2001.
- [28] J. E. Morel, T.-Y. B. Yang, and J. S. Warsa. Linear multifrequency-grey acceleration recast for preconditioned Krylov iterations. *Journal of Computational Physics*, 227:244–264, 2007.
- [29] J. S. Warsa, T. A. Wareing, and J. E. Morel. Krylov iterative methods and the degraded effectiveness of diffusion synthetic acceleration for multidimensional  $S_N$  calculations in problems with material discontinuities. *Nuclear Science and Engineering*, 147(3):218–248, 2004.
- [30] A. Kavenoky and J. Lautard. A finite element depletion diffusion calculation method with space-dependent cross section. *Nuclear Science and Engineering*, 64(2):563–575, 1977.
- [31] S. Santandrea and P. Bellier. An unstructured characteristics scheme with a linear expansion for both fluxes and cross sections. In *Proceedings of the Joint International Topical Meeting on Mathematics & Computation and Supercomputing in Nuclear Applications (M&C + SNA 2007)*, Monterey, California, April 2007.
- [32] P. G. Maginot, J. C. Ragusa, and J. E. Morel. Accurate methods for dfem  $S_N$  transport in slab geometry for non-piecewise constant cross section problems. *Annals of Nuclear Energy*, 73:506–526, 2014.
- [33] G. Bell and S. Glasstone. *Nuclear Reactor Theory*. Van Nostrand Rienhold, Inc., New York, NY, 1970.

- [34] L. J. Lorence, J. E. Morel, and E. W. Larsen. An  $S_2$  synthetic acceleration scheme for the one-dimensional  $S_N$  equations with linear discontinuous spatial differencing. *Nuclear Science and Engineering*, 101:341–351, 1989.
- [35] Y. Wang and J. C. Ragusa. Diffusion synthetic acceleration for high-order discontinuous finite element  $S_N$  transport schemes and application to locally refined unstructured meshes. *Nuclear Science and Engineering*, 166:145–166, 2010.
- [36] E. W. Larsen. Unconditionally stable diffusion-synthetic acceleration methods for the slab geometry discrete ordinates equations. *Nuclear Science and Engineering*, 82:47–63, 1982.
- [37] E. M. Gelbard and L. A. Hageman. Synthetic methods as applied to  $S_N$  equations. *Nuclear Science and Engineering*, 37(2):288–298, 1969.
- [38] M. L. Adams and W. R. Martin. Diffusion synthetic acceleration of discontinuous finite element transport iterations. *Nuclear Science and Engineering*, 111:145–167, 1992.
- [39] J. S. Warsa, T. A. Wareing, and J. E. Morel. Fully consistent diffusion synthetic acceleration of linear discontinuous  $S_N$  transport discretization on unstructured tetrahedral meshes. *Nuclear Science and Engineering*, 141:236–251, 2002.
- [40] T. A. Wareing, E. W. Larsen, and M. L. Adams. Diffusion accelerated discontinuous finite element schemes for the  $S_N$  equations in slab and X-Y geometries. In *Advances in Mathematics, Computations, and Reactor Physics*, Pittsburgh, Pennsylvania, April 28-May 2 1991.
- [41] B. Turcksin and J. C. Ragusa. A diffusion synthetic acceleration scheme for rectangular geometries based on bilinear discontinuous finite elements. In *In-*

*ternational Conference on Mathematics and Computational methods, Applied to Nuclear Science and Engineering*, Sun Vlley, Idaho, May 2013.

- [42] Y. Wang. *Adaptive Mesh Refinement Solution Techniques for the Multigroup  $S_N$  Transport Equations Using a Higher-Order Discontinuous Finite Element Method*. PhD thesis, Texas A&M University, 2009.
- [43] J. S. Warsa, T. A. Wareing, J. E. Morel, J. M. McGhee, and R. B. Lehoucq. Krylov subspace iterations for deterministic  $k$ -eigenvalue calculations. *Nuclear Science and Engineering*, 147:26–42, 2004.
- [44] E. W. Larsen, A. Kumar, and J. E. Morel. Properties of the implicitly time-differenced equations of thermal radiation transport. *Journal of Computational Physics*, 238:82–96, 2013.
- [45] J. E. Morel, B. T. Adams, T. Noh, T. M. Evans J. M. McGhee, and T. J. Urbatsch. Spatial discretizations for self-adjoint forms of the radiative transfer equations. *Journal of Computational Physics*, 214:12–40, 2006.
- [46] J. D. Edwards, J. E. Morel, and D. A. Knoll. Nonlinear variants of the TR/BDF2 method for thermal radiative diffusion. *Journal of Computational Physics*, 230:1198–1214, 2011.
- [47] B. Stroustrup. *Programming: Principles and Practice Using C++*. Pearson Education Inc., Upper Saddle River, New Jersey, 2nd edition, 2014.
- [48] S. Meyers. *Effective C++*. Pearson Education Inc., Upper Saddle River, New Jersey, 3rd edition, 2005.
- [49] J. Burkhardt. QUADRULE. [http://people.sc.fsu.edu/~jburkardt/cpp\\_src/quadrule/quadrule.html](http://people.sc.fsu.edu/~jburkardt/cpp_src/quadrule/quadrule.html), 2011.

- [50] Gaël Guennebaud, Benoît Jacob, et al. Eigen v3. <http://eigen.tuxfamily.org>, 2010.
- [51] S. Balay, S. Abhyankar, M. F. Adams, J. Brown, P. Brune, K. Buschelman, V. Eijkhout, W. D. Gropp, D. Kaushik, M. G. Knepley, L. C. McInnes, K. Rupp, B. F. Smith, and H. Zhang. PETSc users manual. Technical Report ANL-95/11 - Revision 3.5, Argonne National Laboratory, 2014.
- [52] V.E. Henson and U.M. Yang. BoomerAMG: a parallel algebraic multigrid solver and preconditioner. *Applied Numerical Mathematics*, 41:155–177, 2002.
- [53] D. van Hessch. Doxygen manual. <http://www.stack.nl/~dimitri/doxygen/index.html>, 2015.
- [54] Kitware. CMake, a cross-platform open-source build system. <http://www.cmake.org>, 2003.
- [55] K. Salari and P. Knupp. Code verification by the method of manufactured solutions. Technical Report SAND2000-1444, Sandia National Labs, 2000.
- [56] L. Thomason and A. Ellerton Y. Berquin. TinyXml. [www.sourceforge.net/projects/tinyxml](http://www.sourceforge.net/projects/tinyxml), 2010. v2.6.0.
- [57] B. Su and G. L. Olson. An analytical benchmark for non-equilibrium radiative transfer in an isotropically scattering medium. *Annals of Nuclear Energy*, 24(13):1035–1055, 1997.
- [58] A. R. Long, N. A. Gentile, and T. S. Palmer. The iterative thermal emission method: A more implicit modification of IMC. *Journal of Computational Physics*, 277:228–247, 2014.

- [59] A. G. Petschek, R. E. Williamson, and J. K. Wooten Jr. The penetration of radiation with constant driving temperature. Technical Report LAMS-2421, Los Alamos Scientific Lab, 1960.
- [60] E. W. Larsen, J. E. Morel, and W. F. Miller. Asymptotic solutions of numerical transport problems in optically thick, diffusive regimes. *Journal of Computational Physics*, 69:283–324, 1987.
- [61] M. L. Adams and E. W. Larsen. Fast iterative methods for discrete-ordinates particle transport calculations. *Progress in Nuclear Energy*, 40(1):3–159, 2002.